MULTILAYERED SENSOR-ACTUATOR PLATES FOR ACTIVE MITIGATION OF ELASTOPLASTIC IMPACT EFFECTS

by

Akuro Big-Alabo

THESIS SUBMITTED IN FULFILMENT OF THE REQUIREMENTS FOR THE DEGREE OF DOCTOR OF PHILOSOPHY IN MECHANICAL ENGINEERING

SCHOOL OF ENGINEERING
COLLEGE OF SCIENCE AND ENGINEERING
UNIVERSITY OF GLASGOW

May 2015

Abstract

Analytical models have been used here to conduct detailed studies on the elastoplastic response of rectangular plates subjected to normal impact of a rigid sphere. Analytical models have been derived using a *complete modelling approach* in which the equations of motion of the contacting bodies (i.e. the plate and spherical impactor) and a compliance law for the local contact mechanics are used to formulate the impact model. To account for the local contact mechanics, a novel Meyer-type compliance model based on elastic-elastoplastic-fully plastic material behaviour has been formulated and validated using published experimental results. This compliance model was used to investigate the elastoplastic impact response of both transversely inflexible and transversely flexible rectangular plates. Particular attention has been given to solving the nonlinear impact models, leading to the development of a new algorithm to solve the nonlinear models of a half-space impact. The algorithm is simple, inherently stable and converges very quickly. For transversely flexible plate impact, investigations were centred on the elastoplastic impact response of a three-layer laminated plate structure called a *trimorph plate*. The understanding gained from investigating the elastoplastic impact response of an Al/PVDF/PZT trimorph plate was applied to study a newly proposed strategy for active mitigation of elastoplastic impact effects i.e. plastic deformation and/or damage. The idea behind the strategy was to use bonded piezoactuators to actively induce a state of pre-stress in the host layer, which in turn influenced the impact response of the plate. A preliminary qualitative analysis of the proposed strategy was conducted using analytically derived models for a PZT/Al/PZT trimorph plate and the results obtained showed that the proposed strategy can be used to achieve significant levels of mitigation against elastoplastic impact effects.

Table of contents

List of Tables

List of Figures

Acknowledgement

First and foremost, I wish to acknowledge the guidance of Almighty God in my research and the opportunity that He availed me to undertake a PhD research at this time.

I am very grateful to my supervisor, Dr. Philip Harrison, for the support and advice he gave. In particular, I appreciate the fact that he accepted to supervise me when there was a need to change my supervisor after my first year. Also, I wish to express my profound gratitude to my second supervisor, Professor Matthew P. Cartmell (from University of Sheffield), for his continued support, encouragement and advice throughout my research.

To Pastor Chima Dioka and members of the Deeper Christian Life Ministry (DCLM) Glasgow, you made my stay and life in Glasgow complete through the warm fellowship we shared all the time. I pray that God will increase your ministry, and that your message and charity will impact many more lives.

I would like to acknowledge the support of the administrative staff in the School of Engineering, especially Elaine McNamara. To all friends and colleagues at the University of Glasgow, I thank you for the good times we shared and the encouragement we received from one another by sharing our experiences.

To my brothers, Adokiye, Tamunopubo, Sotonye and Miebaka, and my mum, Mrs Kate Big-Alabo, thank you for helping me take care of my responsibilities in Nigeria while I was in Glasgow for my research. Lastly, but not the least, I would like to appreciate my loving wife, Mrs Ameze Big-Alabo, and my cherished daughter, Miss Boma Big-Alabo. Both of you brought an invaluable meaning to my life, and helped me to carry on during the most challenging stages of my research.

Finally, the financial support of the Commonwealth Scholarship Commission (CSC) United Kingdom, in the form of a full PhD Scholarship (CSC Award Reference: NGCA-2011-60) is gratefully acknowledged.

Author's Declaration

The work presented in this thesis is the original work of the author undertaken at the University of Glasgow. The copyright of the material in this thesis belongs to the author. Therefore, the author's permission should be obtained if any part of this thesis is to be reproduced in any form. However, where ideas and conclusions from this thesis are referred to in any academic endeavour, it is expected that the author would be properly acknowledged.

2015

Nomenclature

Abbreviations

CLPT	Classical Laminate Plate Theory
CPT	Classical Plate Theory
ESL	Equivalent Single Layer
FE	Finite Element
FEA	Finite Element Analysis
FILM	Force-Indentation Linearisation Method
FSDPT	First-order Shear Deformation Plate Theory
HSDPT	Higher-order Shear Deformation Plate Theory
MPT	Mindlin Plate Theory
ODE	Ordinary Differential Equation
PDE	Partial Differential Equation
PDEx	Partial Differential Expression
PVDF	Polyvinylidene Flouride
PZT	Lead Zirconate Titanate
RPT	Reissner Plate Theory
RTSDPT	Reddy Third-order Shear Deformation Plate Theory

Symbols

a	Length of plate in x-direction; contact radius
$\bar{a}_x; \bar{a}_y; \bar{a}_z$	Acceleration of plate in x-, y- and z-directions respectively
a_y	Contact radius at yield point
b	Length of plate in y-direction
c	Damping coefficient per unit area
d_{ij}	Piezoelectric stiffness coefficient; $i, j = 1, 2, 3, 4, 5$
e	Coefficient of restitution
h	Total thickness of plate
k_x^0	Curvature of the mid-plane of the plate about x-direction
k_{xy}^0	Curvature of the mid-plane of the plate about x-y plane
k_y^0	Curvature of the mid-plane of the plate about y-direction
m	Modal number in x-direction
m_i	Mass of impactor
m_p	Mass of plate
n	Modal number in y-direction; number of discretisations in the FILM

$q(x,y,t)$	Spatially distributed excitation
u; $u(x,y,z,t)$	Displacement of plate in x-direction
v; $v(x,y,z,t)$	Displacement of plate in y-direction
$w(t)$	Transverse displacement of plate in infinite plate impact model
w; $w(x,y,t)$	Transverse displacement of plate
$w_i(t)$	Displacement of impact in infinite plate impact model
x_i	Displacement of impactor in spring-mass impact model
x_p	Displacement of plate in spring-mass impact model
A_{ij}	Extensional stiffness elements
B_{ij}	Bending-extension stiffness elements
D	Effective bending stiffness of an infinite plate
D_{ij}	Bending stiffness elements
E	Young's modulus
$\bar{E}$	Effective contact modulus
F	Contact force
F_e	Contact force during elastic loading
F_{ep}^{I}	Contact force during nonlinear elastoplastic loading
F_{ep}^{II}	Contact force during linear elastoplastic loading
F_{fp}	Contact force during fully plastic loading
F_m	Maximum contact force
F_p	Contact force at onset of fully plastic loading
F_{rs}	Linearised impact force for discretisation between points r and s
F_{tep}	Contact force at transition point in the elastoplastic loading regime
F_u	Contact force during unloading
F_y	Contact force at yield point
K	Mechanical bending stiffness per unit mass in complete impact model
K_h	Hertz contact stiffness
K_b	Bending stiffness of plate in spring-mass impact model
K_c	Contact stiffness
K_{eff}	Effective bending stiffness of plate in the presence of induced pre-stress
K_l	Linear contact stiffness during elastoplastic loading
K_m	Membrane stiffness of plate in spring-mass impact model
K_p	Linear contact stiffness during fully plastic loading
K_{rs}	Linearised contact stiffness for discretisation between points r and s
K_s	Shear stiffness of plate in spring-mass impact model
K_u	Nonlinear contact stiffness during unloading

L	Characteristic length of plate
$M_x; M_{xx}$	Moment about x-axis
M_{xy}	Moment about x-y plane
$M_y; M_{yy}$	Moment about y-axis
N	Total number of layers in laminate plate
N_a	Number of actuated layers
$N_x; N_{xx}$	Membrane or in-plane force per unit length acting in x-direction
N_{xy}	Membrane or in-plane force per unit length acting on x-y plane
$N_y; N_{yy}$	Membrane or in-plane force per unit length acting in y-direction
P_0	Mean contact pressure
P_{0p}	Mean contact pressure at onset of fully plastic loading
P_{0y}	Mean contact pressure at yield
P_d	Damping force per unit area
P_z	Load per unit area acting normal to plate surface
$Q_{mn}(t)$	Time-dependent modal load coefficient
Q_x	Transverse shear force per unit length projected along the z-direction due to shear stress σ_{xz} acting on the side of plate element
Q_y	Transverse shear force per unit length projected along the z-direction due to shear stress σ_{yz} acting on the side of plate element
$\bar{Q}_{ij}$	Transformed stiffness elements
$\bar{R}$	Effective contact radius
$\bar{R}_d$	Deformed effective radius
S_y	Yield stress
V_0	Initial relative velocity before impact; initial velocity of impactor
V_f	Final relative velocity before impact; final velocity of impactor
W_1	Transverse displacement of plate in complete impact model
W_2	Displacement of impactor in complete impact model
W_{fp}	Work done on the target during fully plastic loading
$W_{mn}(t)$	Time-dependent modal displacement of plate in z-direction
W_p	Work done on the target from the beginning of impact to onset of fully plastic loading
W_{tep}	Work done on the target from the beginning of impact to transition point in the elastoplastic loading regime
W_y	Work done on the target from beginning of impact to yield point
$\dot{\delta}$	Indentation rate; relative velocity of impactor and target
δ_f	Fixed or permanent indentation

δ_m	Maximum indentation
δ_p	Indentation at the onset of fully plastic loading
δ_r	Elastically recovered indentation at end of unloading; indentation at onset of each discretisation in the FILM
δ_{tep}	Indentation at transition point in the elastoplastic loading regime
$\varepsilon_x; \varepsilon_{xx}$	Normal strain in x-direction
ε_{xy}	Shear strain in x-y plane
ε_{xz}	Transverse shear strain in x-z plane
$\varepsilon_y; \varepsilon_{yy}$	Normal strain in y-direction
ε_{yz}	Transverse shear strain in y-z plane
$\varepsilon_z; \varepsilon_{zz}$	Transverse normal strain in z-direction
μ_m	mass ratio
ρ_a	Mass per unit area of an infinite plate
$\sigma_x; \sigma_{xx}$	Normal stress in x-direction
σ_{xy}	Shear stress in x-y plane
σ_{xz}	Transverse shear stress in x-z plane
$\sigma_y; \sigma_{yy}$	Normal stress in y-direction
σ_{yz}	Transverse shear stress in y-z plane
$\sigma_z; \sigma_{zz}$	Transverse normal stress in z-direction
ω_{mn}	Modal frequency of plate
ω_n	Natural frequency of plate
ϕ_x	Rotation of a transverse normal about y-axis
ϕ_y	Rotation of a transverse normal about x-axis
α	Relative induced piezoelectric stiffness; percentage change in bending stiffness of plate in complete impact model
δ	Indentation
η	Factor accounting for relative hardness effect
μ	Damping ratio
ρ	Density
υ	Poisson's ratio
ω	Excitation frequency
$\mathcal{E}_j$	Electric field intensity in j-direction; $j = 1, 2, 3$
Λ	Controllable strain induced by piezoelectric actuation
$\mathcal{K}$	Shear correction factor

CHAPTER ONE

INTRODUCTION

1.1 Background

In a broad engineering sense, a structure is a material of finite dimensions that serves a particular purpose. Structures can be very simple or complex in their geometry and/or material composition. A rectangular steel beam used to support the roofing of a building is an example of a simple structure, while the human skeletal system is an example of a complex structure that supports the human body, and consists of several parts of different sizes and intricate shapes. In addition to the material composition and design geometry, another important factor to consider in structural engineering is the operating conditions of a structure. The operating conditions consist of the boundary condition (i.e. the attachment of the structure in the position of operation), the loading condition and the interactions of the structure with other surfaces. In reality the boundary condition is usually complex, but can be approximated by a simplified condition for analytical and experimental purposes. On the other hand, the loading condition involves a combination of different forms of loading, but most forms have negligible effect on the response of the structure so that only one or two of the various forms are considered during theoretical or experimental analysis. The behaviour of structures under various loading and boundary conditions is of interest to mathematicians, physicist and engineers (civil, mechanical, aerospace, structural and biomechanical). Such understanding, obtained through analytical and experimental investigation, informs design decisions and government policies about structures. For instance, a beam is designed to operate safely under a specified maximum load, while a policy might be made to prevent vehicles, with total mass above a predetermined safe limit, from using a bridge that cannot support such vehicles safely.

Structures are normally subjected to static and/or dynamics loads. The latter may be applied gradually (as in the case of a predetermined harmonic excitation) or suddenly (as in the case of a projectile impact). Suddenly applied loads are generally characterised by very short action times (usually fractions of a second) and generation of very high localised stress in the structure, and in

many cases they occur uncontrollably and accidentally. Accidental loading of structures is a common experience that often results in potentially harmful vibrations, damage, and/or degradation of the structure. Examples of accidental loading of structures include runway debris striking an aeroplane body, space debris impact on space structures, hail stone impact, projectile impact, blast/explosive loading of structures and earthquake loading. Understanding the response of structures to various forms of accidental loading is necessary to determine possible mechanisms that could resist structural damage during accidental loading. Mitigation against structural damage aids structural survivability and integrity under the prescribed operating conditions. Some of the impact damage mitigation strategies investigated in previous studies include the use of high performance alternative materials e.g. hybrid composites instead of metals (Khalili *et al*, 2007c), active impact control (Yigit and Christoforou, 2000; Saravanos and Christoforou, 2002) and ingenious material design (Grunenfelder *et al*, 2014).

An area of accidental loading that is prominent in the literature is the impact of a structure by a solid object (Goldsmith, 2001; Stronge, 2000a; Abrate, 1998). The stress generated during solid object impact is usually very high and often results in plastic deformation and/or damage of the target (structure). Reduction in the design performance of the target occurs when the stress generated is higher than the elastic stress limit of the target material. Most studies on mitigation of structural damage arising from solid object impact are limited to passive applications (Abrate, 1998; Olsson, 2001; 2002; Zheng and Binienda, 2007; Chai and Zhu, 2011). Passive mitigation strategies are defined here as material design strategies that do not be permit controllable structural response under operating conditions e.g. structure fortification. On the other hand, active mitigation strategies are material design strategies that permit controllable structural response under operating conditions e.g. composite material with piezoceramic layer(s) for active vibration suppression. Unlike the active mitigation strategies, passive mitigation strategies are not precisely predictable and controllable, and can be said to be structurally unintelligent. The area of structural intelligence through active mitigation strategies has been largely unexplored (Yigit and Christoforou, 2000). The purpose of this research is to advance knowledge in the area of active mitigation of structural defects due to solid object impact. To achieve this, a laminate architecture in the form of a

trimorph plate (see description of the trimorph plate in Section 2.6) has been investigated for various impact conditions with a view to understanding its impact response during elastoplastic indentation. This investigation is necessary because elastoplastic indentation effects (e.g. plastic deformation in metals or fibre cracking, debonding of fibre from matrix, and delamination in composite laminates) can significantly reduce the performance of the target (Abrate, 1998). Also, the feasibility of controlling elastoplastic indentation effects through actively induced pre-stress is studied using a symmetric sandwich laminate composed of piezoelectric actuators as top and bottom layers. The investigations reveal that active pre-stressing can be employed usefully to mitigate localised structural defects arising from solid object impact.

1.2 Motivation

Investigations conducted on active mitigation of impact damage effects are few compared to studies on passive mitigation. The passive mitigation strategies do not respond to the impact in a precisely predictable and controllable manner. For instance, a stiffened plate generally improves resistance to overall impact damage at the expense of a more localised damage (Yigit and Christoforou, 2000), which can grow and cause failure at a later stage when under the action of design load. This response cannot be altered because the stiffened plate has been designed to mitigate impact damage passively, and as a result the plate cannot be used for optimised damage mitigation under various impact conditions. Active mitigation provides a means of achieving optimised damage mitigation under various impact conditions, and can be applied together with passive mitigation. However, studies on active mitigation of impact damage are limited, and there is apparently no known practical implementation of active mitigation due to technological limitations and lack of in-depth knowledge of the subject matter.

This research is motivated by the need to improve understanding of the dynamics of active mitigation of impact damage and the potential benefit of more robust mitigation that could be achieved for various impact conditions. The benefits of the application of active mitigation strategies include cost savings, reduction of risk to life and structural survivability/re-usability. Technological achievements in active mitigation will be useful in the automobile, aerospace,

marine and biomedical industries, to mention but a few. Additionally, active mitigation strategies can be used together with the already existing passive mitigation strategies to further enhance the impact damage mitigation capacity of structures that are prone to solid object impact.

Although the focus of this thesis is on improving the understanding of elastoplastic impact response and developing a strategy for active control of elastoplastic impact effects, it is important to point out that the trimorph plate architecture investigated in this thesis can also be used for noise and vibration control. In fact, many studies have investigated a trimorph plate or beam configuration, made up of a host material, an actuator layer and a sensor layer, for active vibration control (Abramovich, 1998; Waisman and Abramovich, 2002; Moita *et al*, 2002; 2004; Nguyen and Tong, 2004; Edery-Azulay and Abramovich, 2006; Lin and Nien, 2007). Therefore, a trimorph structure, with integrated actuator and sensor layers, designed for the active control of elastoplastic effects caused by solid object impact could be used for noise and vibration harshness control for most of the time. During an imminent solid object impact the trimorph plate is then actively prepared to mitigate impact damage. This multifunctional capability of a trimorph plate structure with sensing and actuating layers buttresses the need to have a proper understanding of the elastoplastic impact response of the trimorph plate so as to fully utilize its potential. The research presented first considers the elastoplastic impact response of a typical trimorph plate configuration. The understanding gained is subsequently applied to investigate a strategy to actively control elastoplastic impact effects for optimised damage mitigation.

1.3 Aims and objectives

This thesis aims to address two overriding objectives that can be further subdivided into sub-objectives. These are listed below. The chapter addressing each objective is indicated in brackets.

1. **To develop and solve analytical models for the impact dynamics of a trimorph plate by:**

a) Mathematical modelling and vibration analysis of the forced vibration of the trimorph plate for small and large displacements (see Chapter two). This objective involves detailed formulation of the forced vibration models for thin

and moderately thick trimorph plates. The vibration model for the former is formulated using classical laminate plate theory while that of the latter is formulated using first-order shear deformation plate theory. Both vibration models are used to investigate the response of the trimorph plate when subjected to forced harmonic excitation. The effect of layer arrangement on the response characteristics of the trimorph plate is examined.

b) Mathematical modelling of the contact mechanics during elastoplastic indentation of a metallic target by a spherical impactor (see Chapter three). This objective involves estimation of the local indentation and contact force for rate-independent impacts. The latter fall under the category of low- to medium-velocity impacts where the impact velocity is less than 500 [m/s] (Johnson, 1985). The local indentation and contact force of such impact events can be estimated using static contact models. In this thesis, an elastoplastic contact model that accounts for post-yield effects during the loading and unloading stages of the static indentation of a compliant half-space by a rigid spherical indenter is used to estimate the local indentation and impact force.

c) Mathematical modelling of the impact dynamics of the trimorph plate when subjected to elastoplastic indentation of a spherical impactor (see Chapter four). This objective seeks to formulate a model for elastoplastic impact analysis of the trimorph plate that accounts for the vibration of the plate, the motion of the impactor and the local indentation of the plate. This is achieved by combining the vibration model in objective (a), the contact model in objective (b), and the equation of motion of the impactor to form a set of coupled nonlinear differential equations that are solved simultaneously. This modelling approach allows for detailed analysis and produces more accurate results (Abrate, 1998).

d) Solving the impact models for selected boundary conditions and simulating results for specific trimorph plate material composition and dimensions (see Chapter four). One of the challenges in impact analysis is the solution of the impact model, which is generally in the form of one or more nonlinear differential equations. With transversely flexible plates, the solution is even more difficult to derive, since the impact model is a set of coupled nonlinear differential equations. The number of equations to be solved simultaneously is dependent on the number of vibration modes required to obtain a convergent

result, and can vary from as few as five (Saravanos and Christoforou, 2002) to as many as seventy coupled equations (Goldsmith, 2001). Mathematica™ is a powerful computational software package that is capable of solving a wide range of mathematical equations (including differential equations), and permits user-defined programming using existing Mathematica functions. *NDSolve* is an efficient Mathematica function that solves partial and ordinary differential equations numerically. In this objective, the NDSolve function is used to develop customised Mathematica codes for solving the impact model of the trimorph plate.

e) Investigating the impact response characteristics of the trimorph plate under different impact scenarios (see Chapter four). To gain better understanding of the impact response of the trimorph plate, various impact scenarios of physical importance are simulated and analysed. This is achieved by investigating the effect of critical model parameters on the elastoplastic impact response of the trimorph plate. The critical model parameters include impactor size and mass, initial impact velocity, transverse shear deformation of the plate, plate thickness, the aspect ratio and the bending stiffness of the plate.

2. **To investigate the active impact control of a smart trimorph plate by:**

a) Developing previous impact models to accommodate a piezoelectric actuation effect. Lead zirconate titanate (PZT) has been used here as the actuator (see Chapter five). This sub-objective builds on the understanding gained by analysing the elastoplastic impact response of the trimorph plate. A piezoelectric effect, in the form of induced active pre-stress, is incorporated into the impact model formulated in sub-objective (1c). The induced active pre-stress changes the effective transverse stiffness of the plate, which in turn influences the impact response of the sandwich plate.

b) Investigating active control of the elastoplastic indentation response of a smart sandwich plate during solid object impact, by using the impact models that account for the piezoelectric actuation effect (see Chapter five). The impact models are solved and simulated using plausible electric voltage inputs. Next, a comparative analysis of the elastoplastic indentation response of the sandwich plate, both with and without an induced piezoelectric pre-stress, is performed to determine the level of control action that can be

achieved using the proposed control strategy. The feasibility of applying the proposed control strategy for active mitigation of elastoplastic impact effects is examined.

1.4 Scope of study

This thesis focuses on the elastoplastic indentation response of plates subjected to low-velocity impact, and in particular the elastoplastic impact response of the trimorph plate. The local contact mechanics and equations of motion of the impact system are combined to formulate analytical models used to study the low-velocity impact response of plates. The spherical impact of transversely inflexible (very thick) and transversely flexible (moderately thick to thin) plates is studied. For transversely inflexible plates, the investigations are limited to elastoplastic half-space impact analysis of metallic targets and the formulation of an efficient algorithm for the solution of the nonlinear models of a half-space impact. With transversely flexible plates, the investigations are limited to the response of a trimorph plate with a simply-supported boundary condition on all edges, and subjected to a concentrated impact force. The simply-supported boundary condition and concentrated impact force are used for mathematical convenience, but without loss of generality of the qualitative analysis. The qualitative analysis is restricted to low-velocity large mass impact of the trimorph plate, but the findings are applicable to the large mass impact response of any transversely flexible plate. Low-velocity large mass impact events have durations that are typically in the range of milliseconds and this is the response time for piezoelectric actuators, which are the fastest known actuators currently available (Yigit and Christoforou, 2000). Hence, their use in active control of such impact events is considered to be plausible (Yigit and Christoforou, 2000).

In studying the active control of the elastoplastic response of a transversely flexible plate impact, a piezoelectric actuation effect was investigated. The application of piezoelectric actuation is based on an induced pre-stress which could be either tensile or compressive. An impact model incorporating induced piezoelectric pre-stress was formulated for a sandwich plate of PZT/Al/PZT configuration, with the Al layer constrained from in-plane displacements by applying appropriate boundary conditions. Also, the effects of both induced

tensile and compressive pre-stress on the elastoplastic impact response of the sandwich plate is examined.

1.5 Contributions of study

This section summarises the novel contributions that are reported in this thesis. The chapters and chapter sections where the contributions are reported and the articles published based on some of the contributions, are stated. Seven distinct contributions are identified:

1. Vibration models for small and large transverse displacements of the trimorph plate have been formulated and used to perform a vibration analysis (see Chapter two). The analysis shows that the transverse response of the trimorph plate is dependent on the arrangement of the layers. Also, geometric nonlinearity is found to have a significant effect only during large transverse displacement of the trimorph plate. For a moderately thick trimorph plate, transverse shear deformation is found to have an appreciable effect on the transient response of the fundamental mode of vibration and this effect is found to increase at higher modes. Part of the study on vibration analysis of the trimorph plate is published in Big-Alabo and Cartmell (2012).
2. A new contact model for post-yield indentation of a half-space target by a spherical impactor is developed (see Section 3.2). The validity of the contact model is evaluated by comparing simulations of the contact model with published static and dynamic indentation test results. The advantages of the contact model are its simplicity and computational tractability. A detailed formulation of the contact model is published in Big-Alabo *et al* (2015a) and an application of the contact model for elastoplastic impact analysis of a half-space target is published in Big-Alabo *et al* (2014a).
3. A simple method to determine the maximum indentation and force of a half-space target from the impact conditions is presented (see Section 3.3.3.1). The method is based on energy balance principle for rate-independent impact events. The method is illustrated in the form of a flowchart algorithm using the new contact model, and forms part of the work published in Big-Alabo *et al* (2015a).
4. The energy balance algorithm in (3) above is used to formulate a method of calculating the coefficient of restitution during elastoplastic half-space

impact (see Section 3.3.3.1). This method can be applied with any contact model and eliminates the issues of solution convergence that may be associated with solving the nonlinear models for elastoplastic half-space impact.

5. An analytical algorithm, named the force-indentation linearisation method (FILM), for the solution of the impact response of an elastoplastic half-space is formulated (see Section 4.3). Results obtained using the FILM algorithm are validated by comparing with results obtained using numerical integration; results from both methods are found to be in excellent agreement. The main advantages of the FILM algorithm are its simplicity, inherent stability and quick convergence. Additionally, the FILM algorithm solves the nonlinear models for elastoplastic half-space impact with the same relative ease, irrespective of the complexity of the contact model used to estimate the impact force. A detailed formulation of the FILM algorithm and its implementation for selected elastic and elastoplastic impact events is published in Big-Alabo *et al* (2014b).
6. An impact model for the elastoplastic indentation of the trimorph plate is formulated and solved for various impact scenarios (see Section 4.4). A detail analysis, clearly showing the different impact stages that occur during the elastoplastic response of a typical trimorph plate, is conducted. This analysis provides some new insight into the response characteristics of a low-velocity large mass impact. A conference paper (Big-Alabo *et al*, 2015b) developed from part of this study was presented in the COMPDYN 2015 conference held in Crete, Greece from 25 – 27 May, 2015.
7. An impact model for active control of the elastoplastic response of a PZT/Al/PZT sandwich plate is formulated by incorporating a piezoelectric effect (see Section 5.4.1). The control strategy is based on active pre-stress, induced by piezoelectric actuation. Studies are conducted on the effect of both induced tensile and compressive pre-stress on the elastoplastic response of a typical PZT/Al/PZT plate. Results show that significant control action can be achieved. This study suggests a new and practically feasible strategy for active mitigation of structural damage cause by elastoplastic impact.

1.6 Structure of thesis

The remainder of the thesis is divided into five chapters. Additional useful information is provided in the appendix. Aside from this first and the last chapter, chapters are structured such that each contains a brief summary, a literature review, details of the chapter (which include formulation and solution of models and discussions of results) and conclusions of the chapter.

Chapter two presents the vibration analysis of the trimorph plate. Detailed derivations of the vibration models for small and large transverse displacements of the trimorph plate with and without transverse shear deformation effect are presented. The vibration model for large displacements of a thin trimorph plate accounts for membrane stretching. The latter is modelled using the von Kármán geometric nonlinearity. The vibration model without transverse shear deformation effect is developed based on classical plate theory while the model with transverse shear deformation effect is developed based on first-order shear deformation plate theory. The vibration analysis shows the influence of layer arrangement on the response characteristics of the trimorph plate.

Chapter three presents detailed formulation of a new contact model for elastoplastic indentation of a compliant half-space target by a spherical indenter. Validation of the contact model for static and dynamic indentation cases is presented. A simple energy balance approach to determine the maximum indentation and force of a half-space impact event from the impact conditions is discussed. Also, a method for calculating the coefficient of restitution using the energy balance approach is discussed and implemented for the dynamic indentation case studies used to validate the new contact model.

Impact analysis of rectangular plates is discussed in Chapter four. Both transversely inflexible (very thick) and transversely flexible (thin to moderately thick) plates are considered. In each case the impact models are formulated by combining the new contact model with the equations of motion of the impact system. For transversely inflexible plates the impact conditions are similar to that of a half-space and the impact model is a single differential equation that can be solved numerically. Detailed formulation of the FILM algorithm, which is capable of solving the model for a transversely inflexible plate impact, is presented. The FILM algorithm is applied to determine the elastoplastic response of a transversely inflexible plate when the impact force is estimated using (i) a

canonical and (ii) a non-canonical contact model. The implications of applying the FILM algorithm to solve the impact model for an infinitely large transversely flexible plate are discussed in detail. The chapter ends with analysis of the elastoplastic response of an Al/PVDF/PZT trimorph plate to low-velocity large mass impact. Various impact scenarios are simulated and discussed.

Chapter five deals with the active control of the elastoplastic impact response of a PZT/Al/PZT sandwich plate. The impact model for this investigation has been formulated by incorporating a piezoelectric effect in the impact model derived in chapter four. The piezoelectric effect is based on an induced pre-stress created when the Al layer is completely restricted from in-plane displacements and rotations through application of appropriate boundary conditions. Investigations to determine the effect of both induced tensile and compressive pre-stress on the elastoplastic impact response of a PZT/Al/PZT sandwich plate are discussed, and the feasibility of active mitigation of elastoplastic impact effects using the proposed control strategy is discussed. The chapter ends with discussions on the practical implementation issues associated with applying the proposed control strategy for active mitigation of elastoplastic impact effects.

Chapter six summarises the important conclusions derived from the work presented in this thesis. Finally, areas for future research are discussed.

CHAPTER TWO

VIBRATION ANALYSIS OF MULTILAYERED PLATES

Chapter summary

Multilayered plates and panels are used for structural applications ranging from building and construction to transportation systems and space structures. These plates may be in the form of symmetric sandwich laminates with hard face-sheet at the top and bottom to resist damage and a flexible core to absorb damage energy. Another application is in active control of structures where sensing and actuating layers are bonded to traditional materials such as aluminium to sense the response of the plate to an excitation and take a desired control action. Multilayered plates and panels are subject to different kinds of loads (static and/or dynamic) depending on their functions, operating conditions and environment. In response to dynamic loads (excitations) plates vibrate, and these vibrations may lead to damage of the plate. It is therefore necessary to understand the vibration response of multilayered plates. This chapter presents analytical models for investigating the vibration response of multilayered plates. The chapter starts with a brief review on the analytical modelling of plates. Next, detailed formulation of multilayered plate models based on *classical plate theory* – CPT (for thin plates), *first-order shear deformation plate theory* – FSDPT (for moderately thick plates), and *equivalent single layer theory* – ESLT are presented. Then, reduced models in the form of ODEs are derived for transverse vibration analysis of a multilayered plate architecture called *trimorph plate* (Big-Alabo and Cartmell, 2011). Finally, simulation results are presented for small and large displacement analysis of a trimorph plate.

2.1 Review of plate vibration modelling

A plate is a two-dimensional plane structure in which the planar dimensions (length and width) are much larger than the lateral dimension (thickness). Many structural components of engineering interest can be classified as plates. These include floor and foundation slabs, thin retaining walls, lock-gates, bridge decks etc in building and construction; automotive body panels, aircraft bodies, ship hulls, ship decks, submarine bodies etc in transportation systems; and space and

military systems. With the many and diverse applications of plates as structural components it is no surprise that immediate attention should be given to the study of the response of plates under various loading and boundary conditions.

Plates are distinguishable based on the thickness of the plate relative to its characteristic length (length for rectangular plates and diameter for circular plates). On this basis, Szilard (2004) classified plates into four groups as follows:

1. *Membranes* ($h/L < 1/50$) are very thin plates without flexural rigidity, carrying loads by axial and central shear forces.
2. *Stiff plates* ($h/L = 1/50 - 1/10$) are thin plates with flexural rigidity, carrying loads two dimensionally, mostly by internal (bending and torsional) moments and by transverse shear, generally in a manner similar to beams. In engineering practice, the term *plate* is understood to mean a stiff plate unless otherwise specified.
3. *Moderately thick plates* ($h/L = 1/10 - 1/5$) are in many respects similar to stiff plates, with the notable exception that the effects of transverse shear forces on the normal stress components are also taken into account.
4. *Thick plates* ($h/L > 1/5$) have an internal stress condition that resembles that of three-dimensional continua.

More generally, the categorisation is in three groups with the first two classifications mentioned above considered as one group called thin plates. Also, results presented by Reddy (2004) reveal that the transverse shear strain effect is significant when $h/L \geq 1/20$. Therefore, the thickness to characteristic length ratio for moderately thick plates can be extended to $h/L = 1/20 - 1/5$ and that of thin plates becomes $h/L < 1/20$.

Analytical models describing the behaviour of plates are important for rigorous and cost-effective analysis of plate response. The first correct model for plate response was formulated by Claude-Louis Navier (1785 – 1836), who developed a two-dimensional plate model for static bending of a rectangular plate subjected to a distributed load. The model is a fourth-order partial differential equation (PDE), which was solved for simply-supported boundary condition on all edges of the plate using a double trigonometric series that reduces the PDE to a set of algebraic equations. This solution approach is generally called the *Navier solution* and it is limited to plates with simply-supported boundary condition on all edges.

The first complete plate theory, now referred to as the *classical plate theory* or *Kirchhoff plate theory*, was developed by Gustav Kirchhoff (1824 – 1887). Kirchhoff arrived at the same PDE obtained by Navier using virtual displacement principles and defined clearly all the assumptions necessary for the formulation of a plate model. Another notable contribution of Kirchhoff in the development of plate theory was the extension of plate bending theory to include membrane stretching in order to account for the nonlinear effect present during large displacement of plates (Szilard, 2004). However, it was Theodore von Kármán who first modelled the large displacement of plates accurately in 1910. Von Kármán incorporated geometric nonlinearity into the strain-displacement relationship to produce a more accurate prediction of the membrane stretching effect. Hence, the von Kármán type geometric nonlinearity is commonly used with the combined bending and stretching plate theory to model large displacements of plates (Manoach and Trendafilova, 2008; Big-Alabo and Cartmell, 2012; Kazanci and Mecitoğlu, 2008).

The assumption that lines normal to the mid-plane of the undeformed plate remain normal after deformation is an essential part of the formulation of the Kirchhoff plate theory. The implication is that the effect of the transverse shear strains is neglected. Whereas this assumption is valid for thin plates, the same can hardly be said for moderately thick or thick plates where application of the Kirchhoff plate theory leads to an overly stiff response with underestimation of the displacements and overestimation of the natural frequencies and buckling loads (Szilard, 2004). A more accurate plate theory for thick plates should account for the effect of the shear strains, and hence, there is a need to relax the Kirchhoff assumption on the mid-plane normal. In 1945, Reissner developed a plate theory that accounts for transverse shear strains. The *Reissner plate theory* (RPT) is formulated based on an assumed parabolic stress field. Another theory accounting for shear strains was developed by Mindlin in 1951. Mindlin incorporated the shear strain effect using an assumed displacement field. The *Mindlin plate theory* (MPT) is simpler and more widely used compared to the RPT. It is commonly referred to as the *first-order shear deformation plate theory* (FSDPT) even though other FSDPTs have been developed since then (Auricchio and Sacco, 2003; Shimpi *et al*, 2007; Thai and Choi, 2013). A major limitation of the MPT is that it requires a shear correction factor. Reissner estimated this factor to be 5/6 (0.833) while Mindlin estimated it to be $\pi^2/12$

(0.823). Mindlin also stated that the shear correction factor is influenced by the Poisson's ratio of the plate material and estimated that it varied from 0.76 to 0.91 for Poisson's ratio ranging from 0 to 0.5 (Liew *et al*, 1998).

Reddy (1984) presented a third-order shear deformation plate theory to account for the shear strain effect in thick plates. Unlike the FSDPT, where the shear strain is assumed to be constant through the plate thickness, the *Reddy third-order shear deformation plate theory* (RTSDPT) assumes a parabolic variation of shear strain through the plate thickness that vanishes at the top and bottom surfaces. Although the RTSDPT is more complex than the FSDPT it does not require any correction factor. Furthermore, the RTSDPT produces more accurate results than the FSDPT especially at higher modes where shear strain effects are more pronounced (Reddy, 1984). Other shear deformation plate theories exist but these are not discussed here. An extensive review of shear deformation theories as applicable to isotropic and anisotropic plates can be found in Ghugal and Shimpi (2002). Of the 2-D plate theories the CPT, FSDPT of Mindlin and RTSDPT are the most commonly applied plate theories (Abrate, 2011), and they have been shown to produce results that agree with results of 3-D elasticity theory and experimental data.

In recent years, there has been an increasing interest in the response of multilayered plates, especially in the form of composite laminates. For one, desirable operational qualities of structural component such as strength, stiffness, low-weight, wear resistance, thermal and acoustical insulation etc can be achieved by lamination (Jones, 1999). Furthermore, different desirable material properties can be combined into one plate through lamination. For example, Corbett *et al* (1996) reports that studies carried out on the impact resistance of laminated plates show that laminated plates with a hard front layer (to resist indentation), and backed up by a tough ductile layer (to absorb the kinetic energy of the projectile), are an efficient combination to resist projectile impact. This principle is applied in the use of laminated sandwich plates, with viscoelastic cores, as damage tolerant structures with good energy absorbing ability (Zhu *et al*, 2010). The front face of the sandwich laminate always acts to resist the load while the core acts as an energy absorber. Also, laminated plates with smart material layer(s) have been applied for active detection and control of plate response (Moita *et al*, 2004; Nguyen and Tong, 2004; Lin and Nien, 2007; etc).

Due to the above-mentioned advantages, and others not mentioned here, a lot of research effort has been put into developing laminated plate theories. Lamination theory describes the constitutive behaviour of a laminate in terms of the relationship between the stress states and the corresponding strains. The most commonly applied lamination theory is the *equivalent single layer* (ESL) theory. Besides its inherent simplicity and low computational cost, the ESL theory has proved to be efficient in determining the global response i.e. gross deflection, critical buckling loads, fundamental vibration frequencies and mode shape of thin to moderately thick plates (Reddy, 2004). The ESL theory models a laminated plate as a statically equivalent monolithic plate having an effective constitutive behaviour. This is achieved by averaging the stress and moment resultants of the laminated plate through the plate thickness. The simplest ESL theory is the *classical laminate plate theory* (CLPT), which is an extension of the CPT to laminated plates. Big-Alabo and Cartmell (2011) applied the CLPT to study the vibration analysis of a thin asymmetric three-layer rectangular plate subject to a harmonically-varying sinusoidally distributed excitation. This study, which was limited to small displacements, focussed on the effect of the layer arrangement on the vibration response of the plate. A follow-up study was conducted for large displacements (Big-Alabo and Cartmell, 2012) by incorporating the membrane stretching effect and the von Kármán geometric nonlinearity in the CLPT. The FSDPT and RTSDPT can also be applied to laminated plates using the ESL theory (Reddy, 2004).

Although the ESL models can give accurate predictions of the global response of thin to moderately thick laminated plates, they have some limitations. One, the accuracy of the ESL models to predict the global response reduces as the laminate becomes thicker. Two, the ESL models cannot be used to determine the inter-laminar stresses or the stresses at areas of geometric and material discontinuities, and regions of intense loading (Reddy, 2004). For such analysis, 3-D elastic theory or other layer-based theories can be used. The solution of the 3-D elastic theory model can be complex and is computationally expensive. Hence, layer-based theories such as the *Reddy layerwise theory* (Reddy, 2004) and *Murakami zig-zag theory* (Carrera, 2004) that are computationally affordable and yet accurate are used instead. In this research, only the global response of laminated plates is of interest. Therefore, the present work is based on the ESL models.

The rest of this chapter discusses detailed formulations of the CPT and FSDPT. The membrane stretching effect and the von Kármán geometric nonlinearity are both included to model large flexural oscillations of thin plates. Next, the ESL approach is used to derive the constitutive equations for a laminated plate. The application of the laminate constitutive equations to the CPT and FSDPT gives rise to models in the form of PDEs that can be reduced to models in the form of ODEs using the Galerkin approach. Finally, the ODE models are solved and simulated to investigate the vibration response of a trimorph plate.

2.2 Classical plate theory

A seminal work on plate theory and vibration analyses of plates was published by Leissa in 1969. In a 353 page monograph mainly focussed on the CPT, Leissa applied the CPT to give detailed vibration analysis of thin plates of different regular shapes, and under different loading and boundary conditions. Plate theory for large deflection and the effect of shear strains on the vibration response of thick plates was also discussed, though in an introductory manner. Other prominent texts that discuss and apply the CPT to a wide range of problems of engineering interest are those by Timoshenko and Woinowsky-Krieger (1959) and Szilard (2004). The formulation of the plate vibration model based on the CPT as presented here follows the approach used by Timoshenko and Woinowsky-Krieger (1959) and Szilard (2004). In this approach, the equations of motion of a rectangular plate are derived from the balance of forces and moments. Israr (2008) used this approach in formulating the vibration model for a thin aluminium plate with a horizontal central crack and subjected to a transverse point load. An alternative approach that involves the integration of the equations of motion of 3-D elasticity was discussed by Abrate (2011). This alternative approach has been used in formulating the plate vibration model for moderately thick plates based on the FSDPT as shown later in this chapter.

2.2.1 Assumptions used in formulating the rectangular plate vibration model based on the CPT

The following assumptions are applicable in the derivation that follows.

1. The plate is elastic and obeys Hooke's law.

2. The plate is thin i.e. h/L < 1/20.
3. The resultant excitation acting on the plate is in the transverse direction.
4. The mid-plane is not strained during bending and sections taken normal to it remain normal before and after deformation of the mid-plane.
5. Normal stresses transverse to the mid-plane are negligible.
6. Rotary inertia terms are negligible.

2.2.2 Transverse force analysis

Consider an elemental rectangular plate (Figure 2.1) of thickness h, length dy, and breadth dx. The forces and moments are thought of as acting on the mid-plane where the transverse strain is negligible. Using the coordinate system shown below and summing the forces in Figure 2.2 (i.e. along the z-direction) yields

$$-Q_x dy + \left(Q_x + \frac{\partial Q_x}{\partial x} dx\right) dy - Q_y dx + \left(Q_y + \frac{\partial Q_y}{\partial y} dy\right) dx + P_z dxdy - P_d dxdy = m_p \bar{a}_z$$

which simplifies to

$$\frac{\partial Q_x}{\partial x} + \frac{\partial Q_y}{\partial y} + P_z - P_d = \rho h \frac{\partial^2 w}{\partial t^2} \tag{2.1}$$

where Q_x and Q_y are the transverse shear forces per unit length projected along the z-direction due to shear stresses σ_{xz} and σ_{yz} respectively, acting on the sides of the element; P_z is the load acting per unit area normal to the plate surface; P_d is the damping force per unit area; and ρh is the mass per unit area of the plate.

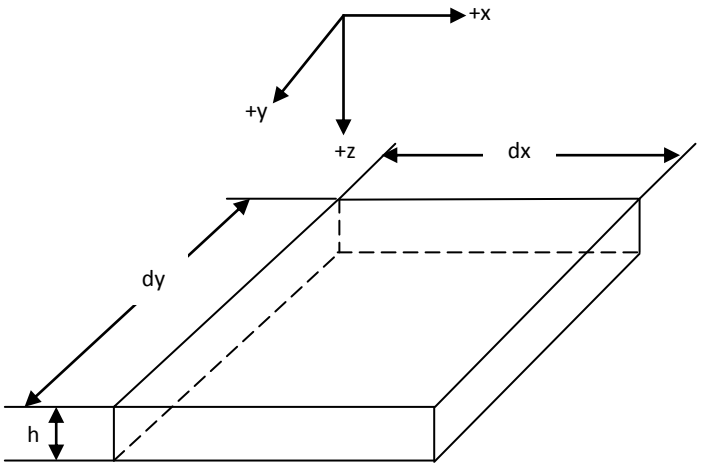

Figure 2.1: *Plate element showing rectilinear coordinate system*

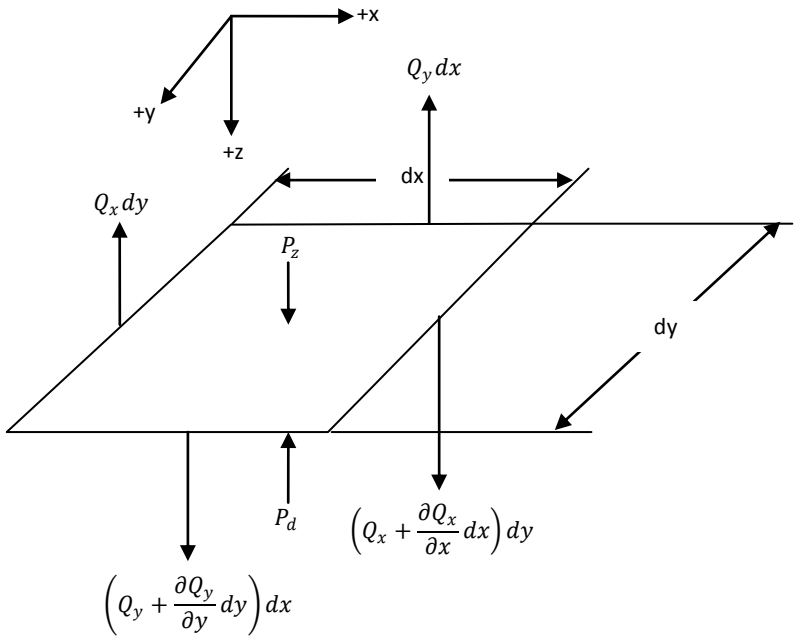

Figure 2.2: *Lateral forces acting on the mid-plane*

$$Q_x = \int_{-h/2}^{+h/2} \sigma_{xz} dz \quad \text{and} \quad Q_y = \int_{-h/2}^{+h/2} \sigma_{yz} dz \tag{2.2}$$

$$P_z = q(x, y, t) \quad \text{and} \quad P_d = c\frac{\partial w}{\partial t} \tag{2.3}$$

where $q(x, y, t)$ is a time-variant spatial load per unit area and c is the damping coefficient per unit area. Using equations (2.1) to (2.3)

$$\frac{\partial Q_x}{\partial x} + \frac{\partial Q_y}{\partial y} = \rho h \frac{\partial^2 w}{\partial t^2} + c\frac{\partial w}{\partial t} - q(x, y, t) \tag{2.4}$$

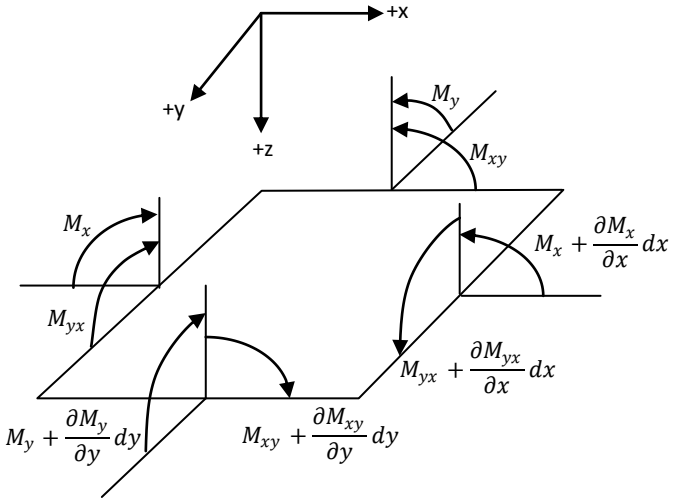

Figure 2.3: *Bending moments acting on the mid-plane*

With reference to Figure 2.3 and taking moments about the x-axis

$$-M_y dx + \left(M_y + \frac{\partial M_y}{\partial y} dy\right) dx - M_{xy} dy + \left(M_{xy} + \frac{\partial M_{xy}}{\partial x} dx\right) dy - Q_y dx \frac{dy}{2}$$
$$- \left(Q_y + \frac{\partial Q_y}{\partial y} dy\right) dx \frac{dy}{2} = 0$$

Neglecting the third-order terms gives

$$\frac{\partial M_y}{\partial y} + \frac{\partial M_{xy}}{\partial x} = Q_y \tag{2.5}$$

Taking moments about the y-axis and neglecting third-order terms,

$$\frac{\partial M_x}{\partial x} + \frac{\partial M_{yx}}{\partial y} = Q_x \tag{2.6}$$

Substituting equations (2.5) and (2.6) into equation (2.4) and noting that $M_{xy} = M_{yx}$ (since $\sigma_{xy} = \sigma_{yx}$),

$$\frac{\partial^2 M_x}{\partial x^2} + 2\frac{\partial^2 M_{xy}}{\partial x \partial y} + \frac{\partial^2 M_y}{\partial y^2} = \rho h \frac{\partial^2 w}{\partial t^2} + c\frac{\partial w}{\partial t} - q(x, y, t) \tag{2.7}$$

where M_x, M_y, and M_{xy} are the bending moments per unit length given by

$$\left.\begin{aligned} M_x &= \int_{-h/2}^{+h/2} \sigma_{xx}\, z dz \\ M_y &= \int_{-h/2}^{+h/2} \sigma_{yy}\, z dz \\ M_{xy} &= \int_{-h/2}^{+h/2} \sigma_{xy}\, z dz \end{aligned}\right\} \tag{2.8}$$

σ_{xx} and σ_{yy} are the normal stresses in the x- and y- directions respectively, and σ_{xy} is the shear stress in the x-y plane. Equation (2.7) is the model for small displacements in the transverse direction. The in-plane displacements are considered next to complete the CPT.

2.2.3 In-plane force analysis

Membrane (in-plane) forces are the forces acting in the plane of the plate i.e. in the x-y plane. They arise because the edges of the plate are allowed to move in the plane of the plate creating reactive forces (membrane forces) at the edge normal to the plate. Figure 2.4 illustrates the in-plane forces acting on a rectangular plate element. Summing the forces in the x-direction (Figure 2.4),

$$-N_x dy + \left(N_x + \frac{\partial N_x}{\partial x} dx\right) dy - N_{xy} dx + \left(N_{xy} + \frac{\partial N_{xy}}{\partial y} dy\right) dx = m_p \bar{a}_x$$

which implies that

$$\frac{\partial N_x}{\partial x} + \frac{\partial N_{xy}}{\partial y} = \rho h \frac{\partial^2 u}{\partial t^2} \tag{2.9}$$

Similarly, summing forces in the y-direction yields

$$\frac{\partial N_{xy}}{\partial x} + \frac{\partial N_y}{\partial y} = \rho h \frac{\partial^2 v}{\partial t^2} \tag{2.10}$$

where N_x, N_y, and N_{xy} are the membrane forces per unit length given by

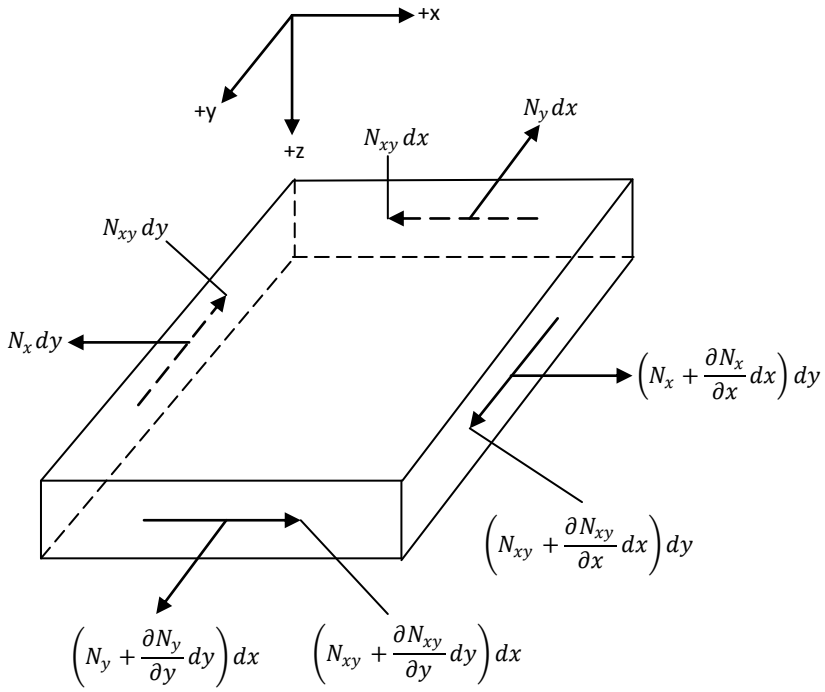

Figure 2.4: *In-plane forces acting on a rectangular plate element*

$$\left.\begin{aligned} N_x &= \int_{-h/2}^{+h/2} \sigma_{xx}\, dz \\ N_y &= \int_{-h/2}^{+h/2} \sigma_{yy}\, dz \\ N_{xy} &= \int_{-h/2}^{+h/2} \sigma_{xy}\, dz \end{aligned}\right\} \tag{2.11}$$

Equations (2.7), (2.9), and (2.10) give the complete equations of motion for small displacements in the three-mutually perpendicular directions of the plate based on CPT. However, the in-plane displacements are usually small in comparison to the transverse displacement and are neglected in most analyses.

2.2.4 In-plane force effect on flexural oscillations

Flexural oscillations (transverse displacements) are classified as small or large based on the ratio of the maximum flexural displacement to the plate thickness. According to Szilard (2004), the oscillations can be considered to be small when this ratio is less than 0.2 otherwise they are large. As shown in Figure 2.4 the external load induces in-plane forces (due to membrane stretching) that can produce in-plane displacements (see equations (2.9) and (2.10)). When small flexural oscillations are considered the induced in-plane forces are negligible, and the in-plane oscillations are also negligible compared to the magnitude of the flexural oscillations. For large flexural oscillations the membrane stretching effects gives rise to in-plane forces that can no longer be neglected. Interestingly, the now significant in-plane forces produce both transverse and in-plane effects. However, the in-plane oscillations can still be neglected when compared to the magnitude of the flexural oscillations.

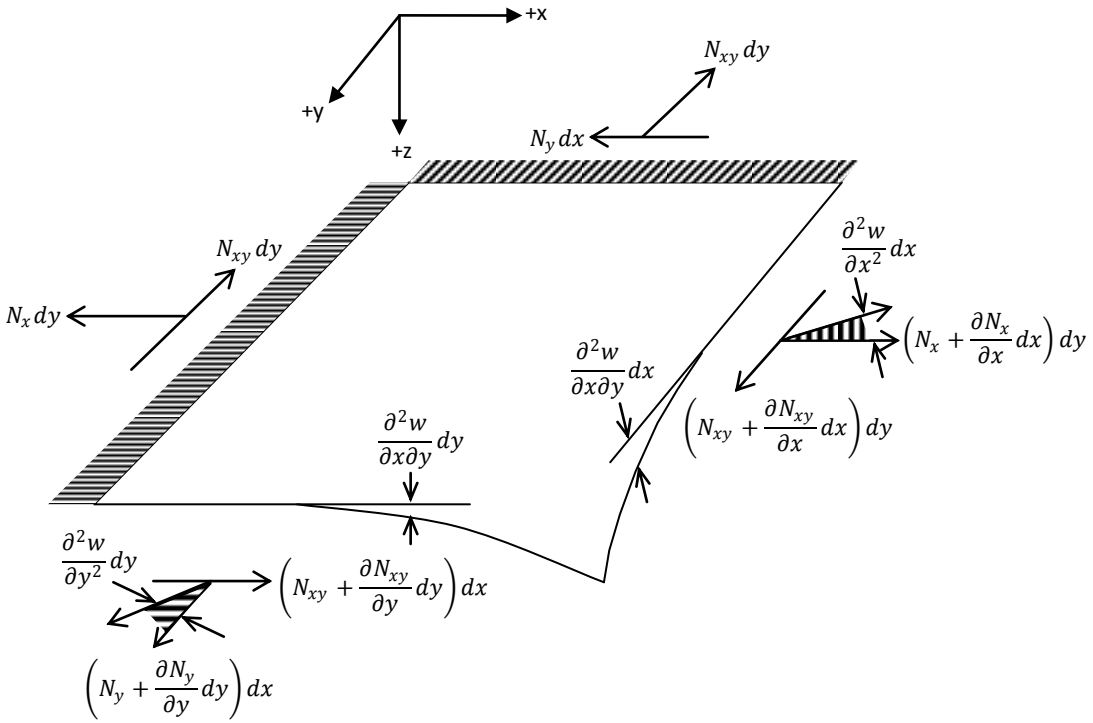

Figure 2.5: *Effect of membrane forces on lateral deflection of plate*

The transverse effect of the induced in-plane forces gives rise to geometric nonlinearities, but also adds to the load-carrying capacity of the plate (Szilard, 2004). This transverse effect can be modelled following the approach of Israr

(2008). The left and rear edges of the plate element are fixed and the equilibrium of the element *dxdy* in the z-direction due to the induced in-plane forces is as shown in Figure 2.5. By taking the sum of all forces in the z-direction,

$$\left(\sum F_z(x,y)\right)dxdy = \left(N_x + \frac{\partial N_x}{\partial x}dx\right)dy\frac{\partial^2 w}{\partial x^2}dx + \left(N_y + \frac{\partial N_y}{\partial y}dy\right)dx\frac{\partial^2 w}{\partial y^2}dy + \left(N_{xy} + \frac{\partial N_{xy}}{\partial x}dx\right)dy\frac{\partial^2 w}{\partial x \partial y}dx + \left(N_{xy} + \frac{\partial N_{xy}}{\partial y}dy\right)dx\frac{\partial^2 w}{\partial x \partial y}dy$$

Neglecting third-order terms and collecting like terms,

$$\sum F_z(x,y) = N_x\frac{\partial^2 w}{\partial x^2} + 2\,N_{xy}\frac{\partial^2 w}{\partial x \partial y} + N_y\frac{\partial^2 w}{\partial y^2} \tag{2.12}$$

$F_z(x,y)$ is the vertical force per unit area due to the induced in-plane forces. Including $\sum F_z(x,y)$ in the equation for transverse displacement of the plate by substituting equation (2.12) into equation (2.7), the equation for flexural oscillations of the plate in the presence of induced in-plane forces is obtained thus:

$$\frac{\partial^2 M_x}{\partial x^2} + 2\frac{\partial^2 M_{xy}}{\partial x \partial y} + \frac{\partial^2 M_y}{\partial y^2} = \rho h\frac{\partial^2 w}{\partial t^2} + c\frac{\partial w}{\partial t} - q(x,y,t) + N_x\frac{\partial^2 w}{\partial x^2} + 2N_{xy}\frac{\partial^2 w}{\partial x \partial y} + N_y\frac{\partial^2 w}{\partial y^2} \tag{2.13}$$

In a general sense, equation (2.13) models the transverse displacement of a rectangular plate in the presence of in-plane loads. In that case, N_x and N_y are the normal in-plane forces (tensile or compressive) in the x- and y-directions respectively, and N_{xy} is the in-plane shear force. This equation can be used for buckling analysis by eliminating the in-plane force(s) not relevant to the problem (Reddy, 2004; Szilard, 2004). The equation can also be used to model the active vibration control of plates with embedded or layered smart materials. For example, when the d_{31} piezoelectric stiffness coefficient of a symmetric sandwich plate with top and bottom piezoactuator layers is activated by electrical voltage input across the plate thickness, an in-plane strain is induced in the x-direction. With the appropriate boundary conditions the induced in-plane strain produces a corresponding induced in-plane force that can influence the transverse response of the plate (see Sections 5.3 and 5.4 for more details). This is the principle applied in active stiffening by induced strain actuation.

Ganilova and Cartmell (2010) studied the vibration control of a sandwich plate with integrated shape memory alloy (SMA) by means of a controllable activation strategy. The effect of the SMA activation was modelled as an induced in-plane force using equation (2.13) with $N_{xy} = 0$ and $N_y = 0$.

2.2.5 Strain-displacement relationships for CPT

One of the assumptions of the CPT is that the transverse normal strain (or stress) is negligible i.e. $\varepsilon_z = \partial w/\partial z = 0$. This implies that $w(x,y,t) = w^0(x,y,t)$; and one kinematic condition is defined. The remaining two kinematic conditions are obtained from the assumption of the CPT that transverse shear strains are negligible. Hence,

$$\varepsilon_{xz} = \frac{\partial u}{\partial z} + \frac{\partial w}{\partial x} = 0 \qquad \text{and} \qquad \varepsilon_{yz} = \frac{\partial v}{\partial z} + \frac{\partial w}{\partial y} = 0 \tag{2.14a}$$

From equations (2.14a),

$$\frac{\partial u}{\partial z} = -\frac{\partial w}{\partial x} \qquad \text{and} \qquad \frac{\partial v}{\partial z} = -\frac{\partial w}{\partial y} \tag{2.14b}$$

Integrating equations (2.14b) with respect to z gives

$$u(x,y,z,t) = u^0(x,y,t) - z\frac{\partial w}{\partial x};\;\; v(x,y,z,t) = v^0(x,y,t) - z\frac{\partial w}{\partial y} \tag{2.14c}$$

The displacement field for the CPT can then be written as:

$$\left.\begin{aligned} u(x,y,z,t) &= u^0(x,y,t) - z\frac{\partial w}{\partial x} \\ v(x,y,z,t) &= v^0(x,y,t) - z\frac{\partial w}{\partial y} \\ w(x,y,t) &= w^0(x,y,t) \end{aligned}\right\} \tag{2.15}$$

The subscript '0' makes reference to the mid-plane. The arguments in the brackets in equations (2.15) will be dropped subsequently for simplicity.

For small transverse displacements, the strain-displacement relationships are given by:

$$\varepsilon_x = \frac{\partial u}{\partial x}; \qquad \varepsilon_y = \frac{\partial v}{\partial y}; \qquad \varepsilon_{xy} = \frac{\partial u}{\partial y} + \frac{\partial v}{\partial x} \tag{2.16}$$

Substituting equations (2.15) into equations (2.16) gives

$$\begin{Bmatrix} \varepsilon_x \\ \varepsilon_y \\ \varepsilon_{xy} \end{Bmatrix} = \begin{Bmatrix} \varepsilon_x^0 + zk_x^0 \\ \varepsilon_y^0 + zk_y^0 \\ \varepsilon_{xy}^0 + zk_{xy}^0 \end{Bmatrix} \tag{2.17}$$

where the strains ε^0 and curvatures k^0 of the mid-plane are

$$\left.\begin{aligned} \varepsilon_x^0 = \frac{\partial u^0}{\partial x}; \quad \varepsilon_y^0 = \frac{\partial v^0}{\partial y}; \quad \varepsilon_{xy}^0 = \frac{\partial u^0}{\partial y} + \frac{\partial v^0}{\partial x} \\ k_x^0 = -\frac{\partial^2 w}{\partial x^2}; \quad k_y^0 = -\frac{\partial^2 w}{\partial y^2}; \quad k_{xy}^0 = -2\frac{\partial^2 w}{\partial x \partial y} \end{aligned}\right\} \tag{2.18}$$

Note that the strains $\varepsilon_{xz}, \varepsilon_{yz}, \text{and } \varepsilon_z$ are zero based on the assumption of the CPT.

For large transverse displacements, the strain-displacement relations are modelled accurately by accounting for the von Kármán geometric nonlinearity as shown.

$$\varepsilon_x = \frac{\partial u}{\partial x} + \frac{1}{2}\left(\frac{\partial w}{\partial x}\right)^2; \; \varepsilon_y = \frac{\partial v}{\partial y} + \frac{1}{2}\left(\frac{\partial w}{\partial y}\right)^2; \; \varepsilon_{xy} = \frac{\partial u}{\partial y} + \frac{\partial v}{\partial x} + \frac{\partial w}{\partial x} \cdot \frac{\partial w}{\partial y} \tag{2.19}$$

Again, by substituting equations (2.15) into equations (2.19), the strain-displacement relationships with von Kármán geometric nonlinearity can be expressed by equations (2.17) with the mid-plane strains and curvatures given as in equations (2.20).

$$\left.\begin{aligned} \varepsilon_x^0 = \frac{\partial u^0}{\partial x} + \frac{1}{2}\left(\frac{\partial w}{\partial x}\right)^2; \varepsilon_y^0 = \frac{\partial v^0}{\partial y} + \frac{1}{2}\left(\frac{\partial w}{\partial y}\right)^2; \varepsilon_{xy}^0 = \frac{\partial u^0}{\partial y} + \frac{\partial v^0}{\partial x} + \frac{\partial w}{\partial x} \cdot \frac{\partial w}{\partial y} \\ k_x^0 = -\frac{\partial^2 w}{\partial x^2}; \quad k_y^0 = -\frac{\partial^2 w}{\partial y^2}; \quad k_{xy}^0 = -2\frac{\partial^2 w}{\partial x \partial y} \end{aligned}\right\} \tag{2.20}$$

2.3 First-order shear deformation plate theory

For a moderately thick plate neglecting the effect of transverse shear strains (as is done with the CPT) leads to significant errors. To address this, a plate theory that accounts for transverse shear strains must be used to model the displacement of a moderately thick plate. The FSDPT of Mindlin is the simplest and most popular of all shear deformation plate theories. Of the ESL theories, it is the best compromise considering simplicity, accuracy, and computational cost (Reddy, 2004). Here, the FSDPT is formulated starting from the equations of motion of linear elastic solids. According to Abrate (2011), the equations of motion of a 3-D solid after neglecting body forces are

$$\frac{\partial \sigma_{xx}}{\partial x} + \frac{\partial \sigma_{xy}}{\partial y} + \frac{\partial \sigma_{xz}}{\partial z} = \rho \frac{\partial^2 u}{\partial t^2} \tag{2.21a}$$

$$\frac{\partial \sigma_{xy}}{\partial x} + \frac{\partial \sigma_{yy}}{\partial y} + \frac{\partial \sigma_{yz}}{\partial z} = \rho \frac{\partial^2 v}{\partial t^2} \tag{2.21b}$$

$$\frac{\partial \sigma_{xz}}{\partial x} + \frac{\partial \sigma_{yz}}{\partial y} + \frac{\partial \sigma_{zz}}{\partial z} = \rho \frac{\partial^2 w}{\partial t^2} \tag{2.21c}$$

σ_{xx}, σ_{yy}, and σ_{zz} are the normal stresses in the x-, y-, and z-directions respectively, and σ_{xy}, σ_{xz}, and σ_{yz} are the shear stress in the planes indicated by their subscripts. Note that the effect of in-plane forces on the flexural displacement is not included in these equations.

To start with, equations (2.21 a – c) are integrated in the z-direction to get

$$\frac{\partial N_x}{\partial x}+\frac{\partial N_{xy}}{\partial y}+\frac{\partial Q_x}{\partial z}=\rho\int_{-h/2}^{+h/2}\frac{\partial^2 u}{\partial t^2}dz \qquad (2.22a)$$

$$\frac{\partial N_{xy}}{\partial x}+\frac{\partial N_y}{\partial y}+\frac{\partial Q_y}{\partial z}=\rho\int_{-h/2}^{+h/2}\frac{\partial^2 v}{\partial t^2}dz \qquad (2.22b)$$

$$\frac{\partial Q_x}{\partial x}+\frac{\partial Q_y}{\partial y}+\int_{-h/2}^{+h/2}\frac{\partial \sigma_{zz}}{\partial z}dz=\rho\int_{-h/2}^{+h/2}\frac{\partial^2 w}{\partial t^2}dz \qquad (2.22c)$$

Equations (2.2) and (2.11) have been applied in arriving at equations (2.22 a – c). The third term on the left hand side (LHS) of equation (2.22c) simplifies to $\sigma_{zz}(h/2)-\sigma_{zz}(-h/2)=q(x,y,t)$, which represents the resultant normal pressure acting on the surface of the plate. Since the FSDPT assumes a constant transverse shear strain across the plate thickness, then $\partial Q_x/\partial z=\partial Q_y/\partial z=0$. Hence,

$$\frac{\partial N_x}{\partial x}+\frac{\partial N_{xy}}{\partial y}=\rho\int_{-h/2}^{+h/2}\frac{\partial^2 u}{\partial t^2}dz \qquad (2.23a)$$

$$\frac{\partial N_{xy}}{\partial x}+\frac{\partial N_y}{\partial y}=\rho\int_{-h/2}^{+h/2}\frac{\partial^2 v}{\partial t^2}dz \qquad (2.23b)$$

$$\frac{\partial Q_x}{\partial x}+\frac{\partial Q_y}{\partial y}+q(x,y,t)=\rho\int_{-h/2}^{+h/2}\frac{\partial^2 w}{\partial t^2}dz \qquad (2.23c)$$

Next, equations (2.21a, b) are multiplied by z and integration in the z-direction is carried out once again.

$$\frac{\partial M_x}{\partial x}+\frac{\partial M_{xy}}{\partial y}+\int_{-h/2}^{+h/2}\frac{\partial \sigma_{xz}}{\partial z}z\,dz=\rho\int_{-h/2}^{+h/2}\frac{\partial^2 u}{\partial t^2}z\,dz \qquad (2.24a)$$

$$\frac{\partial M_{xy}}{\partial x}+\frac{\partial M_y}{\partial y}+\int_{-h/2}^{+h/2}\frac{\partial \sigma_{yz}}{\partial z}z\,dz=\rho\int_{-h/2}^{+h/2}\frac{\partial^2 v}{\partial t^2}z\,dz \qquad (2.24b)$$

Equation (2.8) was applied in arriving at equations (2.24a, b). The third terms on the LHS of equations (2.24a, b) can be simplified using integration by parts. For instance, the third term on the LHS of equation (2.24a) is simplified as shown.

$$\int_{-h/2}^{+h/2}\frac{\partial \sigma_{xz}}{\partial z}z\,dz=\int_{-h/2}^{+h/2}\frac{\partial(\sigma_{xz}z)}{\partial z}dz-\int_{-h/2}^{+h/2}\sigma_{xz}\,dz=\sigma_{xz}z\big|_{-h/2}^{+h/2}-Q_x$$

$\sigma_{xz} z|_{-h/2}^{+h/2}$ is the sum of distributed moments created by the shear stress σ_{xz} acting on the top and bottom surfaces of the plate. Generally, this sum is zero. Therefore,

$$\int_{-h/2}^{+h/2} \frac{\partial \sigma_{xz}}{\partial z} z \, dz = -Q_x$$

Similarly, the third term on the LHS of equation (2.24b) simplifies to

$$\int_{-h/2}^{+h/2} \frac{\partial \sigma_{yz}}{\partial z} z \, dz = -Q_y$$

Using the above simplifications, equations (2.24a, b) become

$$\frac{\partial M_x}{\partial x} + \frac{\partial M_{xy}}{\partial y} - Q_x = \rho \int_{-h/2}^{+h/2} \frac{\partial^2 u}{\partial t^2} z \, dz \qquad (2.25a)$$

$$\frac{\partial M_{xy}}{\partial x} + \frac{\partial M_y}{\partial y} - Q_y = \rho \int_{-h/2}^{+h/2} \frac{\partial^2 v}{\partial t^2} z \, dz \qquad (2.25b)$$

The final aspect in the present formulation of vibration model based on the FSDPT deals with evaluating the RHS of equations (2.23a – c) and (2.25a, b). To do this, the displacement field of the FSDPT must be known and that is discussed next.

2.3.1 Strain-displacement relationships for FSDPT

In the FSDPT, the lines perpendicular to the mid-plane before deformation do not remain so after deformation. The rotations of the mid-plane normal are accounted for by assuming constant through-thickness transverse shear strains. Additionally, the transverse normal strain is negligible as in the CPT. The kinematic assumptions of the FSDPT are expressed mathematically as:

$$\varepsilon_z = \frac{\partial w}{\partial z} = 0; \; \varepsilon_{xz} = \frac{\partial u}{\partial z} + \frac{\partial w}{\partial x} = C_1; \; \varepsilon_{yz} = \frac{\partial v}{\partial z} + \frac{\partial w}{\partial y} = C_2 \qquad (2.26a)$$

C_1 and C_2 are constant through-thickness shear strains in the x-z and y-z plane respectively. Integrating equations (2.26a) with respect to z gives the displacement field of the FSDPT as

$$\left.\begin{aligned} u(x,y,z,t) &= u^0(x,y,t) + z\left(C_1 - \frac{\partial w}{\partial x}\right) \\ v(x,y,z,t) &= v^0(x,y,t) + z\left(C_2 - \frac{\partial w}{\partial y}\right) \\ w(x,y,t) &= w^0(x,y,t) \end{aligned}\right\} \qquad (2.26b)$$

Equations (2.26b) can be written in the form

$$\left.\begin{array}{c} u(x,y,z,t) = u^0(x,y,t) + z\phi_x \\ v(x,y,z,t) = v^0(x,y,t) + z\phi_y \\ w(x,y,t) = w^0(x,y,t) \end{array}\right\} \quad (2.26c)$$

where $\phi_x = C_1 - \partial w/\partial x$ and $\phi_y = C_2 - \partial w/\partial y$ are rotations of a transverse normal about the y- and x-axes respectively. Whereas the displacement field of the CPT has three unknowns, that of the FSDPT has five unknowns i.e. three displacements and two rotations.

During small flexural oscillations the strain-displacements relationships are

$$\varepsilon_x = \frac{\partial u}{\partial x}; \varepsilon_y = \frac{\partial v}{\partial y}; \varepsilon_{xy} = \frac{\partial u}{\partial y} + \frac{\partial v}{\partial x}; \varepsilon_{xz} = \frac{\partial u}{\partial z} + \frac{\partial w}{\partial x}; \varepsilon_{yz} = \frac{\partial v}{\partial z} + \frac{\partial w}{\partial y}; \varepsilon_z = 0 \quad (2.27)$$

By substituting equations (2.26c) into equations (2.27), the strain-displacement relationship for the FSDPT was obtained as

$$\left.\begin{array}{c} \varepsilon_x = \varepsilon_x^0 + zk_x^0 \; ; \; \varepsilon_y = \varepsilon_y^0 + zk_y^0 \; ; \; \varepsilon_{xy} = \varepsilon_{xy}^0 + zk_{xy}^0 \\ \varepsilon_{xz} = \dfrac{\partial w}{\partial x} + \phi_x \; ; \; \varepsilon_{yz} = \dfrac{\partial w}{\partial y} + \phi_y \end{array}\right\} \quad (2.28)$$

where

$$\left.\begin{array}{lll} \varepsilon_x^0 = \dfrac{\partial u^0}{\partial x}; & \varepsilon_y^0 = \dfrac{\partial v^0}{\partial y}; & \varepsilon_{xy}^0 = \dfrac{\partial u^0}{\partial y} + \dfrac{\partial v^0}{\partial x} \\ k_x^0 = \dfrac{\partial \phi_x}{\partial x}; & k_y^0 = \dfrac{\partial \phi_y}{\partial y}; & k_{xy}^0 = \dfrac{\partial \phi_x}{\partial y} + \dfrac{\partial \phi_y}{\partial x} \end{array}\right\} \quad (2.29)$$

2.3.2 Rectangular plate vibration model based on FSDPT

As mentioned earlier, the displacement field of the FSDPT is required to complete the plate vibration model based on the FSDPT. The plate vibration model is obtained by using the displacement field in equations (2.26c) to evaluate the expressions on the RHS of equations (2.23a – c) and (2.25a, b).

$$\rho \int_{-h/2}^{+h/2} \frac{\partial^2 u}{\partial t^2} dz = \rho \int_{-h/2}^{+h/2} \frac{\partial^2}{\partial t^2}(u^0 + z\phi_x)\, dz = I_0 \frac{\partial^2 u^0}{\partial t^2} + I_1 \frac{\partial^2 \phi_x}{\partial t^2} \quad (2.30a)$$

$$\rho \int_{-h/2}^{+h/2} \frac{\partial^2 v}{\partial t^2} dz = \rho \int_{-h/2}^{+h/2} \frac{\partial^2}{\partial t^2}\left(v^0 + z\phi_y\right) dz = I_0 \frac{\partial^2 v^0}{\partial t^2} + I_1 \frac{\partial^2 \phi_y}{\partial t^2} \quad (2.30b)$$

$$\rho \int_{-h/2}^{+h/2} \frac{\partial^2 w}{\partial t^2} dz = I_0 \frac{\partial^2 w}{\partial t^2} \quad (2.30c)$$

$$\rho \int_{-h/2}^{+h/2} \frac{\partial^2 u}{\partial t^2} z dz = \rho \int_{-h/2}^{+h/2} \frac{\partial^2}{\partial t^2}(u^0 z + z^2\phi_x)\, dz = I_1 \frac{\partial^2 u^0}{\partial t^2} + I_2 \frac{\partial^2 \phi_x}{\partial t^2} \quad (2.30d)$$

$$\rho \int_{-h/2}^{+h/2} \frac{\partial^2 v}{\partial t^2} z dz = \rho \int_{-h/2}^{+h/2} \frac{\partial^2}{\partial t^2}\left(v^0 z + z^2\phi_y\right) dz = I_1 \frac{\partial^2 v^0}{\partial t^2} + I_2 \frac{\partial^2 \phi_y}{\partial t^2} \quad (2.30e)$$

where $I_0, I_1,$ and I_2 are inertia components and they are given by:

$$I_0, I_1, I_2 = \rho \int_{-h/2}^{+h/2} (1, z, z^2)\, dz = \rho h, 0, \frac{1}{12}\rho h^3 \qquad (2.30f)$$

I_0 is the pure inertia effect, I_1 is the inertia coupling effect between in-plane and transverse motion, and I_2 is the rotary inertia effect. In general, $I_1 = 0$.

Substituting equations (2.30a – f) into equations (2.23a – c) and (2.25a, b), the vibration model of a moderately thick rectangular plate based on the FSDPT is derived as shown in equations (2.31a – e).

$$\frac{\partial N_x}{\partial x} + \frac{\partial N_{xy}}{\partial y} = \rho h \frac{\partial^2 u^0}{\partial t^2} \qquad (2.31a)$$

$$\frac{\partial N_{xy}}{\partial x} + \frac{\partial N_y}{\partial y} = \rho h \frac{\partial^2 v^0}{\partial t^2} \qquad (2.31b)$$

$$\frac{\partial M_x}{\partial x} + \frac{\partial M_{xy}}{\partial y} - Q_x = \frac{1}{12}\rho h^3 \frac{\partial^2 \phi_x}{\partial t^2} \qquad (2.31c)$$

$$\frac{\partial M_{xy}}{\partial x} + \frac{\partial M_y}{\partial y} - Q_y = \frac{1}{12}\rho h^3 \frac{\partial^2 \phi_y}{\partial t^2} \qquad (2.31d)$$

$$\frac{\partial Q_x}{\partial x} + \frac{\partial Q_y}{\partial y} + q(x, y, t) = \rho h \frac{\partial^2 w}{\partial t^2} \qquad (2.31e)$$

2.4 Constitutive equations of laminated rectangular plates

So far the rectangular plate equations based on the CPT (for thin plates) and the FSDPT (for moderately thick plates) have been expressed in terms of the resultant in-plane forces, moments and transverse shear forces. The expressions for the resultant forces and moments are determined through the constitutive equations of the plate, which express the behaviour of the plate in terms of stresses and strains. For a laminated plate, the constitutive equations can be derived using the ESL approach. This approach represents a laminated plate with several layers as an equivalent monolithic plate having an aggregate constitutive behaviour averaged through the thickness. It is a widely used approach and is capable of giving accurate predictions of the global response of a laminated plate (Reddy, 2004). Given that the present research is concerned only with the global vibration response of rectangular plates, the ESL approach has been applied to develop the constitutive equations for the laminated plate that has been investigated.

The constitutive equations presented here are for anisotropic plates with orthotropic layers. By orthotropic, it is meant that a material has properties differing in three mutually perpendicular directions. Loaded thin and moderately thick rectangular plates can be said to be in a state of plane stress. The mechanical stress-strain relationships for a Hookean-orthotropic lamina under plane stress conditions are (Reddy, 2004)

$$\begin{Bmatrix} \sigma_x \\ \sigma_y \\ \sigma_{xy} \\ \sigma_{xz} \\ \sigma_{yz} \end{Bmatrix} = \begin{bmatrix} \bar{Q}_{11} & \bar{Q}_{12} & \bar{Q}_{16} & 0 & 0 \\ \bar{Q}_{12} & \bar{Q}_{22} & \bar{Q}_{26} & 0 & 0 \\ \bar{Q}_{16} & \bar{Q}_{26} & \bar{Q}_{66} & 0 & 0 \\ 0 & 0 & 0 & \bar{Q}_{55} & \bar{Q}_{45} \\ 0 & 0 & 0 & \bar{Q}_{45} & \bar{Q}_{44} \end{bmatrix} \begin{Bmatrix} \varepsilon_x \\ \varepsilon_y \\ \varepsilon_{xy} \\ \varepsilon_{xy} \\ \varepsilon_{xy} \end{Bmatrix} \tag{2.32}$$

where $\begin{bmatrix} \bar{Q}_{11} & \bar{Q}_{12} & \bar{Q}_{16} & 0 & 0 \\ \bar{Q}_{12} & \bar{Q}_{22} & \bar{Q}_{26} & 0 & 0 \\ \bar{Q}_{16} & \bar{Q}_{26} & \bar{Q}_{66} & 0 & 0 \\ 0 & 0 & 0 & \bar{Q}_{55} & \bar{Q}_{45} \\ 0 & 0 & 0 & \bar{Q}_{45} & \bar{Q}_{44} \end{bmatrix}$ is the transformed (global) stiffness matrix. The elements of the transformed stiffness matrix depend on the angle between the material axes of each lamina and the axes of the laminate. The expressions for calculating the elements of the transformed stiffness matrix can be found in numerous texts dealing with composite laminates (e.g. Staab, 1999; Jones, 1999; Reddy, 2004; Vinson and Sierakowski, 2004).

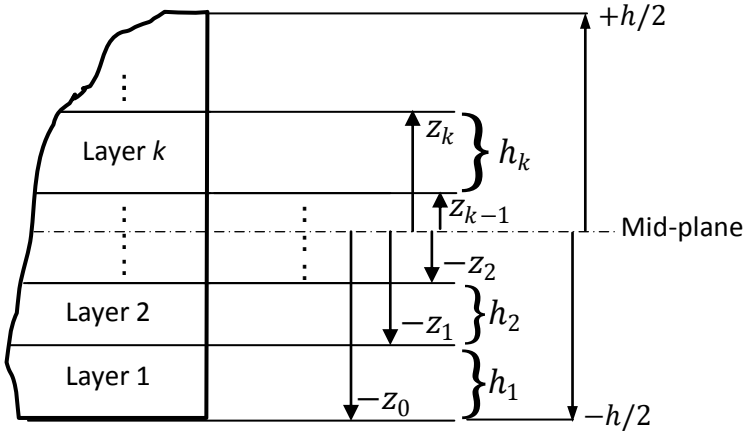

Figure 2.6: *Sketch illustrating vertical geometry of laminate*

The stresses on the laminated rectangular plate are discontinuous in the thickness direction due to change in material properties from one lamina to the other. To evaluate the force and moment resultants of a laminate the discontinuous stresses must be integrated. The ESL approach determines the

stress integration layerwise (i.e. for each lamina) and sums up the force and moment resultants for all the layers to get the force and moment resultants for the laminate. The summation follows a well-defined through-thickness geometry nomenclature as shown in Figure 2.6. The layers of the laminate are numbered bottom-up starting from 1 to *N* and the distances of the layer boundaries are measured from the mid-plane.

In accordance with the ESL approach, the force and moment resultants of a rectangular laminate can be evaluated as

$$\begin{Bmatrix} N_x \\ N_y \\ N_{xy} \end{Bmatrix} = \sum_{k=1}^{N} \int_{z_{k-1}}^{z_k} \begin{Bmatrix} \sigma_x \\ \sigma_y \\ \sigma_{xy} \end{Bmatrix} dz \tag{2.33a}$$

$$\begin{Bmatrix} M_x \\ M_y \\ M_{xy} \end{Bmatrix} = \sum_{k=1}^{N} \int_{z_{k-1}}^{z_k} \begin{Bmatrix} \sigma_x \\ \sigma_y \\ \sigma_{xy} \end{Bmatrix} z dz \tag{2.33b}$$

$$\begin{Bmatrix} Q_x \\ Q_y \end{Bmatrix} = \sum_{k=1}^{N} \int_{z_{k-1}}^{z_k} \mathcal{K}_k \begin{Bmatrix} \sigma_{xz} \\ \sigma_{yz} \end{Bmatrix} dz \tag{2.33c}$$

where k is the layer index, and N is the total number of layers, and $\mathcal{K}$ is the shear correction factor, which is used to account for the fact that the transverse shear stress has a parabolic distribution across the thickness of the plate instead of the assumed constant value. The *k*th layer is bounded by surfaces at z_k and z_{k-1} at the top and bottom respectively.

2.4.1 Constitutive equations for a thin rectangular laminate based on CPT

The constitutive equations of a thin rectangular laminate can be derived by using equations (2.32) and (2.17) in equations (2.33a, b) to get

$$\begin{Bmatrix} N_x \\ N_y \\ N_{xy} \end{Bmatrix} = \begin{bmatrix} A_{11} & A_{12} & A_{16} \\ A_{12} & A_{22} & A_{26} \\ A_{16} & A_{26} & A_{66} \end{bmatrix} \begin{Bmatrix} \varepsilon_x^0 \\ \varepsilon_y^0 \\ \varepsilon_{xy}^0 \end{Bmatrix} + \begin{bmatrix} B_{11} & B_{12} & B_{16} \\ B_{12} & B_{22} & B_{26} \\ B_{16} & B_{26} & B_{66} \end{bmatrix} \begin{Bmatrix} k_x^0 \\ k_y^0 \\ k_{xy}^0 \end{Bmatrix} \tag{2.34a}$$

$$\begin{Bmatrix} M_x \\ M_y \\ M_{xy} \end{Bmatrix} = \begin{bmatrix} B_{11} & B_{12} & B_{16} \\ B_{12} & B_{22} & B_{26} \\ B_{16} & B_{26} & B_{66} \end{bmatrix} \begin{Bmatrix} \varepsilon_x^0 \\ \varepsilon_y^0 \\ \varepsilon_{xy}^0 \end{Bmatrix} + \begin{bmatrix} D_{11} & D_{12} & D_{16} \\ D_{12} & D_{22} & D_{26} \\ D_{16} & D_{26} & D_{66} \end{bmatrix} \begin{Bmatrix} k_x^0 \\ k_y^0 \\ k_{xy}^0 \end{Bmatrix} \tag{2.34b}$$

$[A_{ij}]$,$[B_{ij}]$ and $[D_{ij}]$ for $i,j = 1,2,6$ are the extensional, bending-extension coupling, and bending stiffness matrices respectively, and are determined as

$$\left.\begin{aligned} A_{ij} &= \sum_{k=1}^{N} \bar{Q}_{ijk}\,(z_k - z_{k-1}) \\ B_{ij} &= \frac{1}{2}\sum_{k=1}^{N} \bar{Q}_{ijk}\,(z_k^2 - z_{k-1}^2) \\ D_{ij} &= \frac{1}{3}\sum_{k=1}^{N} \bar{Q}_{ijk}\,(z_k^3 - z_{k-1}^3) \end{aligned}\right\} \tag{2.35}$$

$\bar{Q}_{ijk}$ is the transformed reduced stiffness of the *k*th layer of the laminate, and is related to material properties of the *k*th layer as shown in equations (2.36), assuming the material axes of each layer coincides with the laminate axes.

$$\left.\begin{aligned} (\bar{Q}_{11})_k &= \left(\frac{E_1}{1-\upsilon_{12}\upsilon_{21}}\right)_k \\ (\bar{Q}_{12})_k &= \left(\frac{\upsilon_{12}E_2}{1-\upsilon_{12}\upsilon_{21}}\right)_k \\ (\bar{Q}_{22})_k &= \left(\frac{E_2}{1-\upsilon_{12}\upsilon_{21}}\right)_k \\ (\bar{Q}_{66})_k = (G_{12})_k &= \left[\frac{E_2}{2(1+\upsilon_{12})}\right]_k \\ (\bar{Q}_{16})_k &= (\bar{Q}_{26})_k = 0 \end{aligned}\right\} \tag{2.36}$$

$(\bar{Q}_{16})_k = (\bar{Q}_{26})_k = 0$ for orthotropic anisotropy under plane stress, E is the Young's modulus and υ is the Poisson's ratio. The mid-plane strains and curvatures in equations (2.34a, b) are obtained from equations (2.18) and (2.20) for small and large flexural displacements respectively.

2.4.2 Constitutive equations for a moderately thick rectangular laminate based on FSDPT

The constitutive equations of a moderately thick rectangular laminate can be derived by using equations (2.32) and (2.28) in equations (2.33a – c). For the in-plane force and moment resultants the constitutive equations are the same as equations (2.34a, b), but the mid-plane strains and curvatures are obtained from equation (2.29). For the transverse shear force resultants the constitutive equations are

$$\begin{Bmatrix} Q_x \\ Q_y \end{Bmatrix} = \begin{bmatrix} A_{55} & A_{45} \\ A_{45} & A_{44} \end{bmatrix} \begin{Bmatrix} \varepsilon_{xz} \\ \varepsilon_{yz} \end{Bmatrix} \tag{2.37}$$

where

$$A_{ij} = \sum_{k=1}^{N} \mathcal{K}_k \bar{Q}_{ijk} (z_k - z_{k-1}) \qquad for\ i,j = 4,5$$

If the material axes of each layer coincides with the laminate axes then $A_{45} = 0$ and the transverse shear stresses depend on A_{44} and A_{55} only. In that case, $(\bar{Q}_{44})_k = (G_{23})_k$ and $(\bar{Q}_{55})_k = (G_{13})_k$. $\mathcal{K}_k$ is the shear correction factor for the *k*th lamina.

It has been shown that the shear correction factor of a thick isotropic plate depends on the Poisson's ratio of the material (Liew *et al*, 1998). Wittrick (1987) proposed that the shear correction factor could be determined as $\mathcal{K} = 5/(6 - v)$. Liew *et al* (1998) suggests that Wittrick's shear correction formula is preferable to others incorporating Poisson's ratio effect because of its simplicity and accuracy. With thick laminated plates the shear correction factor depends generally on the laminate properties (Reddy, 2004). Madabhusi-Raman and Daralos (1996) derived an expression for $\mathcal{K}$ in algebraic form for a general *N*-layer rectangular laminate. Their formula appears to be the most comprehensive direct expression for calculating $\mathcal{K}$ that takes into account the laminate properties. Simpler expressions for orthotropic laminates with rectangular cross-section have been proposed by Teh and Haung (1979), Dharmarajan and McCutchen (1973), and Omidvar (1998). Others have used the common value of $\mathcal{K} = 5/6$ in studying shear deformable laminated plates (Bert and Chen, 1978; Li and Mirza, 1995; Reddy, 2004; etc). In the present research, Wittrick's formula has been applied to each layer in determining $\mathcal{K}$ so as to account for the Poisson's ratio effect of each lamina of the trimorph plate.

2.5 Determination of the laminate stiffness coefficients

Alternative expressions to equations (2.35) have been presented by Staab (1999) for the determination of the laminate stiffness coefficients. The stiffness coefficients were expressed in terms of the distance of each lamina centroid measured from the mid-plane, and the thickness of the lamina. Big-Alabo and Cartmell (2011) attempted to simplify algebraically the evaluation of the stiffness coefficients by expressing them in terms of the lamina thicknesses only. While this representation is computationally simple, the mid-plane was not taken into account. Consequently, the bending-extension and bending stiffnesses

calculated using this approach are higher than the actual values. Here the mid-plane has been accounted for and a sign convention has been introduced to ensure consistency with plate deformation theory and to produce accurate results. The sign convention requires that lamina boundaries which lie below the mid-plane are negative while those above the mid-plane are positive (see Figure 2.6). The stiffness coefficients are then expressed in terms of the lamina thicknesses and the total thickness of the laminate.

From Figure 2.6, the following can be deduced geometrically,

$$\left.\begin{aligned} z_k - z_{k-1} &= h_k \\ z_k &= \sum_{i=1}^{k} h_i - h/2 \qquad ; k > 0 \ \ or \\ z_{k-1} &= \sum_{i=1}^{k-1} h_i - h/2 \quad ; k > 1 \end{aligned}\right\} \tag{2.38}$$

where h_k is the thickness of the *k*th layer. If the inequalities in equations (2.38b, c) are not satisfied then $z_k = 0$ and $z_{k-1} = 0$.

$z_k^2 - z_{k-1}^2 = (z_k + z_{k-1})(z_k - z_{k-1}) = (z_k - z_{k-1} + 2z_{k-1})(z_k - z_{k-1})$

Applying equation (2.38), $z_k^2 - z_{k-1}^2 = (h_k + 2z_{k-1})h_k = h_k\left(h_k + 2\sum_{i=1}^{k-1} h_i - h\right)$.

Also, $z_k^3 - z_{k-1}^3 = (z_k - z_{k-1})^3 + 3(z_k - z_{k-1})z_k z_{k-1}$.

Applying equation (2.38), $z_k^3 - z_{k-1}^3 = h_k^3 + 3h_k\left(\sum_{i=1}^{k} h_i - h/2\right)\left(\sum_{i=1}^{k-1} h_i - h/2\right)$.

Consequently, the extension, bending-extension and bending stiffness coefficients for *i*, *j* = 1, 2, 6 can be determined thus:

$$\left.\begin{aligned} A_{ij} &= \sum_{k=1}^{N} \bar{Q}_{ijk}\, h_k \\ B_{ij} &= \frac{1}{2}\sum_{k=1}^{N} \bar{Q}_{ijk}\, h_k \left(h_k + 2\sum_{i=1}^{k-1} h_i - h \right) \\ D_{ij} &= \frac{1}{3}\sum_{k=1}^{N} \bar{Q}_{ijk} \left[h_k^3 + 3h_k \left(\sum_{i=1}^{k} h_i - h/2 \right)\left(\sum_{i=1}^{k-1} h_i - h/2 \right) \right] \end{aligned}\right\} \tag{2.39a}$$

Similarly, the shear stiffness coefficients are calculated from

$$A_{ij} = \sum_{k=1}^{N} \mathcal{K}_k \bar{Q}_{ijk}\, h_k \qquad for\ i,j = 4,5 \tag{2.39b}$$

where $\mathcal{K}_k = 5/(6 - \upsilon_k)$. The validity of equations (2.39a) was confirmed by comparing with results obtained using equations (2.35) and Staab's expressions (1999). All three expressions produced exactly the same results for the

extension, bending-extension, and bending stiffnesses of an Al/PVDF/PZT laminate (see Table 2.1 for material properties).

2.6 Vibration analysis of a trimorph plate

The trimorph plate is a multilayered rectangular plate having three layers bonded adhesively together so that the relative motion between the layers is negligible. Its layers are made up of different materials, and all the material properties are assumed to be isotropic to simplify the modelling. In the vibration analysis presented here the boundary conditions are simply-supported and the trimorph plate is excited by a harmonically-varying sinusoidally distributed load. Figure 2.7 shows a sketch of the system. The layers in Figure 2.7 have different shading patterns suggesting that they are made of different materials.

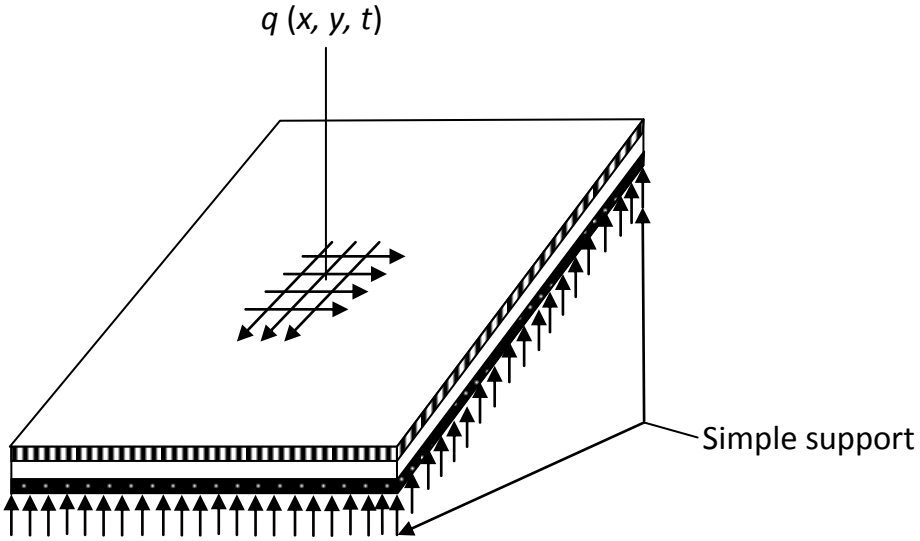

Figure 2.7: *Diagrammatic description of the excited system*

For the general case of an unsymmetric laminate with isotropic layers the following conditions apply (Jones, 1999); $A_{16} = A_{26} = B_{16} = B_{26} = D_{16} = D_{26} = 0$; $A_{11} = A_{22}, B_{11} = B_{22}, D_{11} = D_{22}$. Hence, the constitutive equations for the trimorph plate are:

$$\begin{Bmatrix} N_x \\ N_y \\ N_{xy} \end{Bmatrix} = \begin{bmatrix} A_{11} & A_{12} & 0 \\ A_{12} & A_{11} & 0 \\ 0 & 0 & A_{66} \end{bmatrix} \begin{Bmatrix} \varepsilon_x^0 \\ \varepsilon_y^0 \\ \varepsilon_{xy}^0 \end{Bmatrix} + \begin{bmatrix} B_{11} & B_{12} & 0 \\ B_{12} & B_{11} & 0 \\ 0 & 0 & B_{66} \end{bmatrix} \begin{Bmatrix} k_x^0 \\ k_y^0 \\ k_{xy}^0 \end{Bmatrix} \tag{2.40a}$$

$$\begin{Bmatrix} M_x \\ M_y \\ M_{xy} \end{Bmatrix} = \begin{bmatrix} B_{11} & B_{12} & 0 \\ B_{12} & B_{11} & 0 \\ 0 & 0 & B_{66} \end{bmatrix} \begin{Bmatrix} \varepsilon_x^0 \\ \varepsilon_y^0 \\ \varepsilon_{xy}^0 \end{Bmatrix} + \begin{bmatrix} D_{11} & D_{12} & 0 \\ D_{12} & D_{11} & 0 \\ 0 & 0 & D_{66} \end{bmatrix} \begin{Bmatrix} k_x^0 \\ k_y^0 \\ k_{xy}^0 \end{Bmatrix} \tag{2.40b}$$

In this section, the frequency- and time-domain responses of the trimorph plate are presented for the case of a thin plate and a moderately thick plate. The in-plane displacements are not considered since the interest is on the transverse displacement. The aim of the vibration analysis is to demonstrate the effect of the different possible lamination sequence of a trimorph plate composed of Al, PVDF, and PZT layers on the dynamic characteristic of the trimorph plate. Actually, Big-Alabo and Cartmell have carried out such investigations for small (2011) and large (2012) flexural oscillations of a thin trimorph plate with the latter being a part of the present research. Nevertheless, the investigations are repeated here because the expressions used for calculating the bending-extension and bending stiffnesses in the previous studies produced values higher than the actual values.

2.6.1 Vibration analysis of a thin trimorph plate

The vibration model for small flexural oscillations of the thin trimorph plate can be obtained by substituting equations (2.18) and (2.40b) into equation (2.7), and neglecting in-plane displacements.

$$\rho h\frac{\partial^2 w}{\partial t^2}+c\frac{\partial w}{\partial t}+D_{11}\left(\frac{\partial^4 w}{\partial x^4}+\frac{\partial^4 w}{\partial y^4}\right)+2(D_{12}+2D_{66})\frac{\partial^4 w}{\partial x^2\partial y^2}=q(x,y,t) \tag{2.41}$$

For large flexural oscillations of the thin trimorph plate, the vibration model is obtained by substituting equations (2.20) and (2.40b) into equation (2.13), and neglecting in-plane displacements.

$$\begin{aligned}&\rho h\frac{\partial^2 w}{\partial t^2}+c\frac{\partial w}{\partial t}+D_{11}\left(\frac{\partial^4 w}{\partial x^4}+\frac{\partial^4 w}{\partial y^4}\right)+2(D_{12}+2D_{66})\frac{\partial^4 w}{\partial x^2\partial y^2}\\&-\left\{B_{11}\left[\left(\frac{\partial^2 w}{\partial y^2}\right)^2+\left(\frac{\partial^2 w}{\partial x^2}\right)^2\right]+2B_{12}\frac{\partial^2 w}{\partial x^2}\cdot\frac{\partial^2 w}{\partial y^2}+4B_{66}\left(\frac{\partial^2 w}{\partial x\partial y}\right)^2\right.\\&+\frac{1}{2}\frac{\partial^2}{\partial x^2}\left[B_{11}\left(\frac{\partial w}{\partial x}\right)^2+B_{12}\left(\frac{\partial w}{\partial y}\right)^2\right]+\frac{1}{2}\frac{\partial^2}{\partial y^2}\left[B_{12}\left(\frac{\partial w}{\partial x}\right)^2+B_{11}\left(\frac{\partial w}{\partial y}\right)^2\right]\\&\left.+2B_{66}\frac{\partial^2}{\partial x\partial y}\left[\frac{\partial w}{\partial x}\cdot\frac{\partial w}{\partial y}\right]\right\}+\frac{1}{2}\left[A_{11}\left(\frac{\partial w}{\partial x}\right)^2+A_{12}\left(\frac{\partial w}{\partial y}\right)^2\right]\frac{\partial^2 w}{\partial x^2}\\&+\frac{1}{2}\left[A_{12}\left(\frac{\partial w}{\partial x}\right)^2+A_{11}\left(\frac{\partial w}{\partial y}\right)^2\right]\frac{\partial^2 w}{\partial y^2}+2A_{66}\frac{\partial w}{\partial x}\cdot\frac{\partial w}{\partial y}\cdot\frac{\partial^2 w}{\partial x\partial y}\\&=q(x,y,t)\end{aligned} \tag{2.42}$$

For time-dependent sinusoidally distributed load, the load distribution is given as $q(x,y,t) = q(t)\sin(\pi x/a)\sin(\pi y/b)$ where $q(t)$ is considered as a harmonically varying function for the present investigation. In general, the transverse displacement and external excitation can be expressed in series form as:

$$w(x,y,t) = \sum_{m=1}^{\infty}\sum_{n=1}^{\infty} W_{mn}(t)\, X_m Y_n \tag{2.43a}$$

$$q(x,y,t) = \sum_{m=1}^{\infty}\sum_{n=1}^{\infty} Q_{mn}(t)\sin\left(\frac{m\pi x}{a}\right)\sin\left(\frac{n\pi y}{b}\right) \tag{2.43b}$$

$$Q_{mn}(t) = \frac{4}{ab}\int_0^a\int_0^b q(x,y,t)\sin\left(\frac{m\pi x}{a}\right)\sin\left(\frac{n\pi y}{b}\right)dxdy \tag{2.43c}$$

X_m and Y_n are admissible shape functions that satisfy the boundary conditions but not necessarily the PDE. For time-dependent sinusoidally distributed load, the load coefficient simplifies to a closed-form solution that is independent of the vibration modes i.e. $Q_{mn}(t) = q(t)$. Equations (2.41) and (2.42) can be reduced to ODEs using the Galerkin variational approach (Szilard, 2004). The vibration models have been presented in such a way that the LHS of the equation is a partial differential expression (***PDEx***) in terms of the transverse displacement and the RHS is the external excitation. Thus, the Galerkin variational formula for derivation of the reduced model can be expressed as

$$\int_0^b\int_0^a \big(PDEx - q(x,y,t)\big)\, X_m Y_n\, dxdy = 0 \tag{2.44}$$

For simply-supported boundary condition on all edges of the rectangular plate (SSSS) $X_m = \sin(m\pi x/a)$ and $Y_n = \sin(n\pi y/b)$. Substituting equations (2.41), (2.42) and (2.43a) in equation (2.44) and evaluating the resulting double integral for SSSS, the reduced vibration models for the flexural oscillations of the thin trimorph plate are:

<u>Small oscillations</u>

$$\ddot{W}_{mn} + \bar{c}\dot{W}_{mn} + \bar{D}W_{mn} = \bar{Q}\sin\omega t \tag{2.45}$$

<u>Large oscillations</u>

$$\ddot{W}_{mn} + \bar{c}\dot{W}_{mn} + \bar{D}W_{mn} - \bar{B}W_{mn}^2 - \bar{A}W_{mn}^3 = \bar{Q}\sin\omega t \tag{2.46}$$

where W_{mn} is the time-domain flexural displacement of the (m,n) vibration mode;

$\bar{c} = \frac{c}{\rho h} = 2\mu\sqrt{\bar{D}}$; $\bar{Q} = \frac{q}{\rho h}$ are the damping constant per unit mass and excitation magnitude per unit mass respectively;

$\bar{D} = \frac{\pi^4}{\rho h}\left[D_{11}\left(\frac{m^4}{a^4}+\frac{n^4}{b^4}\right)+\frac{2m^2n^2(D_{12}+2D_{66})}{a^2b^2}\right]$ is the bending stiffness per unit mass;

$\bar{B} = \frac{\pi^2}{\rho h}\left(\frac{32}{3mn}\right)\left[B_{11}\left(\frac{m^4}{a^4}+\frac{n^4}{b^4}\right)+\frac{m^2n^2(B_{12}+B_{66})}{a^2b^2}\right]$ is the bending-extension stiffness per unit mass; and

$\bar{A} = \frac{\pi^4}{32\rho h}\left[3A_{11}\left(\frac{m^4}{a^4}+\frac{n^4}{b^4}\right)+\frac{m^2n^2(6A_{12}-4A_{66})}{a^2b^2}\right]$ is the extensional stiffness per unit mass.

Equations (2.45) and (2.46) have been solved by means of direct numerical integration using the NDSolve function in *Mathematica*™. The plate simulated is a 1 [*m*] x 1 [*m*] square plate with layer thicknesses of 3 [*mm*], 1 [*mm*], and 1 [*mm*] for the Al, PVDF, and PZT layers respectively. The material properties of the layers are the same as in Big-Alabo and Cartmell (2011) (see Table 2.1) and the magnitude of the excitation force used for the simulation is 10 [N/m^2].

Table 2.1: *Material properties of the trimorph plate layers*

Material	Poisson's ratio, υ [-]	Modulus, E [*GPa*]	Density, ρ [kg/m^3]
Al	0.33	70	2700
PVDF	0.44	1.1	1770
PZT	0.3	64	7600

There are six possible lamination sequences of the trimorph plate namely: Al/PVDF/PZT, Al/PZT/PVDF, PVDF/PZT/Al, PVDF/Al/PZT, PZT/Al/PVDF, and PZT/PVDF/Al, and the excitation is directly applied on the top layer. Studies were carried out for the fundamental response mode $(m = n = 1)$ and central displacement of the trimorph plate $(x = a/2; y = b/2)$ using zero initial conditions $(W(0) = \dot{W}(0) = 0)$. Tables 2.2 and 2.3 show the response characteristics for the different lamination sequences of the trimorph plate. The results show that the lamination sequence influences the response characteristics. This means that the lamination sequence of a multilayer laminated plate with more than one material composition can be a basis for selecting the best layer-stacking (Big-Alabo and Cartmell, 2011; 2012). For most applications, a plate with high bending stiffness or undamped natural frequency is desirable. This is because a higher bending stiffness results in lower transverse displacements. According to the results in Tables 2.2 and 2.3 the Al/PVDF/PZT or PZT/PVDF/Al lamination sequence meets this condition better than the other lamination sequences.

Tables 2.2 and 2.3 show that lamination sequences with the same mid-layer material, for example Al/PVDF/PZT and PZT/PVDF/Al, produced identical response characteristics. The implication is that there are three different lamination sequences to choose from rather than six. However, the bending-extension stiffness of those lamination sequences with identical response characteristics differ in sign. The difference in sign explains why the nonlinear steady-state displacements of lamination sequences with the same mid-layer material are slightly different. Also, the extensional stiffness is independent of the lamination sequence, which means that the cubic nonlinearity effect is the same for all the lamination sequences.

The response characteristics of the thin trimorph plate presented in Table 2.2 are for small flexural oscillations while those in Table 2.3 are for large flexural oscillations. The response characteristics were obtained for an excitation frequency equal to the undamped natural frequency. To distinguish between small and large flexural oscillations, the criterion proposed by Szilard (2004) has been applied i.e. that the ratio of the maximum displacement to the plate thickness must be less than 0.2 for small flexural oscillations. Hence a damping ratio of 0.05 was used to simulate small flexural oscillations whereas a ratio of 0.001 was used to simulate large flexural oscillations. The results of the steady-state displacement at the undamped natural frequency (see Table 2.2) reveal that the nonlinearities have a marginal effect during small flexural oscillations. Therefore, the membrane stretching effect can be neglected for small flexural oscillations (Szilard, 2004). However, the nonlinearities have a very strong influence on the response during large flexural oscillations (see Table 2.3 and Figures 2.9a – f). The effect of the nonlinearities is to reduce the magnitude of the flexural oscillations and to shift the natural frequency of the plate to the left of the undamped natural frequency.

Table 2.2: *Response characteristics for small flexural oscillations* $(\mu = 0.05)$

S/N	Layer Arrangement 1-2-3 respectively	Bending stiffness $(\bar{D})$ [N/mkg]	Bending-extensional stiffness $(\bar{B})$ [N/m^{2}kg]	Extensional stiffness $(\bar{A})$ [N/m^{3}kg]	Operating frequency [rad/s]	Damping constant [Ns/mkg]	Linear steady-state response (w/h) [-]	Nonlinear steady-state response (w/h) [-]
1	Al/PVDF/PZT	15661.2	505768.	3.534×10^8	125.145	12.515	0.0731	0.0733
2	Al/PZT/PVDF	11039.4	872978.	3.534×10^8	105.068	10.507	0.104	0.105
3	PVDF/PZT/Al	11039.4	-872978.	3.534×10^8	105.068	10.507	0.104	0.102
4	PVDF/Al/PZT	10488.1	-734421.	3.534×10^8	102.412	10.241	0.109	0.106
5	PZT/Al/PVDF	10488.1	734421.	3.534×10^8	102.412	10.241	0.109	0.109
6	PZT/PVDF/Al	15661.2	-505768.	3.534×10^8	125.145	12.515	0.0731	0.0727

Table 2.3: *Response characteristics for large flexural oscillations* $(\mu = 0.001)$

S/N	Layer Arrangement 1-2-3 respectively	Bending stiffness $(\bar{D})$ [N/mkg]	Bending-extensional stiffness $(\bar{B})$ [N/m^{2}kg]	Extensional stiffness $(\bar{A})$ [N/m^{3}kg]	Operating frequency [rad/s]	Damping constant [Ns/mkg]	Linear steady-state response (w/h) [-]	Nonlinear steady-state response (w/h) [-]
1	Al/PVDF/PZT	15661.2	505768.	3.534×10^8	125.145	0.250	3.645	0.257
2	Al/PZT/PVDF	11039.4	872978.	3.534×10^8	105.068	0.210	5.149	0.250
3	PVDF/PZT/Al	11039.4	-872978.	3.534×10^8	105.068	0.210	5.149	0.233
4	PVDF/Al/PZT	10488.1	-734421.	3.534×10^8	102.412	0.205	5.394	0.228
5	PZT/Al/PVDF	10488.1	734421.	3.534×10^8	102.412	0.205	5.394	0.242
6	PZT/PVDF/Al	15661.2	-505768.	3.534×10^8	125.145	0.250	3.645	0.249

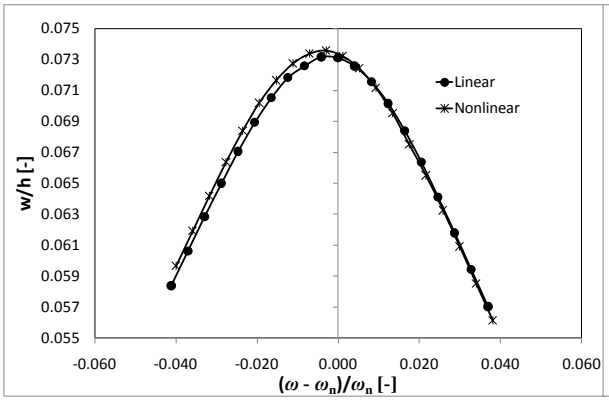

(a) Al/PVDF/PZT

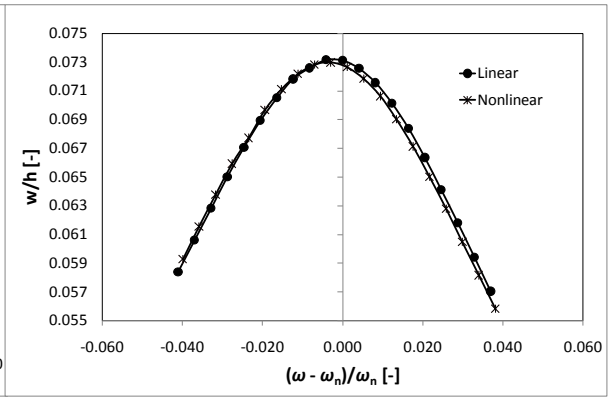

(b) PZT/PVDF/Al

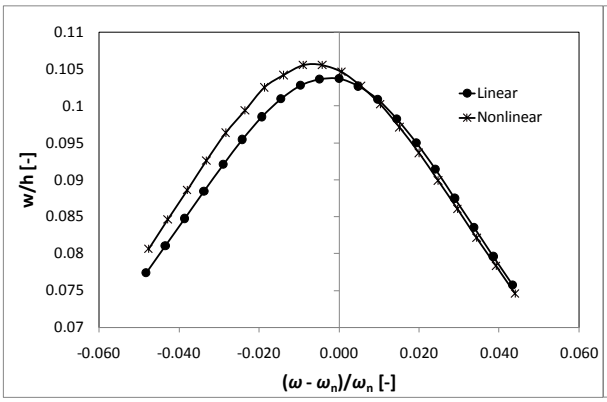

(c) Al/PZT/PVDF

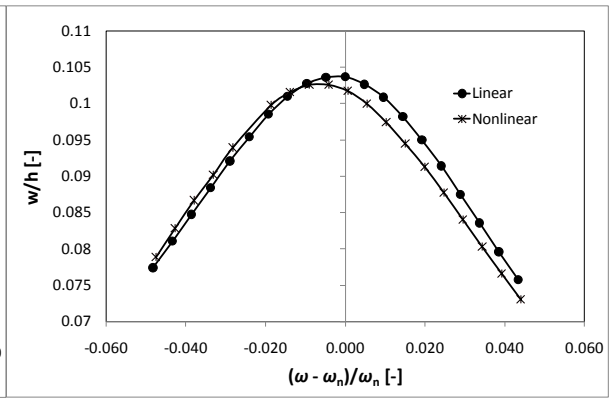

(d) PVDF/PZT/Al

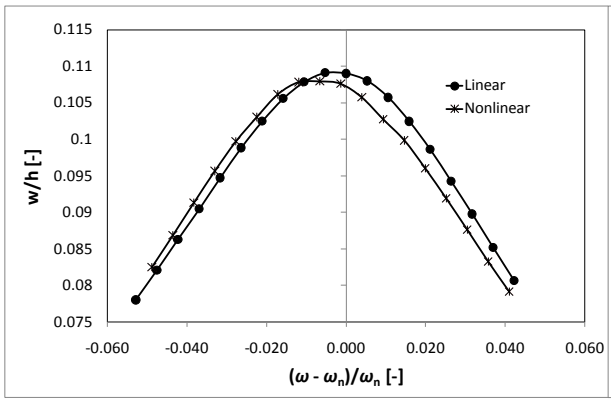

(e) PVDF/Al/PZT

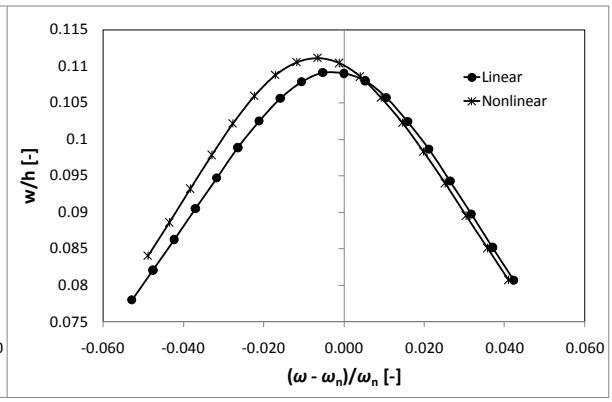

(f) PZT/Al/PVDF

Figure 2.8: *Frequency-response of a thin trimorph plate during small flexural oscillations of the plate centre* ($\mu = 0.05$).

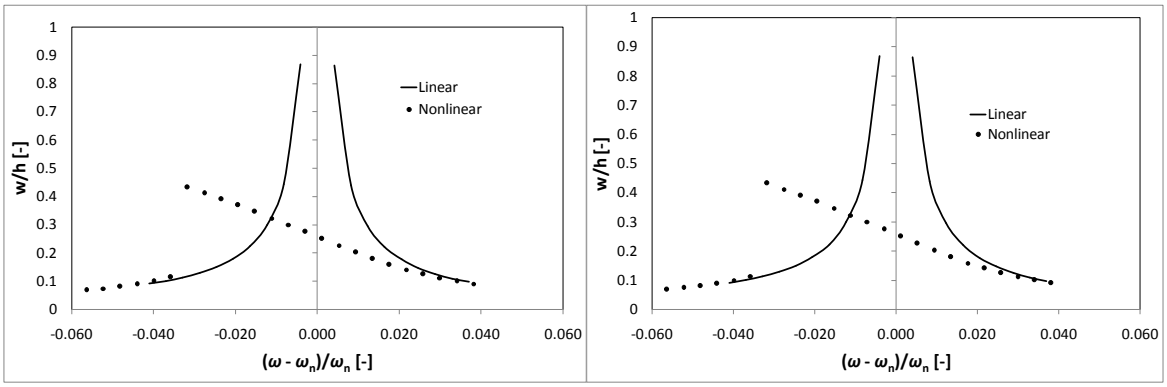

(a) Al/PVDF/PZT (b) PZT/PVDF/Al

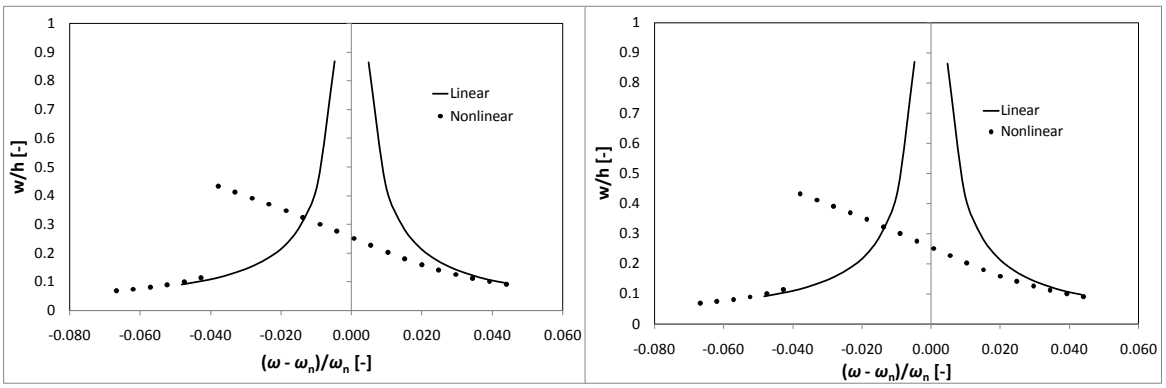

(c) Al/PZT/PVDF (d) PVDF/PZT/Al

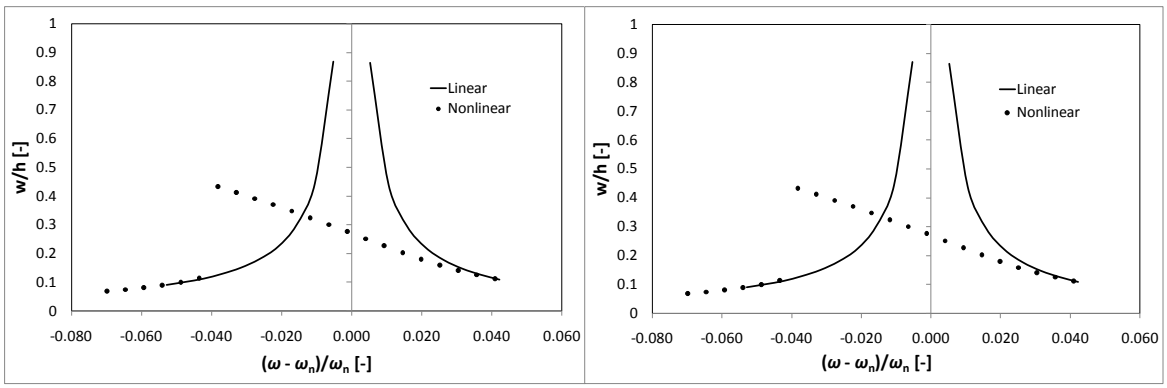

(e) PVDF/Al/PZT (f) PZT/Al/PVDF

Figure 2.9: *Frequency-response of a thin trimorph plate during large flexural oscillations of the plate centre* ($\mu = 0.001$).

Figures 2.8a – f show the frequency-response for small flexural oscillations while Figures 2.9a – f show the frequency-response for large flexural oscillations. These figures reveal that the nonlinear effects due to membrane stretching are negligible for small flexural oscillations, whereas they are significant for large flexural oscillations. Since the frequency-response plots were generated by

solving the reduced models using numerical integration, only one response value was obtained for each excitation frequency. Consequently, both the peak displacement and the corresponding natural frequency of the nonlinear case are not shown in Figures 2.9a – f. In principle there could be more than one nonlinear steady-state response at some excitation frequencies. The complete frequency-response plot for the nonlinear case can be obtained from approximate analytical solutions derived using perturbation analysis, but this is not considered here as the present study is intended to show that membrane stretching effect cannot be neglected during large flexural oscillations.

The reduced nonlinear model (equation 2.46) contains quadratic and cubic nonlinearities. To examine the effect of these nonlinearities on the response of the trimorph plate, frequency-response plots were generated in which either of these nonlinearities could be neglected. Figure 2.10 shows a comparison of the frequency-response for the three possible cases: (a) only the quadratic nonlinearity is considered; (b) only the cubic nonlinearity is considered, and (c) both the quadratic and cubic nonlinearities are considered. The figure reveals that the cubic nonlinearity (case b) produces a much stronger effect than the quadratic nonlinearity (case a). The effect of the quadratic nonlinearity is apparently negligible when both nonlinearities are considered (see cases b and c). Hence, it can be concluded that the nonlinear response of the trimorph plate during large flexural oscillations as modelled here is largely determined by the cubic nonlinearity. This information can be useful for ordering the terms during perturbation analysis. Such analyses are not covered here as they are beyond the scope of the present research.

Time-domain response plots were obtained for the Al/PVDF/PZT lamination sequence. Figures 2.11a, b show the transient and steady-state responses during small flexural oscillation, and the plots confirm that the nonlinearities due to membrane stretching do not affect the time-domain response during small flexural oscillation. In the case of large flexural oscillations, Figures 2.12a, b show that the steady-state flexural oscillations predicted by the reduced linear model are much higher than that predicted by the reduced nonlinear model. The nonlinear response settles more quickly to a steady-state response compared to the linear response. In conclusion, the linear model over-predicts the magnitude of flexural oscillations of the trimorph plate during large flexural oscillations.

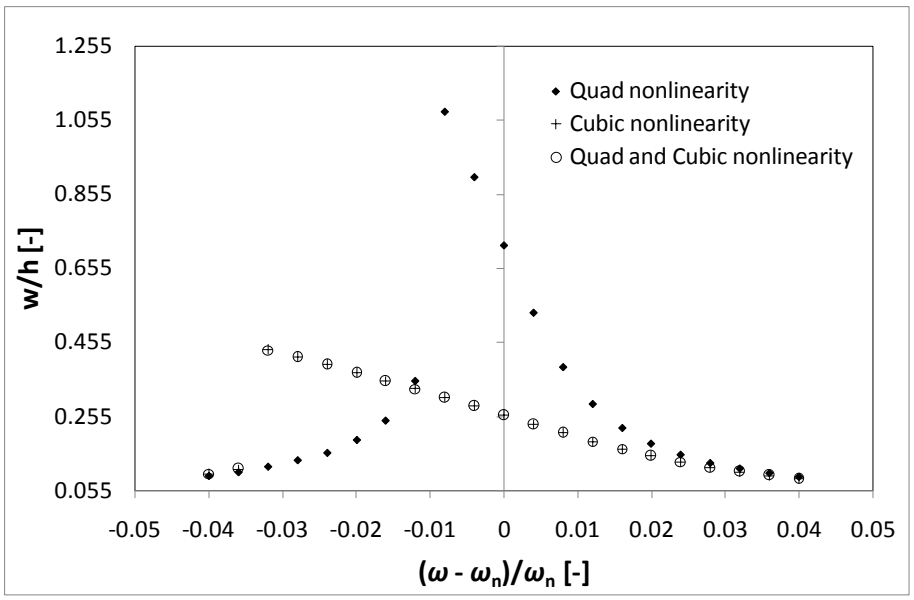

Figure 2.10: *Effect of nonlinear terms on the frequency-response of a thin trimorph plate undergoing large flexural oscillations* $(\mu = 0.001)$.

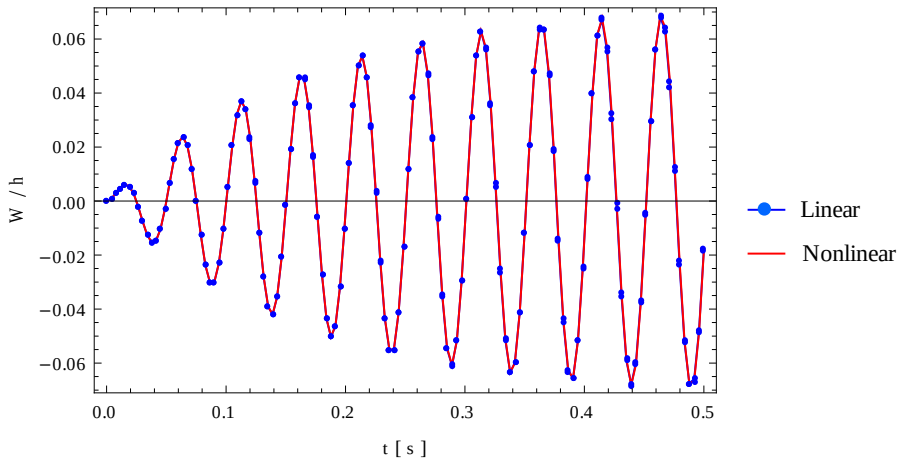

Figure 2.11a: *Transient response of a thin Al/PVDF/PZT plate during small flexural oscillations when excited at the undamped natural frequency.*

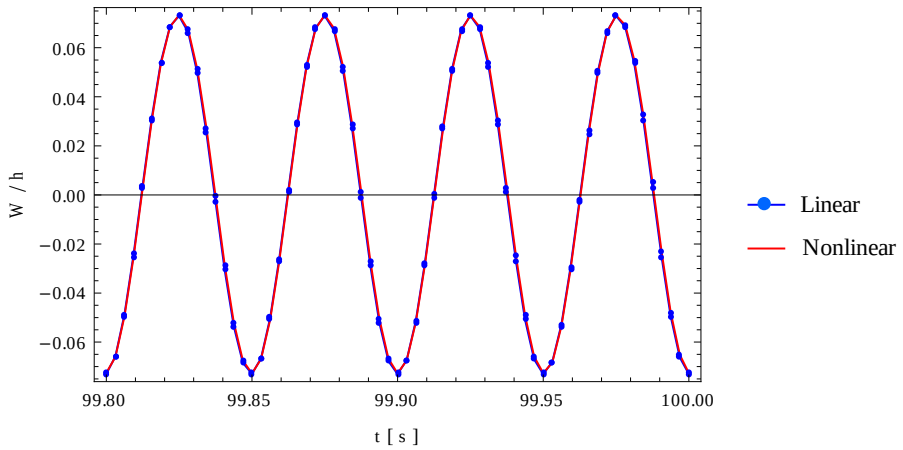

Figure 2.11b: *Steady-state response of a thin Al/PVDF/PZT plate during small flexural oscillations when excited at the undamped natural frequency.*

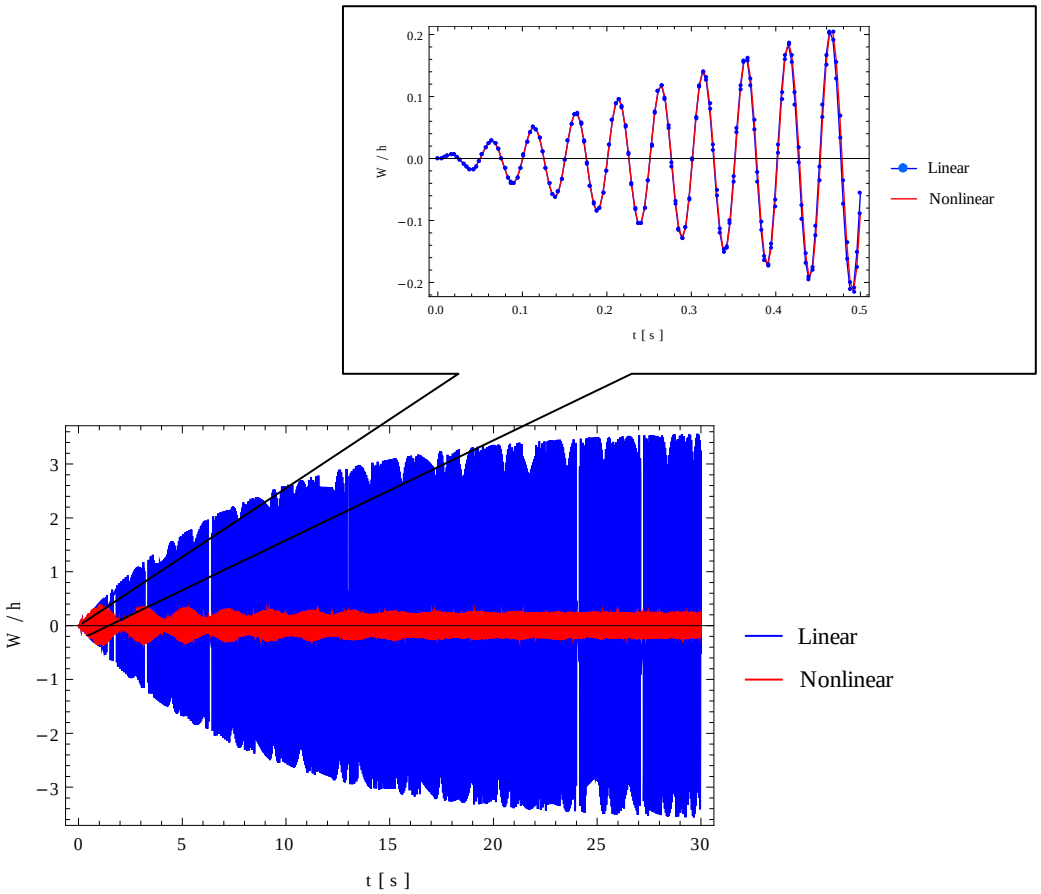

Figure 2.12a: *Complete response of a thin Al/PVDF/PZT plate during large flexural oscillations when excited at the undamped natural frequency.*

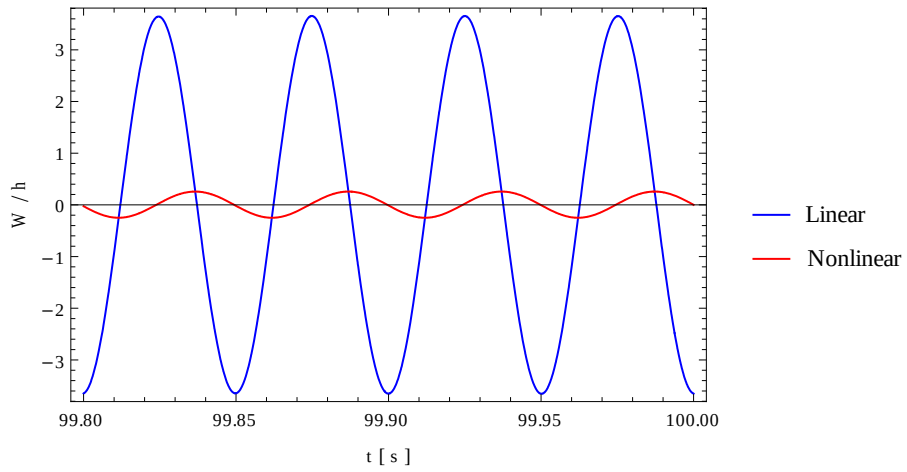

Figure 2.12b: *Steady-state response of a thin Al/PVDF/PZT plate during large flexural oscillations when excited at the undamped natural frequency.*

2.6.2 Vibration analysis of a moderately thick trimorph plate

Large flexural oscillations are uncommon, and in some cases impractical, during the excitation of moderately thick to thick plates. As a result, the present analysis of a moderately thick trimorph plate is restricted to small flexural oscillations. The vibration model for small flexural oscillations of a moderately thick trimorph plate can be derived by substituting equations (2.28), (2.40b) and (2.37) into equations (2.31 c – e). After neglecting the in-plane displacements, the following equations are derived.

$$D_{11}\frac{\partial^2\phi_x}{\partial x^2}+(D_{12}+D_{66})\frac{\partial^2\phi_y}{\partial x\partial y}+D_{66}\frac{\partial^2\phi_x}{\partial y^2}-A_{55}\left(\frac{\partial w}{\partial x}+\phi_x\right)=\frac{\rho h^3}{12}\frac{\partial^2\phi_x}{\partial t^2} \tag{2.47a}$$

$$D_{11}\frac{\partial^2\phi_y}{\partial y^2}+(D_{12}+D_{66})\frac{\partial^2\phi_x}{\partial x\partial y}+D_{66}\frac{\partial^2\phi_y}{\partial x^2}-A_{44}\left(\frac{\partial w}{\partial y}+\phi_y\right)=\frac{\rho h^3}{12}\frac{\partial^2\phi_y}{\partial t^2} \tag{2.47b}$$

$$A_{55}\left(\frac{\partial^2 w}{\partial x^2}+\frac{\partial\phi_x}{\partial x}\right)+A_{44}\left(\frac{\partial^2 w}{\partial y^2}+\frac{\partial\phi_y}{\partial y}\right)+q(x,y,t)=\rho h\frac{\partial^2 w}{\partial t^2} \tag{2.47c}$$

The solution to equations (2.47a – c) can be expressed in series form as

$$\phi_x(x,y,t)=\sum_{m=1}^{\infty}\sum_{n=1}^{\infty}A_{mn}(t)\,X1_m Y_n \tag{2.48a}$$

$$\phi_y(x,y,t)=\sum_{m=1}^{\infty}\sum_{n=1}^{\infty}B_{mn}(t)\,X_m Y1_n \tag{2.48b}$$

$$w(x,y,t)=\sum_{m=1}^{\infty}\sum_{n=1}^{\infty}W_{mn}(t)\,X_m Y_n \tag{2.48c}$$

$A_{mn}(t)$, $B_{mn}(t)$, and $W_{mn}(t)$ are time-dependent coefficients to be determined. The shape functions for SSSS are defined as $X1_m=\cos(m\pi x/a)$, $Y1_n=\cos(n\pi y/b)$, with X_m and Y_n expressed as defined above. If equations (2.47a – c) are rearranged such that the RHS is equal to zero, the Galerkin approach can expressed as

$$\int_0^b\int_0^a(LHS)\,\varphi(x,y)dxdy=0 \tag{2.49}$$

$\varphi(x,y)$ represents the product of the shape functions in the x- and y-directions. $\varphi(x,y)=X1_m Y_n,\ X_m Y1_n,$ and $X_m Y_n$ for equations (2.47a, b, and c) respectively. Substituting equations (2.47a – c), (2.48a – c) and (2.43a) in equation (2.49) and evaluating the resulting double integrals, the reduced ODE models are derived after some algebraic simplification as

$$\begin{bmatrix} I_{11} & 0 & 0 \\ 0 & I_{22} & 0 \\ 0 & 0 & I_{33} \end{bmatrix} \begin{Bmatrix} \ddot{A}_{mn} \\ \ddot{B}_{mn} \\ \ddot{W}_{mn} \end{Bmatrix} + \begin{bmatrix} L_{11} & L_{12} & L_{13} \\ L_{21} & L_{22} & L_{23} \\ L_{31} & L_{32} & L_{33} \end{bmatrix} \begin{Bmatrix} A_{mn} \\ B_{mn} \\ W_{mn} \end{Bmatrix} = \begin{Bmatrix} 0 \\ 0 \\ q(t) \end{Bmatrix} \tag{2.50}$$

where $I_{11} = I_{22} = \rho h^3/12$; $I_{33} = \rho h$

$L_{11} = \left(\frac{\pi m}{a}\right)^2 D_{11} + \left(\frac{\pi n}{b}\right)^2 D_{66} + A_{55}$; $L_{12} = \left(\frac{\pi m}{a}\right)\left(\frac{\pi n}{b}\right)(D_{12} + D_{66})$; $L_{13} = \left(\frac{\pi m}{a}\right) A_{55}$

$L_{21} = L_{12}$; $L_{22} = \left(\frac{\pi m}{a}\right)^2 D_{66} + \left(\frac{\pi n}{b}\right)^2 D_{11} + A_{44}$; $L_{23} = \left(\frac{\pi n}{b}\right) A_{44}$

$L_{31} = L_{13}$; $L_{32} = L_{23}$; $L_{33} = \left(\frac{\pi m}{a}\right)^2 A_{55} + \left(\frac{\pi n}{b}\right)^2 A_{44}$; and

$$A_{44} = A_{55} = \sum_{k=1}^{N} \frac{5E_k \delta_k}{2(6 - \upsilon_k)(1 + \upsilon_k)}$$

Assuming that the rotary inertia effect is neglected then, $I_{11}\ddot{A}_{mn} = I_{22}\ddot{B}_{mn} = 0$. By putting $A_{mn} = K_A W_{mn}$ and $B_{mn} = K_B W_{mn}$ in equations (2.50), the reduced models can be expressed as a single ODE following the approach in Christoforou and Swanson (1991). Therefore,

$$\ddot{W}_{mn} + 2\mu\omega_{mn}\dot{W}_{mn} + \omega_{mn}^2 W_{mn} = \bar{Q}\sin\omega t \tag{2.51}$$

where $\omega_{mn}^2 = (L_{13}K_A + L_{23}K_B + L_{33})/\rho h$; $K_A = (L_{12}L_{23} - L_{13}L_{22})/(L_{11}L_{22} - L_{12}^2)$; $K_B = (L_{12}L_{13} - L_{11}L_{23})/(L_{11}L_{22} - L_{12}^2)$; and μ is the damping ratio. A linear damping term that is proportional to the undamped natural frequency has been added in equation (2.51) to account for the natural viscous damping effect. The reduced model for small flexural oscillations based on the CLPT and FSDPT are the same except for the expression for calculating the undamped natural frequency. The expression for calculating the undamped natural frequency based on the FSDPT incorporates a shear deformation effect which is neglected by the CLPT.

The steady-state solution to equation (2.51) is given as

$$W_{mn}(t) = X_{mn}\, sin(\omega t - \phi_{mn}) \tag{2.52}$$

where X_{mn} is the maximum amplitude of the flexural oscillation and ϕ_{mn} is the phase angle.

$$X_{mn} = \frac{\bar{Q}}{\sqrt{(\omega_{mn}^2 - \omega^2)^2 + (2\mu\omega_{mn}\omega)^2}} \tag{2.53a}$$

$$\phi_{mn} = arctan\left(\frac{2\mu\omega_{mn}\omega}{\omega_{mn}^2 - \omega^2}\right) \tag{2.53b}$$

Equations (2.53a, b) can be rewritten as

$$X_{mn} = \frac{\delta_{st}}{\sqrt{(1-\beta_{mn}^2)^2 + (2\mu\beta_{mn})^2}} \tag{2.54a}$$

$$\phi_{mn} = arctan\left(\frac{2\mu\beta_{mn}}{1-\beta_{mn}^2}\right) \tag{2.54b}$$

where $\delta_{st} = \bar{Q}/\omega_{mn}^2$ is the static deflection of the plate and $\beta_{mn} = \omega/\omega_{mn}$ is the frequency ratio. At resonance $\beta_{mn} = 1$, $X_{mn} = \delta_{st}/2\mu$ and $\phi_{mn} = \pi/2$.

To simulate the dynamic response of the moderately thick trimorph plate, a 100 [*mm*] x 100 [*mm*] square plate with layer thicknesses of 8 [*mm*], 1 [*mm*], and 1 [*mm*] for the Al, PVDF, and PZT layers was investigated. The plate thickness to length ratio is 1/10, which is within the limits for moderately thick plates. The material properties of the layers are the same as in Table 2.1 and a damping ratio of 10^{-5} was used in the simulation. The results for the modal frequencies and steady-state displacements are shown in Table 2.4. A comparison is made between the results obtained from the CLPT model (equation 2.45) and those obtained from the FSDPT model (equation 2.51), and it is observed that the effect of shear deformation as modelled by the present FSDPT is more pronounced at higher vibration modes. Since the actual transverse displacement can be approximated by the sum of the contributions of a finite number of participating modes, then the CLPT model would produce significant errors when it used to model the vibration response of a moderately thick plate.

Table 2.4: *Modal frequencies and responses of a moderately thick Al/PVDF/PZT plate during small flexural oscillations*

Mode		Natural frequency [rad/s]		Modal displacement [w/h x 10^{-3}]	
		CLPT	FSDPT	CLPT	FSDPT
1	1	26129.9	25480.7	2.36458	2.4866
1	3	130649	116483	0.0945832	0.118988
1	5	339688	262791	0.0139916	0.023378
3	1	130649	116483	0.0945832	0.118988
3	3	235169	194332	0.0291923	0.0427505
3	5	444208	324206	0.00818194	0.0153598
5	1	339688	262791	0.0139916	0.023378
5	3	444208	324206	0.00818194	0.0153598
5	5	653247	431667	0.00378333	0.00866427

Time-domain responses for the fundamental mode of vibration are shown in Figures 2.13a, b. Again a comparison is made between the CLPT model and the

FSDPT model during the initial phase of the transient response and during the steady-state response. For both the transient and steady-state responses a phase difference occurs and the magnitudes of the oscillations differ. As expected, the phase difference and the difference in the displacements evolve during the transient response and become constant in the steady-state response.

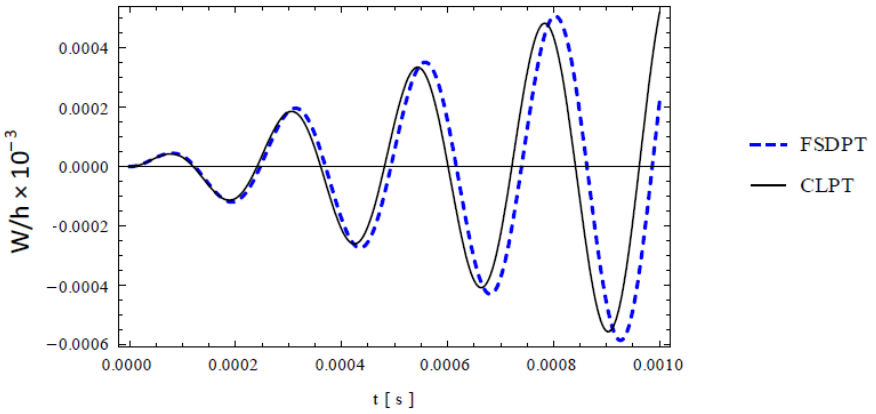

Figure 2.13a: *Transient response of a moderately thick Al/PVDF/PZT plate during small flexural oscillations when excited at the undamped natural frequency.*

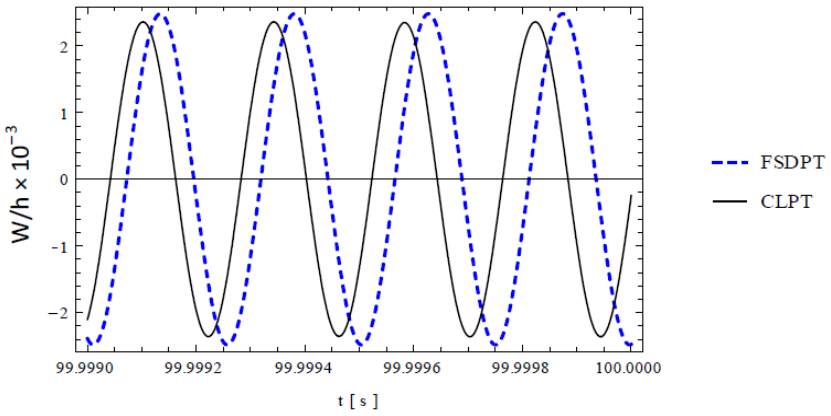

Figure 2.13b: *Steady-state response of a moderately thick Al/PVDF/PZT plate during small flexural oscillations when excited at the undamped natural frequency.*

2.7 Chapter conclusions

This chapter presents a detailed formulation of vibration models for thin and thick rectangular laminated plates, and investigations on the vibration response of a three-layer rectangular laminate called trimorph plate. For the

thin trimorph plate, small and large displacements were investigated and the results reveal that membrane stretching effect could be neglected in the former but not in the later. The membrane stretching effect was modelled by incorporating the von Kármán geometric nonlinearity in the strain-displacement relationship and accounting for the effect of the induced in-plane forces on the flexural oscillations. The final reduced model for large displacements was a forced oscillator with quadratic and cubic nonlinearities, of which the cubic nonlinearity was found to be more influential than the quadratic nonlinearity.

Simulations run for a moderately thick trimorph plate using the CLPT and FSDPT models showed that shear deformation effects are more pronounced at higher modes. The comparison also revealed that significant errors could be introduced in the determination of the natural frequency and the magnitude of the flexural oscillations when the CLPT model is used to analyse the vibration response of a moderately thick trimorph plate because the CLPT model neglects the shear deformation effect.

Investigations into the response characteristics revealed that the lamination sequence of the trimorph plate influenced the response of the plate. Those lamination sequences with the same mid-layer material produced matching response characteristics except for the bending-extension stiffnesses that were found to be equal in magnitude but opposite in sign. The implication is that the best lamination sequence for a given application could be determined from three lamination sequences instead of six possible lamination sequences. The extensional stiffness was found to be the same for all possible lamination sequences, and this means that the effect of the cubic nonlinearity is independent of the lamination sequence.

The relevance of the vibration analysis presented in this chapter is two-fold. First, the vibration models developed here could be used for modelling the impact response of thin and moderately thick laminated plates. An application of the vibration models in modelling the impact response of the trimorph plate is discussed in chapter four. Second, the investigations on the response characteristics of the trimorph plate provide insight into its dynamic behaviour and form a basis for informative determination of the lamination sequence that could be used for further studies, e.g. impact analysis, considering the intended application.

CHAPTER THREE

CONTACT MODEL FOR ELASTOPLASTIC INDENTATION

Chapter summary

Accidental load in the form of impact between a rigid object and a compliant target is a common engineering problem. During such impact there is a surface interaction between the rigid object and the target known as *contact*. Contact models account for the local response (displacement, force, stress, etc) of the rigid object and the target, and they are necessary for more rigorous analysis of the dynamics of the impact system. This chapter presents a new analytical contact model for quasi-static elastoplastic indentation of a half-space by a rigid spherical mass. First, other published contact models for elastoplastic indentation of isotropic and transversely isotropic materials are reviewed. The review is followed by formulation of the new contact model and then, validation of the proposed model using published experimental data. The results of the present contact model are found to be in agreement with the static and dynamic indentation measurements to which they were compared.

3.1 Review of contact models for spherical indentation of elastoplastic half-space

Contact phenomena finds application in many impact processes such as forging, stamping, shot-peening, granular flow in industrial processes and solid object impact on structures. Contact models are normally formulated based on half-space conditions i.e. the local indentation is much smaller than the size of the indented surface. For instance, the Hertz contact model gives the force-indentation relationship for quasi-static loading of a spherical indenter on an elastic half-space. A detailed treatment of the Hertz contact model for different contacting surfaces can be found in Johnson (1985) and Goldsmith (2001). The Hertz contact model is only applicable to small indentations that are elastic, for which the stress in the contact zone is less than the yield stress of the material of the indented surface. When the stress in the contact zone is higher than the yield stress of the material of the indented surface, post-yield effects such as

plastic deformation and/or damage occur and significant deviations from the Hertz contact model are observed (Abrate, 1998).

It has been shown that during impact of a rigid steel ball on a medium hard steel slab yielding occurs at an impact velocity as low as 0.14 [m/s] (Johnson, 1985). Moreover, most practical impact events are characterised by post-yield deformation (Johnson, 1985; Goldsmith, 2001), and therefore it is necessary to account for post-yield deformation effects in the contact model. The effect of the post-yield deformation is to reduce the contact force from that predicted by purely elastic deformations and to produce a permanent indentation at the end of the contact, thereby, making the unloading path different from that of loading. Figure 3.1 shows a sketch of the impact of a spherical mass on an elastoplastic half-space.

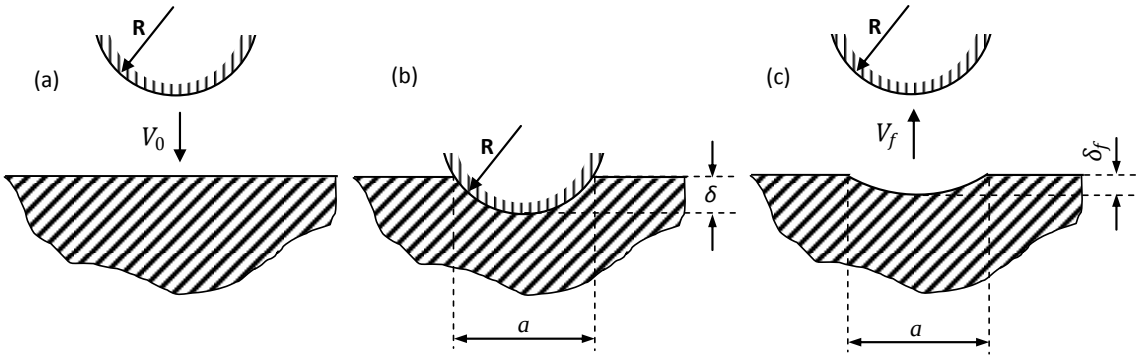

Figure 3.1: *Elastoplastic half-space impact of a rigid spherical indenter on a compliant flat target (a) before impact (b) during impact (c) after impact.*

Contact models that account for post-yield deformation have been developed for metallic targets (Johnson, 1985; Goldsmith, 2001; Stronge, 2000a; Li *et al*, 2002; Brake, 2012) and for composite laminate targets (Cairns, 1991; Yigit and Christoforou, 1994; Majeed *et al*, 2012). These models can be divided into two general groups, namely: those that are developed based on two distinct loading regimes (Goldsmith 2001; Cairns, 1991; Yigit and Christoforou, 1994; Majeed *et al*, 2012) and those that are developed based on three distinct loading regimes (Johnson, 1985; Stronge 2000a; Li *et al*, 2002; Brake, 2012). With metallic targets, three loading regimes (elastic, elastoplastic and fully plastic) and an unloading regime are required for complete description of the contact mechanics (Tabor, 1951; Johnson, 1985; Stronge, 2000a). For a contact model that is based on elastic-elastoplastic-fully plastic loading regimes, the loading

features and force-indentation relationships for the elastic and fully (perfectly) plastic loading regimes are well established. In general, the elastic loading regime starts from the beginning of the loading and ends at the yield point where the mean contact pressure is given as $P_{oy} = 1.1S_y$ (S_y is the yield stress of the target). The elastic loading regime can be modelled accurately using the well-known Hertz contact model. The fully plastic loading regime is characterised by a linear force-indentation relationship and a constant mean pressure of $P_{op} = 2.8S_y$, which is equal to the Brinell hardness of the target (Brake, 2012). The onset of the fully plastic regime occurs at the point where the mean pressure is $2.8S_y$. The main difficulty lies in formulating an analytical model for the elastoplastic loading regime which starts at the yield point and ends at the onset of fully plastic conditions. Selected published models for post-yield indentation of metallic and composite laminate targets are discussed next.

3.1.1 Contact models for post-yield indentation of a metallic half-space

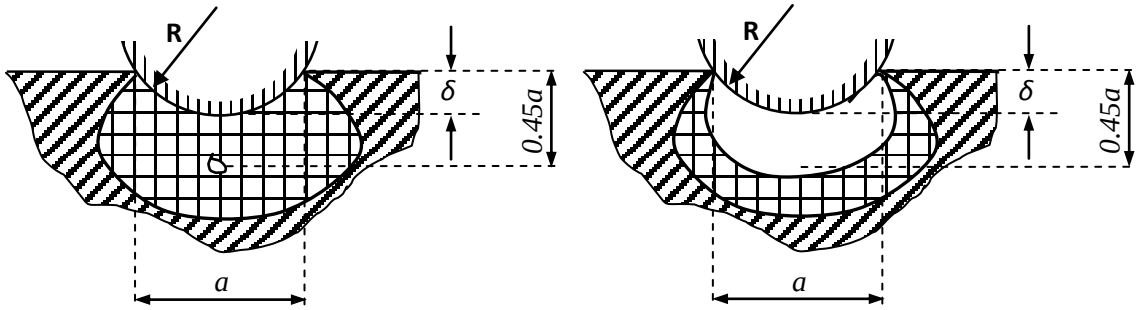

(a) (b)

Figure 3.2: *Elastoplastic deformation at (a) yield (b) the onset of fully plastic loading regime. The cross-hatched area is the surrounding elastically-deformed material while the unshaded area is the plastically-deformed material.*

During post-yield contact loading of a metallic half-space by a rigid spherical indenter, the elastoplastic loading regime is initiated immediately after the metal yields. As a result of yielding, a plastically-deformed material appears below the contact surface at a depth of about half the contact radius (Figure 3.2a). This plastically-deformed material is completely enclosed within a surrounding elastically-deformed material (Johnson, 1985). As the elastoplastic

loading progresses, the plastically-deformed material increases and the surrounding elastically-deformed material decreases. Eventually, fully plastic conditions are met when the plastically-deformed material breaks free to the contact surface and comes in contact with the indenter (Figure 3.2b). This marks the end of the elastoplastic loading regime and the onset of the fully plastic loading regime.

Contact model of Stronge (2000a)

Johnson (1985) used an expanding cavity model to develop an approximate analytical solution to the elastoplastic indentation of a half-space by a blunt indenter (pyramid, cone or sphere). Stronge (2000a) applied Johnson's expanding cavity model in formulating an elastoplastic contact model for quasi-static loading of a half-space using a spherical indenter. Stronge's model of the elastoplastic loading regime is very similar to that of Johnson (1985), except that Stronge uses a different expression for the relationship between the contact radius and indentation during this loading regime. Stronge's contact model is summarised as follows.

Elastic loading regime

Stronge (2000a) modelled this regime using the Hertz contact model as:

$$F = \frac{4}{3}\bar{E}\bar{R}^{1/2}\delta^{3/2} \qquad 0 \le \delta \le \delta_y \tag{3.1}$$

where $\bar{E} = [(1-\upsilon_i^2)/E_i + (1-\upsilon_t^2)/E_t]^{-1}$ and $\bar{R} = [1/R_i + 1/R_t]^{-1}$ are the effective modulus and radius respectively. The subscripts i and t stand for indenter and target respectively, and υ is the Poisson's ratio. The elastic loading regime was considered to terminate at yield where the mean contact pressure is equal to $1.1S_y$ based on Tresca's yield criterion. The indentation and contact force at yield are:

$$\delta_y = \frac{0.681\pi^2\bar{R}S_y^2}{\bar{E}^2};\ F_y = \frac{4}{3}\bar{E}\bar{R}^{1/2}\delta_y^{3/2} \tag{3.2}$$

Elastoplastic loading regime

The elastoplastic loading regime was considered to commence at a mean contact pressure of $1.1S_y$ and terminate at a mean contact pressure of $2.8S_y$. The force-indentation relationship for this regime was derived as:

$$F = F_y\left(\frac{2\delta}{\delta_y} - 1\right)\left[1 + \frac{1}{3.3} ln\left(\frac{2\delta}{\delta_y} - 1\right)\right] \qquad \delta_y \le \delta \le \delta_p \tag{3.3}$$

Stronge (2000a) used $a/a_y = \left(2\delta/\delta_y - 1\right)^{1/2}$ to approximate the relationship between the contact radius and indentation in arriving at equation (3.3). Johnson (1985) used $a/a_y = \left(2\delta/\delta_y\right)^{1/2}$ based on the generally accepted approximation that $a^2 = 2\bar{R}\delta$ for indentation beyond the yield point. This distinction forms the main difference in the models for elastoplastic loading as presented by Stronge (2000a) and Johnson (1985). Also, Stronge's model estimates the end of the elastoplastic loading as $\delta_p \cong 82.5\delta_y$ whereas Johnson's model gives an estimate of $\delta_p \cong 73\delta_y$.

Fully plastic loading regime

This loading regime was modelled using a linear force-indentation relationship based on a constant mean pressure of $P_{0p} = 2.8S_y$, and the contact radius–indentation relationship used was the same as in the elastoplastic loading regime.

$$F = 2.545F_y\left(\frac{2\delta}{\delta_y} - 1\right) \qquad \delta_p \le \delta \le \delta_m \tag{3.4}$$

Restitution

The restitution was modelled as an elastic unloading with a plastic deformation effect for post-yield indentation. As a result of plastic deformation, the model accounts for a permanent indentation $\left(\delta_f\right)$ at the end of the unloading and the effective radius is replaced by a deformed effective radius, $\bar{R}_d$.

$$F = \frac{4}{3}\bar{E}\bar{R}_d^{1/2}\left(\delta - \delta_f\right)^{3/2} \qquad \delta_f \le \delta \le \delta_m \tag{3.5a}$$

where

$$\delta_f = \delta_m - \left(\frac{3F_m}{4\bar{E}\bar{R}_d^{1/2}}\right)^{2/3} \quad ; \quad \bar{R}_d = \begin{cases} \bar{R}\left(2\delta/\delta_y - 1\right) & \delta > \delta_y \\ \bar{R} & \delta \le \delta_y \end{cases} \tag{3.5b,c}$$

F_m and δ_m are the maximum contact force and indentation respectively, and they could be located in any of the loading regimes. When they are located in the elastic loading regime, there is no post-yield effect and $\delta_f = 0$.

The model for the elastoplastic loading regime is a logarithmic function of indentation and cannot be expressed in the form of Meyer's law i.e. $F = K_c\delta^q$ where K_c is the contact stiffness and $q \ge 1$ is an exponent defining the compliance relationship (Goldsmith, 2001). When this model is used for dynamic

impact analysis, it has the potential to introduce computational difficulties due to the more complex nonlinear form in which it is expressed. This may explain why analytical studies on the impact response of metallic targets using this elastoplastic contact model are scarce despite the success of the model in predicting the elastoplastic loading response of metals under static conditions.

Contact model of Li et al (2002)

Li *et al* (2002) developed a theoretical contact model for the elastoplastic loading of a half-space using a spherical indenter by assuming a truncated Hertzian pressure distribution for post-yield indentation. According to this model, the elastoplastic loading regime is assumed to commence at a mean contact pressure of $1.6S_y$ and terminates at the onset of fully plastic loading conditions where the mean contact pressure is considered to be $2.85S_y$ based on finite element results. The truncated pressure was considered to vary with the contact radius according to an equivalent ratio power law relationship. This pressure distribution was then used to derive expressions for calculating the contact force and indentation during the elastoplastic loading. The contact model of Li *et al* (2002) is summarised as follows.

Quasi-static loading

The contact loading consists of three loading regimes namely: elastic, elastoplastic and fully plastic. The expressions for the contact force and indentation in these regimes can be represented in dimensionless form as:

$$\frac{F}{F_y} = \frac{3}{2}\left(\frac{a}{a_y}\right)^2\left(\frac{P_0}{P_{0y}}\right) - \frac{1}{2}\left(\frac{P_0}{P_{0y}}\right)^3 \tag{3.6}$$

$$\frac{\delta}{\delta_y} = \frac{\left(a/a_y\right)^2}{1 + k\left[1 - \left(\delta/\delta_y\right)\left(a/a_y\right)\left(F/F_y\right)\right]^{2/3}} \tag{3.7}$$

The contact parameters at yield are given as:

$$\left.\begin{array}{c} P_{0y} = 1.6S_y \\ a_y = \pi\bar{R}P_y/2\bar{E} \\ F_y = (2/3)\pi a_y^2 P_{0y} \\ \delta_y = a_y^2/\bar{R} \end{array}\right\} \tag{3.8}$$

$\bar{E}$ and $\bar{R}$ are the effective modulus and radius of the contact system defined in equation (3.1).

Elastic loading regime

The elastic loading regime was modelled using the Hertz contact model and terminates when the mean contact pressure is $1.6S_y$. The dimensionless pressure was given as:

$$\frac{P_0}{P_{0y}} = \frac{a}{a_y} \qquad \frac{a}{a_y} \leq 1 \tag{3.9}$$

which when substituted into equation (3.6) simplifies to the Hertz model.

Elastoplastic loading regime

Based on the equivalent ratio power law relationship, the dimensionless mean pressure in this regime was expressed as:

$$\frac{P_0}{P_{0y}} = \frac{\lambda}{1.6} - \frac{\lambda - 1.6}{1.6}\left(\frac{\varepsilon - a/a_y}{\varepsilon - 1}\right)^n \qquad 1 \leq \frac{a}{a_y} \leq \varepsilon \tag{3.10}$$

Fully plastic loading regime

In-line with well established indentation feature of fully plastic loading, the dimensionless mean pressure in this regime is constant and given by:

$$\frac{P_0}{P_{0y}} = \frac{\lambda}{1.6} \qquad \frac{a}{a_y} \geq \varepsilon \tag{3.11}$$

The constants in the model i.e. k, λ, ε and n are proposed to depend on the material properties of the contact system and experimental data. Li *et al* (2002) determined the constants from FEA as $k = 1.23, \lambda = 2.85, \varepsilon = 20$ and $n = 6$.

Restitution

The dimensionless form of the unloading was derived as:

$$\frac{F}{F_y} = \frac{F_m}{F_y} - \left(\frac{\bar{R}_m}{\bar{R}}\right)^{1/2}\left[\left(\frac{\delta_m}{\delta_y}\right)^{3/2} - \left(\frac{\delta}{\delta_y}\right)^{3/2}\right] \tag{3.12}$$

where $\bar{R}_m \geq \bar{R}$ is the effective radius at the maximum contact force during post-yield loading. If the contact loading is purely elastic, then $\bar{R}_m = \bar{R}$ and the unloading path is exactly the same as the loading.

The amount of plastic deformation (δ_p) during post-yield loading was determined as:

$$\delta_p = \left(\delta^{3/2} - \frac{3F}{4\bar{E}\sqrt{\bar{R}_p}}\right)^{2/3} \tag{3.13}$$

Due to post-yield effects, the effective radius was considered to be higher than that for the elastic loading and was determined according to the expression:

$$\frac{a^2}{\bar{R}_p} = \frac{a^2}{\bar{R}} - k\delta_p \tag{3.14}$$

For a given contact radius, δ_p and $\bar{R}_p$ are obtained by solving equations (3.13) and (3.14) simultaneously. $\bar{R}_m$ is the value of $\bar{R}_p$ when $F = F_m$ and $\delta = \delta_m$.

Li *et al* (2002) simulated this model for fully plastic contact loading of a steel half-space by a steel ball that is 50 times more rigid. The results obtained were found to be in good agreement with FE results obtained from ABAQUS simulations. However, the contact model of Li *et al* (2002) requires numerical solution to obtain the static elastoplastic loading response. The labour of computation in using this elastoplastic loading model for dynamic impact analysis would be enormous because of the complex form in which it is expressed. Moreover, the restitution model of this contact model does not guarantee a smooth transition from loading to unloading.

Contact model of Brake (2012)

A more recent analytical contact model accounting for elastoplastic loading of a half-space by a spherical indenter was formulated by Brake (2012). Brake modelled the elastoplastic loading regime by enforcing continuity between the yield point and the onset of fully plastic loading using a *cubic Hermite interpolation polynomial*. The elastoplastic loading regime of this contact model covers a mean contact pressure range of $1.0S_y \leq P_0 \leq 2.8S_y$. Brake's model can be summarised as follows.

Elastic loading regime

This regime was also modelled by the Hertz contact model according to equation (3.1), and was considered to terminate at the yield point. The latter was determined based on Von Mises yield criterion and the contact parameters at yield were given as:

$$\left.\begin{aligned} P_{0y} &= 1.0S_y \\ \delta_y &= \bar{R}\left(\pi S_y/2\bar{E}\right)^2 \\ a_y &= \left(\bar{R}\delta_y\right)^{1/2} \\ F_y &= (4/3)\bar{E}\bar{R}^{1/2}\delta_y^{3/2} \\ a_y^{'} &= (1/2)\left(\bar{R}/\delta_y\right)^{1/2} \\ F_y^{'} &= 2\bar{E}\left(\bar{R}\delta_y\right)^{1/2} \end{aligned}\right\} \tag{3.15}$$

The constants with prime are first derivatives with respect to indentation depth.

Elastoplastic loading regime

Since this regime was modelled by enforcing continuity between the yield point and the onset of fully plastic conditions using an interpolating polynomial, the force-indentation relationship is dependent on the contact parameters at these two points. The contact parameters at the yield point are shown in equation (3.15) whereas those at the onset of fully plastic conditions were derived as:

$$\left.\begin{array}{c} P_{0p} = Hg \times 10^6 \\ \delta_p = \left(P_{0y}/S_y\right)^2 \delta_y \\ a_p = 3\pi\bar{R}P_{0p}/4\bar{E} = (2\bar{R}\delta_p + c_p)^{1/2} \\ F_p = \pi a_p^2 P_{0p} \\ a_p^{'} = 2\bar{R}(2\bar{R}\delta_p + c_p)^{-1/2} \\ F_p^{'} = 2\pi R P_{0p} \end{array}\right\} \qquad (3.16)$$

In equations (3.16), g is the acceleration due to gravity in $[m/s^2]$, H is the effective hardness of the contact system in $[kgf/mm^2]$, and c_p $[m^2]$ is a constant determined at the onset of fully plastic loading. $H = [1/H_i + 2/H_t]^{-1}$ for a flat half-space loaded by a spherical indenter. Also, $c_p = a_p^2 - 2\bar{R}\delta_p = \left(3\pi\bar{R}P_{0p}/4\bar{E}\right)^2 - 2\bar{R}\left(P_{0y}/S_y\right)^2\delta_y$. Hence, the model for the elastoplastic loading regime was formulated as:

$$F = \left(2F_y - 2F_p + (\delta_p - \delta_y)(F_y^{'} + F_p^{'})\right)\left(\frac{\delta - \delta_y}{\delta_p - \delta_y}\right)^3 +$$

$$\left(-3F_y + 3F_p + (\delta_p - \delta_y)(-2F_y^{'} - F_p^{'})\right)\left(\frac{\delta - \delta_y}{\delta_p - \delta_y}\right)^2 + F_y^{'}(\delta - \delta_y) + F_y \qquad (3.17a)$$

$$a = \left(2a_y - 2a_p + (\delta_p - \delta_y)(a_y^{'} + a_p^{'})\right)\left(\frac{\delta - \delta_y}{\delta_p - \delta_y}\right)^3 +$$

$$\left(-3a_y + 3a_p + (\delta_p - \delta_y)(-2a_y^{'} - a_p^{'})\right)\left(\frac{\delta - \delta_y}{\delta_p - \delta_y}\right)^2 + a_y^{'}(\delta - \delta_y) + a_y \qquad (3.17b)$$

Fully plastic loading regime

This regime was considered to commence at a mean contact pressure that is equal to the effective hardness of the contact system. The mean contact pressure remains constant in this loading regime and the contact force varies linearly with indentation.

$$F = \pi a^2 P_{0p} \qquad (3.18)$$

where $a^2 = 2R\delta + c_p$; c_p is computed from the third expression of equation (3.16).

Restitution

Brake modelled the restitution according to equation (3.5a) and the permanent indentation (δ_f) was determined by the same expression used in equation (3.5b). The only difference between Brake's restitution model and that of Stronge (2000a) is the way the deformed effective radius is determined. When unloading from the elastoplastic regime, Brake used an interpolating polynomial to calculate the deformed effective radius.

$$\bar{R}_d = \left(2\bar{R} - 2\bar{R}_p + \left(\delta_p - \delta_y\right)\bar{R}_p'\right)\left(\frac{\delta_m - \delta_y}{\delta_p - \delta_y}\right)^3 + \left(-3\bar{R} + 3\bar{R}_p - \left(\delta_p - \delta_y\right)\bar{R}_p'\right)\left(\frac{\delta_m - \delta_y}{\delta_p - \delta_y}\right)^2 + \bar{R} \qquad (3.19a)$$

During unloading from the plastic regime, two levels of plasticity were considered namely: small and large scale plasticity. The deformed effective radius during small scale plasticity was computed from equation (3.5b) using the largest real value of the fixed indentation obtained from the numerical solution of equation (3.19b).

$$V_m - V_y\frac{\delta_m}{\delta_y} = \frac{\pi}{6}\left(\delta_m - \delta_f\right)\left[3a_m^2 + \left(\delta_m - \delta_f\right)^2\right] \qquad (3.19b)$$

Equation (3.19b) was derived by assuming that the elastically deformed volume is conserved and it varies linearly with the ratio δ_m/δ_y. V_m and V_y are the elastically deformed volume at maximum load and yield respectively, and they are calculated from $V = \pi\delta(3a^2 + \delta^2)/6$. For large scale plasticity, the deformed effective radius was assumed to be equal to the radius of a spherical indentation with depth δ_m and width $2a_m$ i.e.

$$\bar{R}_d = \frac{1}{2}(\delta_m + \frac{a_m^2}{\delta_m}) \qquad (3.19c)$$

In equation (3.19a), the constants R_p and $R_p^{'}$ were determined as:

$$\bar{R}_p = \frac{9F_p^2}{16\bar{E}^2\left(\delta_p - \delta_f\right)^3}; \quad \bar{R}_p' = -\frac{9F_p^2}{64\bar{E}^2\left(\delta_p - \delta_f\right)^4} \qquad (3.19d,e)$$

where δ_f was calculated from equation (3.19b) by putting $V_m = V_p$ and $\delta_m = \delta_p$.

Brake (2012) compared results obtained from this contact model with published static and dynamic loading measurements and the model results of

nine other published contact models. Brake's model was found to perform better than the other contact models in predicting the different experimental data considered. Apparently, Brake's model is preferable to the other models to which it was compared from an accuracy viewpoint. Yet, when simplicity and computational effort are also considered the model of Stronge (2000a) seems to be the best compromise. The main drawback to Brake's model is that is requires more computational effort than most other elastoplastic contact models (Johnson, 1985; Stronge, 2000a; Thornton and Ning, 1998; Majeed *et al*, 2012).

3.1.2 Contact models for post-yield indentation of a transversely isotropic half-space

In Section 3.1.1 selected contact models for post-yield indentation of metals were reviewed. In general, metals exhibit isotropic material behaviour but the same cannot be said for most composite materials. Many composite materials exhibit orthotropic behaviour. The effective transverse modulus during contact loading of orthotropic composite laminates has been shown to be generally insensitive to the in-plane properties, and is mainly dependent on the through-the-thickness properties (Yigit and Christoforou, 1994; Olsson, 1992; Sun and Yang, 1980). This means that transversely isotropic assumptions can be used to model the contact deformation of orthotropic composite laminates. Therefore, contact models for indentation of a transversely isotropic half-space are needed for analytical studies of the contact deformation and impact response of targets made of composite materials.

Sun and Yang (1980) proposed a contact model that accounts for the post-yield effect during indentation of a composite laminate by a spherical indenter. The contact model was developed based on a least squares fit of static indentation test results of glass/epoxy and graphite epoxy composite laminates. The contact model was formulated assuming transversely isotropic behaviour of the composite laminate and the post-yield effects were only captured during the unloading. This post-yield effect was estimated using an experimentally determined constant called the *critical indentation*. A major limitation of this contact model as explained by Christoforou and Yigit (1995) is that it is dependent on some experimentally determined constants, which are case dependent. Another limitation is that the model does not account for post-yield

effects in the loading stage as it is based on purely elastic loading and therefore, it is apparent that it would overestimate the maximum contact force during substantial post-yield deformation. In principle, a purely elastic contact loading would result in a purely elastic unloading due to complete stress reversal. By the same reckoning, the presence of post-yield effects in the unloading stage as confirmed by experiments (Sun and Yang, 1980) implies that the post-yield effects must first appear in the loading stage.

Post-yield loading of metallic targets give rise to plastic deformation, whereas the case of composite laminate targets involves both plastic deformation and damage mechanisms such as fibre breaking/kinking/micro-buckling and layer delamination (Majeed *et al*, 2012). Also, the laminate lay-up, composite weave-style, and the orthotropic behaviour of the composite can influence the impact response significantly. Accounting for all these factors would result in very complex models and therefore, simplifying assumptions are often used. Yigit and Christoforou (1994) developed an elastic-plastic contact model that accounts for post-yield effects in the loading and unloading stages of the indentation of a transversely isotropic composite laminate by a spherical indenter. The model consists of two loading regimes, elastic and elastic-plastic, and an unloading regime that is considered to be elastic. An advantage of this contact model is that the contact parameters can be determined from the material and geometric properties of the contact system. A limitation of the model is that it could significantly underestimate the maximum contact force (Majeed *et al*, 2012).

Majeed *et al* (2012) developed an elastoplastic contact model that attempts to improve on the model of Yigit and Christoforou (1994). Following observations from FE results for the post-yield indentation of a half-space, Majeed *et al* (2012) suggested that the transition to the elastoplastic loading regime occurs at a mean pressure equal to the arithmetic average of the mean pressure at yield and at the onset of fully plastic conditions, i.e. $1.95S_y$. Based on this idea, Majeed *et al* (2012) formulated a contact model consisting of two loading regimes, elastic and elastic-plastic, and one unloading regime. The elastic loading regime was modelled using the Hertz contact model and assumed to terminate at a transition mean pressure of $1.95S_y$. The elastic-plastic loading regime was modelled using the perfectly-plastic assumption of a constant mean

pressure that was considered to be equal to the transition mean pressure. Post-yield effects were captured in the elastic-plastic loading regime and the unloading regime. The model of Majeed *et al* (2012) is summarised as follows.

Elastic loading regime

$$F = K_h \delta^{3/2} \qquad 0 \le \delta \le \delta_p \tag{3.20}$$

where $K_h = (4/3)\bar{E}\bar{R}^{1/2}$; $\bar{E}$ and $\bar{R}$ are the effective modulus and radius of the contact or impact system. $\bar{R}$ has the same definition as in equation (3.1) while $\bar{E}$ is defined for a spherical indenter in contact with a transversely isotropic target as:

$$\bar{E} = [(1 - \upsilon_i^2)/E_i + 1/E_t]^{-1} \tag{3.21}$$

E_t is the effective modulus of the transversely isotropic target and could be estimated as $E_t = 2/c_1 c_3$ (Turner, 1980), where c_1 and c_3 are constant given by

$$c_1 = \sqrt{\frac{E_x/E_z - \upsilon_{xz}^2}{1 - \upsilon_{xy}^2}};\ c_2 = \frac{E_x/2G_{xz} - \upsilon_{xz}(1 + \upsilon_{xy})}{1 - \upsilon_{xy}^2};\ c_3 = \frac{1 - \upsilon_{xy}}{2G_{xy}}\sqrt{\frac{c_1 + c_2}{2}}$$

x and y represent the in-plane directions while z represents the thickness direction. G_{xz} and G_{xy} are shear moduli acting in the planes indicated by their subscripts, and υ_{xz} and υ_{xy} are the corresponding Poisson's ratios. The subscripts 1, 2, and 3 are only used to distinguish the constants and do not have any directional significance.

Another expression for estimating E_t is (Olsson, 1992)

$$\frac{1}{E_t} = \frac{1 - \upsilon_{xz}\upsilon_{zx}}{E_z} \tag{3.22}$$

For most composite laminates the product $\upsilon_{xz}\upsilon_{zx} \cong 0$ (Olsson, 1992). Therefore, the effective modulus of a transversely isotropic laminate is approximately equal to the transverse modulus of its ply i.e. $E_t \cong E_z = E_{33}$. Note that $E_{33} \cong E_{22}$ for most composite laminates. This approximation has been used with excellent success in many impact studies involving composite laminates (Yang and Sun, 1980; Olsson, 1992; Wu and Shyu, 1993; Yigit and Christoforou, 1994; Carvalho and Guedes Soares, 1996).

The indentation at the end of the elastic loading regime was derived as:

$$\delta_p = \frac{9\pi^2 k^2 S_y^2 \bar{R}}{16\bar{E}^2};\quad k = 1.95 \tag{3.33}$$

Elastoplastic loading regime

$$F = K_p(\delta - \delta_p) + K_h \delta_p^{3/2} \qquad \delta_p \le \delta \le \delta_m \tag{3.24}$$

where $K_p = 1.5K_h\delta_p^{1/2}$

Restitution (unloading)

$$F = F_m\left(\frac{\delta - \delta_f}{\delta_m - \delta_f}\right)^{3/2} \qquad \delta_f \le \delta \le \delta_m \tag{3.25}$$

where $\delta_f = \delta_m - \delta_y\left(2\delta_m/\delta_y - 1\right)^{1/2}$; and $\delta_y = 0.681\pi^2 S_y^2\bar{R}/\bar{E}^2$.

Simulations of this contact model for static contact loading of a woven E-glass/polyester composite laminate were found to be in good agreement with the experimental data of Sutherland and Guedes Soares (2005) and FE results obtained using ABAQUS. An advantage of this contact model is that all the contact parameters can be obtained from the material and geometric properties of the contact system. Although Majeed *et al* (2012) applied this contact model to study the post-yield indentation of a specific composite material, it has been observed in the present study that the contact model does not perform well during substantial plastic deformation of metals (see Section 3.3).

3.2 New contact model for post-yield indentation of a half-space by a spherical indenter

A new contact model that accounts for post-yield deformation effects during contact loading and unloading of a half-space by a spherical indenter has been proposed in this study. The formulation of the new contact model was motivated by (i) the gaps found in the attempts by past investigators to model the post-yield loading and restitution phases of the contact loading of a half-space, and (ii) the need to provide a simple, and yet reasonably accurate, contact model that can be easily used for impact modelling. The new contact model is based on three loading regimes consisting of elastic, elastoplastic and fully plastic regimes, and a single-phase restitution regime that is elastically nonlinear. Furthermore, the elastoplastic loading regime is divided into two distinct regions, and each region is modelled with a different force-indentation relationship that depicts the deformation mechanism observed from experiments and FE results. A sketch of the compliance curve for the new contact model is shown in Figure 3.3.

Previous analytical models (Johnson, 1985; Stronge, 2000a; Li *et al*, 2002; Brake, 2012) that are based on the three loading regimes have used single

continuous functions to model the elastoplastic loading regime. However, experimental evidence and FE results reveal that there is a linear loading region preceding the onset of fully plastic loading predicted by indentation theory (Majeed *et al*, 2012). Also, indentation theory and experimental evidence reveal that a nonlinear loading exists in the elastoplastic regime (Majeed *et al*, 2012). Therefore, it is proposed here that the elastoplastic loading regime can be divided into two regions as follows:

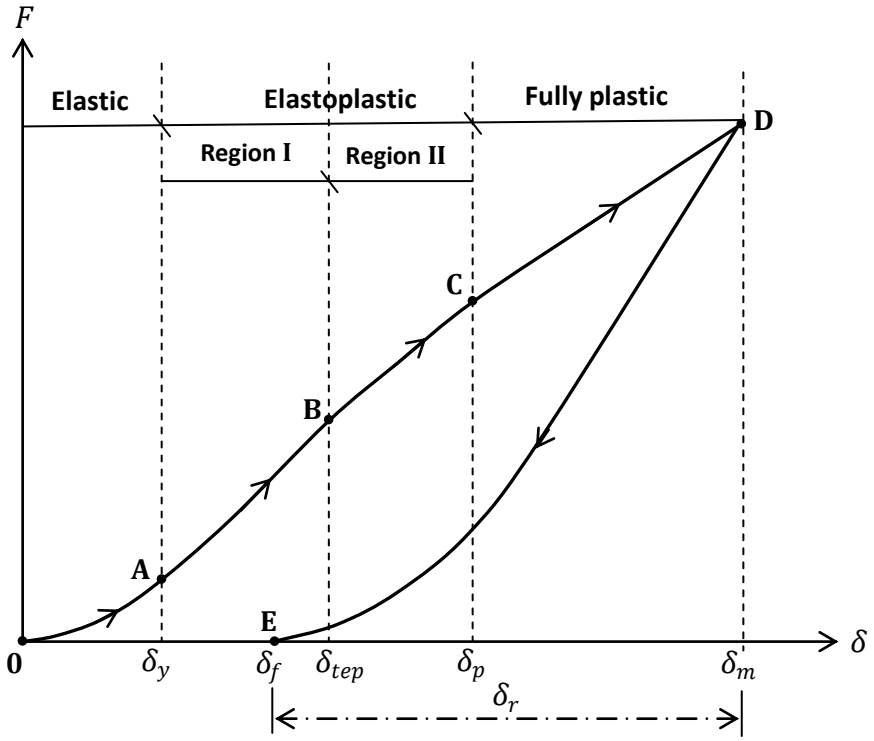

Figure 3.3: *Sketch of compliance curve for the new contact law.*

a. Region I: this is characterised by a nonlinear force-indentation relationship. The onset of this region is the yield point and it ends somewhere in the elastoplastic regime. In this region, the plastically-deformed material is well below the contact surface and it is smaller in comparison with the surrounding elastically-deformed material (Figure 3.4a). This means that the plastically-deformed material is fully contained within the surrounding elastic material and the indenter is only in contact with the elastically-deformed material.
b. Region II: this is characterised by a linear force-indentation relationship. The region commences from the terminus of region I and ends at the onset of fully plastic conditions. Here, the plastically-deformed material is

considered to be comparable or larger in volume than the surrounding elastically-deformed material (Figure 3.4b). The plastically-deformed material grows closer to the contact surface, and breaks free to the contact surface at the end of this region.

In the present study, it is proposed that region I can be modelled by a modified form of the Hertz contact law that incorporates a yield effect. This region is modelled in this way since it has similar characteristics as the elastic loading regime namely: (i) it is nonlinear and (ii) its deformation can be considered to be effectively elastic-like since the plastically-deformed material is small and fully contained within the surrounding elastically-deformed material. Region II is modelled using a linear force-indentation that incorporates the appropriate plastic deformation effect, which is assumed to occur at transition point in the elastoplastic loading regime.

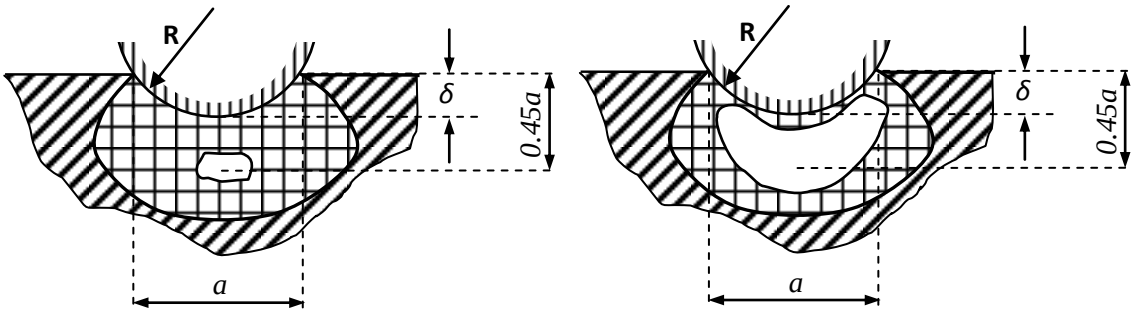

Figure 3.4: *Plastic deformation in the elastoplastic loading regime (a) during nonlinear elastoplastic deformation (b) during linear elastoplastic deformation. The cross-hatched area is the surrounding elastically-deformed material while the unshaded area is the plastically-deformed material.*

The features of these two regions can be seen in the approximate analytical models for the elastoplastic loading regime presented in (Johnson, 1985; Stronge, 2000a). These models incorporate plastic deformation effects and the nonlinear part of the elastoplastic loading appears as a logarithmic function of the indentation. The existence of the two regions in the elastoplastic loading regimes means that there is a transition point from region I to region II. Majeed *et al* (2012) assumed that the transition from region I to region II occurs at the point where the mean contact pressure is equal to the arithmetic average of the mean contact pressures at yield and at fully plastic conditions i.e. the transition

occurs at $P_0 = 1.95S_y$. Although this assumption produced results that are supported by the static indentation experiments of woven E-glass/polyester composite laminate, it requires further validation. In the proposed analysis the indentation and mean contact pressure at the transition point are derived analytically from continuity conditions and existing indentation theory.

Based on the foregoing discussions, the following force-indentation relationships are proposed for modelling the static loading and unloading of a half-space target by a spherical indenter.

Elastic loading regime

$$F_e = K_h \delta^{3/2} \qquad 0 \le \delta \le \delta_y \tag{3.26}$$

Elastoplastic loading regime

- Region I: Nonlinear elastoplastic loading

$$F_{ep}^{I} = K_h \left(\delta - \delta_y\right)^{3/2} + K_h \delta_y^{3/2} \qquad \delta_y \le \delta \le \delta_{tep} \tag{3.27}$$

- Region II: Linear elastoplastic loading

$$F_{ep}^{II} = K_l \left(\delta - \delta_{tep}\right) + K_h \left[\left(\delta_{tep} - \delta_y\right)^{3/2} + \delta_y^{3/2}\right] \qquad \delta_{tep} \le \delta \le \delta_p \tag{3.28}$$

Fully plastic loading regime

$$F_{fp} = K_p \left(\delta - \delta_p\right) + F_{\delta=\delta_p} \qquad \delta_p \le \delta \le \delta_m \tag{3.29}$$

Restitution (unloading)

$$F_u = K_u \left(\delta - \delta_f\right)^{3/2} \qquad \delta_f \le \delta \le \delta_m \tag{3.30}$$

where F_e, F_{ep} , F_{fp}, and F_u are the elastic, elastoplastic, fully plastic, and unloading forces respectively. The superscripts on F_{ep} indicate the region in the elastoplastic regime, and $F_{\delta=\delta_p}$ is the value of the contact force at the onset of fully plastic conditions. K_h is the Hertzian contact stiffness, K_l is the linear stiffness in region II, K_p is the linear stiffness during the fully plastic loading regime and K_u is the nonlinear stiffness during unloading. δ_y is the indentation at yield, δ_{tep} is the indentation at the transition between region I and region II, δ_p is the indentation at the onset of fully plastic conditions and δ_f is the fixed or permanent or non-recoverable indentation. The contact parameters in the model are derived next.

3.2.1 Determination of contact parameters of the new contact model

The contact parameters in the new contact model shown in equations (3.26) – (3.30) depend on the material and geometric properties of the contact system, and they are derived here from indentation theory and continuity conditions as follows.

Elastic loading regime

The only constant in this regime is K_h and it is determined from the Hertz contact theory.

$$K_h = \frac{4}{3}\bar{E}\bar{R}^{1/2} \tag{3.31}$$

$\bar{E}$ and $\bar{R}$ are the effective modulus and radius as defined in equation (3.1).

Region I: Nonlinear elastoplastic loading

Majeed *et al* (2012) modelled this region using Hertz's law and therefore, the effect of post-yield deformation was not accounted for. These have now been accounted for in the present model as shown in equation (3.27). The unknown constants in this region are K_h and δ_y, and K_h is determined from equation (3.31). To derive the expression for δ_y the elastic force at $\delta = \delta_y$ is equated to the product of the mean pressure and contact area at $\delta = \delta_y$. Hence,

$$(F_e)_{\delta=\delta_y} = F_{\delta=\delta_y}$$

where $F_{\delta=\delta_y}$ is the contact force at yield expressed in terms of the mean pressure and following (Stronge, 2000b), can be written as $F_{\delta=\delta_y} = \pi\bar{R}P_{0y}\delta_y$; $P_{0y} = 1.1S_y$ is the mean contact pressure at yield. $(F_e)_{\delta=\delta_y}$ is evaluated by substituting $\delta = \delta_y$ in equation (3.26). Therefore,

$$K_h\delta_y^{3/2} = 1.1\pi\bar{R}S_y\delta_y$$

from which the expression for δ_y is obtained as:

$$\delta_y = \left(1.1\pi\bar{R}S_y/K_h\right)^2 \tag{3.32}$$

Substituting equation (3.31) into equation (3.32),

$$\delta_y = 0.681\pi^2\bar{R}S_y^2/\bar{E}^2 \tag{3.33}$$

Fully plastic loading regime

For convenience, expressions for the constants of the fully plastic loading regime are derived before those of the second region of the elastoplastic loading regime. The unknown constants here are K_p, δ_p and $F_{\delta=\delta_p}$. As mentioned earlier,

the mean pressure in this regime is constant and therefore, the contact force at any point in this regime can be written as:

$$F_{fp} = \pi P_{0p} a^2 \tag{3.34}$$

where $P_{0p} = 2.8S_y$ is the mean contact pressure at fully plastic conditions and a is the contact radius. Since the force-indentation relationship in this loading regime is linear, $a^2 \propto \delta$. A general relationship between the contact radius and indentation can be written as $a^2 = 2\bar{R}\delta + c_p$ where the constant $c_p = a_p^2 - 2\bar{R}\delta_p \neq 0$ can be either positive of negative depending on the values of a_p and δ_p (Brake, 2012). Therefore,

$$a^2 = 2\bar{R}(\delta - \delta_p) + a_p^2 \tag{3.35}$$

Substituting equation (3.35) in equation (3.34) and comparing the resulting expression with equation (3.29), it can be deduced that

$$K_p = 5.6\pi\bar{R}S_y \tag{3.36a}$$

and

$$F_{\delta=\delta_p} = \pi P_{0p} a_p^2 = 2.8\pi S_y a_p^2 \tag{3.36b}$$

where a_p can be determined according to Stronge (2000a) as: $a_p^2 = \bar{R}(2\delta_p - \delta_y)$. Equation (3.36a) represents the case of a perfectly rigid indenter in contact with a perfectly plastic half-space. When equation (3.36a) was used in the simulation of the force-indentation curve for selected experimental cases (Alcalá *et al*, 1998; Bartier *et al*, 2010) the contact force predictions obtained during the fully plastic loading regime were significantly higher than the experimental data to which the predictions were compared. This is because the hardness of the indenters used in the experiments is just a few times higher than the hardness of the indented surfaces and therefore, the indenters cannot be considered to be perfectly rigid. Brake (2012) proposed an effective hardness to account for the effect of the relative hardness. For a spherical indenter in contact with a compliant flat surface, Brake (2012) determined the effective hardness as $H = [1/H_i + 2/H_t]^{-1}$ where $S_y < H < 2.8S_y$. Using this effective hardness a factor accounting for the relative hardness effect is introduced in the present model as: $\eta = H/(2.8S_y) = [1/H_i + 2/H_t]^{-1}/(2.8S_y)$. Hence,

$$K_p = 5.6\pi\eta\bar{R}S_y \tag{3.37}$$

For the experiments of Alcalá *et al* (1998) and Bartier *et al* (2010) the factor was calculated as $\eta = 0.81$ and $\eta = 0.85$ respectively. An average value of $\eta_{av} = 0.83$

was used in equation (3.37) and found to give good predictions of the experimental data. Consequently, the constant K_p is has been calculated as:

$$K_p = 4.65\pi\bar{R}S_y \tag{3.38}$$

If $H_i/H_t \geq 100$ then $\eta \cong 1$, and the indenter can be considered to be rigid so that equation (3.36a) can be used to calculate K_p. In cases where hardness data is unavailable equation (3.38) can be used to calculate K_p otherwise equation (3.37) is used. Note that the value of K_p does not affect the elastoplastic response; but it determines the fully plastic response.

To evaluate completely the contact force in the fully plastic loading regime, the value or expression for δ_p or δ_p/δ_y must be known. In the literature, different expressions have been used for the ratio δ_p/δ_y. Brake (2012) used the expression $\delta_p/\delta_y = (P_{op}/S_y)^2 = 7.84$ where $P_{op} = 2.8S_y$. This expression is the von Mises equivalent of the expression given by Stronge (2000b) that is based on Tresca's yield criterion. Brake (2012) observed that the use of this expression sometimes produces an unrealistic bend in the elastoplastic regime and a smoothing condition was applied to correct this. The condition states that the slope of the contact force at $\delta = \delta_p$ is equal to the slope of the extended Hertzian force at the same indentation i.e. $(dF_e/d\delta)_{\delta=\delta_p} = \left(dF_{fp}/d\delta\right)_{\delta=\delta_p}$. Using equations (3.26) and (3.34), and $\delta_y = (\pi\bar{R}P_{oy}/K_h)^2$ in the smoothing condition, the resulting ratio is $\delta_p/\delta_y = (4P_{op}/3P_{oy})^2 = 13.94$ where $P_{oy} = S_y$ has been used in-line with the von Mises yield criterion. Stronge (2000a) presented an approximate analytical formula that expresses the normalised mean pressure in the elastoplastic loading regime as a function of the normalised indentation. Evaluating this formula at $\delta = \delta_p$ results in $\delta_p/\delta_y = 82.5$, which translates into a force ratio of $F_p/F_y = 417.5$. Johnson (1985) gave a force ratio of $F_p/F_y \approx 400$, and based on Johnson's model for the fully plastic loading regime a ratio of $\delta_p/\delta_y \approx 73$ can be obtained. Stronge (2000a) also reported a ratio of $\delta_p/\delta_y \approx 140$ and a corresponding force ratio of $F_p/F_y \approx 650$ from finite element studies of elastic-perfectly plastic bodies. The results of Johnson (1985) and Stronge (2000a) are close and are based on theoretically valid analytical approximations of the elastoplastic loading regime. Therefore, a ratio of $\delta_p/\delta_y = 82.5$ has been used in the present study. However, parametric studies based on the formulation

of the elastoplastic regime of the new contact model reveal that δ_p/δ_y can be reasonably varied from 28 to 140 as shown in later discussions in this chapter. Hence,

$$\delta_p = 82.5\delta_y = 56.18\pi^2\bar{R}S_y^2/\bar{E}^2 \tag{3.39}$$

Region II: Linear elastoplastic loading

In this region, two constants are to be determined; K_l and δ_{tep}. To obtain expressions for these constants, the following continuity conditions are applied.

Condition 1: The slope of region II is equal to the slope of region I at $\delta = \delta_{tep}$. The condition implies that the linear stiffness of region II is equal to the slope of region I at $\delta = \delta_{tep}$. This condition has been used by Yigit and Christoforou (1994) and Majeed *et al* (2012) when considering transition from a nonlinear behaviour to a linear behaviour. It is dimensionally consistent, and therefore has also been applied in the present modelling. The condition can be expressed mathematically as:

$$\left(\frac{dF_{ep}^{II}}{d\delta}\right)_{\delta=\delta_{tep}} = \left(\frac{dF_{ep}^{I}}{d\delta}\right)_{\delta=\delta_{tep}}$$

from which we get:

$$K_l = 1.5K_h\left(\delta_{tep} - \delta_y\right)^{1/2} \tag{3.40}$$

Condition 2: The value of the linear elastoplastic force is equal to the value of the fully plastic force at $\delta = \delta_p$.

$$\left(F_{ep}^{II}\right)_{\delta=\delta_p} = \left(F_{fp}\right)_{\delta=\delta_p}$$

Substituting equations (3.29) and (3.40) into this condition,

$$K_l\left(\delta_p - \delta_{tep}\right) + K_h\left[\left(\delta_{tep} - \delta_y\right)^{3/2} + \delta_y^{3/2}\right] = F_{\delta=\delta_p} \tag{3.41}$$

From equation (3.41), K_l can be expressed as:

$$K_l = \frac{F_{\delta=\delta_p} - K_h\left[\left(\delta_{tep} - \delta_y\right)^{3/2} + \delta_y^{3/2}\right]}{\left(\delta_p - \delta_{tep}\right)} \tag{3.42}$$

Using equations (3.40) and (3.42), the following nonlinear equation can be obtained.

$$K_h\left(\delta_{tep} - \delta_y\right)^{3/2} - 1.5K_h\left(\delta_{tep} - \delta_y\right)^{1/2}\left(\delta_{tep} - \delta_p\right) = F_{\delta=\delta_p} - K_h\delta_y^{3/2} \tag{3.43}$$

Squaring both sides of equation (3.43) and after some algebraic simplifications (see appendix A.1), a cubic equation in δ_{tep} is obtained as shown in equation (3.44).

$$\delta_{tep}^3 - \Lambda_1 \delta_{tep}^2 + \Lambda_2 \delta_{tep} - \Lambda_3 = 0 \quad (3.44)$$

$\Lambda_1 = 6\delta_p - 3\delta_y$; $\Lambda_2 = 9\delta_p^2 - 6\delta_y \delta_p$; $\Lambda_3 = 4\delta_y^3 - 12\delta_y^2 \delta_p + 9\delta_y \delta_p^2 + (2Z/K_h)^2$; and $Z = F_{\delta=\delta_p} - K_h \delta_y^{3/2}$. The value of δ_{tep} obtained from equation (3.44) is substituted into equation (3.40) to calculate the value of K_l. The solution to equation (3.44) must be within the range $\delta_y < \delta_{tep} < \delta_p$.

Restitution (unloading)

There are two unknown constants in this regime according to equation (3.30). The constants are the unloading stiffness K_u and the non-recoverable indentation δ_f. In order to determine the expressions for these constants, two new variables are needed namely: the maximum indentation δ_m and the maximum contact force F_m. Since this phase is elastic, the force-indentation relationship is analogous to the Hertz contact model for elastic loading. The constants are determined using the same expressions as used by Stronge (2000a):

$$K_u = \frac{4}{3} \bar{E} \bar{R}_d^{1/2} \quad (3.45a)$$

$$\delta_f = \delta_m - \left(\frac{3F_m}{4\bar{E}\bar{R}_d^{1/2}} \right)^{2/3} \quad (3.45b)$$

where $\bar{R}_d$ is the deformed effective radius, and $\bar{R}_d \geq \bar{R}$. Whereas the Hertz stiffness is related to the effective radius, the unloading stiffness is related to a deformed effective radius due to plastic deformation effects (Stronge, 2000a).

The main difference between the present restitution model and that of Stronge (2000a) is in the way $\bar{R}_d$ is determined. Following suggestions of Johnson (1985) and Brake (2012), Big-Alabo *et al* (2014a; 2015a) determined $\bar{R}_d$ as follows: $\bar{R}_d \cong \bar{R}$ when the maximum penetration is in the elastoplastic loading regime or the initial phase of the fully plastic loading regime; and $\bar{R}_d \cong \bar{R} + \delta_m/2$ when the maximum penetration is well into the fully plastic loading regime. The approximations used by Big-Alabo *et al* (2014a; 2015a) could lead to significant underestimation of the permanent indentation at the end of the unloading (Big-Alabo *et al*, 2015a). Johnson (1985) stated that $\bar{R}_d \cong 2.0\bar{R}$ when unloading from the onset of fully plastic conditions if piling and sinking are neglected. Based on FE results of the indentation of an elastic-perfectly plastic material, Li *et al* (2002) determined the value of $\bar{R}_d$ when unloading from the onset of fully plastic indentation as $\bar{R}_d \cong 2.15\bar{R}$. Hill *et al* (1989) reported that $\bar{R}_d$ could reach a value of $2.8\bar{R}$ during indentation of perfectly plastic materials. Hence, it could be said

that $\bar{R}_d$ lies in the range of $\bar{R} \leq \bar{R}_d \leq 2.8\bar{R}$ during post-yield unloading. Since the present contact model consists of a linear elastoplastic loading regime that exhibits an indentation behaviour that is much like that of the fully plastic loading regime, it is assumed that Johnson's suggestion of $\bar{R}_d \cong 2.0\bar{R}$ occurs when unloading from the onset of the linear elastoplastic loading. This means that $\bar{R}_d$ varies between $\bar{R}$ and $2.0\bar{R}$ during unloading from the nonlinear elastoplastic loading regime i.e. $\delta_y \leq \delta_m \leq \delta_{tep}$. Also, based on the observation of Hill *et al* (1989) and to ensure continuity, $\bar{R}_d$ is assumed to vary between $2.0\bar{R}$ and $2.8\bar{R}$ during unloading from the linear elastoplastic loading regime i.e. $\delta_{tep} \leq \delta_m \leq \delta_p$. Finite element studies conducted by Li *et al* (2002) on the variation of $\bar{R}_d$ with indentation revealed that $\bar{R}_d$ is approximately constant once fully plastic conditions are reached. Here, $\bar{R}_d$ is assumed to have a constant value of $2.8\bar{R}$ when unloading from the fully plastic loading regime. Therefore, the following expressions have been used to calculate $\bar{R}_d$.

$$\left.\begin{aligned} \bar{R}_d &= \bar{R} && 0 \leq \delta_m \leq \delta_y \\ \bar{R}_d &= \left[\left(\frac{\delta_m - \delta_y}{\delta_{tep} - \delta_y}\right)^{3/2} + 1\right]\bar{R} && \delta_y \leq \delta_m \leq \delta_{tep} \\ \bar{R}_d &= \left[0.8\left(\frac{\delta_m - \delta_{tep}}{\delta_p - \delta_{tep}}\right) + 2\right]\bar{R} && \delta_{tep} \leq \delta_m \leq \delta_p \\ \bar{R}_d &= 2.8\bar{R} && \delta_m > \delta_p \end{aligned}\right\} \quad (3.46)$$

3.2.2 Normalised form of new contact model

In this section, the contact model presented in equations (3.26) to (3.30) is normalised with respect to the contact force at yield. The normalised contact model is more elegant and easier to compute. Dividing equations (3.26) to (3.30) by $F_y = K_h \delta_y^{3/2}$, the normalised form of the present contact model is derived as shown:

Elastic loading regime

$$\bar{F}_e = \bar{\delta}^{3/2} \qquad 0 \leq \bar{\delta} \leq 1 \quad (3.47)$$

Elastoplastic loading regime

- Region I: Nonlinear elastoplastic loading

$$\bar{F}_{ep}^{I} = \left(\bar{\delta} - 1\right)^{3/2} + 1 \qquad 1 \leq \bar{\delta} \leq \bar{\delta}_{tep} \quad (3.48)$$

- Region II: Linear elastoplastic loading

$$\bar{F}_{ep}^{II} = 1.5\left(\bar{\delta}_{tep} - 1\right)^{1/2}\left(\bar{\delta} - \bar{\delta}_{tep}\right) + \left(\bar{\delta}_{tep} - 1\right)^{3/2} + 1 \qquad \bar{\delta}_{tep} \leq \bar{\delta} \leq \bar{\delta}_p \quad (3.49)$$

Fully plastic loading regime

$$\bar{F}_{fp} = 4.182\left(\bar{\delta} - \bar{\delta}_p\right) + 2.545\left(2\bar{\delta}_p - 1\right) \qquad \bar{\delta}_p \le \bar{\delta} \le \bar{\delta}_m \tag{3.50}$$

Restitution (unloading)

$$\bar{F}_u = \bar{K}_u\left(\bar{\delta} - \bar{\delta}_f\right)^{3/2} \qquad \bar{\delta}_f \le \bar{\delta} \le \bar{\delta}_m \tag{3.51}$$

In equations (3.47) to (3.51), the bar over the forces indicate normalisation with respect to F_y and the bar over the indentations indicate normalisation with respect to δ_y e.g. $\bar{F}_e = F_e/F_y$ and $\bar{\delta} = \delta/\delta_y$. The constant $\bar{\delta}_{tep}$ lies within the range $1 < \bar{\delta}_{tep} < \bar{\delta}_p$, and is obtained from

$$\bar{\delta}_{tep}^3 - \Omega_1\bar{\delta}_{tep}^2 + \Omega_2\bar{\delta}_{tep} - \Omega_3 = 0 \tag{3.52}$$

$\Omega_1 = 6\bar{\delta}_p - 3;\ \Omega_2 = 9\bar{\delta}_p^2 - 6\bar{\delta}_p;$ and $\Omega_3 = 54.268 - 156.352\bar{\delta}_p + 112.632\bar{\delta}_p^2$. Also, $\bar{\delta}_p = 82.5;\ \bar{K}_u = \bar{R}_d/\bar{R}$ and $\bar{\delta}_f = \bar{\delta}_m - \left(3F_m/4\bar{E}\bar{R}_d^{1/2}\right)^{2/3}/\delta_y$. Equation (3.52) can be derived by dividing equation (3.44) by δ_y^3, or solving equations (3.49) and (3.50) simultaneously at $\bar{\delta} = \bar{\delta}_p$. Given that all the coefficients of the cubic equation in $\bar{\delta}_{tep}$ are dependent on $\bar{\delta}_p$, then substituting $\bar{\delta}_p = 82.5$ and solving equation (3.52) gives $\bar{\delta}_{tep} = 13.93$.

3.3 Validation of new contact model

The new contact model formulated above was validated by comparing its results with published experimental data for both static and dynamic indentation cases. Static indention is one in which the initial velocity of the indenter is zero, while dynamic indentation involves an initial velocity greater than zero. For the static indentation analysis the experiments of Alcalá *et al* (1998) and Bartier *et al* (2010) were used for validation; while for the dynamic indentation analysis the coefficient of restitution measurements by Mok and Duffy (1965) and Kharaz and Gorham (2000) were used for validation.

3.3.1 Some observations of the new contact model

To understand the features and workings of the new contact model and to compare with the findings of published analytical models and experimental data, parametric studies were carried out on the present model.

Using Brake's contact model, it was shown that the smoothed formulation for the elastoplastic loading regime always produced the best result and

$\bar{\delta}_p = 13.94$ according to the smoothed formulation. In the current model, the transition point in the elastoplastic loading regime was found to occur at $\bar{\delta}_{tep} = 13.93$. This point coincides with the point at which Brake's smoothed formulation assumes a transition to the fully plastic regime. The implication is that a transition from nonlinear to linear deformation behaviour occurs at this point. Whereas Brake's model suggests that this point (i.e. $\bar{\delta} \cong 13.93$) marks the onset of fully plastic conditions, the present model indicates that the point is located within the elastoplastic loading regime and gives rise to a linear elastoplastic deformation just before fully plastic conditions are reached. The presence of linear elastoplastic deformation behaviour during contact loading has been reported (Majeed *et al*, 2012) and can also be seen in the compliance curve for elastoplastic indentation presented by Johnson (1985).

When $\bar{\delta}_{tep} = 13.93$ is substituted into equation (3.49), the normalised force at the transition point in the elastoplastic loading regime is calculated to be $\bar{F}_{tep} = 47.5$. According to Stronge (2000a), the normalised contact force in the elastoplastic loading regime can be expressed in terms of the normalised mean pressure and indentation as: $F/F_y = \left(P_0/P_{0y}\right)\left(2\delta/\delta_y - 1\right)$. Putting $\bar{\delta}_{tep} = 13.93$, $\bar{F}_{tep} = 47.5$, and noting that $P_{oy} = 1.1S_y$, the mean pressure at $\bar{\delta} = \bar{\delta}_{tep}$ was calculated to be equal to $1.945S_y$. This value, which is approximately equal to $1.95S_y$, is in agreement with the transition mean pressure in the elastoplastic loading regime proposed by Majeed *et al* (2012). However, according to Majeed *et al* (2012) the transition mean pressure occurs when $\bar{\delta} \cong 3.15$, whereas for the present model it occurs at $\bar{\delta} = 13.93$. In agreement with Brake's model the present contact model confirms that the contact deformation changes from nonlinear to linear behaviour when the normalised indentation is equal to 13.94; and in agreement with the model of Majeed *et al* (2012) the present contact model confirms that the contact deformation in the elastoplastic loading regime changes from nonlinear to linear behaviour at a mean pressure of $1.95S_y$. Since the non-dimensional indentation of 13.94 and the mean pressure of $1.95S_y$ occur at the same point according to the present model, it appears that these values are unique constants for the transition point in the elastoplastic loading regime.

The transition point in the elastoplastic loading regime of the current model lies in the range $1 < \bar{\delta}_{tep} < \bar{\delta}_p$, and this transition point is determined

from the cubic equation that was derived from continuity conditions. In a limiting case, $\bar{\delta}_{tep}$ will be equal to $\bar{\delta}_p$, but it is not possible for $\bar{\delta}_{tep}$ to be greater than $\bar{\delta}_p$. Using these practical restrictions, the possible range of applicable values for $\bar{\delta}_{tep}$ was investigated. It was observed that only one of the roots of the cubic equation satisfied the restrictions, and an increase in the value of $\bar{\delta}_p$ resulted in a decrease in the calculated value of $\bar{\delta}_{tep}$ and vice versa. It was found that $\bar{\delta}_{tep} = \bar{\delta}_p$ when $\bar{\delta}_p \cong 27.5$, which is the lower bound for $\bar{\delta}_p$ based on the present model. Although the lower bound for $\bar{\delta}_p$ is much lower than the values proposed by Johnson (1985) and Stronge (2000a), lower values of $\bar{\delta}_p$ have been used is some models (Brake, 2012) and shown to give good predictions of the fully plastic loading regime when compared with static indentation experiments. Since values of $\bar{\delta}_p$ up to 140 have been reported (Stronge, 2000a), the present model suggests that $\bar{\delta}_p$ can be logically varied within the range of $28 \leq \bar{\delta}_p \leq 140$. The corresponding range for $\bar{\delta}_{tep}$ that was calculated from equation (3.52) is $23.84 \geq \bar{\delta}_{tep} \geq 13.28$. Note that the value of $\bar{\delta}_{tep}$ does not change much between $\bar{\delta}_p = 82.5$ (where $\bar{\delta}_{tep} = 13.93$) and $\bar{\delta}_p = 140$ (where $\bar{\delta}_{tep} = 13.28$).

Finite elements analysis (Stronge, 2000a; Hardy *et al*, 1971) and analytical studies (Johnson, 1985; Stronge, 2000a; Brake, 2012; Li *et al*, 2002) have used different values for the normalised indentation at the onset of fully plastic loading. It is proposed here that a value of $\bar{\delta}_p = 82.5$ and a corresponding value of $\bar{\delta}_{tep} = 13.93$ can be used for modelling a static or dynamic elastoplastic indentation based on the present model. However, for cases where using these values in the present model results in predictions that deviate from what is expected, i.e. from experimental data, $\bar{\delta}_p$ can be varied within the range of $28 \leq \bar{\delta}_p \leq 140$ and the corresponding value of $\bar{\delta}_{tep}$ can be obtained by solving equation (3.52).

3.3.2 Static indentation analysis

To validate the present contact model, static indentation compliance curves obtained from predictions of the present contact model were compared with experimental results (Alcalá *et al*, 1998; Bartier *et al*, 2010) and the model

results of Brake (2012). Brake's model was used for comparison with the present model because it was previously compared with nine other published models and shown to provide the best performance in predicting the results of several static and dynamic indentation measurements. Furthermore, this model can be evaluated completely from the contact geometry and material properties of the contact system (as can the present contact model).

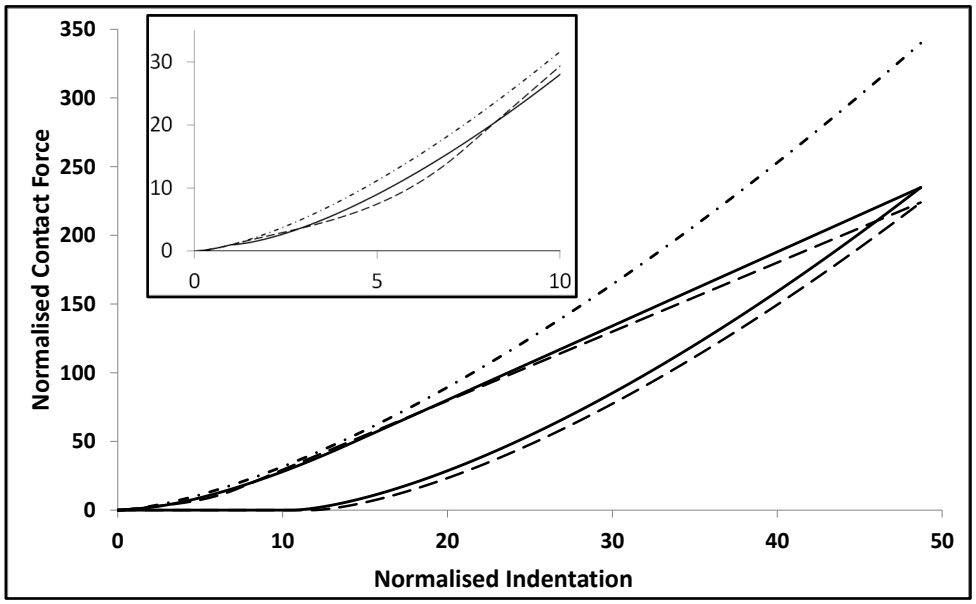

Figure 3.5: *Compliance curve for indentation of two identical SUJ2 Steel balls. Present model - Solid line, Brake's model - Dash line, Hertz model - Dot dash line.*

In Figure 3.5 the compliance curve for the impact between two identical steel balls obtained using the present contact model is shown. The input parameters for the contact system are: modulus = 206 [*GPa*], Poisson's ratio = 0.3 [-], yield stress = 350 [*MPa*], and ball radius = 12.7 [*mm*]. The same problem was studied by Brake (2012) and the model results of Brake produced an unrealistic bend at the beginning of the elastoplastic loading regime (see exploded plot in Figure 3.5). Brake (2012) corrected this bend using a smoothing condition. The present contact model shows no such bend and gives a maximum normalised contact force of 234 when the maximum normalised indentation is 48.7 as compared to 224 from the simulation of Brake's model. Also, the maximum conditions are located in the linear elastoplastic loading regime of the present model, whereas they are located in the fully plastic regime according to Brake's model. However, the loading and unloading paths predicted by both

models are in agreement. Note that the deformed effective radius used in the simulation of the unloading path of the present model was determined from equation (3.19a).

Table 3.1: *Material properties for indentation of pure Nickel by spherical 10% Cobalt-Tungsten Carbide Indenter (Brake, 2012)*

Material Property	Indenter (Tungsten Carbide)	Target (Pure Nickel)
Density [kg/m^3]	14 500	8880
Elastic Modulus [*GPa*]	475	207
Poisson's ratio [-]	0.22	0.31
Yield Strength [*MPa*]	-	148
Hardness [*MPa*]	11 436.6	695.8
Radius [*m*]	7.95×10^{-4}	∞

Figure 3.6 illustrates the results of a tungsten carbide indenter on a pure nickel target. The properties of the contact system are given in Table 3.1. A comparison is made between the results from the present contact model, Brake's model, and measurements of Alcalá *et al* (2012). In Figure 3.6, the present model was simulated with $\bar{\delta}_p = 82.5$ and a corresponding value of $\bar{\delta}_{tep} = 13.93$. The figure shows that the fully plastic loading predicted by the present model deviates significantly from the measured data. To obtain a better prediction of the fully plastic loading, $\bar{\delta}_p$ was assumed to be equal to 30 and the corresponding value for $\bar{\delta}_{tep}$ was calculated as 20.6. The compliance curve in this case is shown in Figure 3.7, which reveals that the present model gives a good estimate of the measured data. The effect of setting $\bar{\delta}_p = 30$ from the proposed general value of $\bar{\delta}_p = 82.5$ is that the indentation range of region II is shortened i.e. $20.6 < \bar{\delta}_{tep} < 30$. Since the reduction of this region gives a better estimate of the measured data for the indentation of the pure nickel target, then the present model suggests that the pure nickel target undergoes more nonlinear elastoplastic deformation than linear elastoplastic deformation. The results from the model of Majeed *et al* (2012) and the Hertz contact model are also illustrated in Figure 3.7, and it can be seen that the loading path is underestimated by the model of Majeed *et al* (2012). While the contact model of Majeed *et al* (2012) does not account for fully plastic loading, the inclusion of a fully plastic model would not improve the results because the contact stiffness

in the fully plastic loading regime is reduced further compared to the elastoplastic loading regime, thereby leading to lower contact force estimates.

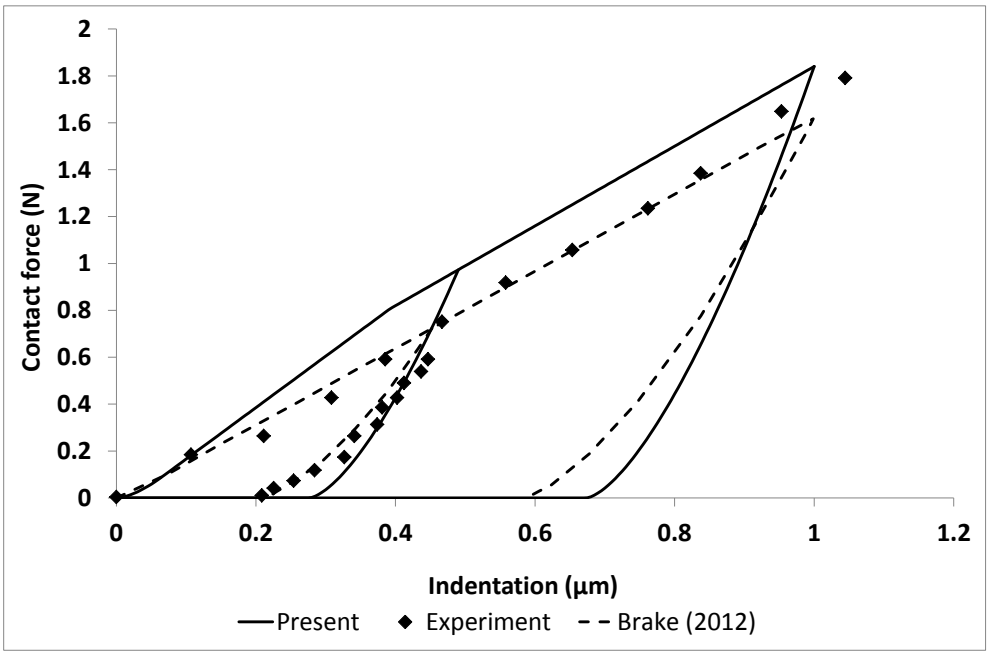

Figure 3.6: *Compliance curve for indentation of pure Nickel. The maximum indentation is well into the fully plastic regime.* $\bar{\delta}_p = 82.5$; $\bar{\delta}_{tep} = 13.93$ *for the present model.*

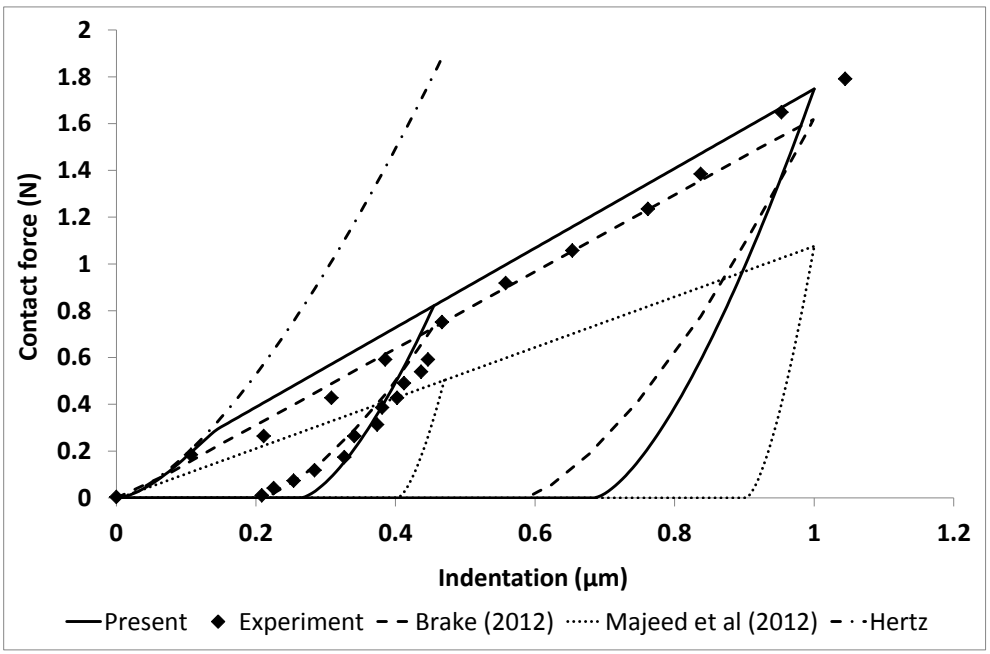

Figure 3.7: *Compliance curve for indentation of pure Nickel. The maximum indentation is well into the fully plastic regime.* $\bar{\delta}_p = 30$; $\bar{\delta}_{tep} = 20.6$ *for the present model.*

Table 3.2: *Material properties for indentation of AISI 1035 Steel by spherical Tungsten Carbide Indenter (Brake, 2012)*

Material Property	Indenter (Tungsten Carbide)	Target (AISI 1035 Steel)
Density [kg/m^3]	14 500	7850
Elastic Modulus [*GPa*]	600	210
Poisson's ratio [-]	0.28	0.30
Yield Strength [*MPa*]	-	300
Hardness [*MPa*]	11 436.6	1528.8
Radius [*m*]	1.25×10^{-3}	∞

Another case studied was the indentation of an AISI 1035 steel target by a tungsten carbide indenter. The properties of the contact system are given in Table 3.2 and the compliance curve is shown in Figure 3.8. The results of the present model were simulated for $\bar{\delta}_p = 82.5$ and $\bar{\delta}_{tep} = 13.93$, and compared with the results from Brake's model (2012), the model of Majeed *et al* (2012), and the measured data of Bartier *et al* (2010). The present model is shown to give a good prediction of the measured data. The unloading path of the present restitution model is in close agreement with the experimental data, while the unloading path of Brake's restitution model deviates from the experimental data towards the end of the unloading. Also, the present model suggests that the steel target undergoes more linear elastoplastic deformation than nonlinear elastoplastic deformation. Again, the model of Majeed *et al* (2012) underestimates the measured loading force and overestimates the permanent indentation at the end of the restitution.

There is a clear difference between the unloading path of the present model and that of Brake's model. This is attributed to the different expressions used by both models to calculate the deformed effective radius of the unloading. For the indentation of pure nickel, Brake's unloading path gives a better estimate of the measured unloading path and permanent indentation compared to the unloading path of the present model (see figure 3.7). However, the unloading path of the present model gives a good estimate of the measured unloading path. In the case of the indentation of AISI 1035 steel alloy, the unloading path of the present model gives a better estimate of the measured unloading path and permanent indentation compared to the unloading path of

Brake's model (see figure 3.8). Therefore, the present restitution model is shown to produce reliable results.

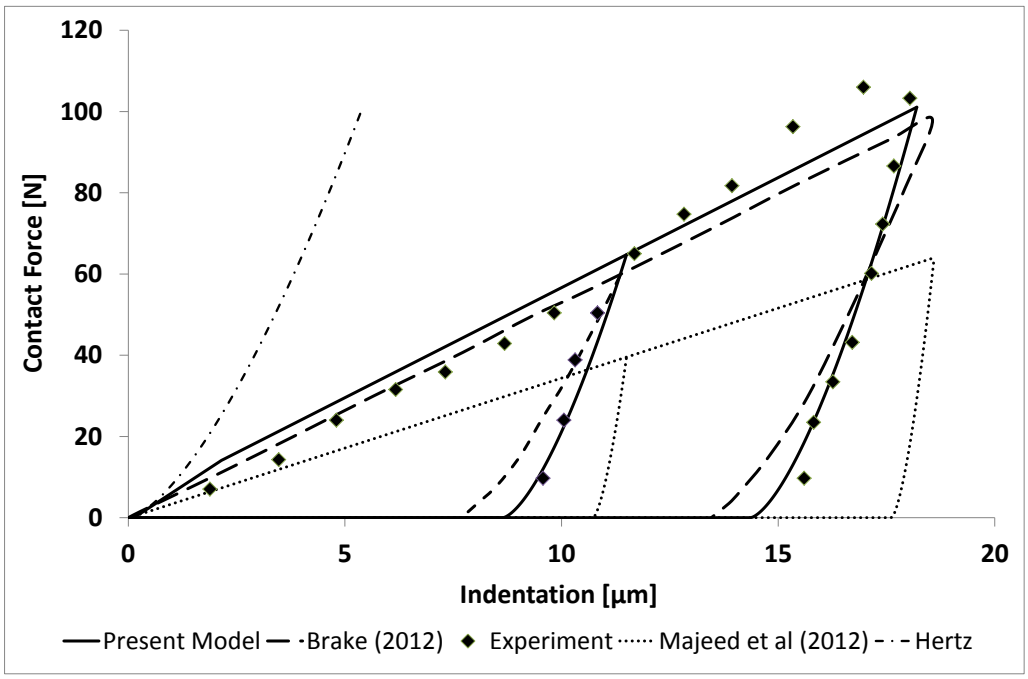

Figure 3.8: *Compliance curve for indentation of AISI 1035 Steel. The maximum indentation is well into the fully plastic regime.* $\bar{\delta}_p = 82.5$; $\bar{\delta}_{tep} = 13.93$ *for the present model.*

For the metallic targets investigated so far, the maximum indentation is well into the fully plastic regime and therefore, the curves in Figures 3.7 and 3.8 do not show the performance of the various models in the elastoplastic loading regime. In order to examine the performance of the various models in the elastoplastic loading regime the indention of an AISI 1035 steel target by a tungsten carbide indenter considered earlier was re-simulated as shown in Figure 3.9. The maximum indention in this simulation is approximately 15 times the indentation at yield, and this has been chosen to reveal the elastoplastic loading regime of each model. The figure shows that the loading path of the present model and that of Brake are close, whereas the model of Majeed and co-workers begins to deviate when the indentation is about 7.5 times the indentation at yield, thus leading to an underestimation of the contact force beyond this point. This investigation is important because it shows that the present model performs well in the elastoplastic regime of the loading phase. Hence, the combination of its simplicity, its ability to predict post-yield contact indentation with

reasonable accuracy, and the fact that it can be completely evaluated from the properties of the contact system makes the present contact model an attractive choice for impact analysis and validation of indentation test results.

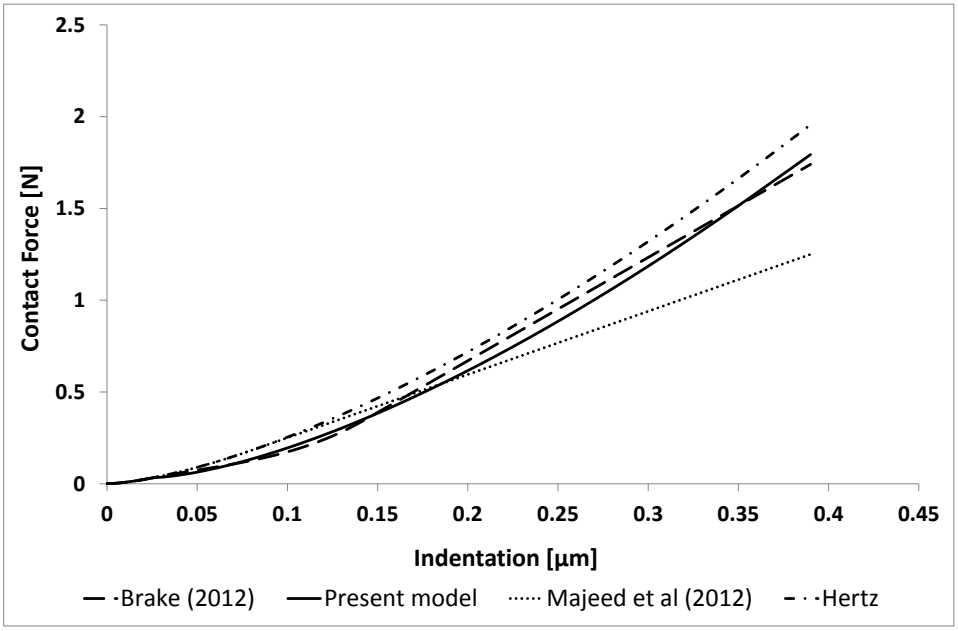

Figure 3.9: *Comparison of elastoplastic loading regime of present model with the models of Brake (2012) and Majeed et al (2012) for indentation of AISI 1035 Steel.*

3.3.3 Dynamic indentation analysis

During elastoplastic impact of a half-space by a spherical impactor part of the initial kinetic energy of the impactor is dissipated as plastic deformation and/or damage of the target. Consequently, the final rebound velocity of the impactor is less than the initial impact velocity. The severity of the impact and the impact energy absorption capacity of the target are measured by the *coefficient of restitution*. It has been shown that the coefficient of restitution is dependent on velocity (Johnson, 1985; Goldsmith, 2001; Jackson *et al*, 2009). Hence, measurements of the coefficient of restitution over a velocity range can be used to validate contact models. In this section, an analytical approach is formulated for determining the coefficient of restitution and applied to the new contact model formulated in Section 3.2. The coefficient of restitution results derived by the application of the analytical approach to the new contact model was compared with published measurements of the coefficient of restitution in order to validate the new contact model.

3.3.3.1 Analytical method for determination of coefficient of restitution

Stronge (2000a) gave three definitions of the coefficient of restitution namely: the kinematic, kinetic and energetic coefficient of restitution. The *kinematic coefficient of restitution* is the negative of the ratio of the final velocity of restitution to the initial impact velocity. The ratio of the impulse change during restitution to the impulse change during impact loading is known as the *kinetic coefficient of restitution*. The square of the *energetic coefficient of restitution* is equal to the negative of the ratio of the elastic energy released during restitution to the energy absorbed during impact loading. It was shown by Stronge (2000a) that these three definitions of the coefficient of restitution are equivalent unless the impacting bodies are rough, the configuration is eccentric and the direction of slip varies during collision. For the normal impact of a rigid spherical mass on a compliant flat half-space, as considered here, the three definitions are equivalent.

Stronge (2000a) applied the energetic approach to derive analytical expressions for calculating the coefficient of restitution. Here the kinematic approach has been applied to determine the coefficient of restitution using the new contact model to estimate the impact force. An analytical approach was developed to determine the final rebound velocity for an elastoplastic half-space impact. The approach combines closed-form integrals of the equations of motion for the loading and unloading regimes and a simple algorithm for calculating the maximum indentation and force of an elastoplastic impact.

Approximate analytical solutions have been derived for the fraction of impact energy dissipated as a non-recoverable elastic wave during elastic impact (Hunter, 1957) and elastic-plastic impact (Hutchings, 1979) on a half-space, but the fraction is negligible in both cases (Hunter, 1957; Hutchings, 1979). Furthermore, Johnson (1985) has shown that the elastoplastic impact response of a metallic half-space can be accurately determined by assuming quasi-static loading and unloading for impact velocities up to 500 [m/s]. Therefore, the impact force for such rate-independent impact events can be determined from an appropriate contact model.

The equation of motion for the impact of a half-space target by a rigid spherical impactor is given as:

$$m_i\ddot{\delta} + F = 0 \tag{3.53}$$

where m_i is the mass of the impactor; δ is the indentation of the target, which is equal to the displacement of the impactor, and the initial conditions are $\delta(0) = 0$, $\dot{\delta}(0) = V_0$; V_0 is the initial impact velocity, F is the impact force and it is subject to the restriction in equation (3.54).

$$F = \begin{cases} F(\delta) & if\ F > 0 \\ 0 & if\ F \leq 0 \end{cases} \tag{3.54}$$

Equation (3.53) can be rewritten as

$$\int_{t_0}^{t} m_i \dot{\delta} d\dot{\delta} = -\int_{t_0}^{t} F(\delta) d\delta \tag{3.55}$$

where t_0 is the time at the onset of an impact loading or unloading regime. Substituting equations (3.26) to (3.30) in (3.55) and evaluating the resulting integral, the following equations were derived for calculating the velocity in the loading and unloading regimes.

Loading regimes

$$\dot{\delta} = \left(V_0^2 - \frac{4K_h}{5m_i}\delta^{5/2}\right)^{1/2} \qquad 0 \leq \delta \leq \delta_y \tag{3.56}$$

$$\dot{\delta} = \left[V_y^2 - \frac{4K_h}{5m_i}\left(\delta - \delta_y\right)^{5/2} - \frac{2K_h}{m_i}\delta_y^{3/2}\left(\delta - \delta_y\right)\right]^{1/2} \qquad \delta_y \leq \delta \leq \delta_{tep} \tag{3.57}$$

$$\dot{\delta} = \left[V_{tep}^2 - \frac{K_l}{m_i}\left(\delta - \delta_{tep}\right)^2 - \frac{95K_h}{m_i}\delta_y^{3/2}\left(\delta - \delta_{tep}\right)\right]^{1/2} \qquad \delta_{tep} \leq \delta \leq \delta_p \tag{3.58}$$

$$\dot{\delta} = \left[V_p^2 - \frac{K_p}{m_i}\left(\delta - \delta_p\right)^2 - \frac{2F_p}{m_i}\left(\delta - \delta_p\right)\right]^{1/2} \qquad \delta_p \leq \delta \leq \delta_m \tag{3.59}$$

Unloading regime

$$\dot{\delta} = -\left[\frac{4K_u}{5m_i}\left(\left(\delta_m - \delta_f\right)^{5/2} - \left(\delta - \delta_f\right)^{5/2}\right)\right]^{1/2} \qquad \delta_f \leq \delta \leq \delta_m \tag{3.60}$$

In deriving equation (3.58) $\delta_{tep} = 13.93\delta_y$ was applied to simplify the resulting expression. The velocities at the transition from one loading regime to the other can be determined from equations (3.56) to (3.58) as follows.

$$V_y = \left(V_0^2 - \frac{4K_h}{5m_i}\delta_y^{5/2}\right)^{1/2} \tag{3.61}$$

$$V_{tep} = \left[V_y^2 - \frac{4K_h}{5m_i}\left(\delta_{tep} - \delta_y\right)^{5/2} - \frac{2K_h}{m_i}\delta_y^{3/2}\left(\delta_{tep} - \delta_y\right)\right]^{1/2} \tag{3.62}$$

$$V_p = \left[V_{tep}^2 - \frac{K_l}{m_i}\left(\delta_p - \delta_{tep}\right)^2 - \frac{95K_h}{m_i}\delta_y^{3/2}\left(\delta_p - \delta_{tep}\right)\right]^{1/2} \tag{3.63}$$

If $\delta_p = 82.5\delta_y$ and the corresponding indentation $\delta_{tep} = 13.93\delta_y$ are substituted in equations (3.62) and (3.63), then

$$V_{tep} = \left(V_y^2 - 506.795\frac{K_h}{m_i}\delta_y^{5/2}\right)^{1/2} \tag{3.64}$$

$$V_p = \left(V_{tep}^2 - 31904.112\frac{K_h}{m_i}\delta_y^{5/2}\right)^{1/2} \tag{3.65}$$

To complete the analytical method for calculating the coefficient of restitution the maximum indentation and impact force must be known. The relative velocity of the impactor and target during half-space impact is zero at the maximum indentation. This condition can be used to determine the maximum indentation and impact force of a half-space impact by using energy balance principles. However, for impacts on slender (flexible) targets, this condition can occur more than once during the impact thus resulting in more than one extremum. Furthermore, the interactions between vibrations of the target and the indentation introduce complications which make the energy balance approach impractical for impact on slender targets (Abrate, 1998).

During an elastoplastic impact on a half-space, the impact energy of the impactor is dissipated through various mechanisms such as elastic compression, elastic waves, plastic deformation, heat and sound. Johnson (1985) showed that for impact velocities up to 500 [m/s], all other mechanisms of impact energy dissipation can be neglected except for elastic compression and plastic deformation. The elastic compression energy is restored back to the impactor during unloading and the plastic deformation is dissipated in the half-space target as a permanent indentation. The range of impact velocities up to 500 [m/s] covers low to medium velocity impacts where strain rate effects can be neglected, and therefore, the impact event can be modelled using quasi-static assumptions (Johnson, 1985). For such impact events, the energy balance approach can be applied with the following assumptions: (i) no energy is lost from the impact system and (ii) the initial kinetic energy of the impactor is equal to the deformation work on the target i.e. elastic and plastic deformation. Based on the energy balance approach, the following expression holds:

$$\frac{1}{2}m_i V_0 = \int_0^{\delta_m} F\, d\delta \tag{3.66}$$

where F represents a general impact force that can be in any of the loading regimes.

In a typical impact event, a spherical impactor with known mass and velocity impacting a half-space target produces a definite maximum indentation that falls into one of the loading regimes discussed above. Therefore, it is necessary to determine the loading regime in which the maximum indentation is located, so that the appropriate force-indentation relationship(s) can be used in the impact analysis. Since the contact force can be represented as a piecewise continuous function of indentation, an iterative algorithm based on the energy balance is proposed here to determine the maximum indentation and impact force. In view of the fact that the impact loading starts from the elastic regime, the first step is to compare the total deformation work done up to the end of the elastic regime (W_y) to the kinetic energy (KE) of the impactor. If $KE < W_y$, then the maximum indentation is in the elastic regime, otherwise the total deformation work done up the end of region I (W_{tep}) is determined and compared with the KE. Again, if $KE < W_{tep}$, then the maximum indentation is in region I, otherwise the process is repeated until the maximum indentation is located in one of the loading regimes. The algorithm for this procedure is shown as a flowchart in Figure 3.10. Also, the total deformation work done from the beginning of the loading to each of the transition points in the loading regime are derived in appendix A.2.

To demonstrate the validity of this approach, the impact of a tungsten carbide ball on a mild steel half-space was investigated. The properties of the steel material are: Young's modulus = 210 [*GPa*], Poisson's ratio = 0.30 [-], and yield strength = 1000 [*MPa*]; and the properties of the tungsten carbide ball are: density = 14500 [kg/m^3], Young's modulus = 600 [*GPa*], and Poisson's ratio = 0.28. The diameter of the ball is 20 [*mm*] and the initial impact velocity is 5 [m/s]. The mass and initial KE of impactor was calculated as 0.06074 [*kg*] and 0.759 [*J*] respectively. Using the flowchart in Figure 3.10, the maximum indentation for this impact event was located in the linear elastoplastic loading regime and calculated as 101.623 [μm]. Hence, equations (3.56) to (3.58) were used to simulate the velocity-indentation response for the loading and equation (3.60) was used to simulate the velocity-indentation response for the unloading. The results obtained are plotted in Figure 3.11. The figure also shows results obtained by direct numerical integration of equation (3.53) with equations (3.26

– 3.30) used to estimate the impact force. The results of the numerical integration are in excellent agreement with the analytical method.

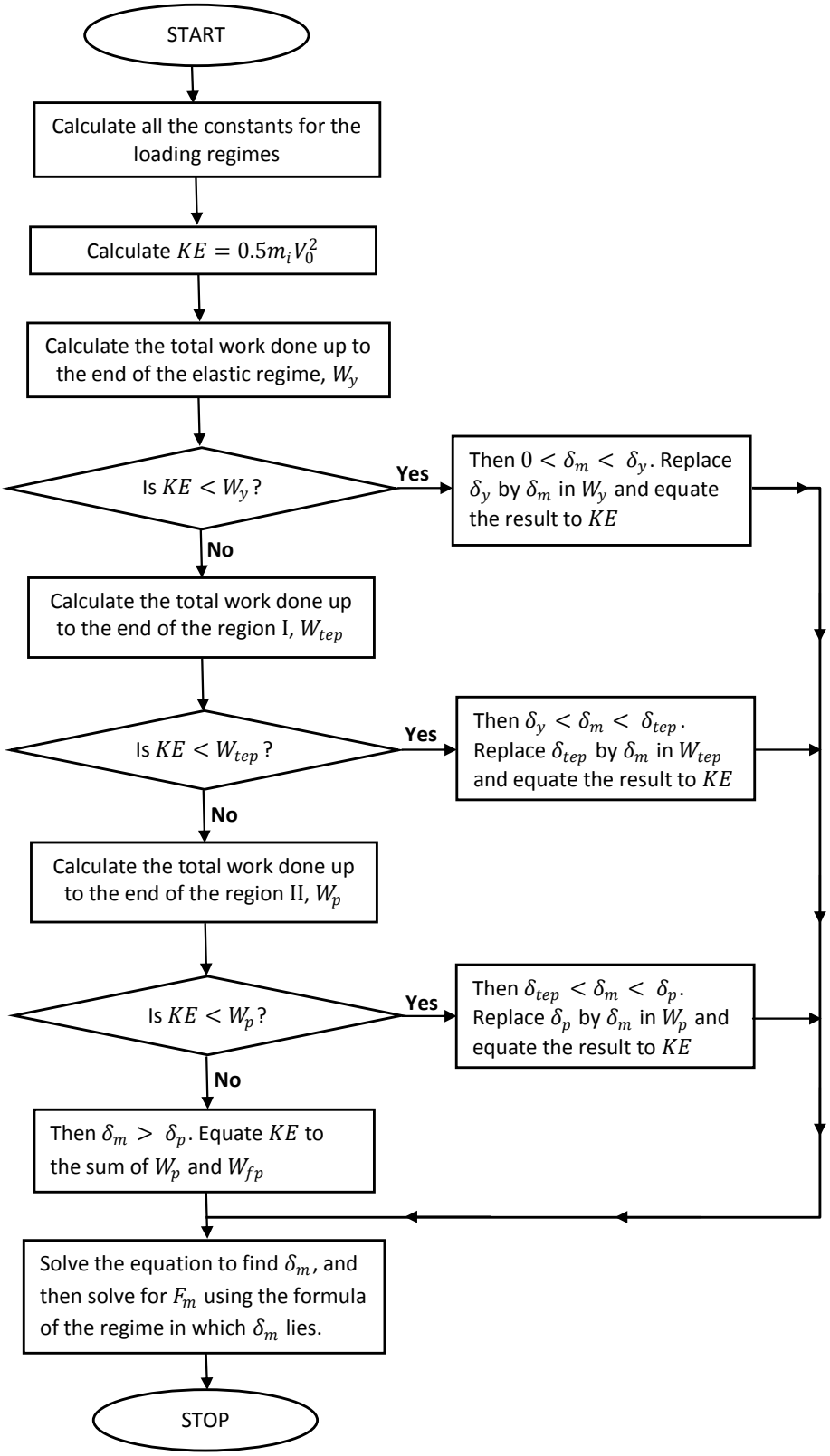

Figure 3.10: *Method to determine the maximum indentation and force during impact*.

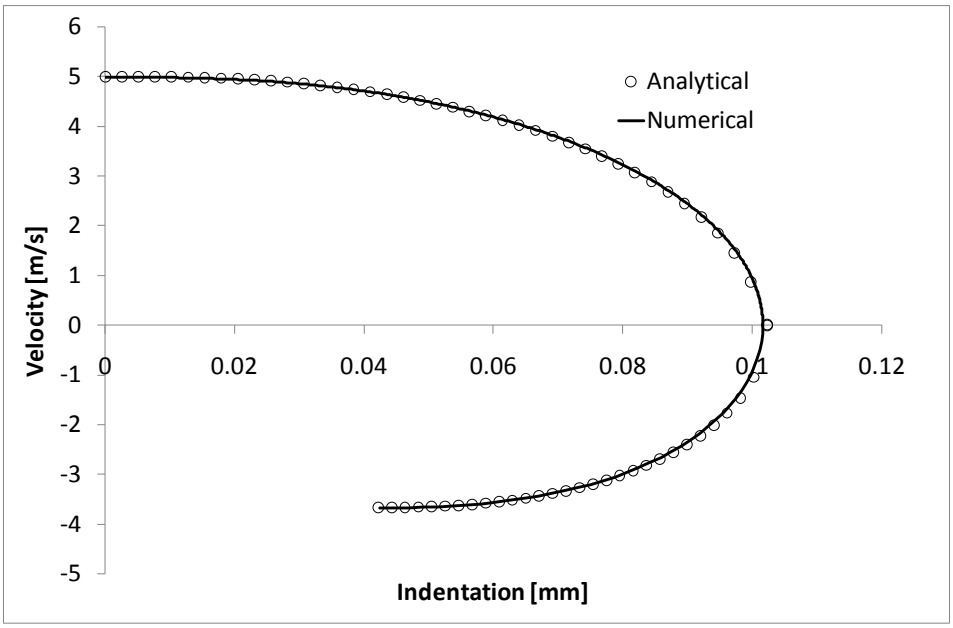

Figure 3.11: *Validation of analytical method for calculating the impactor velocity profile during half-space impact.*

3.3.3.2 Validation of new contact model using dynamic indentation measurements

The most commonly used definition of coefficient of restitution is the kinematic definition and it is expressed mathematically as:

$$e = -\left(\frac{V_f}{V_0}\right) \tag{3.67}$$

where V_f is the rebound velocity of the impactor at the end of the restitution. In Section 3.3.3.1 an analytical method was developed that can be used to determine the velocity-indentation profile for the loading and restitution stages of an elastoplastic impact, and the method was demonstrated using the new contact model presented in Section 3.2. At the end of the restitution $\delta = \delta_f$, and using equation (3.60)

$$V_f = -\left[\frac{4K_u}{5m_i}\left(\delta_m - \delta_f\right)^{5/2}\right]^{1/2} \tag{3.68}$$

V_f depends on the maximum indentation and impact force. The energy-balance algorithm developed earlier can be used to determine the maximum indentation and impact force. The values of the maximum indentation and impact force so obtained are substituted into equation (3.68) to calculate V_f, which is then used to calculate the coefficient of restitution.

It is well established experimentally and theoretically that the coefficient of restitution is dependent on the initial impact velocity. Consequently, attempts have been made to develop analytical expressions (Tabor, 1951; Johnson, 1985; Thornton and Ning, 1997) and FE correlations (Wu *et al*, 2003) for the coefficient of restitution in terms of the initial impact velocity. However, these expressions have been developed based on either perfectly plastic or elastic-perfectly plastic material behaviour. Kharaz and Gorham (2000) showed that coefficient of restitution models developed based on elastic-perfectly plastic or perfectly plastic assumptions underestimate the coefficient of restitution, and therefore, there is a need to use compliance models based on elastic-elastoplastic-perfectly plastic material behaviour to calculate the coefficient of restitution. Coefficient of restitution studies on elastic-elastoplastic-perfectly plastic material behaviour have been carried out either experimentally (Mok and Duffy, 1965; Kharaz and Gorham, 2000; and Goldsmith, 2001) or through numerical integration of the governing differential equation (Li *et al*, 2002; Brake, 2012), which is nonlinear for most of the impact stages. In the present research, a simple analytical method has been developed and implemented using the new contact model. In what follows, the new contact model is validated using published measurements of the coefficient of restitution.

Table 3.3: *Material properties for experiments by Kharaz and Gorham (2000)*

Material Property	Aluminium 2014-T4 [a]	AISI 1055 Steel [b]	Aluminium oxide [a]
Density [kg/m^3]	2800	7850	3960
Elastic Modulus [*GPa*]	72.4	205	370
Poisson's ratio [-]	0.33	0.29	0.22
Yield Strength [*MPa*]	235	560	-
Radius [*m*]	∞	∞	0.0025

[a] From Brake (2012)

[b] From www.Matweb.com (Accessed: 26-09-2014)

Kharaz and Gorham (2000) performed experiments on the normal impact of aluminium oxide spheres on aluminium and steel alloy slabs. The material properties for these experiments were not fully stated by Kharaz and Gorham (2000). Brake (2012) suggested use of the properties of Al 2014-T4 alloy since it has a similar hardness as the Al alloy used by Kharaz and Gorham (2000). Hence,

the properties of Al 2014-T4 and aluminium oxide provided by Brake (2012) have been used in the present simulations. Also, the properties of AISI 1055 steel have been used for the EN9 steel alloy used in the experiments of Kharaz and Gorham (2000). The material properties of the Al 2014-T4 alloy, AISI 1055 steel alloy, and aluminium oxide are shown in Table 3.3.

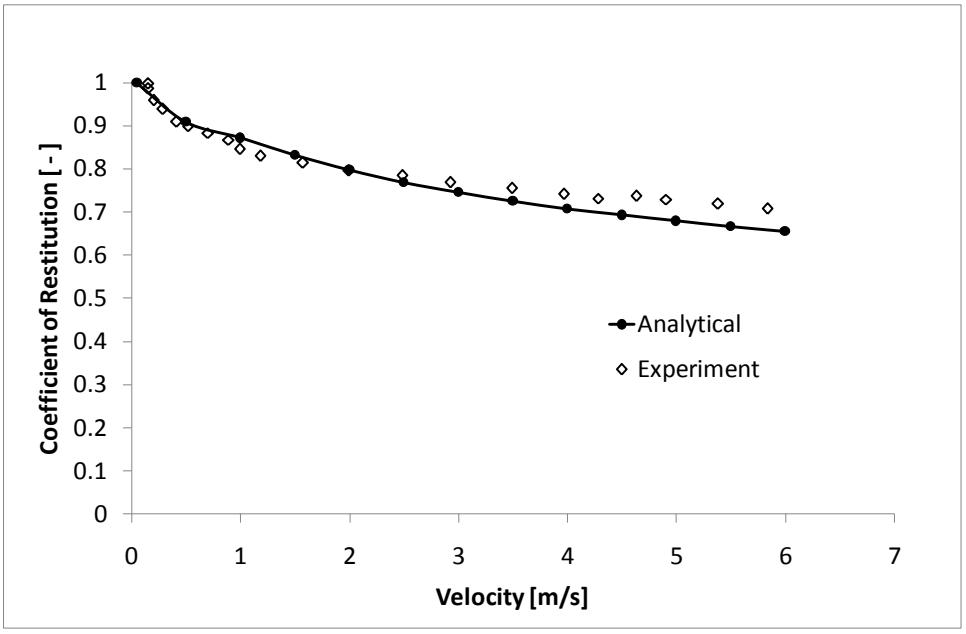

Figure 3.12: *Coefficient of restitution for impact of aluminium oxide sphere on AISI 1055 steel alloy slab.*

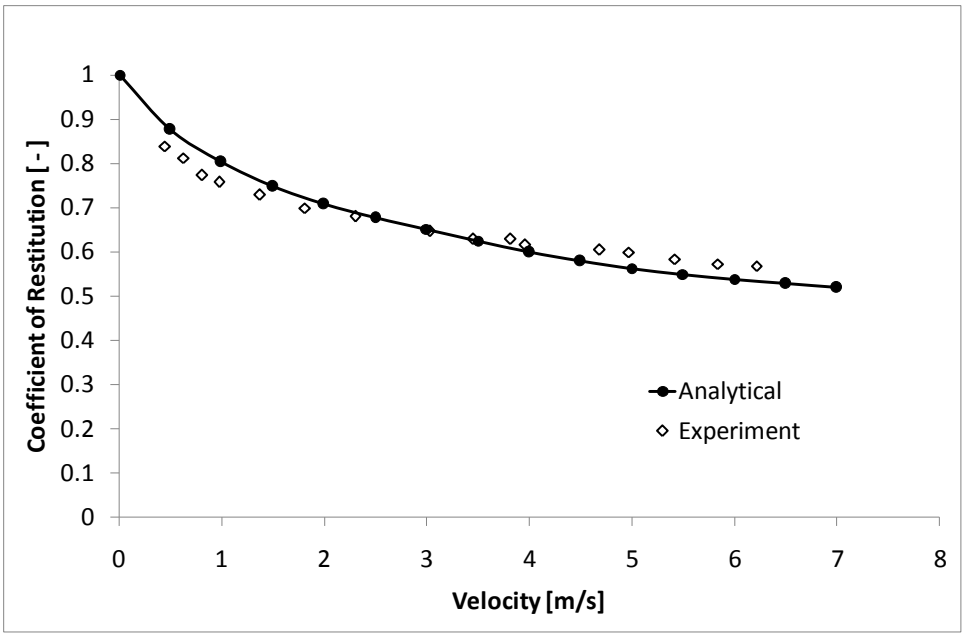

Figure 3.13: *Coefficient of restitution for impact of aluminium oxide sphere on aluminium T2014-T4 alloy slab.*

Figures 3.12 and 3.13 show the experimental results of Kharaz and Gorham (2000) in comparison with results obtained using the new contact model to calculate the coefficient of restitution. The maximum deviation of the model results from the experimental data is less than 10 percent for both impacts i.e. *aluminium oxide - aluminium alloy* and *aluminium oxide - steel alloy* impacts, and only a couple of points have this error margin. For most of the impact velocities, the present model predicts the experimental data with less than 5 per cent error. Hence, the results of the present model are in agreement with the experimental data of Kharaz and Gorham (2000).

Table 3.4: *Material properties for experiments by Mok and Duffy (1965)*

Material Property	Aluminium 6061	Steel C1018	Impactor (steel)
Density [kg/m^3]	2700 [a]	7870 [a]	7870 [a]
Elastic Modulus [GPa]	70.0	200	200
Poisson's ratio [-]	0.30	0.30	0.30
Yield Strength [MPa]	55.2 [a]	310 [a]	310 [a]
Radius [m]	∞	∞	0.00635

[a] From www.Matweb.com (Accessed: 26-09-2014)

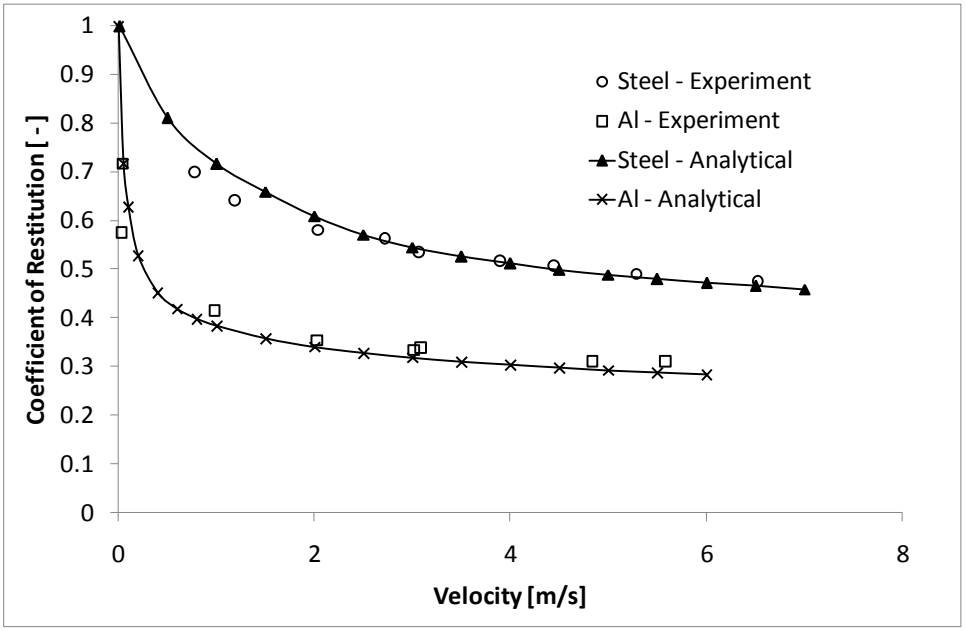

Figure 3.14: *Coefficient of restitution for impact of steel ball on Al 6061 and steel C1018 alloy slabs.*

A second experimental data published by Mok and Duffy (1965) for impacts of steel balls on aluminium and steel alloy slabs was compared with results obtained using the new contact model. The material properties of the specimens

used in the experiments are shown in Table 3.4. The results obtained using the new contact model and the experimental measurements of Mok and Duffy (1965) are shown in Figure 3.14. The figure reveals that the model results are in good agreement with the experimental measurements of Mok and Duffy (1965).

3.4 Chapter conclusions

Analytical models for contact indentation of elastic-elastoplastic-fully plastic materials are relatively few despite the fact that many engineering materials fall under this category. The published contact models for the indentation of elastic-elastoplastic-fully plastic materials are either finite element correlations that are case specific or quite complex analytical models. In this chapter, some of the previously published analytical contact models for indentation of elastic-elastoplastic-fully plastic materials were reviewed and discussed. A simple contact model that accounts for post-yield effects in the loading and restitution stages of the indentation of an elastic-elastoplastic-fully plastic material by a spherical indenter was formulated. In line with observations from previous experiments and FE results reported in the literature (Majeed *et al*, 2012), the elastoplastic loading regime was divided into two regions, nonlinear and linear, and modelled accordingly. Simple expressions have been derived for all constants in the present contact model and the constants can be completely evaluated from the geometric and material properties of the contact system. Also, the model for the restitution phase allows for unloading from any of the loading regimes. Results obtained from the simulation of the new contact model were compared with published static and dynamic indentation experiments, and the new contact model was found to give a good prediction of the experimental data. A key advantage of the new contact model is that it can be readily used for impact modelling and allows for computational tractability because all the stages for the loading and unloading are expressed in the form of Meyer's law (Big-Alabo *et al*, 2014a). The contact modelling approach used here is supported by the observation of Kharaz and Gorham (2000) that compliance models in the form of Meyer's law can be used to model the elastoplastic indentation of elastic-elastoplastic-fully plastic materials.

A simple algorithm for calculating the maximum indentation and contact force during half-space impact has been proposed in this study. The approach

applies energy balance principles and it is applicable to impact events that can be modelled using quasi-static assumptions i.e. low to medium velocity impacts.

An analytical method for calculating the coefficient of restitution during half-space impact was also presented. The method uses the closed-form integral of the governing equation for the restitution of a half-space impact and the maximum indentation and contact force values obtained from the energy balance algorithm to determine the rebound velocity. The value of the rebound velocity so obtained is used to calculate the coefficient of restitution from equation (3.67). The analytical method for calculating the coefficient of restitution can be applied to other contact models (Johnson, 1985; Stronge 2000a; Brake, 2012) for post-yield indentation of elastic-elastoplastic-perfectly plastic materials. The approach is simple and can be used to avoid the possible issues of solution convergence associated with numerical integration of the governing nonlinear equation of a half-space impact.

CHAPTER FOUR

IMPACT ANALYSIS OF RECTANGULAR PLATES SUBJECTED TO NORMAL IMPACT OF A RIGID SPHERICAL IMPACTOR

Chapter summary

This chapter presents analytical investigations on the *normal* (direction perpendicular to the plane of the plate) impact response of rectangular plates impacted by a rigid mass with spherical contact surface. The focus of this chapter is on: (a) the formulation of analytical models for the elastoplastic impact response of *transversely inflexible* (very thick) and *transversely flexible* (thin to moderately thick) rectangular plates, (b) the solution to these models that are generally in the form of nonlinear differential equations, and (c) the effect of different impact parameters on the elastoplastic impact response of transversely flexible rectangular plates. First, a review is presented of analytical modelling approaches for the normal impact of rigid blunt objects on compliant targets. Next, the elastoplastic impact response of transversely inflexible and flexible rectangular plates is investigated using the new contact model, previously presented in chapter 3, and also using other existing static contact models found in the literature to estimate the impact force. Additionally, the formulation and implementation of a new analytical solution algorithm for the solution of nonlinear impact models of transversely inflexible plates is presented. The implications for applying the solution algorithm to determine the impact response of transversely flexible plates are also discussed.

4.1 Review of analytical models for rigid object impact on compliant targets

According to Goldsmith (2001), the first attempt at formulating analytical models for the impact dynamics of a rigid blunt object striking a flexible structure, incorporating the interactions between the local and global deformation of the impact system, can be attributed to Sears (1908) and Timoshenko (1913). The elastic impact of a beam struck axially (Sears, 1908) and transversely (Timoshenko, 1913) by a spherical steel ball was modelled using

the Hertz contact theory and the beam deformation theory. This concept of combining local contact mechanics and structural mechanics in modelling rigid blunt object impact has since been extended to plates and shells. Several impact modelling approaches have been applied based on the response characteristics of the impact system, and these have been summarised in various papers (Abrate, 1998; 2001; 2011; and Chai and Zhu, 2011). Hence, the selection of an appropriate modelling approach for a given impact event is important if accurate results are to be obtained.

To determine the right impact modelling approach for a particular impact event, a means of classifying the impact response must first be established. There are different types of impact response classification reported in the literature. One early classification is based on the impact velocity, and it is used to classify impact events as low-, medium-, and high-velocity impact (Chai and Zhu, 2011). For a low-velocity impact, there is no visible damage although localised internal damage may occur, whereas there is visible and easily detectable large damage during high-velocity impact that may sometimes include perforation and tear. For medium-velocity impact, there may be a small visible level of damage but internal damage is likely to be considerably larger.

Another classification is based on impact duration. According to this classification, the following impact responses are identified (Olsson, 2000; Chai and Zhu, 2011):

(i) When the ratio of the impact duration to the time taken for the first stress wave to propagate through the thickness of the structure is less than or approximately equal to one, the impact response is dominated by 3-D wave propagation. This type of impact response is normally associated with ballistic impacts, which causes visible damage and sometimes perforation of the target.

(ii) When the ratio of the impact duration to the time taken for vibration waves to reach the boundary is equal to, or just greater than one, the impact response is dominated by shear and flexural waves and is a dynamic event. Typical cases involve impact on flexible aero-structures due to hailstone and runway debris.

(iii) When the ratio of the impact duration to the time taken for vibration waves to reach the boundary is far greater than one, the impact response is dominated by the lowest mode of vibration. The response can be modelled

using quasi-static analysis, and a typical case is drop-weight impact normally used in experimental investigations.

Olsson (2000) argued that the limits of the impact velocity criterion is not clearly defined, and suggested the use of a mass ratio instead i.e. impactor/plate mass ratio (μ_m). Based on Olsson's mass criterion, the impact can be divided into small, intermediate and large mass impact. For small mass impact $\mu_m < 1/5$, for large mass impact $\mu_m > 2$, and for intermediate mass impact the mass ratio lies in the range $1/5 < \mu_m < 2$. The response is wave-controlled for small mass impacts and can be modelled using the closed-form solution in Olsson (1992). For large mass impacts, the response is fully boundary-controlled and can be modelled based on quasi-static assumptions using the energy model (Abrate, 1998; Chai and Zhu, 2011) and/or spring-mass model (Chai and Zhu, 2011). For intermediate mass impacts, the response is dominated by highly dynamic interactions between flexural waves, shear waves and local indentation. A model that accounts for all these effects is required for accurate analysis. The mass criterion of Olsson is limited to impact responses in which the impact duration is much longer than the transition time for the through-the-thickness waves, i.e. class (ii) and (iii) in the impact duration classification system described above.

Christoforou and Yigit (1995) used a normalisation technique to investigate the parameters that influence the impact response of a beam based on an elastic-plastic contact law. By normalising the differential equations governing the transverse impact of the beam, all the parameters influencing the impact response were identified. Four non-dimensional parameters that influence the impact response of the beam were obtained, of which the impactor-beam mass ratio was one. The study showed that the mass ratio is not the only parameter influencing the system's impact response and when considered alone, it is not sufficient information for characterisation of impact events. Christoforou and Yigit (1995) concluded that the normalisation technique can be used to obtain the parameters that influence an impact event and these parameters can be used for scaling purposes.

Yigit and Christoforou (1995) used the normalisation technique to determine the parameters that influence the impact response of a beam based on the linearised version of an elastic-plastic contact law. Three non-dimensional parameters that influence the impact response of the beam were

identified in that study. The parameters were regrouped into a single non-dimensional parameter called the *dynamic impact number* (DIN). The latter was used to classify the impact response as locally dominated, quasi-static, or dynamic. The DIN was found to vary from zero to one. A value of zero represents a locally-dominated response – the so called half-space impact – while a value of one represents a quasi-static response. When the DIN is between 0 and 1, the response is classified as dynamic. Also, a *dynamic ratio* was defined as the ratio of the maximum impact force obtained from the dynamic solution to the maximum impact force obtained from an equivalent half-space solution, and this dynamic ratio was found to be a dependent on the DIN.

Christoforou and Yigit (1998a) used the normalisation technique to investigate the impact response of a plate based on a linearised elastic-plastic contact law. The analysis showed that the impact response of the plate was governed by two non-dimensional parameters related to the dynamic ratio; the relative stiffness (λ), which accounts for the mechanical stiffness effect, and the loss factor (ζ), which accounts for the material damping effect. A characterisation diagram was developed which showed that the relationship between the dynamic ratio and the loss factor can be used to characterise the response of the plate for different plate stiffnesses. The characterisation diagram was used to classify the impact response of the plate as local, transitional (dynamic), and fully global (quasi-static). The relative stiffness was found to govern the quasi-static response while the loss factor governed the infinite plate (wave-controlled or initial) response. The local response was shown to be governed by an additional parameter; a non-dimensional velocity called the '*characteristic impact parameter*'. The characteristic impact parameter was normalised to unity in this analysis. The transitional response was governed by all three parameters i.e. relative stiffness, the loss factor and characteristic impact parameter. However, the characterisation diagram was obtained based on a linearised elastic-plastic contact law, an approximation of actual contact behaviour, which does not account for certain details of the impact response (e.g. permanent indentation) and is capable of introducing significant errors in the estimation of the impact response history (Yigit and Christoforou, 1995).

In conclusion, there is no universal impact response classification parameter or approach. Although the classification approaches based on a single

variable such as impact velocity, time, mass, and energy have proven to be useful, a combination of factors obtained using the normalisation technique shows more potential and can provide a wider scope of application. Nevertheless, all the classification techniques considered here are important and knowledge of the various techniques is necessary when deciding the impact modelling approach to be used for a particular impact event. The characteristics and solution methods for the impact response of plates, based on the different classification methods described in the above review, are summarised in Figure 4.1. Chia and Zhu (2011) presented a similar classification diagram but the one presented in Figure 4.1 is more detailed. The decision boxes in Figure 4.1 are used to select the classification method. For example, the first decision box raises the question: Is the classification based on impact velocity?

Moving now to modelling approaches, Abrate (1998, 2001) presented an overview of various impact models and grouped these models into four categories namely: (a) spring-mass models, (b) energy-balance models, (c) complete models, and (d) infinite plate models. These models are now briefly explained, and their applications and limitations are discussed.

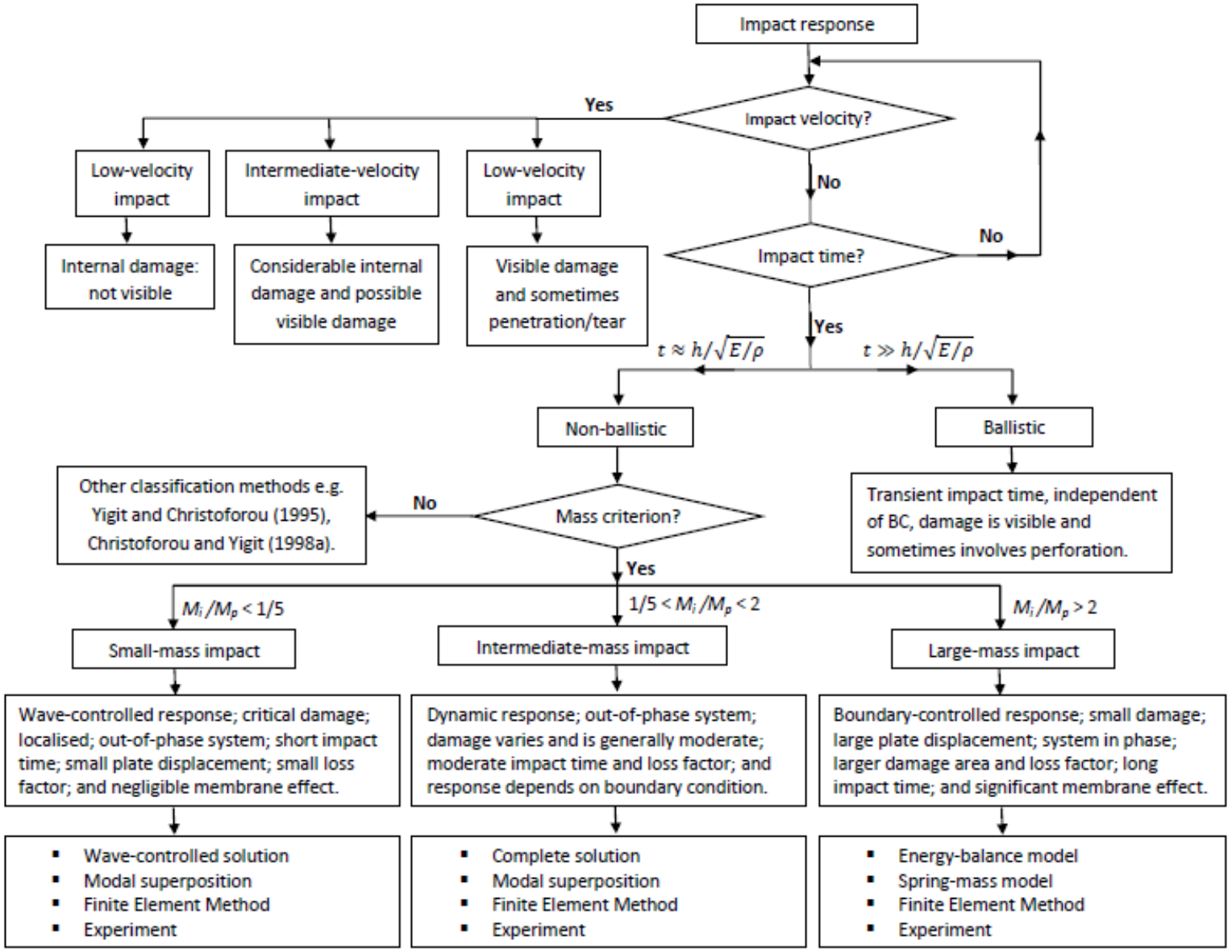

Figure 4.1: *Characteristics and solution methods for different impact classifications.*

4.1.1 The spring-mass model

According to this model, the impactor and plate are represented by equivalent rigid masses while the plate and contact stiffnesses are represented by equivalent springs. In the complete two-degree of freedom (DOF) model, there are two nonlinear springs (for the contact and membrane stiffnesses) and two linear springs (for the bending and shear stiffnesses) – see Figure 4.2a. The single-DOF spring-mass model is normally used for a case where the local indentation is negligible i.e. quasi-static bending response (Figure 4.2b) or the vibration response of the plate is negligible i.e. half-space impact response (Figure 4.2c). Anderson (2005) used a single-DOF model to study the response of composite sandwich laminates to large mass impact. Olsson (2002) studied the response of a composite sandwich plate to a small mass impact using a single-DOF spring-mass model with a dashpot. Half-space impact analysis using a single-DOF model has been discussed by Abrate (1998, 2001), and can be used to validate the dynamic indentation test results (Brake, 2012). Most studies that use the 2-DOF spring-mass system to model the impact response of a plate ignore the membrane stiffness i.e. $K_m = 0$ (Abrate, 1998), and in some studies the contact stiffness is linearised (Khalili *et al*, 2007a; 2007b).

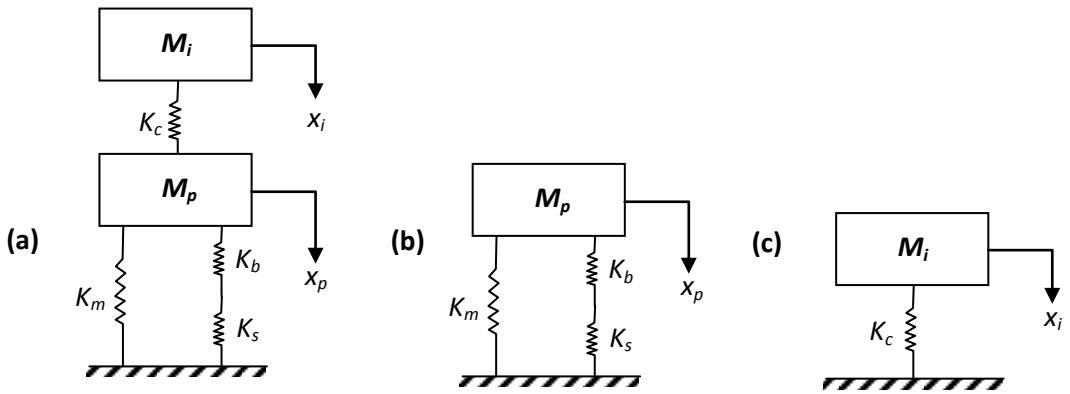

Figure 4.2: *Spring-mass models (a) Complete 2-DOF (b) SDOF for quasi-static impact (c) SDOF for half-space impact.*

Equations for spring-mass models

$$m_p \ddot{x}_p + K_{bs} x_p + K_m x_p^3 - F = 0 \tag{4.1}$$

$$m_i \ddot{x}_i + F = 0 \tag{4.2}$$

$$F = K_c \delta^q \tag{4.3}$$

where $\delta = x_i - x_p$ is the indentation, q is the contact law power exponent which is equal to 3/2 for Hertzian contact, and $1/K_{bs} = 1/K_b + 1/K_s$. The subscripts i and p represent the impactor and plate respectively. The formulas for the stiffnesses (K_b, K_s, K_m) can be found in Olsson (2001) and Chai and Zhu (2011). Equations (4.1 – 4.3) are the complete set of equations for the 2-DOF spring-mass system (Figure 4.2a). For Figure 4.2b, equations (4.1) and (4.3) are used with the assumption that $\ddot{x}_p \cong 0$ for quasi-static analysis. For Figure 4.2c, equations (4.2) and (4.3) are used with the assumption that $x_p \cong 0$ for half-space analysis.

4.1.2 The energy-balance model

The energy-balance model is normally based on the assumption that both the local deformation and bending of the plate occur quasi-statically. Therefore, at the maximum indentation the velocity of the impactor is zero and the initial kinetic energy of the impactor is completely transferred to the plate without any loss. The initial kinetic energy of the impactor is converted into the following energy components in the structure: bending, shear, membrane, contact and damage energies (Abrate, 1998). Mathematically, we can write:

$$\frac{1}{2} m_i V_0^2 = E_b + E_s + E_m + E_c + E_d \tag{4.4}$$

A valid assumption for quasi-static bending of a plate is that its inertia can be neglected. Hence, from equation (4.1):

$$F = K_{bs} \bar{x}_p + K_m \bar{x}_p^3 \tag{4.5}$$

where $\bar{x}_p$ is the maximum displacement of the plate at the impact point. Some impact analyses are carried out up to damage initiation so that E_d is usually neglected when using equation (4.4) (Abrate, 1998). The contact force obtained by neglecting E_d can be used to determine the onset and propagation of delamination damage (Olsson, 2001; 2002). Using equations (4.3 – 4.5), applying the Hertz contact model, and assuming that $E_d = 0$ it can be shown that (Abrate, 1998; Olsson, 2002):

$$\frac{1}{2} m_i V_0^2 = \frac{1}{2} K_{bs} \bar{x}_p^2 + \frac{1}{4} K_m \bar{x}_p^4 + \frac{2}{5} K_c^{-2/3} \left(K_{bs} \bar{x}_p + K_m \bar{x}_p^3 \right)^{5/3} \tag{4.6}$$

Equation (4.6) can be solved numerically to obtain the maximum displacement of the plate, from which the maximum contact force and indentation can be obtained using equations (4.5) and (4.3) respectively. The energy-balance model

is used where the contact force history is unimportant and the impact response of the plate is not significantly affected by the contact law. Foo *et al* (2011) used the energy-balance approach to predict the low-velocity impact response of a sandwich composite plate, while Olsson (2002) used the energy-balance approach to predict the impact response and damage in sandwich panels.

4.1.3 The infinite plate model

The infinite plate model was originally formulated by Zener (1941) as an approximate closed-form solution for the initial response of the elastic impact of an isotropic plate. It was later extended to orthotropic plates by Olsson (1992), who applied it to study the elastic impact of orthotropic composite laminates. Since this model predicts the initial impact response before the first vibration waves are reflected back from the boundary, the infinite plate response is independent of the boundary conditions. The model suggests that the impact response of an infinite plate is governed by a single parameter called the inelastic parameter (Zener, 1941; Olsson, 1992). A more general form of the infinite plate model derivation based on Meyer's law has been formulated (Abrate, 1998; Chai and Zhu, 2011).

When the inelastic parameter has a value of zero the impact is that of a half-space. A value between zero and one represents an inelastic impact, and values larger than one represent impact with large indentation and damage. Chai and Zhu (2011) observed that the impact duration approaches infinity for values of the inelastic parameter greater than one, and suggested that the infinite plate model should be used only for cases where the inelastic parameter is less than one. A possible explanation for this apparent dilemma is that the impact response becomes boundary-controlled when the inelastic parameter is much greater than one (Abrate, 2001). Hence, the solution of the infinite plate response breaks down, and in this case, it appears in the form of infinite impact duration. A limitation of the infinite plate model is that it can only be used for the analysis of wave-controlled impacts. Zheng and Binienda (2007) studied the effect of permanent indentation on the delamination threshold for small mass impact of laminated plates by using the infinite plate model and a linearised elastic-plastic contact model.

4.1.4 The complete model

The complete model accounts for the dynamics of the plate, the local contact mechanics of the impact system, and the dynamics of the projectile. Plate deformation theories such as classical laminate plate theory (CLPT), shear deformation theories (e.g. first-order shear deformation plate theory (FSDPT) and higher-order shear deformation plate theory (HSDPT)), and layerwise theories are used to model the displacement of the plate, while an appropriate compliance model such as the models discussed in chapter three can be used to model the contact mechanics. The dynamics of the impactor is modelled using equation (4.2). All three models (plate, impactor, and contact) must be solved simultaneously to determine the system's impact response. During solid object impact, the primary interest is usually focussed on deformation of the plate and therefore, the dynamics of the impactor is not usually investigated. However, the impactor shape, mass and velocity can influence the impact response of the plate (Nosier *et al*, 1994; Abrate, 1998; Goldsmith, 2001; Chai and Zhu, 2011).

Khalili *et al* (2007a; 2007b) used a complete model to determine the dynamic response of a smart hybrid composite plate subjected to low-velocity impact. The impact models were formulated based on the FSDPT of a rectangular composite plate with embedded SMA wires, the 2-DOF spring-mass model, and a linearised contact model. The 2-DOF spring-mass model was solved simultaneously with the linearised contact model to determine the impact force history, which was then used as an input to the dynamic model of the plate. Christoforou and Swanson (1991) studied the impact response of composite plates using a complete model. The impact model used in this study combined the FSDPT of composite plates with a linearised contact model, and a closed-form solution of the impact response was obtained using the Laplace technique. Again, the impact response of composite plates was also investigated by Carvalho and Guedes Soares (1996) using the FSDPT of composite plates and the Hertz contact law. A nonlinear integral equation was obtained and solved using the Newmark integration method. Results obtained from the numerical integration method were compared with those obtained from the closed-form solution of Christoforou and Swanson (1991), and it was observed that both methods were in good agreement. Nosier *et al* (1994) studied the impact response of composite plates subjected to low-velocity impact using a layerwise

plate theory. The layerwise theory was used together with a modified Hertz contact law to model the impact response of the composite plate. The modified Hertz law accounts for permanent indentation effects only during the unloading response. The impact model was formulated into an integral equation which was solved by a numerical scheme that was called time-finite-element. It was concluded that the layerwise theory provides more accurate and detailed results for the interlaminar stresses when compared with the equivalent single-layer theories (CLPT, FSDPT, and HSDPT). The complete modelling approach gives a more accurate description of an impact event, but comes at the cost of increased computational expenses.

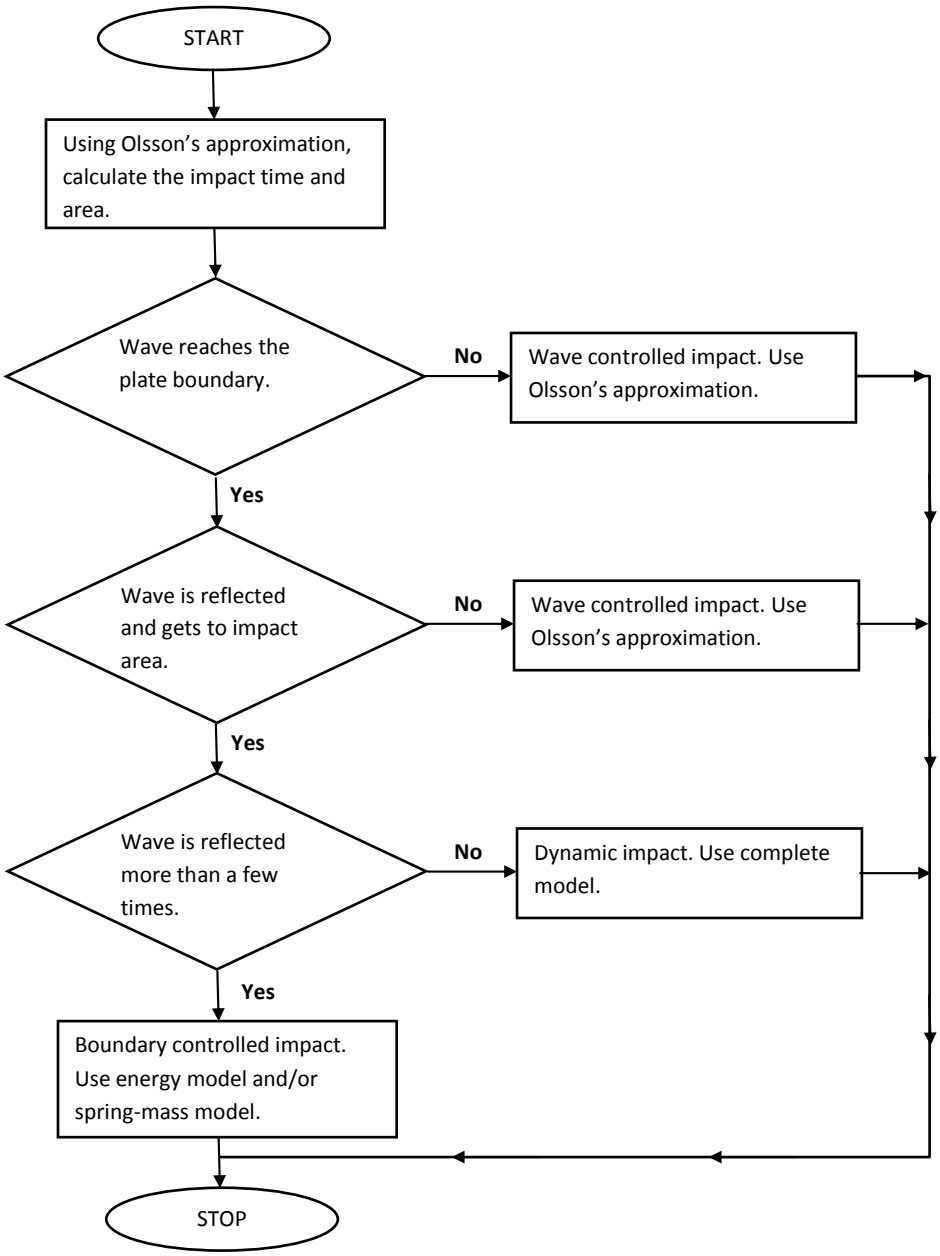

Figure 4.3: *Method for selection of impact model.*

Abrate (2001) proposed a method for selecting an appropriate modelling approach for a given impact event from the four models described above. The selection method is based on the application of 'Olsson's approximation' as an initial criterion, and is summarised in the flowchart diagram in Figure 4.3.

In the present study, the response of rectangular plates subjected to elastoplastic impact of a rigid impactor with spherical contact surface has been examined. Quasi-static impact events during which the influence of the local deformation is negligible have not been considered here. The impact response of transversely inflexible and flexible plates has been investigated analytically, and the solutions to the models have been obtained primarily by direct numerical integration using the NDSolve function in *Mathematica*™ (see the Wolfram Documentation Centre for details on the NDSolve function (Wolfram Research Inc., 2012)). Additionally, a new stable and fast-converging algorithm for the solution of nonlinear impact models of transversely inflexible plates has been formulated and used to solve selected impact examples. In order to perform a detailed investigation, the complete modelling approach has been used to determine the impact response of transversely flexible plates. Parametric studies have been carried out to examine the effect of various impact parameters on the elastoplastic impact response of a transversely flexible trimorph plate with a view to establishing a possible impact parameter that could be realistically altered for active control of the impact response.

4.2 Elastoplastic impact response analysis of transversely inflexible rectangular plates

A transversely inflexible plate is a very thick plate that undergoes negligible flexural oscillations when subjected to a forced excitation e.g. a rectangular metallic slab. However, it is locally compliant to indentation. The local indentation of the plate is equal to the displacement of the impactor, and the boundary conditions do not affect the impact response. In this case, the impact response of the plate can be approximated by the well-known half-space solution. Half-space impact conditions have been used in many experimental investigations (Tillet, 1954; Lifshitz and Kolsky, 1964; Mok and Duffy, 1965; Kharaz and Gorham, 2000) and finite element studies (Hardy *et al*, 1971; Li *et al*, 2000; Wu *et al*, 2003; 2005). Analytical investigations can be used to validate

such experimental measurements and finite element results. The governing equation of a half-space impact was given in equation (3.53) as:

$$m_i\ddot{\delta} + F = 0 \tag{4.7}$$

where m is the mass of the impactor; δ is the indentation of the plate, which is equal to the displacement of the impactor, and the initial conditions are $\delta(0) = 0$, $\dot{\delta}(0) = V_0$; V_0 is the initial impact velocity, F is the impact force and it is subject to the restriction in equation (3.54).

Numerical solutions of Equation (4.7) can be readily obtained when the contact force is estimated from a Meyer-type compliance model (Goldsmith, 2001). A key advantage of the new contact model formulated in Section 3.2 is that Meyer-type compliance models have been used to model all the loading and unloading regimes involved, especially the elastoplastic loading regime. This means that numerical solutions can be obtained without difficulty when the new contact model is used to estimate the impact force of an elastoplastic half-space impact. Note that the impact analysis in this section is restricted to normal impacts where rate effects can be neglected and other impact energy dissipation mechanisms such as friction and non-recoverable elastic waves are negligible. The dynamic equations representing each impact stage and the initial conditions for solving these equations are formulated based on the new contact model as shown.

Elastic impact loading

$$m_i\ddot{\delta} + K_h\delta^{3/2} = 0 \tag{4.8}$$

Initial conditions: $\delta(0) = 0; \dot{\delta}(0) = V_0$.

Elastoplastic impact loading

- Nonlinear elastoplastic impact loading

$$m_i\ddot{\delta} + K_h\left(\delta - \delta_y\right)^{3/2} + K_h\delta_y^{3/2} = 0 \tag{4.9}$$

Initial conditions: $\delta\left(t_y\right) = \delta_y; \dot{\delta}\left(t_y\right) = V_y$. The time to yield is defined by t_y and is obtained by solving the first initial condition using the solution to equation (4.8). V_y is the velocity at t_y and is calculated from equation (3.61).

- Linear elastoplastic impact loading

$$m_i\ddot{\delta} + K_l\left(\delta - \delta_{tep}\right) + K_h\left[\left(\delta_{tep} - \delta_y\right)^{3/2} + \delta_y^{3/2}\right] = 0 \tag{4.10}$$

Initial conditions: $\delta(t_{tep}) = \delta_{tep}; \dot{\delta}(t_{tep}) = V_{tep}$. The time to the transition point in the elastoplastic loading regime is defined by t_{tep} and is obtained by solving the first initial condition using the solution to equation (4.9). V_{tep} is the velocity at t_{tep} and is calculated from equation (3.64).

Fully plastic impact loading response

$$m_i\ddot{\delta} + K_p(\delta - \delta_p) + F_{\delta=\delta_p} = 0 \tag{4.11}$$

Initial conditions: $\delta(t_p) = \delta_p; \dot{\delta}(t_p) = V_p$. The time to the onset of the fully plastic loading is defined by t_p and is obtained by solving the first initial condition using the solution to equation (4.10). V_p is the velocity at t_p and is calculated from equation (3.65).

Restitution (unloading) stage

$$m_i\ddot{\delta} + K_u(\delta - \delta_f)^{3/2} = 0 \tag{4.12}$$

Initial conditions: $\delta(t_m) = \delta_m; \dot{\delta}(t_m) = 0$. Maximum conditions are defined at time t_m and this is obtained by solving the first initial condition using the solution to equation (4.11). The maximum indentation, δ_m, is obtained from the algorithm presented in Figure 3.10. Expressions for calculating all the contact parameters in equations (4.8 – 4.12) are given in Section 3.2.

Equations (4.8 – 4.12) were used to investigate the normal impact of a tungsten carbide ball on a rectangular mild steel slab. The material properties of the impactor are: density = 14500 [kg/m^3], Young modulus = 600 [*GPa*], and Poisson's ratio = 0.28 [-]. The material properties of the mild steel are: density = 7850 [kg/m^3], Young modulus = 210 [*GPa*], Poisson's ratio = 0.30 [-], and yield strength = 1000 [*MPa*]. The diameter of the spherical impactor is 20 [*mm*] and the mass of the projectile was calculated to be 0.06074 [*kg*]. Unless otherwise stated, these material and geometrical properties have been used to study the impact response of transversely inflexible plates.

Two impact velocities were considered, case 1: 0.5 [m/s] and case 2: 5.0 [m/s]. The impact force, indentation depth and velocity of the nonlinear and linear elastoplastic impact events are shown as functions of time in Figure 4.4 (case 1) and Figure 4.5a (case 2) respectively. The impact responses were obtained through direct numerical integration of equations (4.8 – 4.10, 4.12) using the NDSolve function in *Mathematica*™. The legend for Figures 4.4 – 4.8 are given in Table 4.1. The line colours represent the various impact stages while

the line styles represent the impact histories for the indentation (short-dash line), velocity (dotted-line) and impact force (solid line). These impact cases were investigated by Big-Alabo *et al* (2014a) using the new contact model. The expressions for the deformed effective radius used by Big-Alabo *et al* (2014a) are different from the expressions used in the present analysis as explained in Section 3.2. Therefore, the impact durations, permanent indentations, final kinetic energies and coefficients of restitution obtained in the present analysis are different from the results obtained in Big-Alabo *et al* (2014a). Since the present analysis gives a better estimate of the unloading response as explained in Section 3.2, the results shown here are an improvement on the results of Big-Alabo *et al* (2014a).

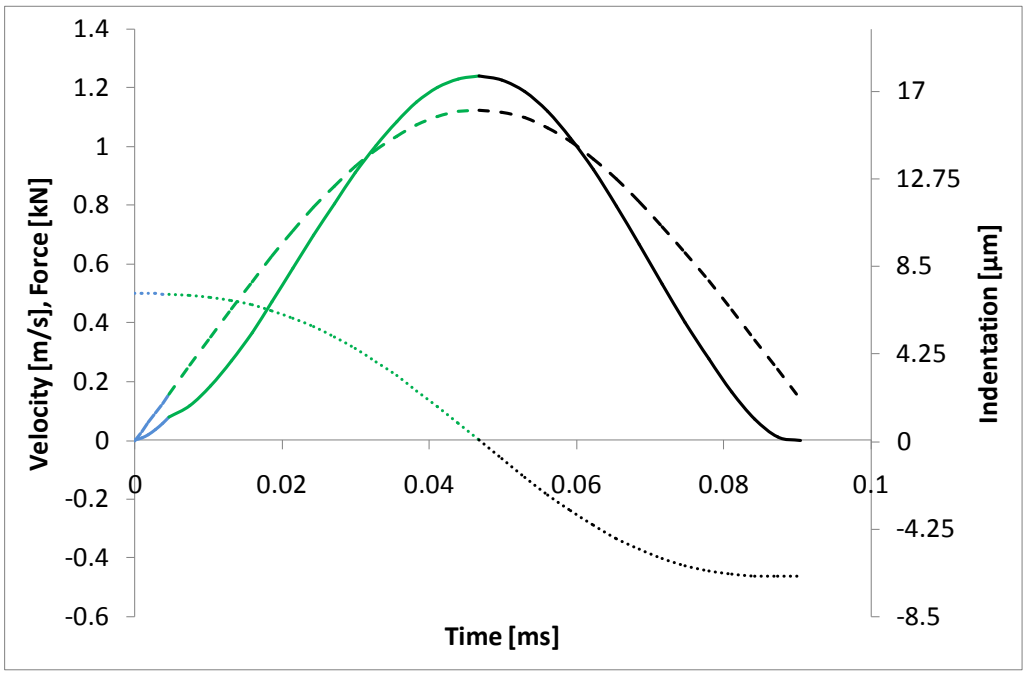

Figure 4.4: *Impact response of a steel slab dynamically loaded by a tungsten carbide ball into the nonlinear elastoplastic stage;* $V_0 = 0.5\ [m/s]$.

Table 4.1: *Legend for impact response of transversely inflexible plate*

Description	Plot line-type
Indentation (Short-dash line)	– – – – – –
Velocity (Dotted line)	.....
Force (Solid line)	———
Elastic response (Blue line)	———
Nonlinear elastoplastic response (Green line)	———
Linear elastoplastic response (Red line)	———
Restitution response (Black line)	———

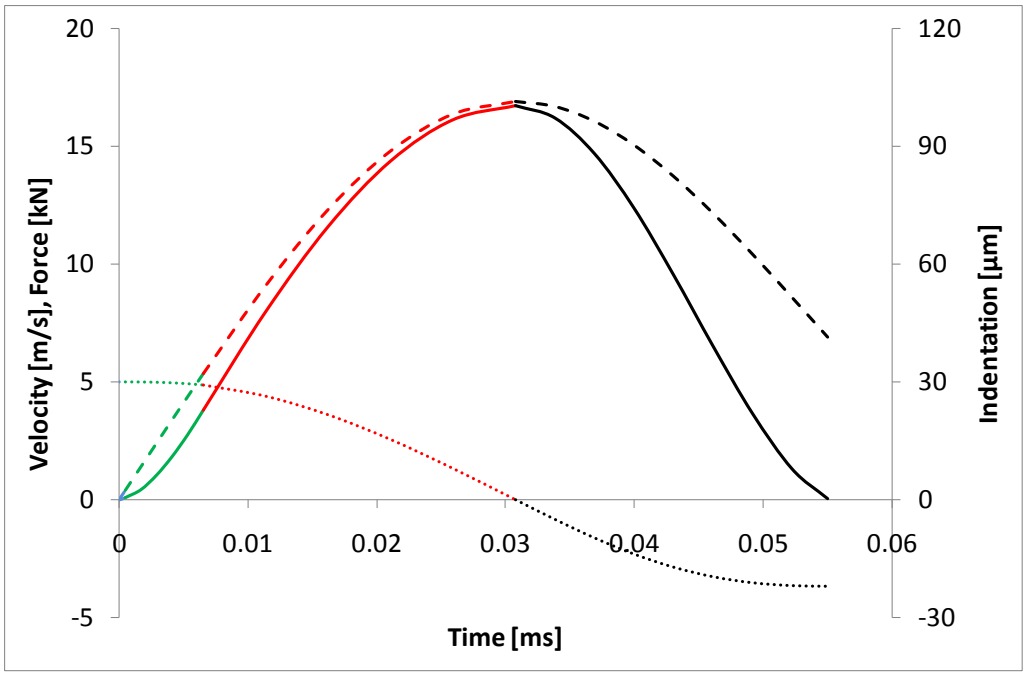

Figure 4.5a: *Impact response of a steel slab dynamically loaded by a tungsten carbide ball into the linear elastoplastic stage;* $V_0 = 5.0\ [m/s]$.

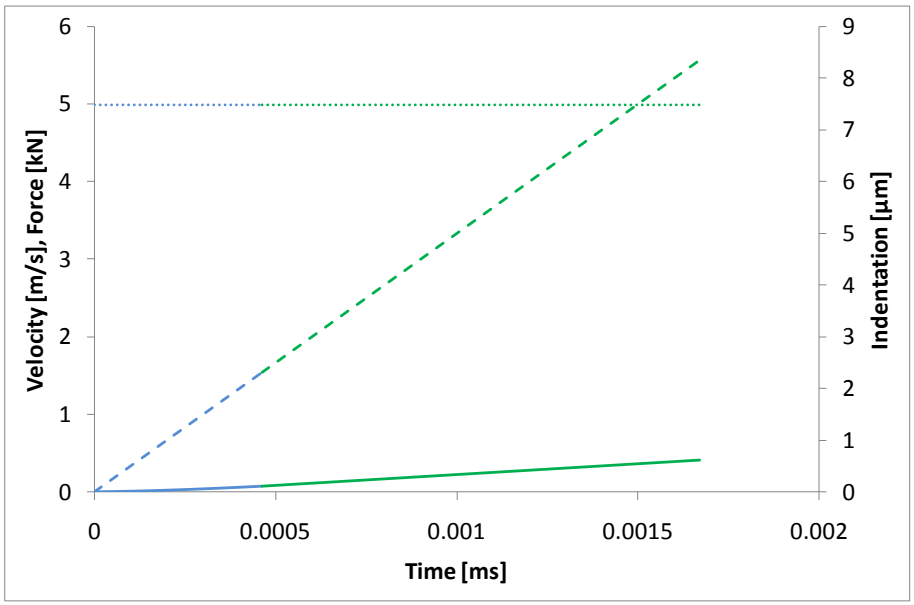

Figure 4.5b: *Initial impact response of a steel slab dynamically loaded by a tungsten carbide ball showing the elastic stage;* $V_0 = 5.0\ [m/s]$.

The impact velocity of 0.5 $[m/s]$ resulted in a maximum penetration with $\delta_m/\delta_y \cong 7$ which reaches the nonlinear elastoplastic loading stage, while the impact velocity of 5.0 $[m/s]$ resulted in a maximum penetration with $\delta_m/\delta_y \cong 44$ which reaches the linear elastoplastic loading stage. The elastic loading response

is seen to be visible when $V_0 = 0.5\ [m/s]$ (Figure 4.4), and cannot be neglected without introducing considerable errors in the estimation of the impact histories. When $V_0 = 5.0\ [m/s]$ the purely elastic response is barely noticeable compared to the rest of the loading response (Figure 4.5a) and can be neglected. Figure 4.5b shows the initial response when $V_0 = 5.0\ [m/s]$ and reveals that the elastic response has a negligible influence on the loading response since the initial impact velocity barely changes at the end of the elastic loading response ($V_y = 4.99976[m/s]$).

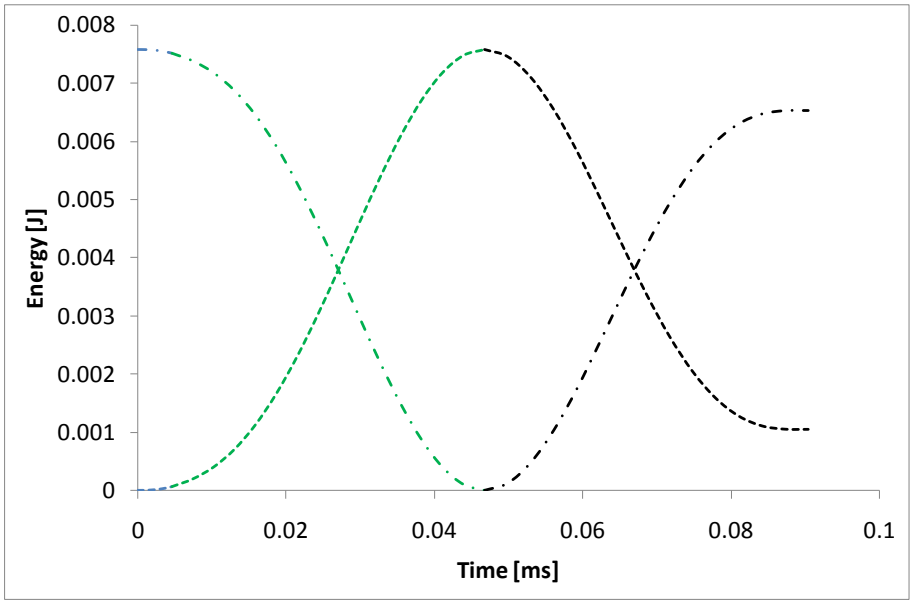

Figure 4.6: *Energy evolution during impact of tungsten carbide ball on a mild steel slab for* $V_0 = 0.5\ [m/s]$. *Kinetic energy: dash-dot line; Work done: short-dash line.*

The evolution of the kinetic energy of the impactor and work done on the target by the impact force, in the loading and restitution stages, for initial impact velocities of 0.5 $[m/s]$ and 5.0 $[m/s]$ are shown in Figures 4.6 and 4.7 respectively. In Figure 4.6, 13.8% of the initial KE of the impactor is dissipated as plastic work whereas 45.9% is dissipated in Figure 4.7. The implication is that increasing the initial impact velocity results in the dissipation of more of the impactor's initial KE as non-recoverable plastic work. This observation agrees with the finding of Christoforou and Yigit (1998a) that a half-space impact response is strongly influenced by the normalised impact velocity. Other results for the impact response of the steel slab are summarised in Table 4.2, and the

variation of the coefficient of restitution with initial impact velocity is shown in Figure 4.8.

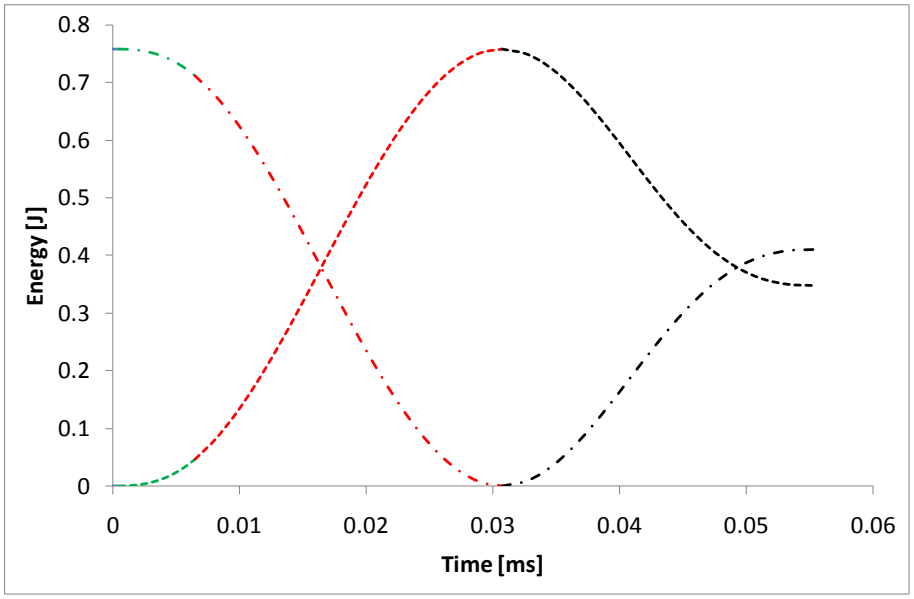

Figure 4.7: *Energy evolution during impact of tungsten carbide ball on a mild steel for* $V_0 = 5[m/s]$. *Kinetic energy: dash-dot line; Work done: short-dash line.*

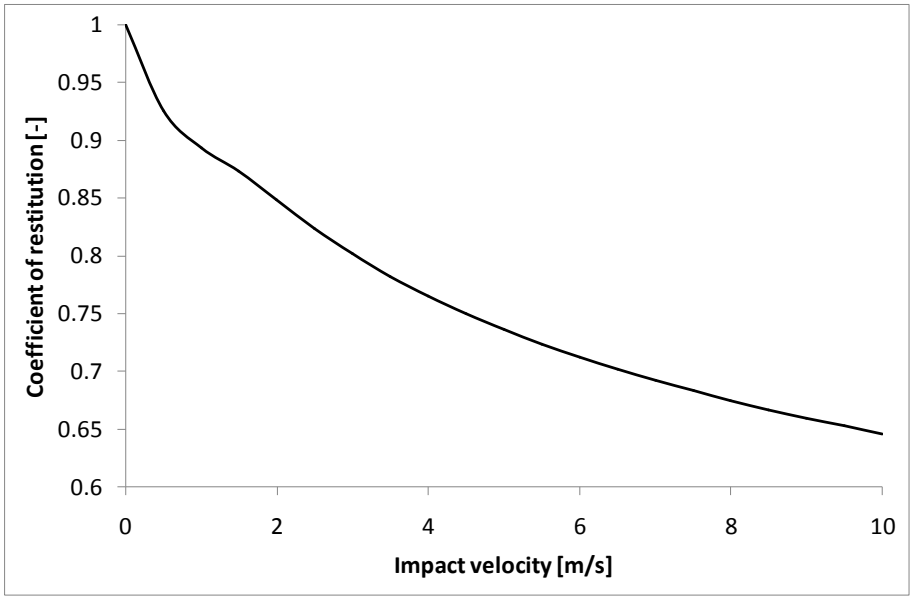

Figure 4.8: *Coefficient of restitution for impact of tungsten carbide ball on a mild steel slab.*

Table 4.2: *Results of the impact response of steel*

Impact parameters	Results	
	$V_0 = 0.5[m/s]$	$V_0 = 5.0[m/s]$
Impact duration [μs]	90.41	55.31
Time at maximum indentation [μs]	46.76	30.72
Permanent indentation [μm]	2.05	40.18
Maximum indentation [μm]	16.10	101.62
Maximum impact force [kN]	1.24	16.73
Final rebound velocity [m/s]	0.46	3.68
Coefficient of restitution [-]	0.93	0.74

4.3 Algorithm for the solution of the impact model of transversely inflexible rectangular plates

The impact response of a transversely inflexible plate (half-space) has been modelled using the new contact model presented in Section 3.2. Solutions of the impact models (equations 4.8 – 4.12) have been obtained by direct numerical integration. The new contact model uses Meyer-type compliance models to estimate the force during the loading and unloading stages of an impact event. Half-space impact models in which the impact force is estimated by Meyer-type compliance models can be readily solved by numerical integration (Goldsmith, 2001). The case is different when compliance models that cannot be expressed in terms of Meyer's law are used to estimate the impact force. This is because the convergence of a conventional numerical scheme is not always guaranteed in this context (Big-Alabo *et al*, 2014a).

Meyer's law is generally regarded as the canonical form (i.e. standard form) for most static contact models (Goldsmith, 2001). Yet, many existing elastoplastic contact loading models cannot be expressed in terms of Meyer's law (Stronge, 2000a, Li *et al*, 2002; Jackson and Green, 2005; Brake, 2012). This may explain why the application of these models to estimate the indentation, velocity and force histories during half-space impact do not appear in the literature despite their wide use for static indentation analyses. Therefore, there is a need to develop either Meyer-type compliance models for the elastoplastic loading regime (which has been done in Section 3.2) or more efficient solution algorithms that could be used to solve the nonlinear models of an elastoplastic half-space impact irrespective of the compliance model that has been used to estimate the impact force.

Goldsmith (2001) used a small-increment numerical integration scheme based on discretisation of the nonlinear force in the time-domain to obtain the impact histories of an elastic impact from the nonlinear integral form of equation (4.8). The computational effort and stability of this scheme is a function of the nature of the nonlinearity in the differential equation and the time-increment used. Abrate (1998) used the Newmark time integration scheme for the solution of the impact response of an elastic half-space. The Newmark scheme is a direct numerical integration scheme that involves discretisation of the displacement, velocity, and acceleration in the time-domain. In order to ensure convergence of the solution the Newmark scheme normally requires the application of a fine-tuned time increment and involves many iteration steps. Majeed *et al* (2012) used a nonlinear finite element method to obtain the force-time history of an elastoplastic half-space impact; the finite element method results were found to be in good agreement with the results obtained from the simulation of equation (4.7) using their contact model. Also, numerical integration solvers in computational software packages such as the NDSolve function in *Mathematica*™ can be used to solve equation (4.7) when F is a nonlinear function of δ as demonstrated in Figures 4.4 – 4.7. The NDSolve function solves differential equations numerically using an optimised routine that automatically selects an integration method from a list of embedded conventional methods such that convergence and computational efficiency are ensured. Given that the NDSolve function uses conventional numerical methods (Wolfram Research Inc., 2012) e.g. explicit Runge-Kutta, implicit Runge-Kutta, and predictor-corrector Adams method, the issues of stability and convergence inherent in these methods spring-up sometimes in the output of the function. Consequently, the NDSolve function does not always converge on a solution in all cases.

The problem with the finite element method and existing numerical integration approaches is that they are conditionally stable, often complicated, and usually require a large number of iterations to obtain accurate results and are therefore often difficult to verify by means of hand calculation. In this section, a new iterative solution algorithm called the *Force-Indentation Linearisation Method* (FILM) is presented. The FILM uses closed-form solutions derived from piecewise linearisation of the nonlinear impact force to determine the impact histories of a half-space impact. In contrast to the conventional

numerical schemes in which key variables are discretised in the time-domain, the FILM discretises the impact force with respect to indentation depth. The limitations associated with the numerical methods and finite element methods as stated above are completely eliminated by the FILM.

The FILM was applied by Big-Alabo *et al* (2014b) to determine the complete impact histories for both elastic and elastoplastic impact events in which the contact model of Majeed *et al* (2012) was used to estimate the impact force of the elastoplastic impact. The study showed that the results of the FILM solution matched results obtained by direct numerical integration. In this section, the FILM has been generalised for the solution of half-space impact models in which the impact force is estimated from canonical or non-canonical compliance models. First, the general concept of the FILM is discussed and thereafter the concept is applied to formulate solutions for impact models that are based on canonical and non-canonical compliance models. Finally, the implications for applying the FILM to solve impact models of transversely flexible plates are discussed.

4.3.1 Concept of the FILM

Closed-form solutions of a half-space impact response can be obtained when a linearised force-indentation relationship is used. Hence, if the nonlinear force-indentation curve between the initial and end states of an impact stage is approximated using several line segments joined end to start, then each line segment representing a linear force-indentation relationship gives a closed-form solution that is only applicable to the range of indentation it covers. The slopes of the line segments represent linearised contact stiffnesses, and the slopes change between the initial and end states of the impact stage considered. This changing slope results in a changing force-indentation relationship that can be used to update the solution from one piecewise linearisation to the next.

Figures 4.9 a-c shows a typical nonlinear force-indentation relationship with various approximations. Obviously, Figure 4.9c with three line segments gives a better description of the impact histories compared to Figures 4.9a and 4.9b. The implication is that increasing the number of line segments produces a better approximation of the nonlinear force-indentation curve and gives a more accurate estimation of the impact history.

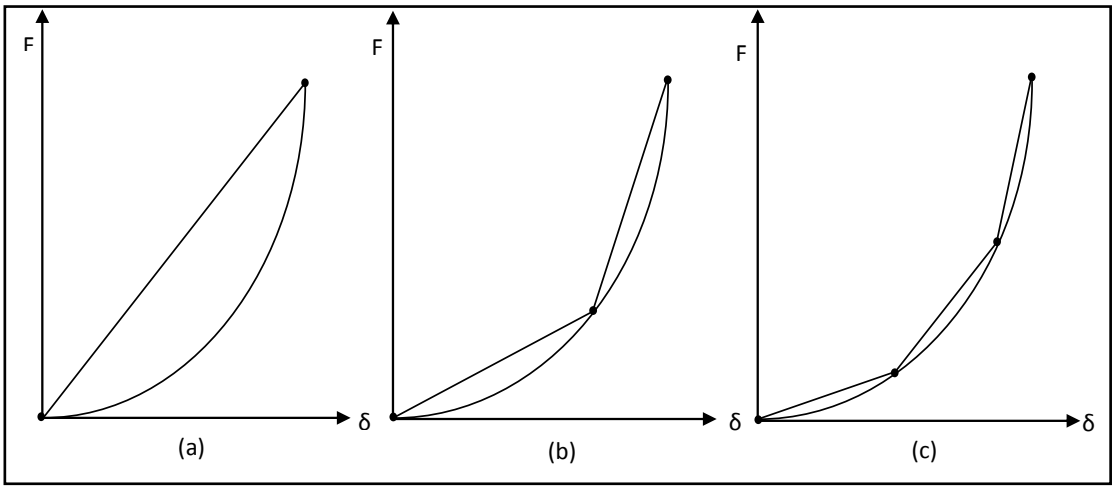

Figure 4.9: *Linear discretisation of nonlinear force indentation relationship (a) one line (b) two lines (c) three lines.*

The FILM produces closed-form solutions for the impact response for each piecewise linearisation of the nonlinear impact force. The closed-form solutions for each piecewise linearisation do not oscillate or diverge and this makes the FILM inherently stable unlike other commonly used numerical methods (Goldsmith, 2001; Abrate, 1998) and the finite element methods.

Let us assume that $F(\delta)$ is a nonlinear function of δ as shown in Figure 4.10 and $F_i = F(\delta_i)$ where i represents any point on the nonlinear force-indentation relationship. Then from Figure 4.10, $F_{01} =$ slope of $\overline{01} \times (\delta_{01} - \delta_0) + F_0$ where F_{01} is the linearised force for the segment of $F(\delta)$ between point 0 and point 1. Hence,

$$F_{01} = \frac{F_1 - F_0}{\delta_1 - \delta_0}(\delta_{01} - \delta_0) + F_0 = \frac{F(\delta_1) - F(\delta_0)}{\delta_1 - \delta_0}(\delta_{01} - \delta_0) + F(\delta_0) \tag{4.13}$$

Similarly,

$$F_{12} = \frac{F(\delta_2) - F(\delta_1)}{\delta_2 - \delta_1}(\delta_{12} - \delta_1) + F(\delta_1) \tag{4.14}$$

And generally,

$$F_{rs} = \frac{F(\delta_s) - F(\delta_r)}{\delta_s - \delta_r}(\delta_{rs} - \delta_r) + F(\delta_r) \tag{4.15}$$

where $r = 0,1,2,3,\dots,n-1$ and $s = r+1$ are the initial and end states of each segment respectively. During unloading $r = n, n-1, n-2, \dots, 2,1$ are the initial states while $s = r-1$ are the end states. F_{rs} is the linearised force for each segment and it can be written as:

$$F_{rs} = K_{rs}(\delta_{rs} - \delta_r) + F(\delta_r) \tag{4.16a}$$

where

$$K_{rs} = \frac{F(\delta_s) - F(\delta_r)}{\delta_s - \delta_r} \tag{4.16b}$$

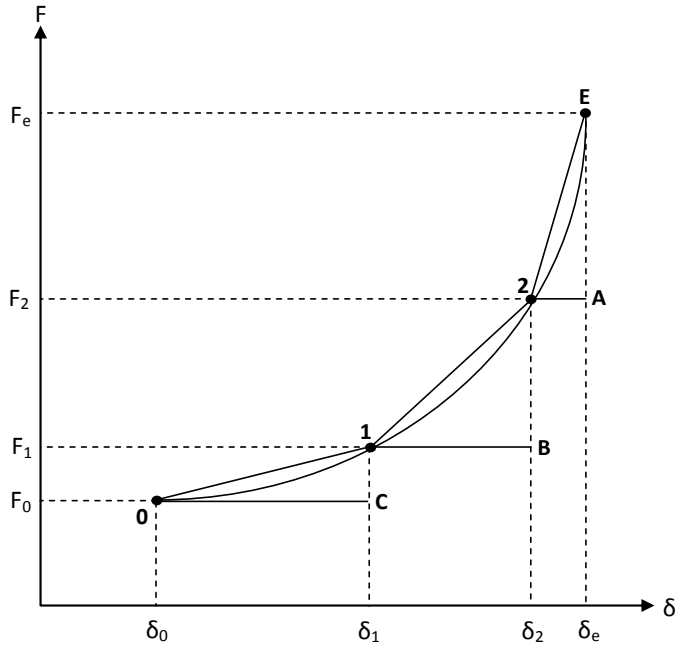

Figure 4.10: *Tri-linear approximation of a general nonlinear impact force used to demonstrate the concept of the FILM.*

Supposing each segment has an equal indentation range i.e. $\Delta\delta$ is constant, then δ_r can be expressed for n segments as:

$$\delta_r = \delta_0 + r(\delta_e - \delta_0)/n \tag{4.17}$$

When equation (4.16a) is substituted in equation (4.7), a linear differential equation is obtained from which closed-form solutions can be derived for each segment. This simple concept, combined with the energy balance principle (see Section 3.3.3.1), can be used to derive the complete solution of a half-space impact irrespective of the nature of nonlinearity in the compliance model used to estimate the impact force.

4.3.2 Solution of half-space impact modelled based on a canonical compliance law using the FILM

As mentioned earlier, Meyer's law is the standard form for static contact models. Meyer's law can be expressed as (Goldsmith, 2001):

$$F = K_c \delta^q \tag{4.18}$$

where K_c is the contact stiffness and $q \geq 1$ is a number defining the power law relationship between the contact force and indentation. For example K_c is equal to the Hertzian contact stiffness (see equation 3.31) and $q = 3/2$ during elastic impact. A more general form of Meyer's law, incorporating post-yield effects can be written as:

$$F = K_c(\delta - \delta_0)^q + F_0 \tag{4.19}$$

where δ_0 and F_0 are the indentation and contact force at the onset of a loading or unloading regime. During the elastic impact response $\delta_0 = 0$ and $F_0 = 0$, while for post-yield impact response, $\delta_0 \neq 0$ and $F_0 \neq 0$. Therefore, the model for a half-space impact, governed by a canonical compliance law that accounts for post-yield effects, can be written as:

$$m_i\ddot{\delta} + K_c(\delta - \delta_0)^q + F_0 = 0 \tag{4.20}$$

The FILM is only applied when $q > 1$ and equation (4.20) is nonlinear. If $q = 1$, then equation (4.20) is linear and closed-form solutions can be obtained directly without need for the FILM or any other numerical integration scheme.

Using equation (4.19) in equation (4.15),

$$F_{rs} = \frac{K_c(\delta_s - \delta_0)^q - K_c(\delta_r - \delta_0)^q}{\delta_s - \delta_r}(\delta_{rs} - \delta_r) + K_c(\delta_r - \delta_0)^q + F(\delta_0) \tag{4.21}$$

From equation (4.17),

$$\delta_s = \delta_{r+1} = \delta_r + (\delta_e - \delta_0)/n \tag{4.22}$$

Note that δ_e is the indentation at the end of the loading or unloading stage considered (see Figure 4.10), and δ_e can be obtained from the compliance model used or the energy balance algorithm (see Figure 3.10) when it is equal to the maximum indentation. Substituting equation (4.22) in equation (4.21), and after algebraic simplifications, the linearised contact force for each discretisation can be written as:

$$F_{rs} = K_{rs}(\delta_{rs} - \delta_r) + K_c(\delta_r - \delta_0)^q + F_0 \tag{4.23}$$

where

$$K_{rs} = nK_c(\delta_e - \delta_0)^{q-1}\left[\left(\frac{s}{n}\right)^{3/2} - \left(\frac{r}{n}\right)^{3/2}\right] \tag{4.24}$$

Substituting equation (4.23) in equation (4.7), the governing equation for the impact response of each discretisation is given by:

$$m_i\ddot{\delta}_{rs} + K_{rs}\delta_{rs} = K_{rs}\delta_r - K_c(\delta_r - \delta_0)^q - F_0 \tag{4.25}$$

Equation (4.25) is a non-homogeneous linear differential equation and the complete solution can be readily obtained as:

$$\delta_{rs} = R_{rs}\,\mathrm{Sin}(\omega_{rs}t + \varphi_{rs}) + C_{rs} \tag{4.26}$$

and taking the first derivative of equation (4.26), the velocity profile is given by:

$$\dot{\delta}_{rs} = \omega_{rs}R_{rs}\,\mathrm{Cos}(\omega_{rs}t + \varphi_{rs}) \tag{4.27}$$

$R_{rs} = (A_{rs}^2 + B_{rs}^2)^{1/2}$; $C_{rs} = (K_{rs}\delta_r - K_c(\delta_r - \delta_0)^q - F_0)/K_{rs}$; $\omega_{rs} = \sqrt{K_{rs}/m_i}$; and $\varphi_{rs} = \tan^{-1}(B_{rs}/A_{rs}) - \omega_{rs}t_r$. As usual, the constants A_{rs} and B_{rs} are determined from the initial conditions $\delta(t_r) = \delta_r$ and $\dot{\delta}(t_r) = \dot{\delta}_r$.

Determination of the initial conditions for each discretisation

When $r = 0$, the linearised contact law, F_{01}, starts from the onset of the loading or unloading stage under consideration, and the initial conditions can be determined from the contact model used to estimate the impact force e.g. see equations (4.8 – 4.12). Given that the start-point of F_{12} is the same as the endpoint of F_{01}, then the initial conditions of F_{12} are the same as the end conditions of F_{01}. In general, the initial conditions of F_{rs} for any $r \geq 1$ are the same as the end conditions of the preceding discretisation. Since the displacements at the boundaries of each discretisation are known i.e. $\delta_r = \delta_0 + r(\delta_e - \delta_0)/n$, then one initial condition is already available. To get the second initial condition, the known displacements are substituted into equation (4.26) to get the time at the initial condition as:

$$t_r = (\mathrm{ArcSin}[(\delta_r - C_{rs})/R_{rs}] - \varphi_{rs})/\omega_{rs} \tag{4.28}$$

From trigonometry, $\mathrm{ArcSin}(\theta) + \mathrm{ArcCos}(\theta) = \pi/2$. Therefore,

$$t_r = \left(\frac{\pi}{2} - \mathrm{ArcCos}[(\delta_r - C_{rs})/R_{rs}] - \varphi_{rs}\right)/\omega_{rs} \tag{4.29}$$

The second initial condition is then determined by substituting equation (4.29) in equation (4.27). More generally, the time at the boundaries of each discretisation can be expressed as:

$$t_r = \left(\frac{\pi}{2} \pm \mathrm{ArcCos}[(\delta_r - C_{rs})/R_{rs}] - \varphi_{rs}\right)/\omega_{rs} \tag{4.30}$$

In equation (4.30), the second term in the outer bracket of the numerator is negative during the loading stage (as in equation (4.29)) and positive during the restitution stage. The change in the sign of this term during the restitution stage is due to the fact that the contact force is reversed. At maximum conditions, this term vanishes so that $t_m = (\pi/2 - \varphi_{rs})/\omega_{rs}$. For each discretisation, equation (4.30) is used to determine the time boundaries for the linearised contact force, and then, equations (4.26), (4.27) and (4.23) are used to extract

data points for the indentation, velocity and contact force histories within the time boundaries.

The above FILM solution, for a half-space impact response modelled based on a canonical compliance law, is demonstrated using the tungsten carbide – mild steel impact discussed in Section 4.2. The material properties of the impact system remain the same, while the impact velocity used in the present investigation is 0.25 $[m/s]$. It is recalled that an impact velocity of 0.5 $[m/s]$ produced a maximum indentation that is located in the nonlinear elastoplastic loading regime. Hence, the impact stages involved for an impact velocity of 0.25 $[m/s]$ are: elastic loading, nonlinear elastoplastic loading and elastic unloading; all of which are modelled with nonlinear canonical compliance models according to the new contact model. This means that the FILM can be applied to all the impact stages involved.

Application of the FILM to the solution of the elastic loading response

The elastic loading response covers the indentation range $0 \leq \delta \leq \delta_y$. Based on the new contact model $\delta_0 = 0$; $F_0 = 0$; $K_c = K_h$; $q = 3/2$; and $\delta_e = \delta_y$. From the FILM solution, the following changes apply to the elastic loading response.

$F_{rs} = K_{rs}(\delta_{rs} - \delta_r) + K_h\delta_r^{3/2}$; $\quad K_{rs} = nK_h\delta_y^{1/2}\left[(s/n)^{3/2} - (r/n)^{3/2}\right]$; $\quad \delta_r = r\delta_y/n$;

$C_{rs} = \left(K_{rs}\delta_r - K_h\delta_r^{3/2}\right)/K_{rs}$.

Application of the FILM to the solution of the nonlinear elastoplastic loading response

The nonlinear elastoplastic loading response covers the indentation range $\delta_y \leq \delta \leq \delta_m$. The maximum indentation, δ_m, is estimated using the energy-balance algorithm in Figure 3.10. Following this algorithm the maximum indentation for the present impact event is estimated from:

$$\frac{1}{2}m_i V_0^2 = 0.4K_h\delta_y^{5/2} + 0.4K_h\left(\delta_m - \delta_y\right)^{5/2} + K_h\delta_y^{3/2}\left(\delta_m - \delta_y\right) \tag{4.31}$$

Based on the new contact model, $\delta_0 = \delta_y$; $F_0 = F_y = K_h\delta_y^{3/2}$; $K_c = K_h$; $q = 3/2$; and $\delta_e = \delta_m$. From the FILM solution, the following changes apply to the nonlinear elastoplastic loading response.

$F_{rs} = K_{rs}(\delta_{rs} - \delta_r) + K_h\left(\delta_r - \delta_y\right)^{3/2} + F_y$;

$K_{rs} = nK_h\left(\delta_m - \delta_y\right)^{1/2}\left[(s/n)^{3/2} - (r/n)^{3/2}\right]$;

$\delta_r = \delta_y + r\left(\delta_m - \delta_y\right)/n$; and $C_{rs} = \left(K_{rs}\delta_r - K_h\left(\delta_r - \delta_y\right)^{3/2} - F_y\right)/K_{rs}$.

Application of the FILM to the solution of the unloading response

The unloading response covers the indentation range $\delta_f \leq \delta \leq \delta_m$. From the new contact model $\delta_0 = \delta_f$; $F_0 = 0$; $K_c = K_u$; $q = 3/2$; and $\delta_e = \delta_m$. From the FILM solution, the following changes apply to the unloading response.

$F_{rs} = K_{rs}(\delta_{rs} - \delta_r) + K_u\left(\delta_r - \delta_f\right)^{3/2}$;

$K_{rs} = nK_u\left(\delta_m - \delta_f\right)^{1/2}\left[(s/n)^{3/2} - (r/n)^{3/2}\right]$;

$\delta_r = \delta_f + r\left(\delta_m - \delta_f\right)/n$; and $C_{rs} = \left(K_{rs}\delta_r - K_u\left(\delta_r - \delta_f\right)^{3/2}\right)/K_{rs}$.

Note that the unloading response has been discretised from the bottom-up, which is why the onset is at the point $\left(\delta_f, 0\right)$ instead of (δ_m, F_m) as might be expected. The bottom-up discretisation has been used for mathematical convenience and it gives the same results as would have been obtained if the discretisation was done from the top-down and the onset is at (δ_m, F_m). Additionally, the sign change of the middle term in equation (4.30) during unloading makes the bottom-up solution to be consistent with the top-down solution.

The above FILM solution was implemented in a customised *Mathematica*™ code (see appendix B.1) that was used to estimate the impact response of the tungsten carbide – mild steel impact system. The code was run using five discretisations in each of the impact stages and the close-form solutions derived for each discretisation were used to extract data points for plotting the impact histories. Figure 4.11 shows the results of the FILM approach compared with numerical integration results obtained using the NDSolve function; the results are in excellent agreement.

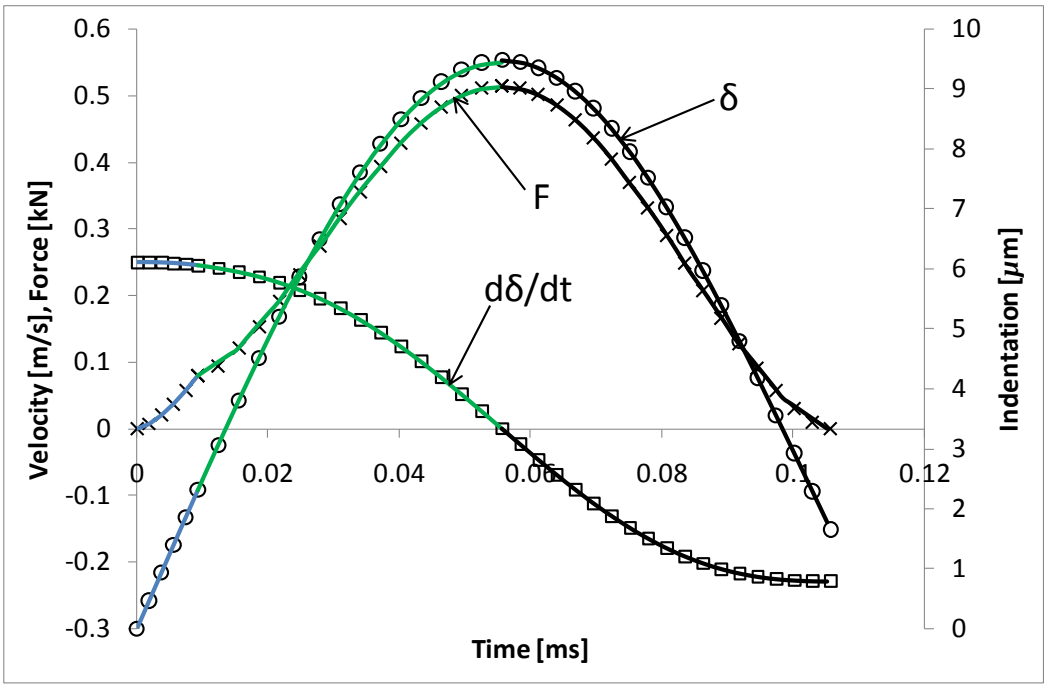

Figure 4.11: *Comparison of the results of the FILM solution and numerical integration method. Lines – FILM solution; Markers – numerical solution. See Table 4.1 for line colour definition.*

4.3.3 Solution of half-space impact modelled based on a non-canonical compliance law using the FILM

Non-canonical compliance models are those that cannot be expressed in terms of equation (4.19); examples include the elastoplastic loading models of Stronge (2000a) and Brake (2012). Conventional numerical integration schemes do not guarantee convergent solutions for half-space impact models in which non-canonical compliance models are used to estimate the impact force (Big-Alabo *et al*, 2014a). This is because of the more complex nonlinear form in which such contact models are expressed. The FILM is shown here to be a solution algorithm that guarantees convergent solutions when non-canonical contact models are used to estimate the impact force of a half-space impact. Interestingly, the FILM approach produces the solution with the same relative ease as it does with a half-space impact model based on a canonical contact model. This is because the number of discretisations need not be increased to guarantee convergent solutions even when a more complex contact model is used to estimate the impact force. To demonstrate this, the FILM algorithm is applied to solve the tungsten-carbide impact problem discussed in Section 4.3.2 when the contact model of Stronge (2000a) is used to estimate the impact force.

The contact model of Stronge (2000a) was discussed in Section 3.1.1. The elastic loading regime was modelled using the Hertz contact model, while the model for the elastoplastic loading regime used a logarithmic function of indentation depth. The model for the unloading regime is a modified form of the Hertz model that accounts for the effect of permanent indentation. All three regimes are modelled using nonlinear force-indentation relationships and therefore, the corresponding impact response models are nonlinear and would normally require numerical solution. In the following analysis, the FILM approach is applied to determine the impact histories when Stronge's contact model is used to estimate the impact force.

Application of the FILM to the solution of the elastic loading response

The FILM solution for the elastic loading stage of the impact response is the same as in Section 4.3.2 since Stronge (2000a) also used the Hertz model to estimate the elastic impact response.

Application of the FILM to the solution of the nonlinear elastoplastic loading response

For convenience Stronge's elastoplastic loading model is restated here.

$$F = F_y\left(\frac{2\delta}{\delta_y} - 1\right)\left[1 + \frac{1}{3.3} ln\left(\frac{2\delta}{\delta_y} - 1\right)\right] \qquad \delta_y \le \delta \le \delta_p \qquad (4.32)$$

The nonlinear elastoplastic loading response covers the indentation range $\delta_y \le \delta \le \delta_m$. Again, the maximum indentation, δ_m, is estimated using the energy-balance principle. Using equation (4.32) Stronge (2000a) derived the indentation work from the beginning of the elastic loading to any point in the elastoplastic loading regime as:

$$W = W_y\left\{0.47 + 0.53\left(\frac{2\delta}{\delta_y} - 1\right)^2 + 0.189\left(\frac{2\delta}{\delta_y} - 1\right)^2 ln\left(\frac{2\delta}{\delta_y} - 1\right)\right\} \qquad (4.33)$$

where $W_y = 0.4K_h\delta_y^{5/2}$. Therefore, the maximum indentation of an elastoplastic impact can be determined based on Stronge's model by equating the deformation work in equation (4.33) to the initial impact energy as follows:

$$\frac{1}{2}m_i V_0^2 = W_y\left\{0.47 + 0.53\left(\frac{2\delta_m}{\delta_y} - 1\right)^2 + 0.189\left(\frac{2\delta_m}{\delta_y} - 1\right)^2 ln\left(\frac{2\delta_m}{\delta_y} - 1\right)\right\} \qquad (4.34)$$

Based on Stronge's elastoplastic model, $\delta_0 = \delta_y$; $F_0 = F_y = K_h\delta_y^{3/2}$; and $\delta_e = \delta_m$.

Using equations (4.7), (4.16) and (4.32), the linearised model for each discretisation of the elastoplastic response was derived based on the FILM as shown below.

$$m_i\ddot{\delta}_{rs} + K_{rs}\delta_{rs} = K_{rs}\delta_r - F_y\left(\frac{2\delta_r}{\delta_y} - 1\right)\left[1 + \frac{1}{3.3}ln\left(\frac{2\delta_r}{\delta_y} - 1\right)\right] \tag{4.35}$$

where $F_{rs} = K_{rs}(\delta_{rs} - \delta_r) + F_y\left(\frac{2\delta_r}{\delta_y} - 1\right)\left[1 + \frac{1}{3.3}ln\left(\frac{2\delta_r}{\delta_y} - 1\right)\right]$. Hence, the following changes apply to the FILM solution (equations (4.26), (4.27), and (4.29)).

$$K_{rs} = 2K_h\delta_y^{1/2}\left\{1 + \frac{n}{6.6}\left[\left(\frac{2\delta_s - \delta_y}{\delta_m - \delta_y}\right)ln\left(\frac{2\delta_s - \delta_y}{\delta_y}\right) - \left(\frac{2\delta_r - \delta_y}{\delta_m - \delta_y}\right)ln\left(\frac{2\delta_r - \delta_y}{\delta_y}\right)\right]\right\};$$

$$\delta_r = \delta_y + r(\delta_m - \delta_y)/n;\ \ C_{rs} = \frac{1}{K_{rs}}\left\{K_{rs}\delta_r - F_y\left(\frac{2\delta_r}{\delta_y} - 1\right)\left[1 + \frac{1}{3.3}ln\left(\frac{2\delta_r}{\delta_y} - 1\right)\right]\right\}.$$

Application of the FILM to the solution of the unloading response

Stronge's model for the unloading response is the same as that of the new contact model formulated in Section 3.2. The only difference is the expression used to calculate the deformed effective radius. Hence, the FILM solution for the unloading response formulated in Section 4.3.2 is applicable here.

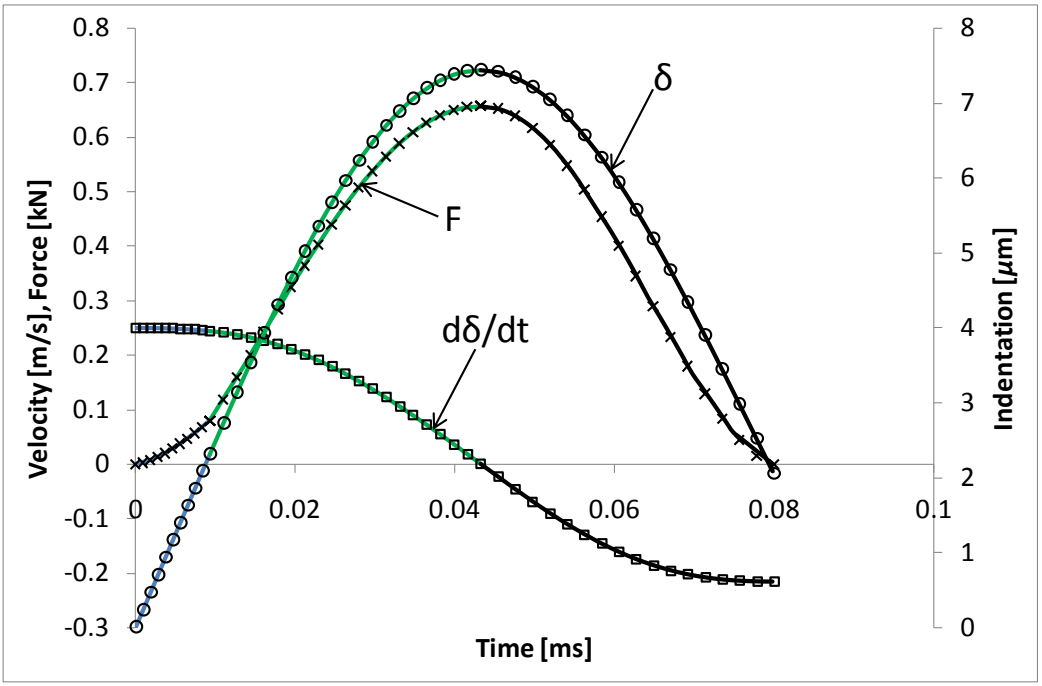

Figure 4.12: *Comparison of the results of the FILM solution and numerical integration method. Lines - FILM solution; Markers - numerical solution. Contact model used: Stronge (2000a). See Table 4.1 for colours used in plotting the FILM results.*

The FILM solution derived above for the various impact stages was implemented in a customised *Mathematica*™ code and used to estimate the impact response of the tungsten carbide – mild steel impact case study. The code was run using five discretisations in each of the impact stages and the closed-form solutions derived for each discretisation were used to extract data points for plotting the impact histories. Figure 4.12 shows the results of the FILM approach in comparison with results obtained by numerical integration using the NDSolve function. Some key results of the tungsten carbide – mild steel impact response based on the newly proposed contact model and Stronge's contact model are given in Table 4.3. Results reveal that the contact model used to estimate the impact force can greatly influence the prediction of the impact response. In view of the fact that the new contact model has been validated using published static and dynamic indentation test results (see Section 3.3), the predicted impact response based on the new contact model is considered to be reliable.

Table 4.3: *Tungsten carbide – mild steel impact response results obtained using FILM*

Impact parameters	Results	
	New contact model	Stronge's contact model
Impact duration [μs]	105.14	79.78
Time at maximum indentation [μs]	55.57	43.24
Permanent indentation [μm]	1.78	2.09
Maximum indentation [μm]	9.45	7.44
Maximum impact force [N]	513.41	657.29
Final rebound velocity [m/s]	0.23	0.22
Coefficient of restitution [-]	0.92	0.87

4.3.4 Implications of applying the FILM approach for the solution of the impact response of transversely flexible plates

During normal impact of transversely inflexible plates, which can be modelled using half-space assumptions, the flexural oscillations are negligible. The impact energy is primarily used for local indentation of the plate when other mechanisms of energy dissipation such as elastic waves and friction can be neglected, and the impact force can be estimated using quasi-static indentation

models (Johnson, 1985). The implication is that the impactor velocity is zero at maximum conditions. These features of a half-space impact allow for the use of the energy-balance principle in estimating the maximum indentation during impact loading (Abrate, 1998). For normal impact of transversely flexible plates the flexural oscillations of the plate cannot be neglected, and the interactions between the flexural oscillations and the local indentation determine the impact response. This means that the vibration model of the plate and a compliance model accounting for local indentation must be used in modelling the impact response (see Section 4.4 for more details). The response is dynamic and complex, making it impossible to use the energy-balance principle to determine the maximum indentation for a transversely flexible plate impact (Abrate, 1998).

In order to determine the impact response using the FILM approach the indentation and impact force at the end of the loading must be known. The end conditions of the impact loading are used as the initial conditions and other inputs for the unloading response. While it is possible to have this information from the energy-balance principle in the case of a transversely inflexible plate impact, it is not possible in the case of a transversely flexible plate impact. However, the impact loading phase during a transversely flexible plate impact ends when the impactor velocity is zero because the impact loading is due to the deceleration of the impactor. If the end indentation of the impact loading is chosen a priori, such that this assumed end indentation is definitely higher than the actual end indentation, then the condition of zero impactor velocity can be used as a test condition to determine the actual end of the impact loading. In principle the maximum indentation of the corresponding elastic half-space impact is always greater that the actual end indentation of the transversely flexible plate impact and this can therefore be conveniently used as the assumed end indentation.

The maximum indentation of a transversely flexible plate impact occurs when the relative velocity of the impactor and the plate is zero. For impact events in which the impact force does not oscillate, the condition of zero relative velocity occurs only once and this is at the maximum indentation point. Hence, the zero relative velocity condition is sufficient to determine the point where the maximum indentation occurs when the impact force does not oscillate. This does not mean that the zero relative velocity condition can be

used to determine the maximum indentation before implementing the FILM approach. Rather, the zero relative velocity condition can only be used as a test condition in the implementation of the FILM approach to know when the maximum indentation is reached. The infinite plate impact is an example of an impact event that is characterised by a non-oscillating impact force, and therefore can be solved using the FILM.

In cases where the impact force oscillates, the zero relative velocity condition occurs more than once, making it necessary to have another condition to determine the maximum indentation point. Apparently, such a complementary condition is not known. Hence, the zero relative velocity condition is not sufficient to determine the maximum indentation when the impact force oscillates. The oscillation of the impact force is due to the influence of vibration waves reflected from the boundary. Thus, the FILM approach is more difficult to implement for a transversely flexible plate impact with an oscillating impact force. Therefore, the FILM approach is recommended for transversely flexible plate impacts with non-oscillatory impact force i.e. small mass impacts.

As explained above the FILM approach can be used to solve the infinite plate model with slight modifications. To demonstrate this, an elastic impact problem studied by Olsson (1992) is considered here. The material and geometrical properties of the graphite/epoxy composite laminate plate and steel impactor used by Olsson (1992) are given in Table 4.4. The infinite plate model for an orthotropic composite plate is a single differential equation given by (Chai and Zhu, 2011; Olsson, 1992)

$$\ddot{\delta} + \frac{1}{8\sqrt{\rho D}}\dot{F} + \frac{F}{m_p} = 0 \tag{4.36}$$

where ρ_a is the mass per unit area of the plate $[kg/m^2]$, D is the effective mechanical bending stiffness of the plate $[Nm]$, m_i is the mass of the impactor $[kg]$ and F is the impact force $[N]$. The effective stiffness is calculated as $D = [(A+1)/2]\sqrt{D_{11}D_{22}}$ where $A = (D_{12} + 2D_{66})/\sqrt{D_{11}D_{22}}$. The D_{ij} constants are bending stiffness constants that are calculated from the material properties of the plate, as discussed in Section 2.5. The impact force can be estimated using a static contact model and is a function of the local indentation i.e. $F = F(\delta)$. Hence, substituting an appropriate static contact model in equation (4.36) would

produce a differential equation in $\delta(t)$, the solution of which gives the local indentation history. The local indentation is expressed as: $\delta(t) = w_i(t) - w(t)$ where $w_i(t)$ and $w(t)$ are respectively the displacements of the impactor and the plate at the point of impact. The displacement of the plate at the point of impact is given by:

$$w(t) = \frac{1}{8\sqrt{\rho D}} \int_{t_0}^{t} F(\tau)\, d\tau \tag{4.37}$$

where t_0 is the time at the onset of the impact stage considered, and $t_0 = 0$ for elastic impact.

The complete solution of the infinite plate impact model can be determined once the local indentation history is obtained from the solution of equation (4.36). The local indentation history is used to determine the impact force history from the static contact model that was initially substituted into equation (4.36), and the impact force so obtained is substituted into equation (4.37) to determine the displacement of the plate at the point of impact. Thereafter, the displacement of the impactor can be obtained from the solutions of the local indentation and plate displacement. Also, the velocities of the impactor and the plate can be obtained by differentiating the solutions of the respective displacements.

Table 4.4: *Properties of the steel –laminate impact system (Olsson, 1992)*

Material properties
Graphite/epoxy (T300/934) composite plate: Lamination sequence = $[0/90/0/90/0]_s$; $\rho = 4.132\ [kg/m^2]$; $D_{11} = 154.9\ [Nm]$; $D_{12} = 4.76\ [Nm]$; $D_{22} = 91.4\ [Nm]$; $D_{66} = 8.97\ [Nm]$; $h = 2.69\ [mm]$; $A = 200 \times 200\ [mm^2]$;
Impactor (Steel): $m = 8.3\ [g]$; $V_0 = 3\ [m/s]$; $R_i = 6.35\ [mm]$
Other inputs: Effective contact modulus $= 9.72\ [GPa]$; $R_t = \infty$

During elastic impact of transversely flexible composite plates, the Hertz contact model can be used to estimate the impact force. Using the Hertz contact model in equation (4.36) the model for elastic impact response is derived thus:

$$\ddot{\delta} + \frac{3K_h}{16\sqrt{\rho D}} \delta^{1/2} \dot{\delta} + \frac{K_h}{m_p} \delta^{3/2} = 0 \tag{4.38}$$

The initial conditions are $\delta(0) = 0$ and $\dot{\delta}(0) = V_0$. Equation (4.38) is a nonlinear differential equation and would normally require a numerical solution. Using the FILM approach by substituting the linearised contact force for the Hertz contact model (see Section 4.3.2) into equation (4.37), the impact response model for each discretisation of the impact force can be derived as:

$$\ddot{\delta}_{rs} + \frac{K_{rs}}{8\sqrt{\rho D}}\dot{\delta}_{rs} + \frac{K_{rs}}{m_p}\delta_{rs} = \frac{K_{rs}\delta_r - K_h\delta_r^{3/2}}{m_p} \tag{4.39}$$

where $K_{rs} = nK_h\delta_m^{1/2}\left[(s/n)^{3/2} - (r/n)^{3/2}\right]$; $\delta_r = r\delta_m/n$; $r = 0, 1, 2, 3, \ldots, n-1$; $s = r + 1$; and n is the number of discretisations. Since the maximum indentation of the infinite plate model cannot be determined from the onset as explained above, the maximum indentation of the corresponding elastic half-space impact is used and the zero relative velocity condition is tested for each linearisation to determine the point when the actual maximum indentation is reached. This maximum indentation is less than that of the corresponding elastic half-space impact (Olsson, 1992). However, the impact loading ends when the impactor velocity is zero. This second condition is also tested to determine the end of the impact loading and to determine the initial conditions at the beginning of the unloading stage.

Equation (4.39) can be rewritten as

$$\ddot{\delta}_{rs} + 2\lambda_{rs}\dot{\delta}_{rs} + \omega_{rs}^2\delta_{rs} = P_{rs} \tag{4.40}$$

where $\lambda_{rs} = (1/16)\sqrt{m_p K_{rs}/\rho D}$; $\omega_{rs} = \sqrt{K_{rs}/m_p}$; and $P_{rs} = \left(K_{rs}\delta_r - K_h\delta_r^{3/2}\right)/m_p$ are the damping constant, circular frequency of the linearised response and constant load respectively. Equation (4.40) describes the motion of an initially excited damped oscillator with a constant load. The solution depends on the value of the damping constant, λ_{rs}, i.e. whether the motion is under-damped, critically-damped, or over-damped. The complete solutions to equation (4.40) are comprised of the particular and homogeneous solutions for the different cases of damping and are given as:

Under-damped $(0 < \lambda_{rs} < 1)$

$$\delta_{rs} = R_{rs}e^{-\lambda_{rs}\omega_{rs}t}\,\mathrm{Sin}(\omega_{drs}t + \varphi_{drs}) + C_{rs} \tag{4.41}$$

Critically-damped $(\lambda_{rs} = 1)$

$$\delta_{rs} = e^{-\omega_{rs}t}\left[A_{rs} + B_{rs}t\right] + C_{rs} \tag{4.42}$$

Over-damped $(\lambda_{rs} > 1)$

$$\delta_{rs} = e^{-\lambda_{rs}\omega_{rs}t}\left[D_{rs}e^{\omega_{rs}\left(\lambda_{rs}^2-1\right)^{1/2}t} + E_{rs}e^{-\omega_{rs}\left(\lambda_{rs}^2-1\right)^{1/2}t}\right] + C_{rs} \qquad (4.43)$$

where $\omega_{drs} = \omega_{rs}\sqrt{1-\lambda_{rs}^2}$ is the damped circular frequency of the under-damped response;

$R_{rs} = e^{\lambda_{rs}\omega_{rs}t_r}\left[\left(\dot{\delta}_r + \lambda_{rs}\omega_{rs}(\delta_r - C_{rs})\right)^2/\omega_{drs}^2 + (\delta_r - C_{rs})^2\right]^{1/2}$ is an initial-value constant that determines the amplitude of the homogeneous solution for the under-damped response;

$\varphi_{drs} = \tan^{-1}\left[\omega_{drs}(\delta_r - C_{rs})/\left(\dot{\delta}_r + \lambda_{rs}\omega_{rs}(\delta_r - C_{rs})\right)\right] - \omega_{drs}t_r$ is the phase angle of the homogeneous solution for the under-damped response;

$A_{rs} = \left[-\dot{\delta}_r t_r + (\delta_r - C_{rs})(1-\omega_{rs}t_r)\right]e^{\omega_{rs}t_r}$ and $B_{rs} = \left[\dot{\delta}_r + \omega_{rs}(\delta_r - C_{rs})\right]e^{\omega_{rs}t_r}$ are initial-value constants of the critically-damped response;

$D_{rs} = \left[\frac{\omega_{rs}(\delta_r - C_{rs})\left(\lambda_{rs}+\left(\lambda_{rs}^2-1\right)^{1/2}\right)+\dot{\delta}_r}{2\omega_{rs}\left(\lambda_{rs}^2-1\right)^{1/2}}\right]e^{\left[\lambda_{rs}-\left(\lambda_{rs}^2-1\right)^{1/2}\right]\omega_{rs}t_r}$ and

$E_{rs} = \left[\frac{\omega_{rs}(\delta_r - C_{rs})\left(-\lambda_{rs}+\left(\lambda_{rs}^2-1\right)^{1/2}\right)-\dot{\delta}_r}{2\omega_{rs}\left(\lambda_{rs}^2-1\right)^{1/2}}\right]e^{\left[\lambda_{rs}+\left(\lambda_{rs}^2-1\right)^{1/2}\right]\omega_{rs}t_r}$ are initial-value constants of the over-damped response; and

$C_{rs} = P_{rs}/\omega_{rs} = \left(K_{rs}\delta_r - K_h\delta_r^{3/2}\right)/K_{rs}$ is the particular solution.

The evaluation of the solutions (equations (4.41 – 4.43)) depends on the initial conditions, i.e. $\delta(t_r) = \delta_r$ and $\dot{\delta}(t_r) = \dot{\delta}_r$. Since the indentation at the boundaries of each discretisation, δ_r, is known, then the time at the boundaries of each discretisation, t_r, can be determined by substituting $\delta_{rs} = \delta_r$ when $t = t_r$ in equations (4.41 – 4.43). Closed-form solutions for t_r cannot be obtained from the resulting nonlinear equations and so t_r is to be determined using conventional numerical methods for finding roots of nonlinear equations e.g. the Newton-Raphson method. Therefore, application of the FILM approach to the infinite plate model is semi-analytical since the time at the boundaries must be obtained numerically.

The above solution of the FILM approach was developed into a customised code (see appendix B.2) that was used to solve the elastic impact response of the steel – composite laminate impact mentioned above. Given that the time boundaries are determined numerically, the FILM approach requires many discretisations to obtain accurate solutions. In the FILM simulation of the response of the steel – composite laminate impact, $n = 50$ was used initially to ensure that very accurate results were obtained for the impact response up to

the maximum indentation. The zero relative velocity condition was satisfied at the 23rd discretisation. The actual maximum indentation obtained for the infinite plate response was 44.2 [μm] while the corresponding half-space maximum indentation used for the discretisation was 96.0 [μm]. Once the actual maximum indentation was reached, the restitution algorithm of the FILM approach was used with $n = 20$ to obtain the response from this maximum indentation to the end of the impact where the indentation is zero. Normally the restitution algorithm of the FILM approach should be applied to the infinite plate problem at the end of the impact loading when the impactor velocity is zero. But in the present simulation it was applied at the point of maximum indentation to simplify the computations in FILM algorithm; this did not affect the results because the model for loading and restitution are the same for elastic impact.

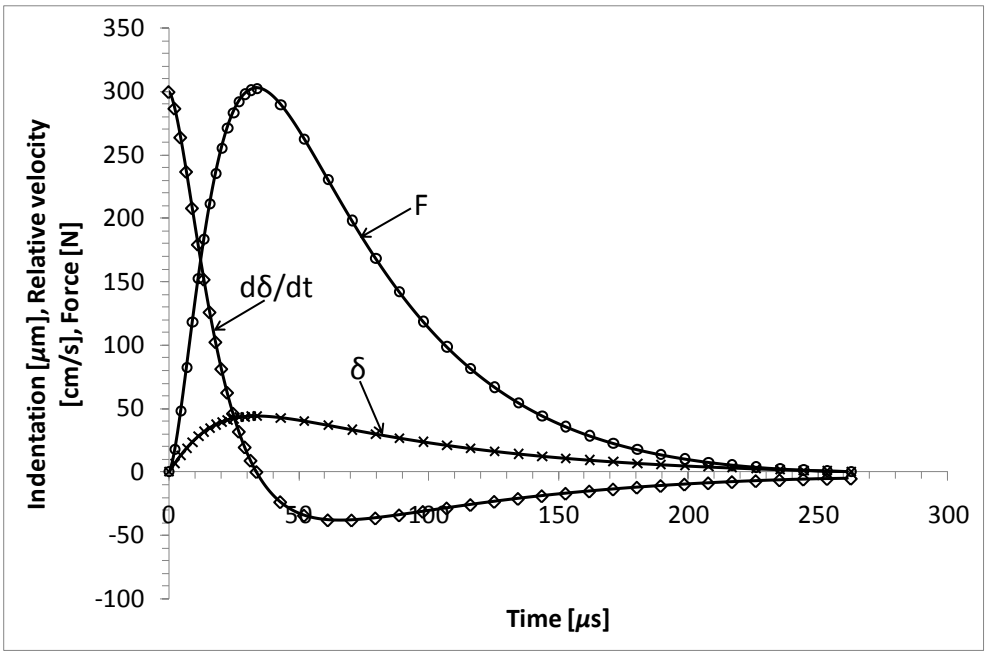

Figure 4.13: *Comparison of the results of the FILM solution and numerical integration method for elastic impact of [0/90/0/90/0]$_s$ graphite/epoxy (T300/934) composite plate. Lines – FILM solution; Markers – numerical solution.*

Although the application of the FILM approach to the infinite plate model requires many iterations to guarantee accurate results, the stability of the approach is independent of the number of discretisation i.e. the FILM approach is stable with few discretisations, such as $n = 10$. The implication of the unconditional stability of the FILM approach is that convergent solutions can always be obtained for the infinite plate problem irrespective of the contact

model used to estimate the impact force. Results obtained from the FILM approach and direct numerical integration of equation (4.38) using the NDSolve function are plotted in Figure 4.13. Both results are in excellent agreement and shows that the FILM solution is accurate.

4.4 Impact response of transversely flexible rectangular plates

A transversely flexible plate undergoes flexural oscillations when subjected to impact loading. Such plates are used in many structural applications (e.g. building panels, car and airplane bodies, ceilings and floorings) in environments where they can be exposed to impact from blunt projectiles. Therefore, a good understanding of the impact response of transversely flexible plates is necessary for design decision-making, damage diagnosis, and active control of impact response. The response of a transversely flexible plate to a blunt object impact is governed by the interaction between flexural oscillations and local indentation of the plate. The simplest analytical cases of transversely flexible plate impacts are the asymptotic cases of the infinite plate response and the quasi-static bending response. Each of these asymptotic cases is modelled by a single differential equation (Abrate, 2001). In general, the model for the impact response of transversely flexible plates is a set of coupled differential equations that accounts for the flexural oscillations of the plate, the local indentation and the displacement of the impactor. This model has been referred to as the complete model (Abrate, 2001) and is applied in the analysis of this section to investigate the impact response of a transversely flexible trimorph plate.

Transversely flexible plates may sometimes be subject to accidental impact by blunt projectiles that could damage the plate. Analytical models that are capable of predicting the impact response of a transversely flexible plate could be used to determine the extent of damage and for design purposes. Analytical studies of the normal impact of rigid spheres on transversely flexible monolithic and laminated rectangular plates abound in the literature. Most of these studies deal with elastic impact (Zener, 1941; Christoforou and Swanson, 1991; Olsson, 1992; Carvalho and Guedes Soares, 1996; Abrate, 1998; Goldsmith, 2001), and those that deal with elastoplastic impact use simplified models for the elastoplastic indentation (Christoforou and Yigit, 1998a; 1998b; Saravanos and

Christoforou, 2002; Zheng and Binienda, 2007) that may introduce significant errors in the prediction of the impact response of the plate (Christoforou and Yigit, 1998b). The use of well validated elastoplastic contact models in the complete modelling approach is quite challenging computationally, but has the advantage of producing more reliable results and of providing details of the impact response that would not have been obtained otherwise.

In this section, a flexible laminated plate structure called a trimorph plate is investigated analytically for low-velocity, large mass impact. Large mass impact is investigated because the impact duration falls within a range (milliseconds) that could allow for realistic impact control action using piezo-actuation (Yigit and Christoforou, 2000). The analytical modelling of the trimorph plate combined the flexural oscillation models of the trimorph plate (see Section 2.6) with the new contact model (see Section 3.2) and the single degree of freedom model for the impactor displacement. This combination produces a set of $p+1$ coupled differential equations that must be solved simultaneously; p represents the number of participating harmonics (vibration modes). During low to medium velocity impact the vibrations of the target are small in comparison to the plate thickness so that additional nonlinearities arising from large displacements (see Section 2.6) can be safely ignored. It is also customary to neglect natural viscous damping because the impact response is highly transient and does not allow sufficient time for natural viscous damping effects to become significant. The modelling approach used in this study allows for the use of various boundary conditions, though the present analysis has been limited to simply-supported boundary conditions for mathematical convenience. The reduced models for the impact response of a simply-supported transversely flexible plate based on the complete model are given as:

$$\left\{ \ddot{W}_1 \right\}_{mn} + (1-\alpha)K\{W_1\}_{mn} = F(t)\{\gamma\}_{mn} \qquad (4.44a)$$

$$\ddot{W}_2 = -F(t)/m_i \qquad (4.44b)$$

where W_1 is the plate displacement; W_2 is the displacement of the impactor; K is the effective mechanical bending stiffness of the plate and is calculated as in Section 2.6; D_{ij} are bending stiffness elements and can be calculated as in Section 2.5; a and b are the planar dimensions of the plate; α is a parameter to alter the effective stiffness of the plate; m and n represent vibration mode numbers; m_i is the mass of the impactor; $F(t) = F(\delta(t))$ is the impact force

acting at the point of contact and is estimated from a static contact model; and $\delta = W_2 - W_1$ is the local indentation of the plate. The load coefficient γ is defined by the distribution of the external excitation (see equation 2.43c). For a point load at (x_0, y_0)

$$\gamma = \frac{4}{\rho hab} \mathrm{Sin}\left(\frac{m\pi x_0}{a}\right) \mathrm{Sin}\left(\frac{n\pi y_0}{b}\right) \qquad (4.45a)$$

For uniformly distributed load over a rectangular patch of width l_1 and length l_2

$$\gamma = \frac{16}{\rho hmncd} \mathrm{Sin}\left(\frac{m\pi\lambda}{a}\right) \mathrm{Sin}\left(\frac{n\pi\eta}{b}\right) \mathrm{Sin}\left(\frac{m\pi l_1}{2a}\right) \mathrm{Sin}\left(\frac{n\pi l_2}{2b}\right) \qquad (4.45b)$$

where ρ is the plate density; h is the total thickness of the plate; λ and η are the distances of the centre of the patch from the edges of the plate. The rectangular patch covers the region defined by: $\lambda - l_1/2 < x < \lambda + l_1/2$ and $\eta - l_2/2 < y < \eta + l_2/2$. The load coefficients for other types of load distribution can be found in the literature (Nosier *et al*, 1994; Reddy, 2004; Szilard, 2004). Results presented in this section are obtained using equation (4.45a).

Equation (4.44a) was derived from the vibration models presented in Section 2.6 by neglecting natural viscous damping and replacing the harmonic excitation by a general excitation force. Equation (4.44a) is in vector form and consists of $(m+1)(n+1)/4$ equations because m and n are odd for central displacement of the plate. Equations (4.44a) and (4.44b) were solved, together with the new contact model, using customised codes that automatically generate the number of equations based on the specified values of m and n, and solves the equations simultaneously using the NDSolve function (see appendix B.3). The contact model of Majeed *et al* (2012) was used for comparison because of its simplicity. While this model underestimates the contact force during substantial elastoplastic indentation of metals (see Figures 3.7 and 3.8), it was nevertheless shown to produce similar estimates as the new contact model for indentations in the range $0 < \delta < 8\delta_y$ (see Figure 3.9). Since the impact events investigated here have maximum indentations that fall within this range, using the model of Majeed *et al* (2012) for the purpose of comparison is reasonable.

4.4.1 Validation of modelling and solution approach

To validate the combined modelling (complete model) and solution (numerical integration using NDSolve function in *Mathematica*™) approach used in the present analysis, a well-known impact problem first studied by Karas (1939) and known as the 'Karas problem' is re-examined. This problem has been studied by many others including Goldsmith (2001) and Abrate (1998) and can be considered as a benchmark case. The impact event involves the elastic impact of a simply-supported square steel plate struck by a steel ball. The material and geometrical properties of the impact system were obtained from Abrate (1998) as follows: density = 7806 [kg/m^3], Young's modulus = 206.8 [*GPa*] and Poisson's ratio = 0.3 [-]; Impactor diameter = 0.02 [m]; impact velocity = 1.0 [m/s]; Plate dimensions = 0.2 × 0.2 × 0.008 [m^3]. The impactor mass was calculated to be 0.0327 [kg]. Since the impact is elastic the Hertz contact model is used to estimate the impact force, and the bending stiffness is calculated as $K = [Eh^2/12\rho(1-\upsilon^2)][(m/a)^2 + (n/b)^2]^2$ for a monolithic plate (Karas, 1939); where E, ρ, and υ are the Young's modulus, density and Poisson ratio respectively.

The results obtained by Karas (1939), Abrate (1998) and the present approach are compared in Figures 4.14a and 4.14b. Karas (1939) and Abrate (1998) both used the complete modelling approach, but while the former solved the reduced models using a small-increment time integration scheme the latter employed the Newmark time integration scheme. The impactor – plate mass ratio is 0.0131 and this means that the impact is a small mass impact (Olsson, 2000). Small mass impacts are dominated by highly dynamic flexural oscillations and therefore, the solution to the reduced models of the complete modelling approach requires that a good number of harmonics are considered to obtain accurate results (Goldsmith, 2001). Karas (1939) used 70 harmonics while the present solution was found to converge using 42 harmonics (i.e. m = 13 and n = 11). The results of all three methods are in good agreement. This shows that the results obtained using the NDSolve function are reliable. Hence, the NDSolve function has been used to solve the elastoplastic impact models of the trimorph plate investigated in this study.

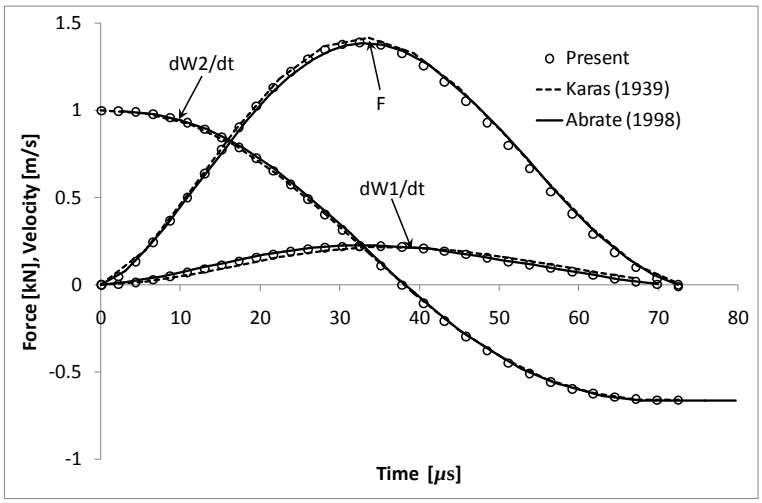

Figure 4.14a: *Force and velocity histories for impact of a steel ball on a transversely flexible steel plate. dW1/dt – plate velocity, dW2/dt – impactor velocity, F – Force.*

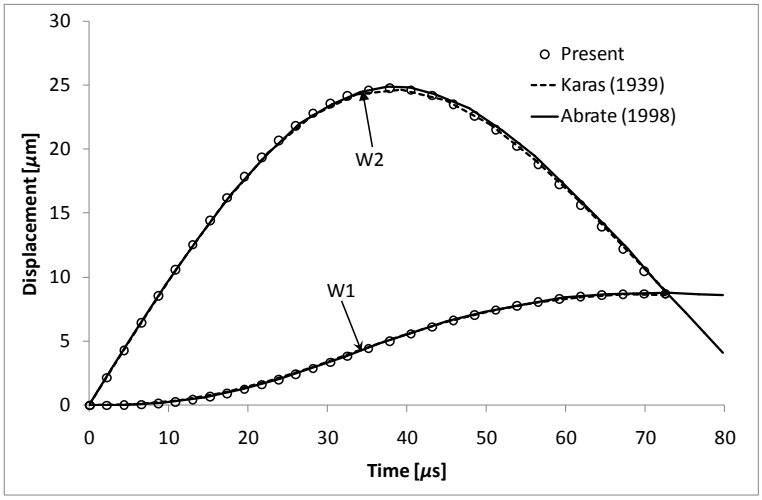

Figure 4.14b: Displacement histories for impact of a steel ball on a transversely flexible steel plate.W1 – plate displacement, W2 – impactor displacement.

4.4.2 Elastoplastic impact response analysis of a transversely flexible trimorph plate

It is generally accepted in the literature that the elastoplastic indention during contact loading commences at the yield point of the complaint material. The impact velocity at which the elastoplastic indentation begins during impact of a steel slab by a steel ball has been calculated as 0.14 [m/s] by Johnson (1985). This means that elastoplastic indentation would be expected at practical impact speeds (Goldsmith, 2001). Another look at the 'Karas problem' shows

that the maximum indentation during the impact loading is 20.36 [μm]. Karas did not state the yield stress of the steel plate because it is not needed for elastic impact analysis. Typical values of the yield stress for medium carbon steel range from 245 [MPa] to 1740 [MPa] (Source: www.Matweb.com; Accessed: 13-10-2014). The indentation at which elastoplastic indentation begins can be determined from equation (3.2) (Stronge, 2000a; Majeed *et al*, 2012). For a yield stress of 1740 [MPa] the indentation at yield was calculated as 15.75 [μm] using equation (3.2) and this value is lower than the maximum indentation when the impact is considered to be elastic. This means an impact velocity of 1.0 [m/s] would give rise to elastoplastic indentation when the plate material is medium carbon steel. In that case the Hertz contact model would not be ideal for estimating the impact response. This section presents detailed investigations of the elastoplastic impact response of a transversely flexible trimorph plate when struck in the transverse direction by a rigid projectile with spherical contact surface. First, the material properties of the trimorph plate are discussed and then results of the elastoplastic impact response of the trimorph plate are considered.

4.4.2.1 Material properties of a transversely flexible trimorph plate

In order to estimate the impact force using static indentation models, the material properties (Young's modulus, Poisson ratio and yield stress) of the impactor and plate must be known. For the trimorph plate impact problem, the impactor is considered to be made of a homogeneous isotropic material and the material properties can be readily obtained from property tables e.g. www.Matweb.com. However, the material properties of the trimorph plate in the transverse direction (z-direction) cannot be obtained from property tables because the plate consists of three different isotropic materials bonded together. Ideally, experimental measurements of the material properties of the trimorph plate would be available. In the absence of such experimental data the properties can be determined from finite element simulations or approximate analytical techniques.

An approximate analytical solution to the problem is the 'strength of materials' approach (Khalili *et al*, 2007c). Khalili *et al* (2007c) used this approach to determine the transverse properties of a rectangular sandwich plate

subjected to low-velocity impact. The sandwich plate was composed of two symmetric composite laminate layers with a transversely flexible core. Two different sandwich compositions were investigated. The first sandwich plate was made of IM7/5260 composite face-sheets and a glass phenolic honeycomb core, while the second plate was made of LTM45EL-CF0111 carbon fibre face-sheets and high-density 110WF polymethacryimide foam core. In studying the response of a functionally graded rectangular plate to low-velocity impact, Shariyat and Farzan (2013) determined the transverse material properties of a plate made up of a layer of zirconia on top and aluminium underneath using the strength of materials approach. Since the plate was considered to be functionally graded the volume fraction of each layer was determined from a power law that is generally applied to functionally graded materials (Reddy, 2004; Shariyat and Farzan, 2013). Shariyat and Jafari (2013) studied the impact response of a functionally graded circular plate resting on an elastic foundation. The plate was made of an alumina layer on top and an aluminium layer below. The transverse properties of the plate were determined using strength of materials approach. Larson and Palazotto (2009) estimated the transverse material properties of a functionally graded rectangular plate made of a titanium boride (TiB) layer on top and a Titanium (Ti) layer below using four different property estimation methods, namely: the rule of mixtures method (strength of materials approach), the self consistent method, the Mori-Tanaka spheres method and the Mori-Tanaka needles method. All four methods were found to produce similar estimates of the transverse properties of the TiB/Ti plate. A comparison with published data showed that the rule of mixtures approach produced good estimates of the transverse properties of the TiB/Ti plate. Furthermore, a comparison was made of the maximum impact force determined from strain gauge measurements and material property estimates from the four methods. The comparison showed that the rule of mixtures approach produced similar estimates of the maximum contact force to predictions using the other approaches.

In this investigation, the strength of materials approach has been applied to estimate the transverse material properties of the trimorph plate because of its simplicity and ability to produce good estimates of the transverse material properties for laminated plates made up of different materials. Khalili *et al* (2007c) suggested that the strength of materials approach could be used under

plane stress conditions, quasi-static loading, and when the effect of the in-plane material properties of the target on the transverse deformation, can be neglected. These conditions apply to the impact of the trimorph plate, and therefore, the strength of materials approach is considered to be suitable for the present investigation.

The strength of materials approach can be used to estimate the Young's modulus, Poisson ratio, density and yield stress of the trimorph plate as shown.

$$\left.\begin{array}{c} E_t = h/(h_1/E_1 + h_2/E_2 + h_3/E_3) \\ v_t = (v_1 h_1 + v_2 h_2 + v_3 h_3)/h \\ \rho_t = (\rho_1 h_1 + \rho_2 h_2 + \rho_3 h_3)/h \\ S_{yt} = h/\left(h_1/S_{y1} + h_2/S_{y2} + h_3/S_{y3}\right) \end{array}\right\} \tag{4.46}$$

where $h = h_1 + h_2 + h_3$ is the total thickness of the plate, the subscript, t, represents the target which here is the plate; the subscripts 1, 2, and 3 represent the layers of the plate from bottom to top; h_k, E_k, v_k, ρ_k, and S_{yk} are the thickness, Young's modulus, Poisson's ratio, density and yield stress of the *k*th layer of the trimorph plate, respectively. The first three equations of equations (4.46) have been used by Khalili *et al* (2007c), Shariyat and Farzan (2013) and Shariyat and Jafari (2013). For the last equation in equations (4.46), it is considered that because the yield point is the elastic limit then the effective transverse yield stress of the trimorph plate can be determined in the same way as the Young's modulus. The assumption on the yield stress is not based on theory or experimental observation, but at least it attempts to account for the yield effect of all the materials of the trimorph plate.

4.4.2.2 Results and discussions on the elastoplastic impact response of an Al/PVDF/PZT trimorph plate

A study of the elastoplastic impact response of a transversely flexible trimorph plate with layers arranged as Al/PVDF/PZT from top to bottom was carried out. The spherical surface of the impactor is in contact with the aluminium layer. This layer arrangement of the trimorph plate has been used for the impact studies because it has already been shown to exhibit the highest mechanical bending stiffness (see Table 2.2). The material and geometrical properties of the plate layers are shown in Table 4.5, and unless otherwise stated, these properties are used in all the analyses that follow.

Table 4.5: *Material and geometrical properties of the layers of the trimorph plate*

Material	ν [-]	E [GPa]	ρ [kg/m^3]	S_y [MPa]	h [mm]
Al	0.33	70	2700	320	3.0
PVDF	0.44	1.1	1770	50	1.0
PZT	0.3	64	7600	250	1.0

The other material and geometrical properties of the impact system are: $a = 100\ [mm]$; $b = 100\ [mm]$; $m_i = 1.0\ [kg]$; $V_0 = 0.30\ [m/s]$; $E_i = 210\ [GPa]$; $\nu_i = 0.30$; $R_i = 10\ [mm]$; $\alpha = 0$. Impactor material: steel.

Effect of number of vibration modes used in the solution

The accuracy of the solution of the impact response of the Al/PVDF/PZT plate depends on the number of participating modes used in the solution. The impact force history was determined for different numbers of participating modes as shown in Figure 4.15. The figure shows that nine participating modes (i.e. $m = n = 5$) are sufficient to guarantee accurate results. This observation was made previously by Khalili *et al* (2007a) who carried out a similar convergence study for the elastic impact response of a SMA-composite hybrid plate. The mass ratio of the impactor-trimorph plate system in Figure 4.15 is 5.72, which implies that the impact event is a large mass impact (Olsson, 2000). Also, the convergence study carried out by Khalili *et al* (2007a) was for a large mass impact. The impact response of a large mass impact is dominated by the fundamental mode of vibration (Olsson, 2000; Abrate, 2001) and this explains why the solution converges using just a few vibration modes. Hence, the results presented and discussed in this section have been obtained using a nine mode approximation. In Figure 4.15, the blue lines represent the elastic loading response, the red lines represent the elastoplastic loading response, and the black lines represent the response when unloading from an elastoplastic loading stage. This colour definition has also been used in later figures.

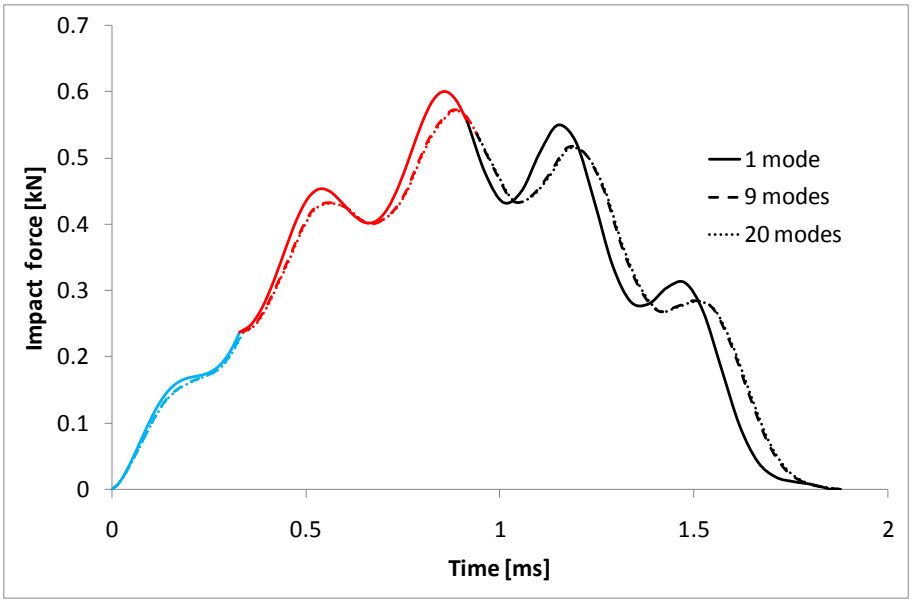

Figure 4.15: *Effect of number of modes used in the solution of the impact model on the accuracy of the results obtained for the Al/PVDF/PZT plate.*

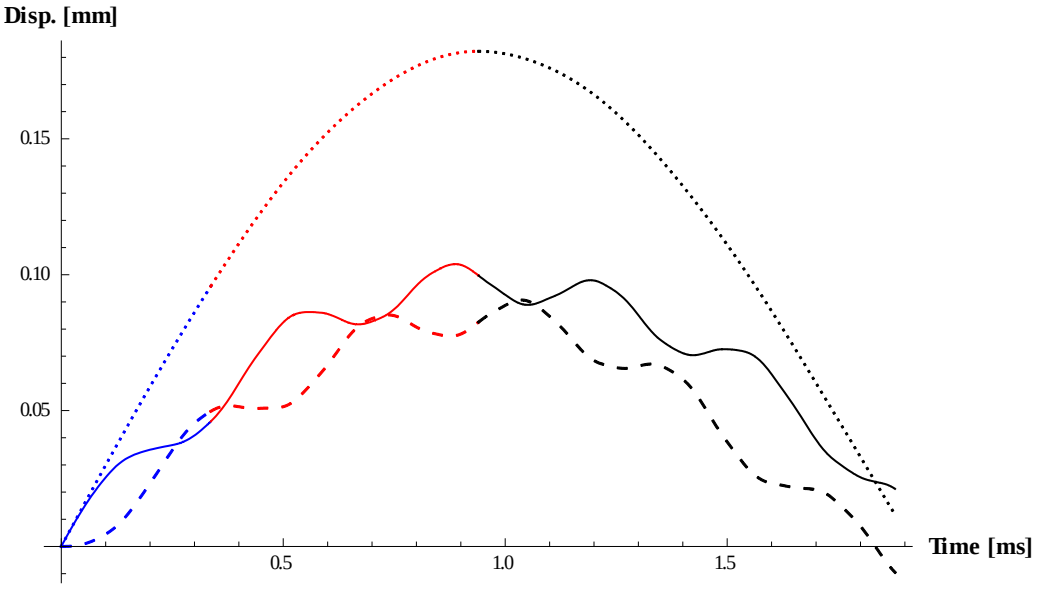

Figure 4.16: *Displacement histories of Al/PVDF/PZT plate impacted by steel impactor. Dotted line - impactor disp., short-dash line - plate disp., solid line - indentation.*

Figure 4.16 shows the displacements during the elastoplastic impact response of the Al/PVDF/PZT plate. The displacement of the impactor is smooth whereas there are oscillations in the displacement of the plate giving rise to oscillations in the indentation. The response has a maximum indentation of 103.95 [μm], which occurs in the elastoplastic loading regime, and a permanent

indentation of 21.16 [μm]. The maximum contact force is 573.95 [N] and the impact duration is 1.88 [ms]. The loading ends when the velocity of the impactor is zero and this occurs when the time is 0.94 [ms] (see Figure 4.17). The indentation plot (see Figure 4.16) shows that the point of maximum indentation (0.89 [ms], 103.95 [μm]) is different compared to the end point of the impact loading (0.94 [ms], 99.7 [μm]), and this observation has also been reported previously by Abrate (1998).

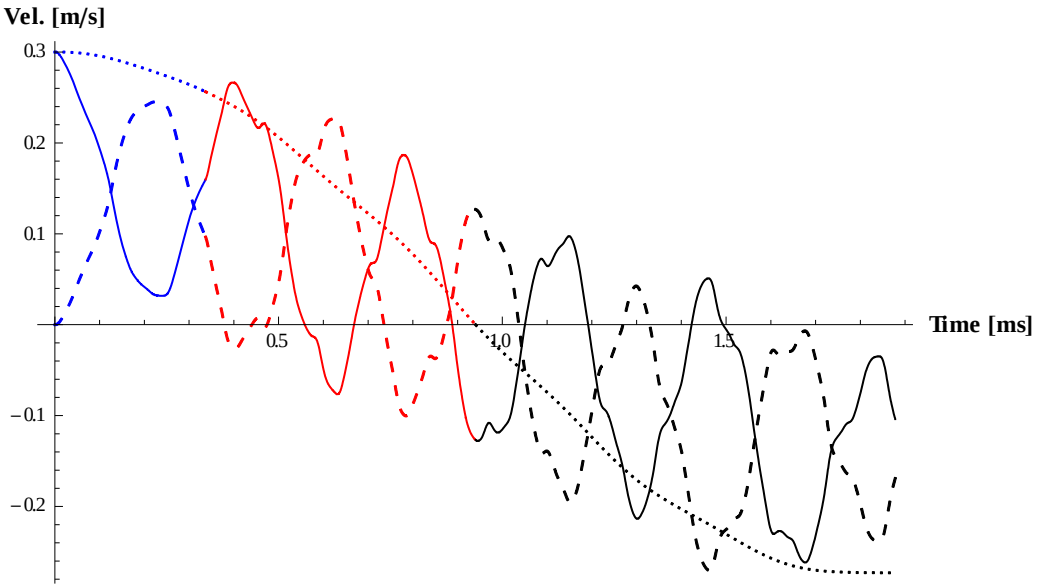

Figure 4.17: *Velocity histories of Al/PVDF/PZT plate struck by steel impactor. Dotted line - impactor velocity, short-dash line - plate velocity, solid line - relative velocity.*

Effect of contact model used to estimate the impact force

Figure 4.18 shows the impact force history for an initial impact velocity of 2.0 [m/s], and compares the results obtained when three different contact models (newly proposed contact model, the contact model of Majeed *et al* (2012) and the Hertz contact model) are used to estimate the impact force. The force histories predicted by all three models are in good agreement, demonstrating that the force history is not sensitive to the contact model used. The insensitivity of the force history to the contact model arises because the event is a large mass impact (Abrate, 1998; Chai and Zhu, 2011). For this reason, some investigators (Khalili *et al*, 2007a; 2007b; Abrate 2001; Anderson, 2005) use simplified contact models that do not account for elastoplastic indentation effects to predict the impact response of plates subjected to large mass impact.

Whereas the use of such simplified contact models could significantly reduce the computational effort involved and produce reliable estimates of the maximum contact force and impact duration, they ignore the fact that elastoplastic deformation may occur and therefore do not provide any information on the elastoplastic response when it does occur.

As Figure 4.19 reveals, the indentation history predicted by the Hertz contact model is different from that predicted by the elastoplastic contact models. The elastoplastic contact models predict significant elastoplastic deformation with a permanent indentation at the end of the impact. The new contact model predicts a maximum indentation of 0.37 [*mm*] and a permanent indentation of 59.8 [*μm*], the contact model of Majeed *et al* (2012) predicts 0.38 [*mm*] and 65.7 [*μm*] respectively, while the Hertz contact model predicts a maximum indentation of 0.34 [*mm*] and no permanent indentation (see Figure 4.19). This shows that the contact model used for predicting the impact response of a large mass impact can limit the information that can be obtained. Details of an elastoplastic response, such as the permanent and maximum indentation depth, are needed to develop and implement robust damage mitigation strategies. This makes the choice of contact model used to study large mass impact events an important consideration.

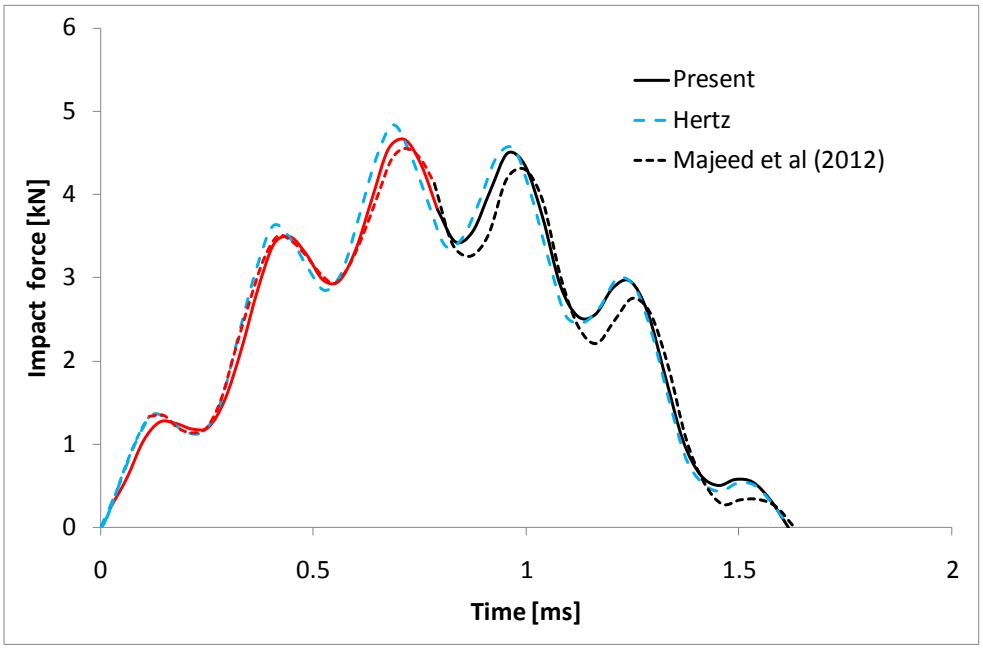

Figure 4.18: *Force history of Al/PVDF/PZT plate struck by steel impactor with initial impact speed of 2.0 [m/s].*

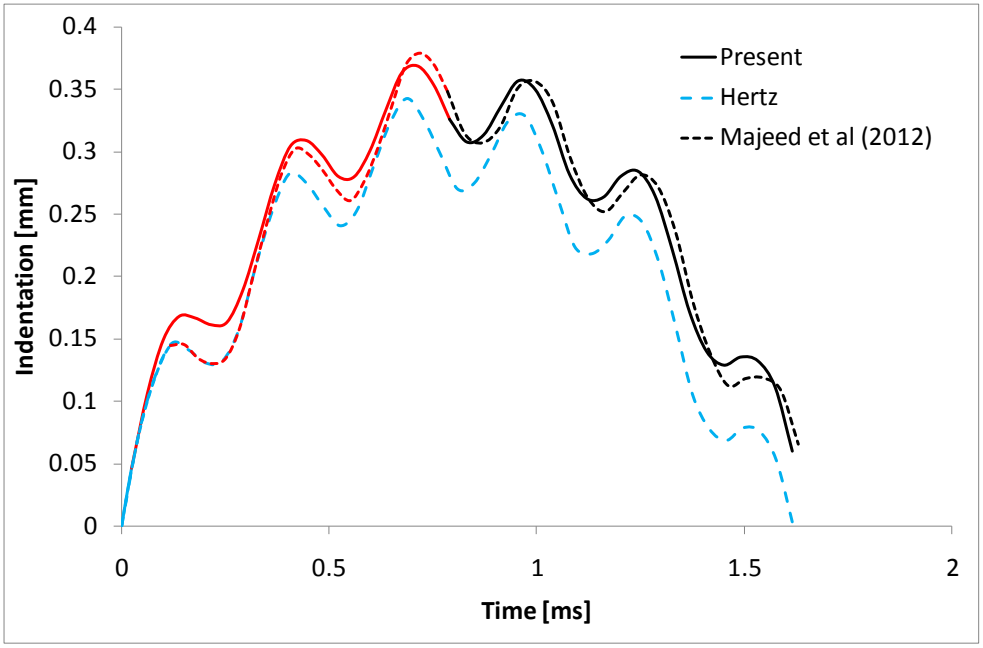

Figure 4.19: *Indentation history of Al/PVDF/PZT plate struck by steel impactor with initial impact speed of 2.0 [m/s].*

Effect of transverse shear deformation

In Section 2.6.2 it was shown that transverse shear deformation affects the displacement of a plate when the plate is moderately thick. The transverse shear deformation effect was modelled using the FSDPT. The effect of transverse shear deformation, on the impact response of a moderately thick trimorph plate, was investigated by comparing the impact response of the Al/PVDF/PZT plate obtained using both the CLPT and FSDPT. A thickness of 8.0 [*mm*] was used for the aluminium layer, making a total plate thickness of 10.0 [*mm*]. Since the planar dimension of the trimorph plate is 100 × 100 [mm^2], the thickness to length ratio is 1/10, satisfying the geometrical condition for moderately thick plates. The impact response, based on the two plate theories (CLPT and FSDPT) are shown in Figures 4.20 a – c. The results show that shear deformation affects the plate displacement (Figure 4.20a) but has negligible effect on the indentation and impact force histories (Figures 4.20b, c). This is because shear deformation effects become more pronounced at higher vibration modes, which have very little effect on the response of a large mass impact, as considered here. The present investigation is limited to the indentation and impact force of large mass impact events and therefore, all other results have been obtained using the CLPT.

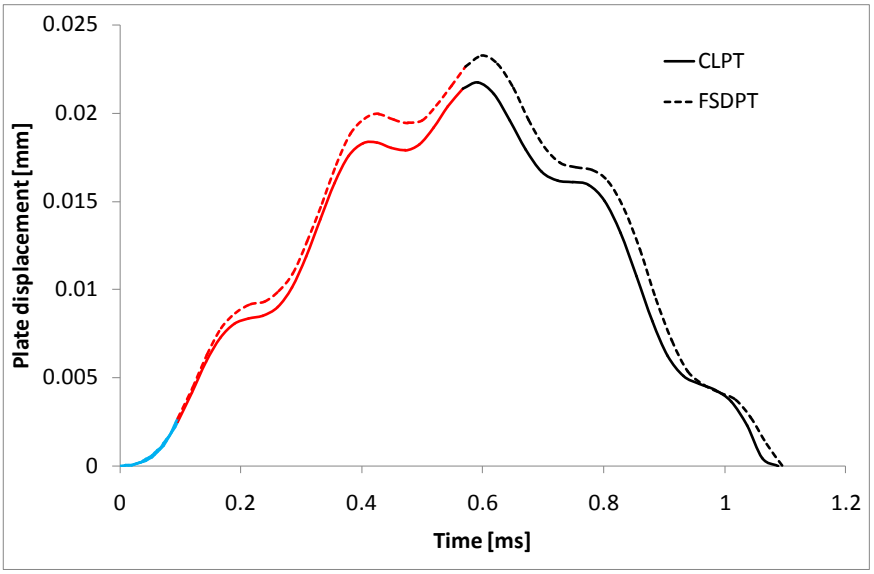

Figure 4.20a: *Plate displacement during impact of Al/PVDF/PZT plate based on CLPT and FSDPT.*

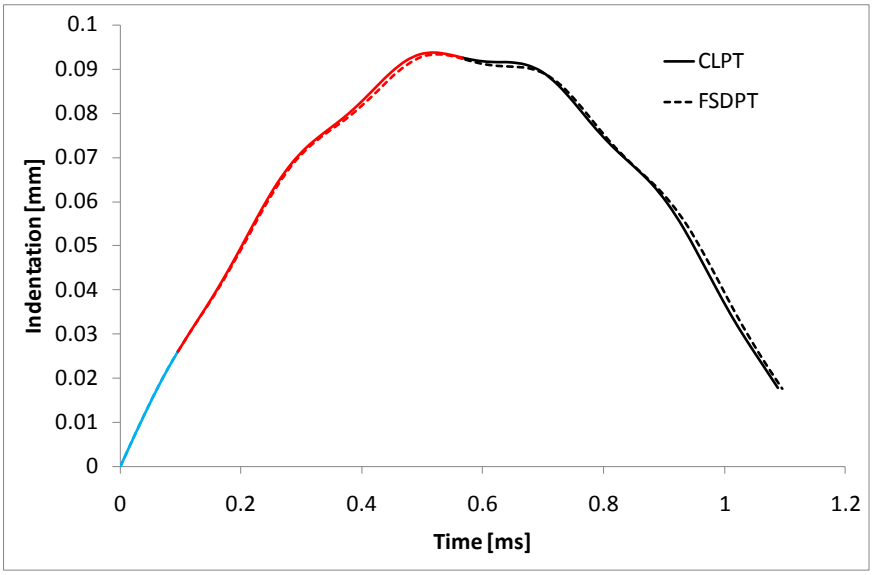

Figure 4.20b: *Indentation response during impact of Al/PVDF/PZT plate based on CLPT and FSDPT.*

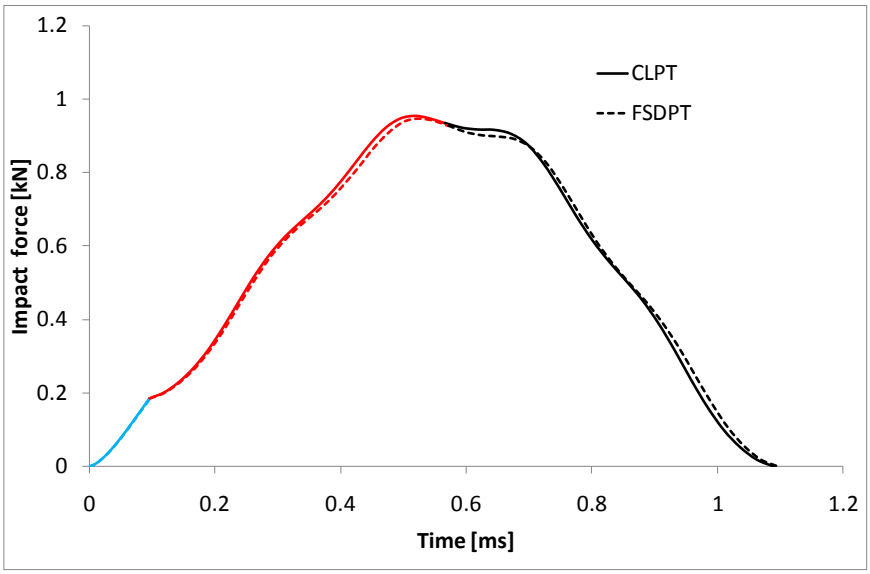

Figure 4.20c: *Force response during impact of Al/PVDF/PZT plate based on CLPT and FSDPT.*

For better understanding of the impact response of the Al/PVDF/PZT plate, the influence of critical impact and geometrical parameters on the impact response is investigated. The effects of impactor mass, impactor size, initial impact velocity and the thickness and aspect ratio of the plate, on the impact response were examined and the results are shown in Figures 4.21 to 4.25.

Effect of impactor mass

To study the effect of the impactor mass on the impact response of the Al/PVDF/PZT plate, the impactor mass was varied without changing the radius of the impactor in contact with the plate. In practice this can be achieved by using impactors with hemispherical contact end. A comparison of the contact force histories for different impactor masses is shown in Figure 4.21. It is observed that a higher impactor mass results in a higher maximum impact force, longer impact duration and more oscillations in the impact force. Also, the permanent indentation increases with increasing impactor mass. Note that comparison of the permanent indentation is performed by visual inspection of the plots for the impact force histories; the larger the vertical height of the elastoplastic response (red lines), the larger the permanent indentation and vice versa. This observation is found to be consistent with permanent indentation results of the indentation history plots. The latter are not shown because they are not necessary for the discussions in this investigation.

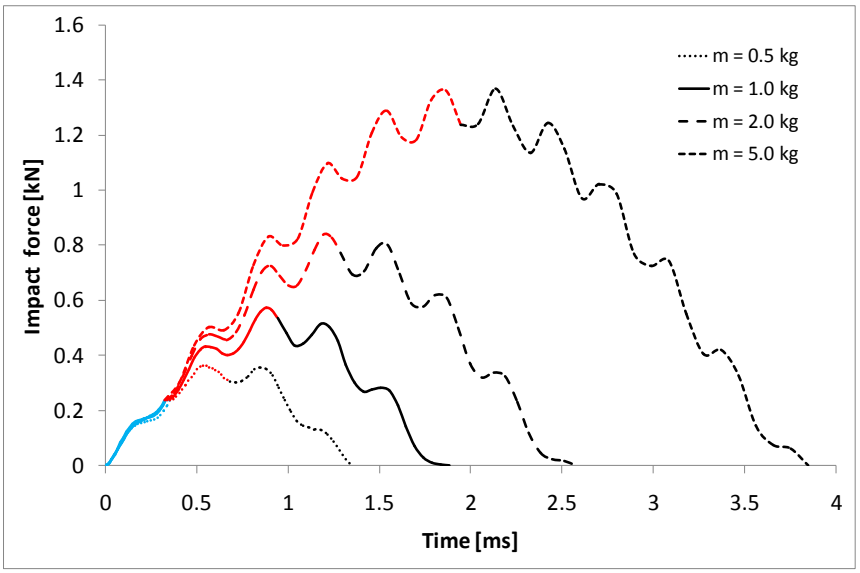

Figure 4.21: *Effect of impactor mass on the impact response of Al/PVDF/PZT plate.*

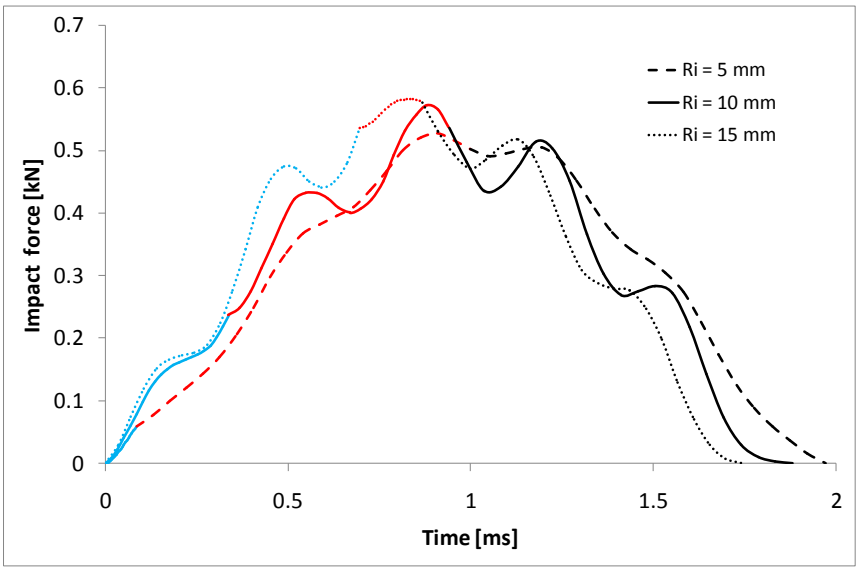

Figure 4.22: *Effect of impactor size on the impact response of Al/PVDF/PZT plate.*

Effect of impactor size

The impactor size is represented by the radius of the impactor in contact with the target. The radius of the impactor was varied without changing the impactor mass. Again, this can be achieved in practice by using impactors with hemispherical contact end. The effect of the impactor size is simulated using the impact force histories, as shown in Figure 4.22. An increase in the impactor size results in a higher maximum impact force, shorter impact duration, and

smaller permanent indentation. This suggests that a higher maximum impact force does not always mean more local damage.

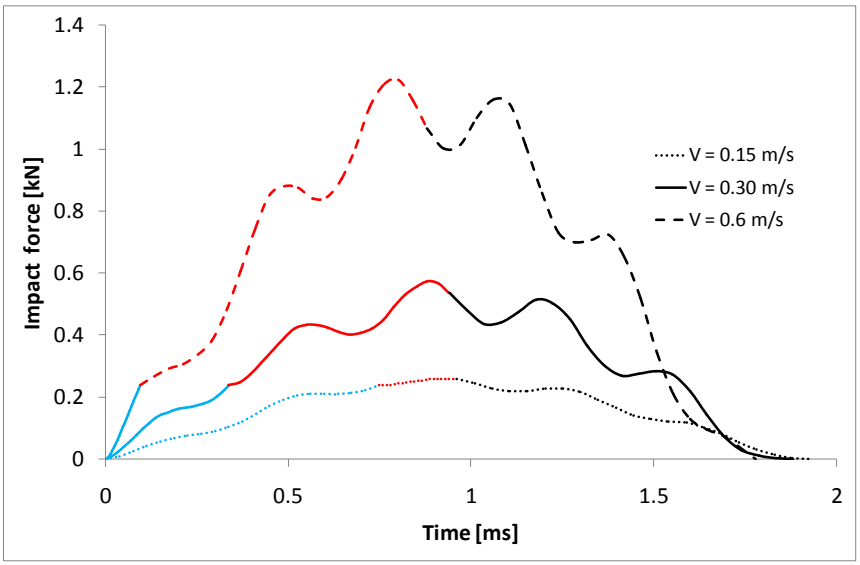

Figure 4.23: *Effect of impact velocity on the impact response of Al/PVDF/PZT plate.*

Effect of initial impact velocity

The effect of the initial impact velocity on the impact response of the Al/PVDF/PZT plate is shown in Figure 4.23. For a drop weight impact, an increase in the drop height increases the initial impact velocity and vice versa. The results reveal that a higher initial impact velocity results in a higher maximum impact force, larger permanent indentation and slightly shorter impact duration.

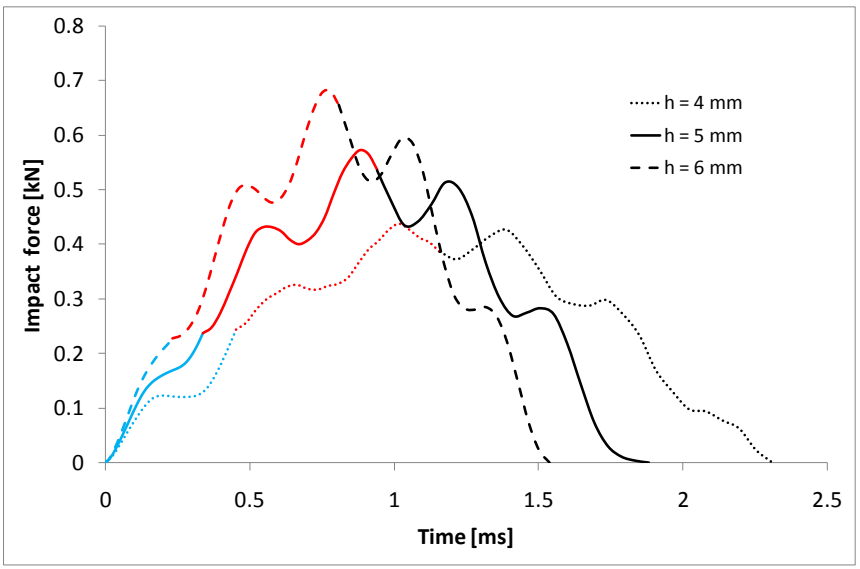

Figure 4.24: *Effect of thickness on the impact response of Al/PVDF/PZT plate.*

Effect of plate thickness

The total thickness of the Al/PVDF/PZT plate was varied by changing the thickness of the Al layer. Hence, the thicknesses of the Al layer used in the simulations are 2 [*mm*], 3 [*mm*] and 4 [*mm*]. The thickness effect is shown in Figure 4.24. The figure shows that increasing the total thickness of the plate results in a shorter impact duration and higher maximum impact force. Also, the permanent indentation increases due to more a localised response.

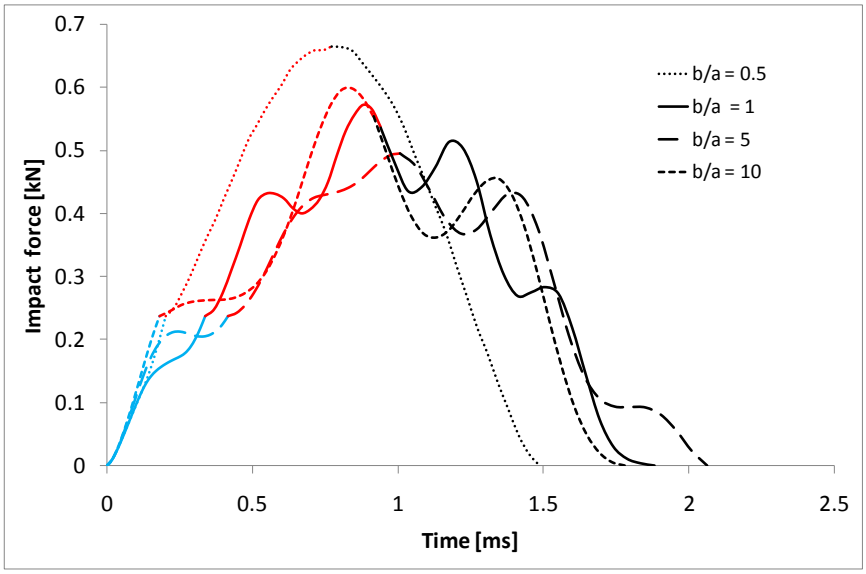

Figure 4.25: *Effect of aspect ratio on the impact response of Al/PVDF/PZT plate.*

Effect of plate aspect ratio

The effect of the aspect ratio of the plate (i.e. the ratio of the planar dimensions) on the impact response was considered by simulating the impact response for four different aspect ratios as shown in Figure 4.25. An ideal aspect ratio for comparison is 1. Figure 4.25 shows that for an aspect ratio of 0.5, the response becomes more localised and it is characterised by a higher maximum impact force, shorter impact duration, more post-yield deformation and less oscillations. For an aspect ratio of 5, the maximum contact force is lower and the impact duration is longer. This is because the plate with an aspect ratio of 5 is more flexible than that with an aspect ratio of 1. However, an aspect ratio of 10 shows a slightly more localised response in comparison to an aspect ratio of 1. This shows that the flexibility of a plate during impact cannot be fully understood by considering the aspect ratio alone.

Consideration of initial impact energy

Figure 4.26 shows the impact response of the Al/PVDF/PZT plate for the same initial impact energy but different impactor mass and velocity. The response for the impact event with smaller impactor and higher initial velocity produces a more localised response, leading to higher permanent indentation, less oscillations in the impact force and shorter impact duration. Hence, the initial impact energy alone is not sufficient to give a good description of the kind of impact response to expect.

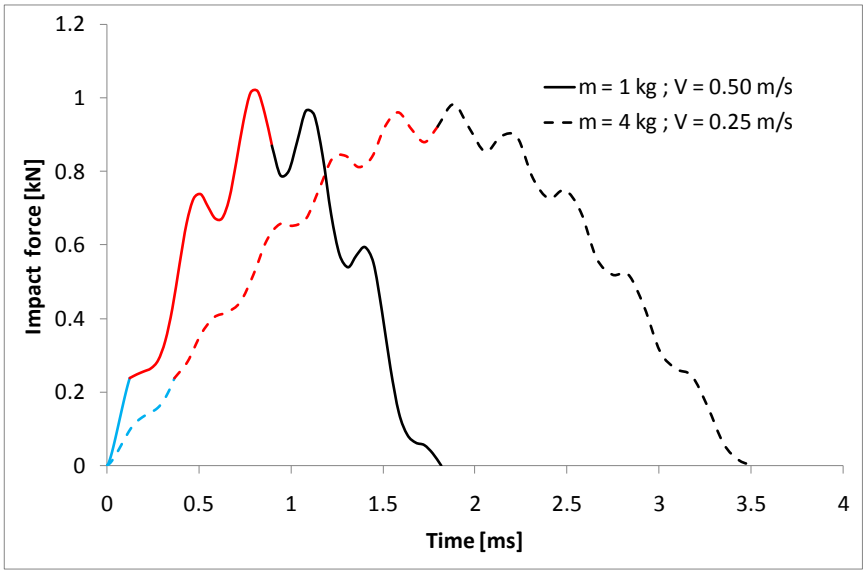

Figure 4.26: *Impact response of Al/PVDF/PZT plate for the same impact energy and different impact mass and velocity.*

Effect of flexibility of trimorph plate

A major goal of this research is to investigate the possibility of applying the trimorph plate with a piezo-actuating layer for mitigation of elastoplastic impact effects. It has been shown that piezoelectric actuation can be used to alter the effective stiffness (flexibility) of a structure by making it apparently stiffer or more compliant (Waisman and Abramovich, 2002). The effective stiffness of a structure with piezoelectric layer actuation is the sum of the mechanical stiffness and the induced piezoelectric stiffness. The latter may be positive or negative, depending on whether the induced piezoelectric stress is tensile or compressive. The effect of flexibility on the impact response of plates has been studied by Christoforou and Yigit (1998b). However, only a few studies have attempted to investigate the application of piezo-actuation during impact (Yigit

and Christoforou, 2000; Saravanos and Christoforou, 2002). A parametric study was carried out to demonstrate that the flexibility of a trimorph plate could be exploited to mitigate impact effects. To achieve this, a parameter, α, used to alter the effective stiffness of the trimorph plate without changing the dimensions or material properties of the plate (as would be expected during piezo-actuation – see Section 5.4.1) was introduced as shown in equation (4.44a). α represents the percentage change in the effective stiffness of the plate. When $\alpha < 0$, the plate is apparently less flexible and when $\alpha > 0$, the plate is apparently more flexible. The normal case is represented by $\alpha = 0$ when the effective stiffness is determined by the mechanical stiffness only.

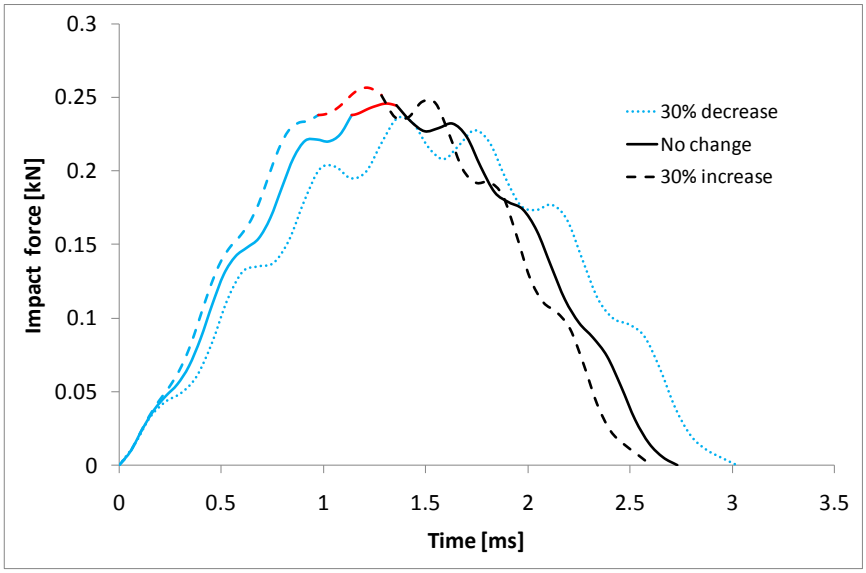

Figure 4.27: *Influence of apparent flexibility on the impact response of Al/PVDF/PZT plate.*

Figure 4.27 shows the effect of α on the impact response of the Al/PVDF/PZT plate. In this figure, the mass of the impactor is 2.0 [*kg*] and the impact velocity is 0.1 [*m/s*]. Three cases are considered for illustration purposes i.e. $\alpha = 0,\ \alpha = -0.3,$ and $\alpha = 0.3$. The reference point is taken when the effective stiffness is equal to the mechanical stiffness i.e. $\alpha = 0$. For $\alpha = 0$, the maximum impact force is 246.15 [*N*], the impact duration is 2.73 [*ms*] and the permanent indentation is 3.36 [*μm*]. When $\alpha = -0.3$, the effective stiffness is 30% higher than normal ($\alpha = 0$) and the impact response, which is more localised, is characterised by a higher maximum impact force (263.45 [*N*]),

shorter impact duration (2.60 [*ms*]) and larger permanent indentation (5.10 [*μm*]). For $\alpha = 0.3$, the effective stiffness is 30% lower than normal and the response has become purely elastic with no permanent indentation. The maximum impact force is about 4.0% lower than for $\alpha = 0$ and the impact duration is longer (3.02 [*ms*]). The implication is that an impact, which should ordinarily result in a permanent indentation, can be converted to one with no permanent indentation. This result is significant because it demonstrates that alteration of the effective stiffness of the plate could be exploited to either reduce or completely eliminate elastoplastic impact effects. In general, an increased flexibility through reduction of the effective stiffness of the plate would result in reduced local effects and increased global effects, and vice versa. The alteration of the effective stiffness of a plate with piezoactuator layer(s) can be achieved through the piezo-actuation effect (Waisman and Abramovich, 2002); this notion is investigated further in the next chapter.

4.5 Chapter conclusions

This chapter presents a detailed treatment of the impact response of rectangular plates. The impact response of two kinds of plate was studied, namely: transversely inflexible (very thick) and transversely flexible (thin to moderately thick) plates. For the former, the response was predicted using half-space assumptions and the investigations showed that the contact model used to predict the impact force was an important factor on the resulting predictions. It was also observed that the amount of impact energy dissipated as non-recoverable plastic deformation was a function of the initial impact velocity, i.e. a high initial velocity results in more non-recoverable plastic deformation.

An analytical solution algorithm called the FILM was developed to solve the nonlinear models for the elastoplastic impact response of transversely inflexible plates. The solution algorithm was shown to produce results which matched those obtained by direct numerical integration of the nonlinear models using the NDSolve function in *Mathematica*™. The implications of applying the FILM to solve the nonlinear impact models for a transversely flexible plate were discussed, and it was suggested that the FILM could be used to solve small mass impact problems where there are no oscillations in the impact force. An example of a small mass impact event with non-oscillating impact force is the infinite

plate impact, and the FILM was successfully used to determine the impact response of an infinite plate case study. The strengths of the FILM approach are its simplicity, inherent stability, fast-convergence rate and the fact that it could be checked manually. However, when it is applied to solve the nonlinear models of a transversely flexible plate it becomes semi-analytical, because the time at the boundaries of each discretisation must be determined numerically. A computer implementation is then required and the number of discretisations needed to obtain accurate results is more compared to the case of transversely inflexible plates.

The vibration models formulated in Chapter two and the new contact model developed in Chapter three were combined in Section 4.4 of this chapter using the complete modelling approach, to investigate the impact response of a transversely flexible trimorph plate. The investigations show that the contact model used to predict the impact force of a large mass impact event can significantly affect the resulting predictions, and also limit detailed description of the impact response. Transverse shear deformation was found to have no significant effect on the indentation and impact force histories of a moderately thick trimorph plate subjected to large mass impact. Critical impact and geometrical parameters such as impactor mass, impactor velocity, impactor size, plate thickness and plate aspect ratio were shown to influence the impact response of the trimorph plate. Finally, a parametric study was carried out to show that elastoplastic impact effects could be reduced or eliminated by altering the effective stiffness of the plate; an observation that could be exploited for active impact control. Control of the effective stiffness is practically realisable using piezoactuators and further investigations of this notion are discussed in Chapter five.

CHAPTER FIVE

MITIGATION OF ELASTOPLATIC IMPACT EFFECTS USING PIEZOACTUATORS

Chapter summary

Low-velocity impact of transversely flexible structures by rigid blunt objects could result in damage of the structure. Studies on the mitigation of the impact damage effects are mostly limited to passive mitigation strategies such as structural fortification using materials with higher stiffness and better impact energy absorption using sandwich construction with foam core. Relatively little has been done in the area of active mitigation of low-velocity impact damage. This chapter investigates the active mitigation of low-velocity impact damage by means of induced pre-stress. The investigations were carried out analytically using a novel nonlinear elastoplastic contact model (see Section 3.2) in the complete modelling approach (see Section 4.4) to account for the localised response of the plate considered. A linear piezoelectric theory was incorporated into the impact model to account for induced strain actuation. The investigation focuses on the effect of an induced pre-stress, produced by piezoelectric actuation, on the impact response of a rectangular plate incorporating PZT layers, and on how this effect can be utilised for active mitigation of elastoplastic impact effects. The chapter concludes with a discussion of the possible technological issues involved with practical implementation of induced pre-stress as an active mitigation strategy against elastoplastic impact effects.

5.1 Review of impact damage of transversely flexible plates

The impact of thin flexible plates by rigid blunt object normally results in very high localised stresses that can damage the plate (Abrate, 1998). Therefore, impact damage of flexible structures is an active area of theoretical, numerical and experimental research. Understanding of impact damage of thin plates is still evolving because it is a very complex and transient (micro- to milliseconds) phenomenon involving many variables (material properties of the plate and impactor, impactor shape and mass, relative impact speed of the plate

and impactor, geometry of the plate, and boundary conditions of the plate) and different failure mechanisms. For thin monolithic metallic plates impact damage occurs in the form of localised plastic deformation and/or perforation (Goldsmith, 2001). During low- to medium-velocity impact on a thin monolithic metallic plate, plastic deformation may occur without perforation, but the plastic deformation can lead to a significant change of the plate stiffness, relative to its original design value. The damage mechanism of thin monolithic metallic plates during high-velocity impact involves both plastic deformation and perforation. With thin laminated plates, impact damage may involve both permanent deformation and/or delamination. Delamination is potentially dangerous because even though it may be initiated at a high load compared to the load required to initiate local permanent deformation, the delamination damage propagates at a much lower load once initiated. In composite laminates, delamination is caused by the global effect of the impact (Yigit and Christoforou, 2000), whereas the local effect of the impact produces a permanent deformation that is due to both plastic deformation of the matrix and damage of the fibres, i.e. fibre breaking, kinking, and/or micro-buckling. The local permanent deformation can be estimated using static contact models that account for post-yield effects (Yigit and Christoforou, 1994).

Olsson (2001) formulated analytical models for the prediction of impact damage initiation and growth during large mass impact. The models were developed based on quasi-static bending assumption and the local indentation was estimated using the Hertz contact model. The study revealed that the critical load for delamination was generally insensitive to both the geometry and boundary conditions, when the effects of membrane stretching are neglected. The analytical model was validated by comparing analytical predictions with experimental results. Olsson (2003) studied the delamination onset of laminated composite plates during small mass impact. The expression for the peak impact load was derived based on the Hertz contact model and from the closed-form solutions of three asymptotic impact cases namely: (i) fully immobile plate response, (ii) fully mobile plate with only bending response and (iii) fully mobile plate with only transverse shearing response. The predicted peak load obtained using the analytical formulation compared well with previously published experimental results. The expression for the peak impact load was then used to determine the threshold impact velocity required to initiate delamination.

Olsson *et al* (2006) derived closed-form solutions to determine the delamination threshold load and velocity for small mass impact upon flexible plates. The closed-form solutions were derived based on a modified form of the Hertz contact model that accounts for thickness effect. The results of the closed-form solution were shown to be in good agreement with selected finite element results and previously published experimental data. Zheng and Binienda (2007) studied the effect of permanent indentation on the delamination threshold of composite plates subjected to small mass impact. A linearised elastoplastic contact model was used to derive a closed-form solution for the peak contact force. The threshold impact velocity to initiate delamination was determined using the peak contact force and a quasi-static delamination threshold load criterion. The study revealed that the peak force predicted, when the impact force is estimated using the elastic Hertz contact model, is significantly higher than that predicted when an elastoplastic contact model is used to estimate the impact force. It was concluded that using the Hertz contact model to estimate the impact force could lead to significant errors in the estimation of the delamination threshold.

As explained earlier delamination in a composite laminate is caused by the global effect of the impact. The local effect of the impact may lead to permanent indentation which is another type of impact damage. Permanent indentation is produced as a result of elastoplastic indentation during impact loading. Contact models for elastoplastic indentation have been developed for composite laminates (Sun and Yang, 1980; Yigit and Christoforou, 1994; Majeed *et al*, 2012) and metallic targets (Stronge, 2000a; Brake, 2012; and the new contact model presented in Section 3.2) and can be used to estimate the permanent indentation. Furthermore, elastoplastic contact models give a more accurate prediction of the impact response compared to the Hertz contact model (Yigit and Christoforou, 1994; Majeed *et al*, 2012). Since the size of the permanent indentation and the initiation of delamination are dependent on the maximum impact force it is important to predict the maximum impact force accurately, hence, the need to use elastoplastic contact models for impact damage analysis.

The severity and type of damage (local or global) during impact of a laminated plate depends on the impact force. The implication is that impact damage effects can be mitigated by controlling the impact force. Increasing the

shock effect of the impact force leads to greater permanent deformation (local damage) and less delamination (global damage) and vice versa (Yigit and Christoforou, 2000). Since the impact response of a transversely flexible plate is determined by interactions between the plate vibration and the impactor displacement, a change in the vibration response of the plate inevitably leads to a change in the impact response. Vibration control of a transversely flexible plate can be achieved via induced strains produced by the actuation of bonded PZT layers (Mitchell and Reddy, 1995; Liew *et al*, 2004). Hence, the impact force can be controlled by the application of induced strains produced by the actuation of bonded PZT-layers. In this chapter a strategy is proposed for the mitigation of elastoplastic impact effects i.e. plastic deformation and damage. The strategy is based on the use of induced-strain effect of bonded PZT layers to control the impact force, and consequently the impact damage. An elastoplastic contact model is applied in the formulation of the impact models to give a more accurate estimate of the impact damage.

5.2 Impact damage mitigation

Impact damage of flexible structures due to low-velocity impact by rigid blunt objects can be very severe and potentially dangerous. For instance the impact of a freely flying runway debris on an aeroplane body can cause severe localised damaged. Damage mitigation in this case should address the reduction of damage effects on the structure since the debris is considered to be sacrificial. In a situation where an accidental impact occurs between a pedestrian and a car body, the car body becomes sacrificial in relation to the pedestrian. Hence, damage mitigation in this case should address reduced shock transfer to the pedestrian and this may be achieved by reducing the local effect of the impact. Several studies have been carried out to investigate novel strategies for mitigating impact damage effects. This section discusses some of the passive and active strategies that have been investigated in previous studies.

5.2.1 Passive mitigation of impact damage

Mitigation of impact damage is generally considered under two sub-areas namely: *impact damage resistance* and *impact damage tolerance*. The former is concerned with resistance to damage formation and propagation while the later

is concerned with the ability of the impacted structure to safely perform its intended function within an allowable damage size (Olsson, 2001; Emile and Matthew, 2003). Impact damage mitigation strategies may improve either or both. Impact damage resistance is normally achieved through structural stiffening while impact damage tolerance is achieved using more resilient materials or structural designs that are capable of absorbing most of the impact energy in a way that minimises the damage size and retains structural integrity. A lot has been done in the area of passive mitigation of impact damage. Some of the passive mitigation strategies that have been applied to laminated composite structures include fibre toughening, matrix toughening, interface toughening, introduction of through-the-thickness reinforcement, selective interlayering and use of hybrid composites (Angioni *et al*, 2011). Emile and Matthew (2003) discussed various passive mitigation strategies for the development of impact damage tolerant composites for aerospace structures. The passive mitigation strategies discussed were essentially novel material design concepts that included stitching, Z-pinning and 3-D composites. The authors concluded that the best material design concepts for impact damage resistance are planar woven and non-crimp fabric composites, while Z-pinned composites were recommended for impact damage tolerance. It was also stated that 3-D composites show considerable promise for impact tolerant material design. The potential of 3-D composites as impact tolerant materials have also been discussed by Mouritz *et al* (1999) and Kamiya *et al* (2000). A more recent study (Mouritz and Cox, 2010) revealed that up to 20% increase in mechanical properties can be achieved with 3-D composites compared to their equivalent 2-D composites.

Shape memory alloys (SMAs) have being used for passive mitigation of impact damage although they belong to the category of smart materials. In their passive state SMAs can absorb significant levels of impact energy through plastic deformation and stress-induced phase transformation, i.e. changing from an austenitic to martensitic phase (Angioni *et al*, 2011). Lau *et al* (2004) studied the low-velocity impact response of glass-epoxy composite plates fitted with integrated stitching in the form of SMA wires. The stitched SMA wires helped to improve the through-the-thickness reinforcement of the glass-epoxy composite plate. Experimental and theoretical results revealed that the tensile strength of the SMA stitched composite plate was increased and the number of impact-

induced translaminar cracks was reduced compared to the unstitched composite plate. Analytical studies conducted by Khalili *et al* (2007a; 2007b) showed that SMA wires embedded within a thin composite plate could significantly improve the damage resistance of the composite plate to low-velocity impact. The volume fraction, orientation and through-the-thickness location of the SMA wires were all found to influence the impact damage of the plate. More on the passive impact damage resistance and damage suppression using hybrid composites with embedded SMA wires, can be found in Angioni *et al* (2011).

5.2.2 Active mitigation of impact damage

The literature on active mitigation of impact damage of flexible structures when impacted by rigid blunt objects is limited (Yigit and Christoforou, 2000). This can be attributed to the fact that active mitigation of impact damage is challenging due to the complex and highly transient nature of the problem. Many impact events typically occur in a time frame of micro- to milliseconds and may not allow sufficient time for any meaningful control action to be taken during the impact. Furthermore, the uncertainties in estimating the impactor parameters (mass, velocity and size) make it difficult to determine the appropriate level of active mitigation (Yigit and Christoforou, 2000). Nevertheless, the active mitigation of impact damage using embedded SMA wires has been investigated (Khalili *et al*, 2007d; Angioni *et al*, 2011) and a good review of investigations in this area can be found in Angioni *et al* (2011). Khalili *et al* (2007d) studied the effect of active stiffening in relation to the low-velocity impact response of a composite plate with embedded SMA wires. The stiffness of the hybrid composite plate incorporating SMA wires was divided into two groups, namely: *essential* and *acquired* stiffness. The former is the stiffness of the manufactured hybrid composite plate without any activation, while the latter is the extra stiffness induced in the manufactured hybrid composite plate following activation. The sum of the essential and acquired stiffnesses gives the total stiffness of the hybrid composite plate when the active elements (SMA wires in this case) are actuated. The results of the study by Khalili *et al* (2007d) showed that the interactive effect between the essential stiffness and the acquired stiffness can improve the impact damage resistance of the SMA hybrid

composite plate, compared to a similar hybrid composite plate with embedded steel wires.

The smart stiffening procedure proposed by Khalili *et al* (2007d) is conceptually reasonable but impractical with SMA actuators because of the relatively slow response time of SMA wire; typically 3 – 4 seconds (Thompson and Loughlan, 1995). An impact event would have finished before actuation of the SMA wires could be realised. Therefore, actuators that can operate within realistic impact times are more suitable candidates for active impact mitigation. Piezoactuators are the fastest known actuators, having a response time of a few milliseconds (Thompson and Loughlan, 1995; Yigit and Christoforou, 2000). As observed from the results presented in Section 4.4.2.2 and previous studies (Anderson, 2005; Olsson, 2002; Yigit and Christoforou, 2000; Saravanos and Christoforou, 2002; Khalili *et al*, 2007a; 2007b) large mass impact events usually have an impact duration of a few milliseconds. Hence, piezoactuators can be used for active mitigation of large mass impact damage. On the other hand, small to medium mass impact events normally have impact durations in the range of microseconds and therefore only the post-impact induced damage effects may be actively mitigated in such cases (Yigit and Christoforou, 2000).

Yigit and Christoforou (2000) proposed a linear quadratic regulator (LQR) controller for active impact control and showed that the energy transferred to the structure can be reduced by active control of the panel stiffness. The technique was used to create a more localised impact response, thereby reducing the vibration energy absorbed by the structure. Saravanos and Christoforou (2002) studied the impact response of adaptive piezoelectric laminated plates. Control of the impact response of the piezoelectric laminated plate was implemented using *state feedback* and *output feedback* controllers. The former was based on LQR controllers while the latter was based on the signals produced by piezoelectric sensors. The study demonstrated that considerable reductions in the impact force of laminated plates can be achieved by active plate bending or damping induced by piezoelectric actuators. However, the main issues with the practical implementation of the controllers used in that study were:

a) The state feedback controllers require prior knowledge of all the state variables (impactor and plate displacements and velocities). This

information may be difficult to estimate in real time (Yigit and Christoforou, 2000).

b) The sensory feedback controllers require sufficient time in order to provide feedback signals for use by the actuators. Given that the maximum impact force generally occurs during the impact loading which is usually within a time of about half the impact duration, the maximum or critical impact effects may have occurred before the sensor-actuator feedback loop is complete.

A notable limitation of the study by Saravanos and Christoforou (2002) is that the impact models were formulated based on a linearised elastoplastic contact law that takes no account of permanent indentation effects. In the present investigation, an elastoplastic contact model that accounts for permanent indentation effects has been used. Also, the impact damage mitigation strategy proposed here is based on the concept of pre-stressing induced by piezo-actuation; this idea is explored in Section 5.4.

5.3 Piezoelectric actuation effect

Piezoelectric effect is a physical phenomenon exhibited by certain crystalline materials whereby these materials generate surface electric charges when an external stress is applied (Preumont, 2011). Examples of materials that exhibit this behaviour are Rochelle salt, quartz, tourmaline and lead zirconate titanate (PZT). This effect was discovered more than a century ago by the Curie brothers. The production of surface electricity due to an externally applied stress is known as the *direct piezoelectric effect* and is normally applied for sensing. The *converse piezoelectric effect* is also possible and involves the generation of induced strain in the material upon application of an electrical voltage. The converse effect is applied in actuators to generate precisely controllable induced strains (or stresses).

In their natural state piezoceramics do not exhibit any piezoelectricity. Natural piezoceramics contain crystals that have no centre of symmetry and the electric dipoles are randomly oriented with a net macroscopic dipole of zero. This state of natural piezoceramics occurs below a critical temperature called the *Curie temperature*. Piezoelectric effects are imparted to piezoceramic through a process known as *poling*. During poling a high direct current electric

field is applied to the piezoceramic below the Curie temperature. This causes the dipoles to align and produces a net macroscopic dipole in the poling direction that remains after the electric field has been removed. Once a net dipole is created in the piezoceramic, it acquires piezoelectricity and can convert mechanical energy to electric energy and vice versa. The piezoelectric property of a poled piezoceramic is lost if it is subjected to a temperature above its Curie temperature or when a high electric field is applied in a direction opposite to the poling direction. This process is known as *depoling*. The best known piezoceramics that can be used as actuators are the PZTs and they are capable of achieving induced strains of up to 1000 microstrain (Chopra, 2002). A good discussion on smart materials including piezoceramics has been presented by Chopra (2002). Also, discussions on piezoelectric laminate theory for distributed sensing and actuation can be found in Lee (1999), Reddy (1999) and Preumont (2011).

As explained above, poled piezoceramics can produce electric charges when a stress is applied and also produce induced strains when an electric field is applied. The constitutive equations (stress-strain relationship) of a poled piezoceramic layer after neglecting thermal effects are given as (Reddy, 1999; Chopra 2002):

$$\begin{Bmatrix}\sigma_{xx}\\ \sigma_{yy}\\ \sigma_{xy}\\ \sigma_{xz}\\ \sigma_{yz}\end{Bmatrix} = \begin{bmatrix}\bar{Q}_{11} & \bar{Q}_{12} & 0 & 0 & 0\\ \bar{Q}_{12} & \bar{Q}_{22} & 0 & 0 & 0\\ 0 & 0 & \bar{Q}_{66} & 0 & 0\\ 0 & 0 & 0 & \bar{Q}_{55} & 0\\ 0 & 0 & 0 & 0 & \bar{Q}_{44}\end{bmatrix}\left(\begin{Bmatrix}\varepsilon_{xx}\\ \varepsilon_{yy}\\ \varepsilon_{xy}\\ \varepsilon_{xy}\\ \varepsilon_{xy}\end{Bmatrix} - \Lambda\right) \tag{5.1}$$

where Λ is the controllable strain induced by piezoelectric actuation, and the other symbols are defined in Section 2.4. The elements of the mechanical stiffness matrix in equation (5.1) are defined in Section 2.4.1. The induced piezoelectric strains for piezoceramics are determined as (Chopra, 2002):

$$\Lambda = \begin{bmatrix}0 & 0 & d_{31}\\ 0 & 0 & d_{32}\\ 0 & 0 & 0\\ 0 & d_{24} & 0\\ d_{15} & 0 & 0\end{bmatrix}\begin{Bmatrix}\mathcal{E}_1\\ \mathcal{E}_2\\ \mathcal{E}_3\end{Bmatrix} \tag{5.2}$$

where d_{jk} represent the piezoelectric strain (or stiffness) coefficients and $\mathcal{E}_j$ represents the electric field intensity in the *j*th direction. d_{jk} can be defined as the ratio of the relative strain along the *k*-axis to the applied electric field along the *j*-axis (Thompson and Loughlan, 1995). Typically, the poling direction for

piezoceramics is the 3-direction (see Figure 5.1). Hence, d_{31} and d_{32} characterises direct strains in the 1- and 2-directions, produced by an electric field in the 3-direction ($\mathcal{E}_3$). Also, d_{24} and d_{15} characterises the shear strains in the 2-3 and 3-1 planes produced by electric fields $\mathcal{E}_2$ and $\mathcal{E}_1$ respectively. Note that $d_{31} = d_{32}$ and $d_{24} = d_{15}$ for piezoceramics.

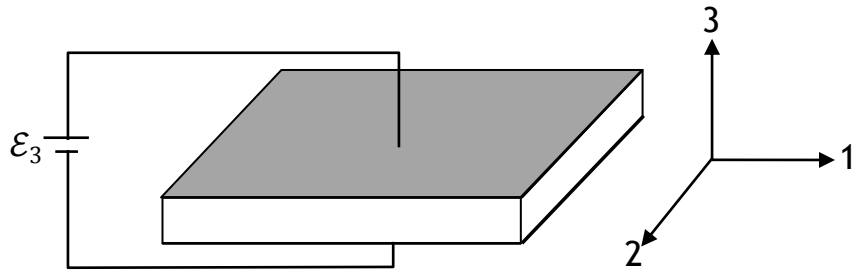

Figure 5.1: *Piezoelectric sheet poled along the 3-direction and having planar surface covered with electrode.*

Equation (5.1) represents the converse piezoelectric effect of a poled piezoceramic. The equations for the direct piezoelectric effect after neglecting thermal effects are given as (Reddy, 1999):

$$\begin{Bmatrix} D_1 \\ D_2 \\ D_3 \end{Bmatrix} = \begin{bmatrix} 0 & 0 & 0 & 0 & d_{15} \\ 0 & 0 & 0 & d_{24} & 0 \\ d_{31} & d_{32} & 0 & 0 & 0 \end{bmatrix} \begin{Bmatrix} \varepsilon_{xx} \\ \varepsilon_{yy} \\ \varepsilon_{xy} \\ \varepsilon_{xy} \\ \varepsilon_{xy} \end{Bmatrix} + \begin{bmatrix} e_{11} & 0 & 0 \\ 0 & e_{22} & 0 \\ 0 & 0 & e_{33} \end{bmatrix} \begin{Bmatrix} \mathcal{E}_1 \\ \mathcal{E}_2 \\ \mathcal{E}_3 \end{Bmatrix} \tag{5.3}$$

where e_{ij} represents the dielectric constant under constant strain. Equation (5.1) is used to derive the actuator equations while equation (5.3) is used to derive the sensor equations. Since the investigation in this chapter is limited to the application of actuation effect, the sensor equations are not presented here. For derivation of the sensor equations for distributed sensing reference can be made to the following literature (Lee, 1999; Reddy, 1999; Chopra, 2002; and Preumont, 2011).

For thin laminated plates the effect of transverse shear strains can be neglected and equation (5.1) becomes

$$\begin{Bmatrix} \sigma_{xx} \\ \sigma_{yy} \\ \sigma_{xy} \end{Bmatrix} = \begin{bmatrix} \bar{Q}_{11} & \bar{Q}_{12} & 0 \\ \bar{Q}_{12} & \bar{Q}_{22} & 0 \\ 0 & 0 & \bar{Q}_{66} \end{bmatrix} \begin{Bmatrix} \varepsilon_{xx} \\ \varepsilon_{yy} \\ \varepsilon_{xy} \end{Bmatrix} - \begin{bmatrix} \bar{Q}_{11} & \bar{Q}_{12} & 0 \\ \bar{Q}_{12} & \bar{Q}_{22} & 0 \\ 0 & 0 & \bar{Q}_{66} \end{bmatrix} \begin{bmatrix} 0 & 0 & d_{31} \\ 0 & 0 & d_{32} \\ 0 & 0 & 0 \end{bmatrix} \begin{Bmatrix} \mathcal{E}_1 \\ \mathcal{E}_2 \\ \mathcal{E}_3 \end{Bmatrix} \tag{5.4}$$

The first term on the right-hand-side of equation (5.4) represents the stresses due to the mechanical properties of the lamina while the second term

represents the stresses due to the piezoelectric properties, and the left-hand-side of the equation represents the resultant stresses. The strain vector $\{\varepsilon_{xx} \quad \varepsilon_{yy} \quad \varepsilon_{xy}\}^T$ is defined in equation (2.17). Note that $\varepsilon_{xx} = \varepsilon_x$ and $\varepsilon_{yy} = \varepsilon_y$. Integrating equation (5.4) along the thickness direction for each lamina and summing the resulting expression for all layers of the laminate gives

$$\begin{Bmatrix} N_{xx} \\ N_{yy} \\ N_{xy} \end{Bmatrix} = \begin{bmatrix} A_{11} & A_{12} & A_{16} \\ A_{12} & A_{22} & A_{26} \\ A_{16} & A_{26} & A_{66} \end{bmatrix} \begin{Bmatrix} \varepsilon_{xx}^0 \\ \varepsilon_{yy}^0 \\ \varepsilon_{xy}^0 \end{Bmatrix} + \begin{bmatrix} B_{11} & B_{12} & B_{16} \\ B_{12} & B_{22} & B_{26} \\ B_{16} & B_{26} & B_{66} \end{bmatrix} \begin{Bmatrix} k_{xx}^0 \\ k_{yy}^0 \\ k_{xy}^0 \end{Bmatrix} - \begin{Bmatrix} N_{xx}^p \\ N_{yy}^p \\ N_{xy}^p \end{Bmatrix} \tag{5.5}$$

where

$$\begin{Bmatrix} N_{xx}^p \\ N_{yy}^p \\ N_{xy}^p \end{Bmatrix} = \sum_{k=1}^{N_a} \begin{bmatrix} \bar{Q}_{11} & \bar{Q}_{12} & 0 \\ \bar{Q}_{12} & \bar{Q}_{22} & 0 \\ 0 & 0 & \bar{Q}_{66} \end{bmatrix} \begin{Bmatrix} d_{31}\mathcal{E}_3 \\ d_{32}\mathcal{E}_3 \\ 0 \end{Bmatrix} h_k \tag{5.6}$$

N_a is the number of piezo-actuated layers. The stiffness matrices and the strain and curvature vectors in equation (5.5) are already defined in Sections 2.2.5 and 2.4.1. Equation (5.6) represents the induced in-plane piezoelectric force and can be used to determine the force transferred to the host structure. Similarly, if equation (5.4) is multiplied by z and integration is carried out through the thickness of each layer, then, the moment resultants after summation for all the layers of the laminate are:

$$\begin{Bmatrix} M_{xx} \\ M_{yy} \\ M_{xy} \end{Bmatrix} = \begin{bmatrix} B_{11} & B_{12} & B_{16} \\ B_{12} & B_{22} & B_{26} \\ B_{16} & B_{26} & B_{66} \end{bmatrix} \begin{Bmatrix} \varepsilon_{xx}^0 \\ \varepsilon_{yy}^0 \\ \varepsilon_{xy}^0 \end{Bmatrix} + \begin{bmatrix} D_{11} & D_{12} & D_{16} \\ D_{12} & D_{22} & D_{26} \\ D_{16} & D_{26} & D_{66} \end{bmatrix} \begin{Bmatrix} k_{xx}^0 \\ k_{yy}^0 \\ k_{xy}^0 \end{Bmatrix} - \begin{Bmatrix} M_{xx}^p \\ M_{yy}^p \\ M_{xy}^p \end{Bmatrix} \tag{5.7}$$

where

$$\begin{Bmatrix} M_{xx}^p \\ M_{yy}^p \\ M_{xy}^p \end{Bmatrix} = \sum_{k=1}^{N_a} \begin{bmatrix} \bar{Q}_{11} & \bar{Q}_{12} & 0 \\ \bar{Q}_{12} & \bar{Q}_{22} & 0 \\ 0 & 0 & \bar{Q}_{66} \end{bmatrix} \begin{Bmatrix} d_{31}\mathcal{E}_3 \\ d_{32}\mathcal{E}_3 \\ 0 \end{Bmatrix} h_k z_k^a \tag{5.8}$$

z_k^a represents the distance from the mid-plane of the laminate to the centre of the k^{th} actuator layer. The piezoelectric force and moment resultants are only induced by actuated layers otherwise they are equal to zero irrespective of whether the layer is made up of a piezoelectric material or not. Equations 5.5 and 5.7 show that in the absence of an external stress (i.e. zero mechanical strains and curvatures) the in-plane force resultants and bending moment resultants are equal to the induced piezoelectric forces and moments respectively.

5.4 Active mitigation of elastoplastic impact effects using piezoactuators

The impact mitigation or control strategy proposed by Saravanos and Christoforou (2002) is based on strains and strain rates that are induced by piezoelectric actuators during the impact process. The induced strains produced active bending moments while the induced strain rates produced active damping. Actively induced bending moment and damping influence the plate vibrations which in turn influences the impact response. A challenge to the practical implementation of this strategy is that there may not be sufficient time for the actuator effect to be realised once the impact has been initiated because *in situ* sensory feedback is required and the impact duration is usually very short. However, the works of Saravanos and Christoforou (2002) and Yigit and Christoforou (2000) are important feasibility studies that provide qualitative insight to the underlying mechanics of impact control and how impact damage could be actively mitigated.

Perhaps a more practical strategy would be to actively prepare the material for the imminent impact using the concept of active pre-stressing. The term 'pre-stress' is used to imply that the induced stresses are generated in the structure before impact. Therefore, an active pre-stress is one that is generated just before a remotely sensed imminent impact occurs. Discussions on remote sensing are presented in Section 5.5. It is well known that pre-stressing a plate or beam by applying in-plane forces can increase or reduce its bending stiffness depending on whether a tensile or compressive force is applied (Reddy, 2004). Hence, it is proposed here that piezoactuator layers bonded to a plate can be used to actively alter the effective bending stiffness of the plate. This can be achieved by pre-stressing the plate using induced in-plane strains produced by the piezoactuators. In Section 4.4.2.2 it was shown that alteration of the effective bending stiffness of a plate influences its impact response. If pre-stressing of the plate is actively effected before an impact event is initiated, then, the plate can be 'braced' ready to receive the impact. Such active pre-stressing can be exploited to mitigate impact damage effects; demonstrating this is the main goal of this chapter.

Active pre-stressing created through induced tensile stresses produced by embedded SMA wires has been investigated in the vibration analysis of composite

beams and plates (Żak and Cartmell, 2000; Żak *et al*, 2003). Also, the application of pre-stress, induced by piezoactuators, in the vibration analysis and control of beams and plates has been studied by many others (Oguamanam *et al*, 1998; Hernandes *et al*, 2000; Waisman and Abramovich, 2002; Donadon *et al*, 2002). These studies show that the dynamic response of plates and beams can be significantly influenced by active pre-stress. When the pre-stress is due to induced tensile stresses (Żak and Cartmell, 2000; Oguamanam *et al*, 1998) the smart plate/beam becomes apparently stiffer i.e. its effective bending stiffness increases, and this phenomenon is known as *stress stiffening* (Oguamanam *et al*, 1998) or *active stiffening* (Waisman and Abramovich, 2002). In most studies in this area, active stiffening has been the focus of the investigation, but it is noted that a plate or beam with embedded or layered actuators can also be made to be more compliant, using induced compressive in-plane stresses (Waisman and Abramovich, 2002). Khalili *et al* (2007d) studied the effect of active stiffening on the impact response of a thin composite plate with embedded SMA wires. It was shown that the active stiffening induced by the wires can be used to improve impact resistance of the composite plate. However, as mentioned earlier, a drawback in using SMAs to actively induce pre-stress for impact damage mitigation is their relatively slow response. Studies on the effect of active pre-stressing induced by piezoactuators, on the impact response of smart structures have yet to be seen in the literature. The analysis that follows uses analytical models to investigate the effect of active pre-stressing, on the impact response of a plate with integrated piezoactuator layers. This is followed by a discussion on how piezoactuator pre-stressing can be practically implemented in order to mitigate elastoplastic impact effects.

5.4.1 Analytical models for investigating impact damage mitigation using active piezoelectric pre-stressing

A vibration model for the flexural oscillations of a thin rectangular plate in the presence of in-plane forces was derived in Section (2.2.4), see equation (2.13). After neglecting natural viscous damping equation (2.13) becomes:

$$\frac{\partial^2 M_x}{\partial x^2} + 2\frac{\partial^2 M_{xy}}{\partial x \partial y} + \frac{\partial^2 M_y}{\partial y^2} = \rho h \frac{\partial^2 w}{\partial t^2} - q(x,y,t) + N_x^i \frac{\partial^2 w}{\partial x^2} + 2N_{xy}^i \frac{\partial^2 w}{\partial x \partial y} + N_y^i \frac{\partial^2 w}{\partial y^2} \quad (5.9)$$

where N_x^i, N_{xy}^i, and N_y^i are initial in-plane forces. These forces are considered to be initial forces because they are applied prior to the application of any external excitation or static load and hence, they can be used to represent a pre-stress (initial stress) in the plate when the edges of the plate are fully restrained from in-plane displacements. In the present analysis, these forces are assumed to be created by piezo-actuation and can therefore be determined from equations (5.5) and (5.6) as:

$$\begin{Bmatrix} N_x^i \\ N_y^i \\ N_{xy}^i \end{Bmatrix} = -\begin{Bmatrix} N_{xx}^p \\ N_{yy}^p \\ N_{xy}^p \end{Bmatrix} = -\sum_{k=1}^{N_a} \begin{bmatrix} \bar{Q}_{11} & \bar{Q}_{12} & 0 \\ \bar{Q}_{12} & \bar{Q}_{22} & 0 \\ 0 & 0 & \bar{Q}_{66} \end{bmatrix} \begin{Bmatrix} d_{31}\mathcal{E}_3 \\ d_{32}\mathcal{E}_3 \\ 0 \end{Bmatrix} h_k \tag{5.10}$$

Assuming the electric potential across the actuators is constant then $\mathcal{E}_3 = V/h_k$, where V is the applied electric voltage. Equation (5.10) shows that $N_{xy}^i = 0$.

In order to simplify the analysis, but without loss of generality, a thin symmetric rectangular sandwich plate comprising of two PZT layers perfectly bonded at the top and bottom surface of an aluminium layer (PZI/Al/PZT) is investigated (see Figure 5.2). Due to the symmetry of the PZI/Al/PZT plate there are no stiffness coupling terms (i.e. $B_{ij} = 0$). Also, if the voltages applied on both actuators are equal in magnitude and in phase then there will be no induced piezoelectric moments; only induced in-plane forces are produced. Therefore, equation (5.7) becomes

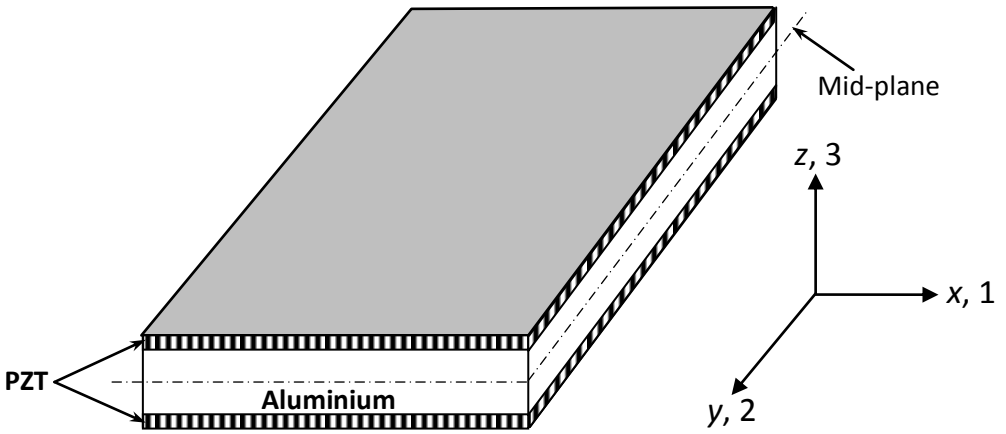

Figure 5.2: *Symmetric PZT/Al/PZT laminate with PZT layers pole in the 3 - direction.*

$$\begin{Bmatrix} M_{xx} \\ M_{yy} \\ M_{xy} \end{Bmatrix} = \begin{bmatrix} D_{11} & D_{12} & 0 \\ D_{12} & D_{22} & 0 \\ 0 & 0 & D_{66} \end{bmatrix} \begin{Bmatrix} k_{xx}^0 \\ k_{yy}^0 \\ k_{xy}^0 \end{Bmatrix} \tag{5.11}$$

Note that for symmetric laminates with multiple isotropic layers the following conditions apply: $A_{16} = A_{26} = B_{16} = B_{26} = D_{16} = D_{26} = 0$ (Jones, 1999), and these conditions have been applied in arriving at equation (5.11). Also, $\bar{Q}_{11} = \bar{Q}_{22}$ so that $D_{11} = D_{22}$. Substituting equation (5.11) in equation (5.9) and using the curvature relations in equations (2.18) of Section 2.2.5, the following PDE is derived:

$$\rho h \frac{\partial^2 w}{\partial t^2} + D_{11}\left(\frac{\partial^4 w}{\partial x^4} + \frac{\partial^4 w}{\partial y^4}\right) + 2(D_{12} + 2D_{66})\frac{\partial^4 w}{\partial x^2 \partial y^2} + N_x^i \frac{\partial^2 w}{\partial x^2} + N_y^i \frac{\partial^2 w}{\partial y^2} = q(x, y, t) \tag{5.12}$$

After applying the Galerkin solution approach (see Section 2.6.1) to equation (5.12) the following reduced model was derived.

$$\{\ddot{W}_1\}_{mn} + K_{eff}\{W_1\}_{mn} = \frac{4F(t)}{\rho hab}(-1)^{(m+n-2)/2} \tag{5.13}$$

where W_1 is the displacement of the plate, $F(t)$ is the impact force and

$$K_{eff} = \frac{\pi^4}{\rho h}\left[D_{11}\left(\frac{m^4}{a^4} + \frac{n^4}{b^4}\right) + \frac{2m^2n^2(D_{12} + 2D_{66})}{a^2b^2}\right] + \frac{\pi^2}{\rho h}\left[N_x^i\left(\frac{m^2}{a^2}\right) + N_y^i\left(\frac{n^2}{b^2}\right)\right]$$

In arriving at equation (5.13) the external excitation was considered to be a point load at the centre of the plate. The effective bending stiffness is comprised of both the mechanical stiffness and the induced piezoelectric stiffness as shown above. Equation (5.13) can be written as:

$$\{\ddot{W}_1\}_{mn} + (1 - \alpha)K\{W_1\}_{mn} = \frac{4F(t)}{\rho hab}(-1)^{(m+n-2)/2} \tag{5.14}$$

where

$$\alpha = \left[N_{xx}^P\left(\frac{m^2}{a^2}\right) + N_{yy}^P\left(\frac{n^2}{b^2}\right)\right] \Big/ \pi^2\left[D_{11}\left(\frac{m^4}{a^4} + \frac{n^4}{b^4}\right) + \frac{2m^2n^2(D_{12} + 2D_{66})}{a^2b^2}\right] \tag{5.15a}$$

and K is the mechanical bending stiffness of the plate given as:

$$K = \frac{\pi^4}{\rho h}\left[D_{11}\left(\frac{m^4}{a^4} + \frac{n^4}{b^4}\right) + \frac{2m^2n^2(D_{12} + 2D_{66})}{a^2b^2}\right] \tag{5.15b}$$

α is the *relative induced piezoelectric stiffness* defined here as the ratio of the total induced piezoelectric stiffness to the mechanical stiffness of the plate (K). If no voltage is applied $\alpha = 0$, and when $\alpha = 1$ the plate buckles under the action of induced piezoelectric compressive stress. Equation (5.14) is similar to equation (4.44a) of Section 4.4; the only difference being that α is considered to be constant for all vibration modes in the latter while it is dependent on the

mode of vibration in the former. Hence, α as used in Section 4.4.2.2 can be thought of as an average or effective relative induced piezoelectric stiffness.

Assuming that only the d_{31} piezoelectric stiffness coefficient is actuated then, $d_{32} = 0$; $N_{xx}^{P} = \bar{Q}_{11} d_{31} V$ and $N_{yy}^{P} = \bar{Q}_{12} d_{31} V$ for each actuator. Thus, the relative induced piezoelectric stiffness can be expressed as:

$$\alpha = \frac{2E_a d_{31} V}{1 - v_a^2} \left[\left(\frac{m^2}{a^2} \right) + v_a \left(\frac{n^2}{b^2} \right) \right] \Big/ \pi^2 \left[D_{11} \left(\frac{m^4}{a^4} + \frac{n^4}{b^4} \right) + \frac{2m^2 n^2 (D_{12} + 2D_{66})}{a^2 b^2} \right] \quad (5.16)$$

where E_a and v_a are the Young's modulus and Poisson ratio of the actuator material. Note that because two identical actuators under the same voltage are involved the piezoelectric stiffness is multiplied by 2.

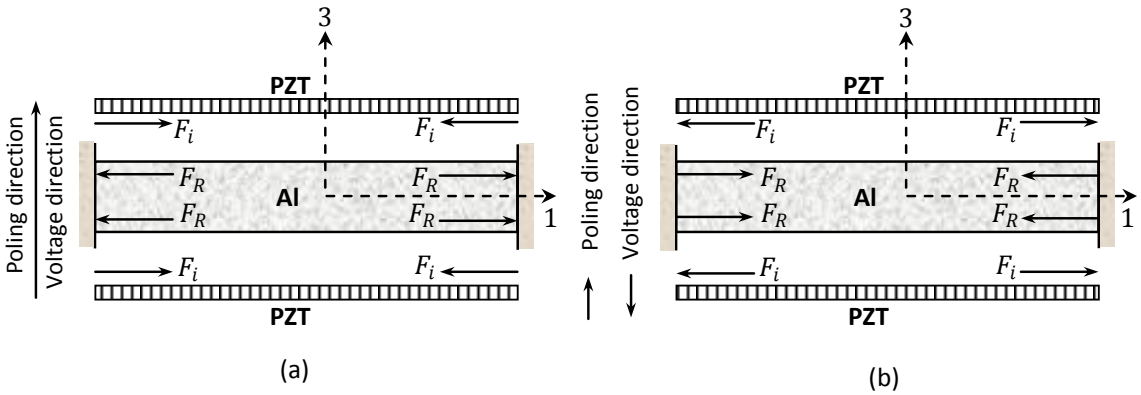

Figure 5.3: *Free body diagram during activation of d_{31} stiffness coefficient of a symmetric PZT/Al/PZT laminate. (a) Voltage and poling direction in-phase; (b) voltage and poling direction are 180° out-of-phase. F_R is the reactive force transferred to the host layer and F_i is the induced force in the piezoelectric layer due to applied voltage.*

The mechanism by which the pre-stress induced in the host material is generated is shown in Figure 5.3. Figure 5.3 illustrates the effect when the d_{31} piezoelectric stiffness coefficient is activated. The effectiveness with which the piezoelectric force generated in the actuator can be transferred to the host material is determined by the bonding layer. Part of the piezoelectric force is converted to shear forces in the bonding layer and this conversion is determined by the shear lag factor of the bonding layer (Chopra, 2002). The higher the shear lag factor, the more the conversion of the induced piezoelectric force to shear forces. For a perfect bonding condition (i.e. a very thin bond layer) the shear lag factor is negligible, and the induced piezoelectric force is considered to be

completely transferred to the host structure (Chopra, 2002). In the present analysis a perfect bonding condition is assumed between the Al and PZT layers.

A voltage applied in the poling direction of the piezoactuator (positive voltage) tends to shrink the piezoactuator layer because the d_{31} stiffness coefficient is negative (Preumont, 2011). An equal reactive in-plane tensile force is generated on the host layer to which the piezoactuator layer is bonded, and because the plate is restrained from planar displacements a tensile pre-stress is created in the plate (i.e. $\alpha < 0$). This gives rise to the well known stress stiffening effect (see Figure 5.3a). For the two piezoactuator layers bonded on the top and bottom surfaces of the host layer the total pre-stress created in the plate is the sum of the stresses induced by each actuator. Similarly, if the voltage is applied opposite to the poling direction (negative voltage) an in-plane tensile force is generated in the actuator layers and a reactive in-plane compressive force is created on the host layer resulting in a compressive pre-stress ($\alpha > 0$). The implication is that the plate becomes more compliant to transverse load (see Figure 5.3b). If the voltage applied at the top piezoactuator layer is equal and opposite to that applied at the bottom piezoactuator layer, then the plate undergoes pure bending. This situation is not necessary for the present investigation, but further information can be found in Chopra (2002) and Lazarus (1989).

The equation of the impactor is the same as equation (4.44b) i.e.

$$\ddot{W}_2 = -F(t)/m_i \tag{5.17}$$

where W_2 is the displacement of the impactor and m_i is the mass of the impactor. The impact force $F(\delta(t)) \geq 0$ is estimated using the elastoplastic contact model presented in Section 3.2. The local indentation is given as $\delta(t) = W_2 - W_1$.

5.4.2 Results and discussions on mitigation of elastoplastic impact effects using PZT/Al/PZT plate

The above models were used to investigate the low-velocity impact response of a PZT/Al/PZT plate subjected to induced active pre-stress (tensile or compressive). The mechanical properties of the Al and PZT layers are the same as in Table 4.5, given in Section 4.4.2.2. The applied voltage is ± 200 [*V*] and the piezoelectric stiffness coefficient used in the simulations is $d_{31} =$

$-254 \times 10^{-12}[m/V]$ (Oguamanam *et al*, 1998). The planar dimension of the plate is 300 x 300 [mm^2] and the thicknesses of the Al and PZT layers are 2.40 [*mm*] and 50.0 [μm] respectively. The impactor mass, initial velocity, and radius are 0.30 [*kg*], 0.50 [m/s], and 10 [*mm*] respectively. The impactor is made of steel and the material properties are given in Section 4.4.2.2.

The plate has a length to thickness ratio of 120, which means that the plate is highly transversely flexible. Such high transverse flexibility (i.e. very thin plate) is required if the induced piezoelectric stress is to have a significant effect on the transverse response of the plate (Oguamanam *et al*, 1998). From an analytical point of view, the solution of the complete impact model, when a plate with high transverse flexibility is involved, is more complicated because the solution is very sensitive to the physical input parameters and the number of vibration modes used to approximate the solution. Consequently, in many cases a convergent numerical solution can be difficult to obtain. One way to overcome this difficulty is to use fewer vibration modes in the solution, though this comes at the cost of reduced accuracy. In Section 4.4.2.2 it was shown that 9 modes of vibration is sufficient to produce a convergent solution for large mass impact of a thin to moderately thick plate. Hence, equations (5.14) and (5.17) have been solved for $m = n = 5$ (i.e. 9 vibration modes) because the impact response for the cases investigated here exhibit typical characteristics of large mass impact i.e. the displacements of the impactor and plate at the point of impact are almost the same. This does not mean that improved accuracy cannot be obtained with more than 9 vibration modes, but that 9 vibration modes are considered to be sufficient for the present purpose, i.e. to demonstrate the effect of actively induced pre-stress on the subsequent impact damage.

Three cases were considered namely: (a) no pre-stress (b) an induced tensile pre-stress and (c) an induced compressive pre-stress. The applied voltage in each case are 0 [*V*], 200 [*V*], and – 200 [*V*] respectively. In solving the models (equations (5.14) and (5.17)) the elastic loading response is terminated at the point where the dynamic indentation is equal to the static yield indentation (see Section 3.2) and the elastoplastic loading response is terminated when the impactor velocity is zero. The unloading response is terminated at the point where the indentation is equal to the static permanent indentation. This is consistent with the assumption that the impact force during low- to medium-velocity impacts can be estimated from static contact models (Johnson, 1985).

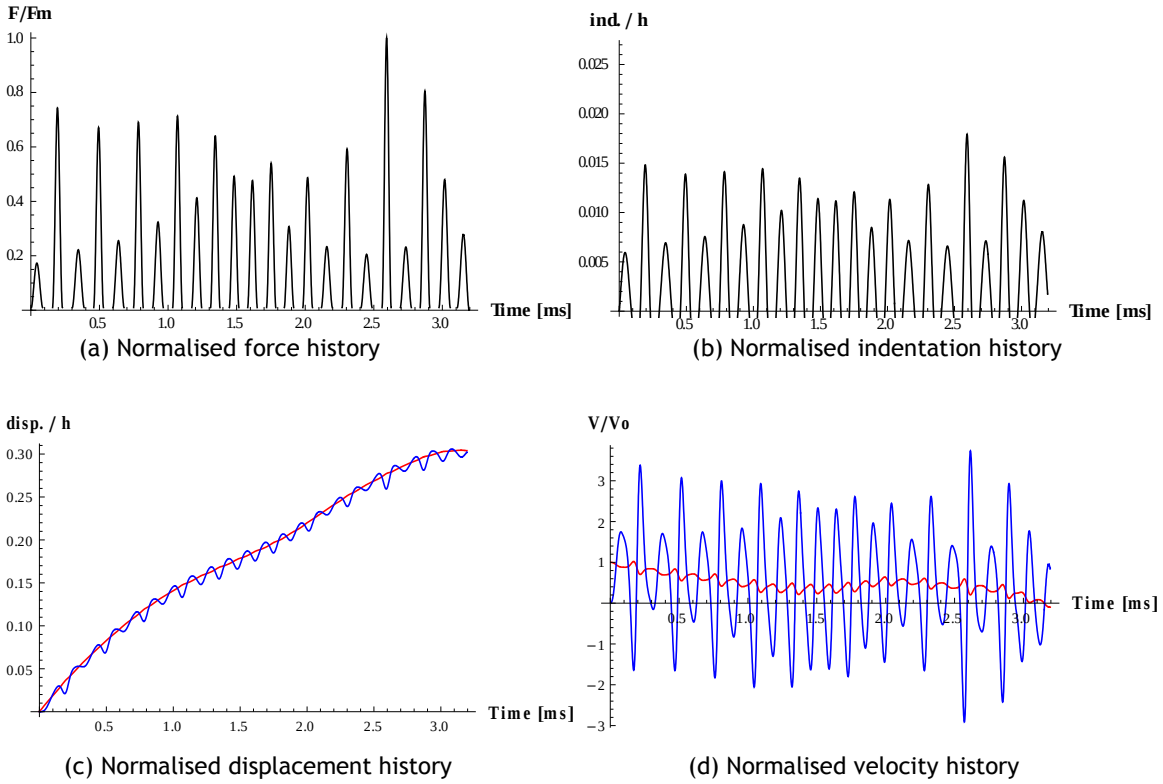

(a) Normalised force history

(b) Normalised indentation history

(c) Normalised displacement history

(d) Normalised velocity history

Figure 5.4: *Low-velocity impact response of PZT/Al/PZT with no induced pre-stress. Blue line – plate response; red line – impactor response.*

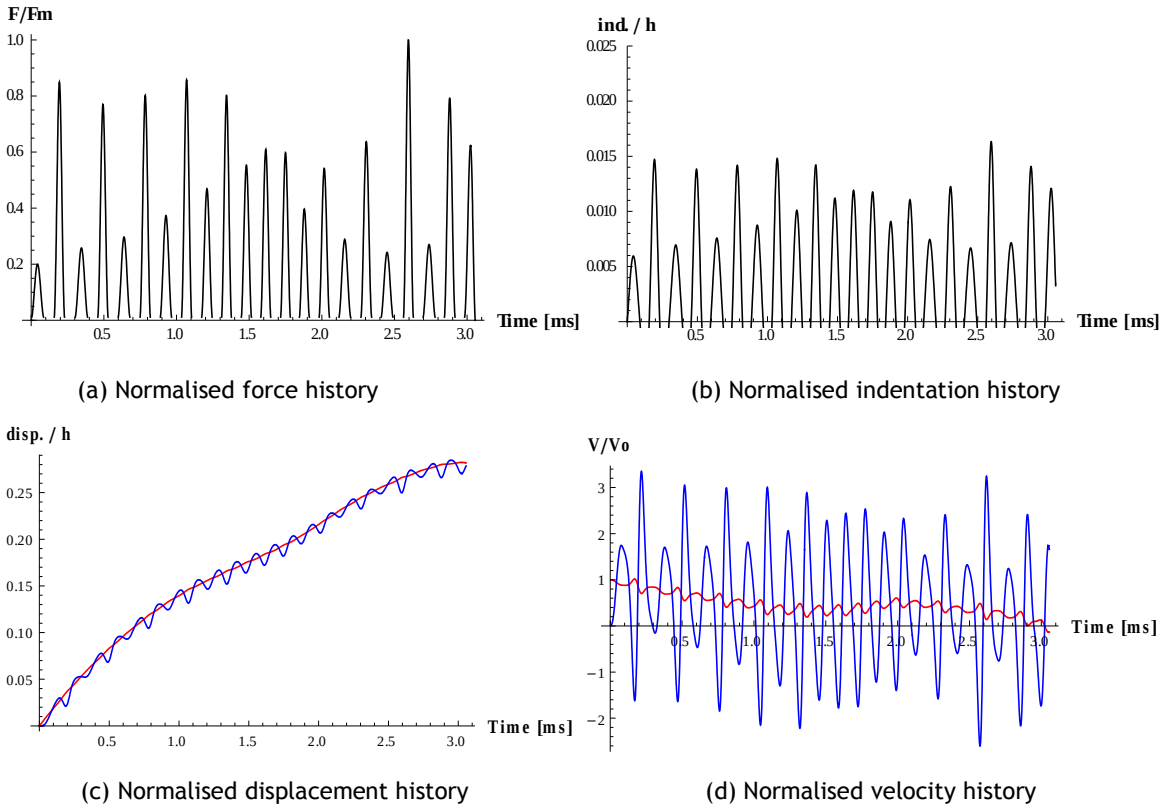

(a) Normalised force history

(b) Normalised indentation history

(c) Normalised displacement history

(d) Normalised velocity history

Figure 5.5: *Low-velocity impact response of PZT/Al/PZT with induced tensile pre-stress. Blue line – plate response; red line – impactor response.*

Plots for the time histories of the impact force, indentation, and the impactor and plate displacements and velocities for the three cases (a – c) are shown in Figures 5.4 – 5.6. The force history is normalised with respect to the maximum impact force while the displacements and indentation histories are normalised with respect to the total thickness of the plate. The velocity history is normalised with respect to the initial impact velocity. The plots reveal that the impact response is mainly dominated by the global response (i.e. the displacement of the plate is large compared to the indentation), which is the distinguishing characteristic of a large mass impact. This observation is noteworthy given that the impactor-plate mass ratio for the present example is 0.46 and the impact event can therefore not be classified as a large mass impact based on the frequently used 'Olsson's mass criterion' i.e. mass ratio ≥ 2 for large mass impact (Olsson, 2000). It seems that Olsson's mass criterion may be limited by the length to thickness ratio because the plate under investigation has a ratio of 120 and its response is globally dominated for the impact event considered even though the mass ratio is well below what would be expected to produce a globally dominated response according to Olsson's mass criterion.

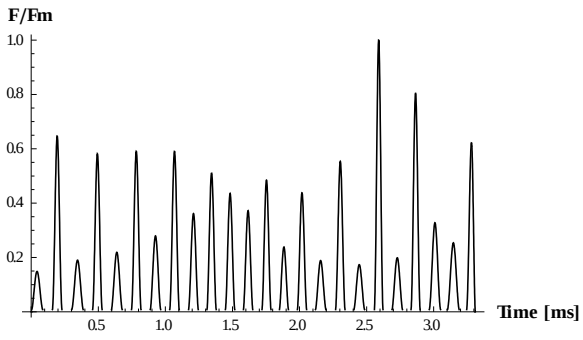

(a) Normalised force history

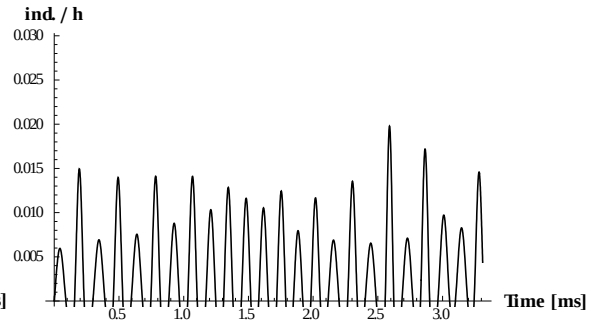

(b) Normalised indentation history

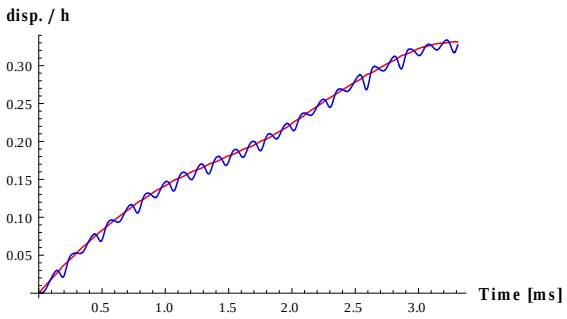

(c) Normalised displacement history

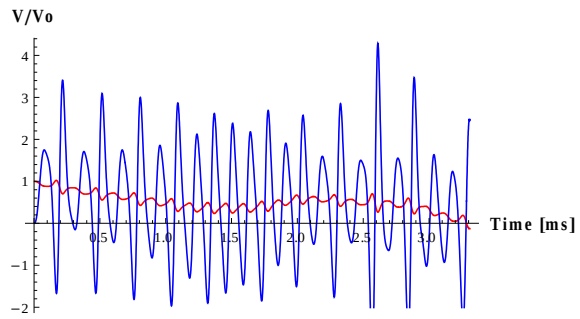

(d) Normalised velocity history

Figure 5.6: *Low-velocity impact response of PZT/Al/PZT with induced compressive pre-stress. Blue line - plate response; red line - impactor response.*

The local indentation (Figures 5.4b, 5.5b, and 5.6b) is relatively small compared to the displacement of the impactor and the plate (Figures 5.4c, 5.5c, and 5.6c), which are similar. This means that most of the initial impact energy is converted into vibration energy in the plate. The velocity histories (Figures 5.4d, 5.5d, and 5.6d) show a gradual dissipation of the initial impact energy, while at the same time the highly dynamic interactions between the impactor and the plate (see Figures 5.4c, 5.5c, and 5.6c) result in multiple impacts (Figures 5.4a, 5.5a, and 5.6a). The maximum impact force and indentation occur at the 19^{th} impact in all three cases.

Table 5.1: *Modal dependence of mechanical and piezoelectric stiffnesses*

Modes		**Mechanical bending stiffness, K [N/mkg]**	**Relative induce piezoelectric stiffness, α [-]**
m	*n*		
1	1	6.725×10^5	± 0.2093980
1	3	1.681×10^7	± 0.0238391
1	5	1.136×10^8	± 0.0081014
3	1	1.681×10^7	± 0.0599199
3	3	5.447×10^7	± 0.0232664
3	5	1.943×10^8	± 0.0091963
5	1	1.136×10^8	± 0.0241136
5	3	1.943×10^8	± 0.0154387
5	5	4.203×10^8	± 0.0083759

In Section 5.4.1, expressions for the mechanical bending and induced piezoelectric stiffnesses were derived (see equations (5.15) and (5.16)) and shown to depend on the vibration mode. Table 5.1 shows the modal dependence of the mechanical bending and induced piezoelectric stiffnesses for the nine vibration modes used in approximating the solution of the impact response, for an applied voltage of ± 200 [V]. The induced piezoelectric stiffnesses shown in Table 5.1 are negative for tensile pre-stress and positive for compressive pre-stress. The results show that the induced piezoelectric stiffness is most effective at the fundamental mode of vibration. At higher vibration modes, both the effect of the mechanical bending and induced piezoelectric stiffnesses continue to diminish. The effect of the induced piezoelectric stiffnesses can be increased by using a thinner plate, i.e. a higher length to thickness ratio (Oguamanam *et al*, 1998) or by increasing the applied voltage. The increase in the voltage is limited by the dielectric breakdown voltage of the actuator and the critical buckling load of the plate.

Table 5.2: *Effect of actively induced pre-stress on critical impact parameters*

Impact parameters	No pre-stress	Tensile pre-stress	Compressive pre-stress
Maximum contact force , F_m [*kN*]	2.208	1.907	2.570
Maximum indentation, δ_m [*μm*]	44.85	40.82	49.47
Permanent indentation, δ_f [*μm*]	4.34	8.15	10.97
Duration of elastic loading response [*μs*]	0 – 3.95	0 – 3.95	0 – 3.95
Duration of elastoplastic loading response [*μs*]	3.95 – 3151.04	3.95 – 3023.12	3.95 – 3284.86
Duration of unloading response [*μs*]	3151.04 – 3194.69	3023.12 – 3055.87	3284.86 – 3309.94
Duration of impact response [*ms*]	3.195	3.056	3.310
Time at which maximum force occurred [*ms*]	2.593	2.596	2.590
Final rebound velocity [*m/s*]	0.0491	0.0691	0.0649
Number of impacts [-]	23	22	24

The effect of active pre-stressing on the impact response of the PZT/Al/PZT plate is summarised in Table 5.2. The results of critical impact parameters are compared for the three cases. These impact parameters are considered to be critical because they determine the damage size and shock effect of the impact, and the amount of energy absorbed by the plate. The nominal case used for comparison is the impact without pre-stress (column 2). The induced tensile pre-stress resulted in a reduction of the maximum impact force by 13.63% while the induced compressive pre-stress increased the maximum impact force by 16.39%. For single impact events, application of a tensile pre-stress produces a maximum impact force higher than the nominal case (no pre-stress), while a compressive pre-stress produces a maximum impact force lower than the nominal case (see Figure 4.27). In contrast, the present impact event is characterised by multiple impacts and the complex nature of such an impact event can produce a higher maximum impact force for either tensile or compressive pre-stress condition. In the present investigation the compressive pre-stress condition produced a higher maximum impact force (see Table 5.2). Overall, the effect of the induced tensile pre-stress appears to be more beneficial than the effect of the compressive pre-stress, and gives a better mitigation of elastoplastic impact effects in terms of a lower maximum impact force, a smaller number of impacts and a smaller impact energy absorption by

the plate (as shown by the final rebound velocity). The only apparent drawback of the effect of the induced tensile pre-stress is that it produced a permanent indentation that is higher than the nominal case.

The impact durations for the impact stages of all three cases reveal that the impact response is dominated by the elastoplastic loading response. The elastic loading response occurs in less than 0.2% of the impact duration while the unloading response occurs in about 1.0% of the impact duration. The implication is that the elastoplastic loading response takes place for more than 98.0% of the impact duration. This underscores the importance of using elastoplastic contact models that account for post-yield effects in impact analysis. Furthermore, elastoplastic contact models that account for post-yield effects can be used to predict the permanent indentation, as in the present analysis, which may be difficult to obtain otherwise.

The total mass of the PZT layers in the PZT/Al/PZT plate studied is 0.0684 [*kg*], just 11.73% of the mass of the Al layer (0.5832 [*kg*]). The maximum impact force predicted when a tensile pre-stress is actively induced at an applied voltage of 200 [*V*] is 1.907 [*kN*] (see Table 5.2). If the PZT layers are taken off and a passive Al plate of equivalent thickness as the total thickness of the PZT/Al/PZT plate is subjected to the same impact conditions, then the maximum impact force predicted would be 2.444 [*kN*]. Since the mass of the passive Al plate is 0.6075 [*kg*] and the mass of the PZT/Al/PZT plate is 0.6516 [*kg*], it can be concluded that a 7.26% increase in the mass of the plate (i.e. when the PZT/Al/PZT plate is used instead of the Al plate) gives rise to a 21.97% reduction in the maximum impact force, when a tensile pre-stress is actively induced at an applied voltage of 200 [*V*]. On the other hand, a comparison for the case of PZT/Al/PZT with no pre-stress and with tensile pre-stress (see Table 5.2) show that the maximum impact force is reduced by 13.63%, when a tensile pre-stress is induced at a voltage of 200 [*V*]. These trade-offs could be further enhanced by optimising the effect of the induced pre-stress. The optimisation of the induced pre-stress is beyond the scope of the present work and is left for future research.

5.5 Implementation issues of the proposed strategy for active impact damage mitigation

So far the focus of this chapter has been the investigation of the effect of active pre-stress on the low-velocity impact response of a PZT/Al/PZT laminate plate using analytical models that account for permanent indentation of the local response. It was shown that both tensile and compressive pre-stress could influence the impact response significantly and for the particular impact event investigated, an induced tensile pre-stress produced better mitigation of the elastoplastic impact effects than an induced compressive pre-stress. The proposed strategy of active pre-stressing using piezoceramic actuators can be used to develop a controller for optimised impact damage mitigation. The primary objective of such a control algorithm would be to actively redistribute the impact energy absorbed by the target structure to meet pre-determined impact damage mitigation solutions. The pre-determined impact damage mitigation solutions include an increase in the local damage in favour of less structural damage (Yigit and Christoforou, 2000), a reduction of the energy absorbed by the structure in favour of higher rebound energy (impact resistance), and an elongation of the impact duration by allowing absorption of more vibration energy in favour of reducing the shock effect of the impact. For instance, during impact of runway debris on an airplane the local indentation effects may be critical and are of concern, whereas vibrations are small and harmless. In this case it would be useful to have the structure absorb more vibration energy in favour of less local indentation. Another example may be the impact of a car body and a pedestrian; here it would be beneficial to reduce the shock effect of the impact and enhance the vibration energy absorption of the structure.

Basically, the impact energy of a low-velocity impact can be dissipated as local indentation energy, vibration energy, and rebound energy of the impactor. Other possible mechanisms of dissipation such as sound and friction energy are negligible (Johnson, 1985; Abrate, 1998). The indentation energy produces local damage effects such as permanent indentation, cracks and perforation, while the vibration energy produces global damage effects such as delamination and noise. Altering the structural stiffness can influence the energy dissipation

mechanism and this can be achieved through actively induced pre-stress, as demonstrated above.

The practical implementation of induced pre-stress using a controller design to actively mitigate impact damage effects would require remote sensing of the impactor parameters before the impact takes place. Required impactor parameters include mass, velocity, size, contact geometry and material composition. Even though it may not be practically possible to obtain a precise estimate of the impactor details in real time, very good estimates can be obtained using available remote sensing technologies such as high speed camera, LIDAR (light detection and ranging), radar and sonic sensors. These technologies are already implemented in autonomous vehicles and space technologies for obstacle avoidance and foreign object detection and analysis (Bicho *et al*, 2000; Mujica, 2014). Additionally, the control system would require a database of materials to estimate the impactor's material properties once the composition of the impactor had been determined from the remotely sensed information.

After the impactor parameters are estimated, the impact models presented in this chapter could be used to estimate the passive impact response of the smart plate, and then, the critical response parameters could be matched with the predetermined control objectives in order to estimate the input voltage for active mitigation. Very high speed processors with parallel computing abilities that can analyse the remotely sensed information and determine the control input voltage in fractions of a second are required to achieve this. Since remote sensing can be achieved while the impactor is still a few seconds away (Mujica, 2014), it is concluded that active pre-stressing as a strategy for mitigation of elastoplastic impact effects would seem to be practically feasible.

Although the focus of the present chapter has been on the mitigation of elastoplastic impact effects using a symmetric sandwich laminate (PZT/Al/PZT), the trimorph plate configuration with piezoelectric actuator (PZT) and sensor (PVDF) layers integrated on a host layer can also be used for active pre-stressing. In this case, the sensor layer could be use for *in situ* sensing and provide information for active control of the post-impact response. This arrangement might be useful in a situation where active damping can be used to suppress the post-impact vibration in order to forestall global response damage effects. Since the actuator is in an unsymmetric laminate arrangement, its activation would produce an in-plane force and a bending moment. The bending

moment would produce an initial bending prior to impact and the in-plane force would produce a pre-stress in the plate. Actuation in this trimorph arrangement will most likely be less effective than in the PZT/Al/PZT arrangement with two actuators and no bending moment. Hence, in situations where *in situ* sensing may be needed, other symmetric arrangements such as PVDF/PZT/Al/PZT/PVDF or $(PZT)_2/Al/(PZT)_2$ could be investigated. In the latter case, the outermost PZT layers could be used as *in situ* sensors.

5.6 Chapter conclusions

In this chapter the vibration models discussed in chapter two, and the new elastoplastic contact model formulated in chapter 3, were combined with linear piezoelectric theory to formulate impact models that were used to investigate the effect of actively induced pre-stress on the impact response of a smart plate. A symmetric laminate was modelled and investigated. Simulations using the models demonstrated that actively induced pre-stress can influence the impact response of the symmetric laminate plate significantly. In this case study, it was found that a significant reduction in maximum impact force can be achieved by the smart plate. It was therefore proposed that actively induced pre-stress could potentially be a very useful mitigation strategy against elastoplastic impact effects. Also, the issues associated with the practical implementation of a controller designed to mitigate elastoplastic impact effects using the proposed active pre-stress strategy were discussed. It was argued that due to the availability of very efficient remote sensors and high speed processors with parallel computing features, such a controller is practically feasible.

CHAPTER SIX

CONCLUSIONS AND RECOMMENDATIONS

6.1 Conclusions of thesis

The elastoplastic impact response of a multilayered plate, described here as a trimorph plate, has been investigated using analytical models. To obtain more accurate results and details of the elastoplastic impact response an impact modelling approach known as the complete modelling approach was used to formulate the impact model of the trimorph plate. This approach combines the equations of motion of the contacting bodies, in this case the trimorph plate and a spherical impactor, and the compliance model for the local contact mechanics to formulate the impact model. Hence, in developing the research presented within this thesis the vibration characteristics of the trimorph plate was investigated first. A key finding from this investigation is that the vibration response of the trimorph plate is dependent on the arrangement of its layers. Next, a novel elastoplastic compliance model for impact analysis was formulated and validated using published experimental results. This was followed by detailed investigations on the elastoplastic impact response of rectangular plates, in which the local contact mechanics was accounted for using the newly formulated elastoplastic compliance model. Based on the observations and conclusions of the elastoplastic impact analysis of the trimorph plate, a newly proposed strategy for mitigation of elastoplastic impact effects, i.e. plastic deformation and/or damage, was investigated.

The elastoplastic response of both transversely inflexible and transversely flexible rectangular plates during impact of a spherical mass was studied. For transversely inflexible plates, the impact models were formulated using the equation of motion of the impactor and the new compliance model. Results from the simulation of the impact models for transversely inflexible plates showed that the elastic loading response has a negligible influence on the impact response when the maximum penetration is located well into the linear elastoplastic regime. It was observed that the fraction of the initial impact energy absorbed as plastic deformation increased as the initial impact velocity increased. Additionally, an efficient algorithm capable of solving the nonlinear models of a half-space impact was formulated. The algorithm, which has been

called force-indentation linearisation method (FILM), is simple, inherently stable and converges within a few iterations; typically between five and ten. The FILM algorithm solves the nonlinear models of a half-space impact with the same relative ease irrespective of the complexity of the compliance model used to estimate the impact force. The results obtained using the FILM algorithm showed an excellent match with results obtained from direct numerical integration of the nonlinear models governing the half-space impact. Also, the FILM algorithm proved to be accurate when applied to solving the nonlinear model for elastic impact response of an infinitely large transversely flexible plate. Unlike the case of a transversely inflexible plate impact where the FILM algorithm is completely analytical, it becomes semi-analytical when applied to solve the nonlinear impact model of a transversely flexible plate. This is because the time at the boundaries of each discretisation is now determined using an implicit formulation. The implication is that more iteration is required to obtain accurate solutions to the nonlinear impact models of transversely flexible plates.

Investigations on the elastoplastic impact response of a transversely flexible plate were carried out using the trimorph plate. The investigations were limited to low-velocity large mass impact. A convergence test on the solution of the trimorph plate impact model showed that the first nine modes of vibration are sufficient to guarantee accurate results. The effect of transverse shear deformation, compliance model used to estimate the impact force, impactor mass, impactor size, initial impact velocity, plate thickness, plate aspect ratio and bending stiffness, on the elastoplastic impact response of a typical trimorph plate configuration was investigated. The results showed that the effect of transverse shear deformation on the elastoplastic impact response of the trimorph plate is negligible. All the other impact parameters considered were shown to have a significant influence. The response characteristics influenced by these impact parameters include: oscillations in the impact force history, maximum impact force, impact duration and permanent indentation. The permanent indentation is indicative of the amount of plastic deformation and/or local damage that occurred during the impact loading (Majeed *et al*, 2012).

Analysis of the effect of transverse bending stiffness on the elastoplastic impact response of the trimorph plate showed that the flexibility of the plate can influence its elastoplastic response significantly. This observation, which is supported by previous studies (Christoforou and Yigit, 1998b) was used to

investigate a newly proposed strategy for active mitigation of elastoplastic impact effects. The strategy is based on using a bonded piezoelectric layer to actively induce a state of pre-stress in the substrate layer. The pre-stress induced in the substrate layer influences the flexibility of the plate, which in turn influences the elastoplastic impact response. This strategy was investigated for a PZT/Al/PZT plate configuration using an impact model that accounts for the effect of induced piezoelectric pre-stress on the transverse flexibility of the plate. This effect was captured in the impact model through a non-dimensional parameter called relative induced piezoelectric stiffness. The latter is defined here as the ratio of the total induced piezoelectric stiffness to the mechanical bending stiffness of the plate.

Simulations of the impact model were carried out for both tensile and compressive pre-stress states created by an applied voltage of 200 volts. The results obtained were compared to a no pre-stress state and the comparison showed that the elastoplastic impact effects such as permanent indentation can be significantly altered through induced piezoelectric pre-stress. This strategy can be used to design a controller for active mitigation of elastoplastic impact effects. The input information required by the controller (i.e. impactor speed, mass, size and material composition) would be obtained by remote sensing technology such as camera and radar sensors. The use of remote sensors would avail the piezoactuators with sufficient time to provide active response to an imminent impact. However, *in situ* sensors can also be used to provide information for active control of the post-impact response of the plate. Additionally, the proposed strategy for active mitigation of elastoplastic impact effects can be used together with existing passive mitigation strategies to further enhance the impact damage mitigation capacity of structures. The potential benefits of the application of the proposed mitigation strategy include cost savings, reduction of risk to life and structural survivability/re-usability.

In conclusion, analytical models for impact analysis of structures should account for elastoplastic effects since it has been sufficiently demonstrated in this thesis and in the literature (Johnson, 1985; Goldsmith, 2001; Majeed *et al*, 2012) that significant elastoplastic deformation occurs at typical low-velocity impacts. Furthermore, neglecting elastoplastic effects in impact analysis could introduce significant errors in the predicted impact response (Abrate, 1998) and limit the details that can be obtained. The work presented in this thesis provides

an insightful analysis of the elastoplastic impact response of both transversely inflexible and transversely flexible rectangular plates. The modelling of the local contact mechanics for low-velocity impact events has been improved and particular attention has been paid to the solution of nonlinear impact models, which are usually difficult to solve. New solution methods that are easy to implement are developed, especially for transversely inflexible plate impact, and the NDSolve function in *Mathematica*™ is shown to be an efficient numerical integration tool for solving nonlinear impact models. Finally, investigations on active mitigation of elastoplastic impact effects reveal its viability and reinforce the need for more research activity in this area, which is largely unexplored at present.

6.2 Recommendations for future research

The methodology of the present research is to use analytical models to investigate the elastoplastic response of rectangular plates subjected to spherical object impact, and to explore the possibility of active mitigation of elastoplastic impact effects in transversely flexible plates. In applying this methodology, a traditional impact modelling approach, which has been proven to produce reliable results for over a century, has been applied. The traditional approach is to use a well validated static compliance model to estimate the impact force of a rate-independent impact event i.e. low- to medium-velocity impact. Once the static compliance model is substituted for the force in the equations of motion of the contacting bodies and the indentation is defined as the relative displacement of the contacting bodies, the impact model so obtained can be considered to be reliable. However, there are two major areas of the present work where further validation would give credence to the quantitative analysis.

The trimorph plate is a composite laminate consisting of three layers with different material properties. This means that yielding in the trimorph plate is quite complex. Furthermore, effective transverse properties of the trimorph plate are needed for the analytical models. The effective transverse properties have been estimated using the strength of materials approach, which is an approximate method. It is therefore necessary to verify the analytical results of the elastoplastic impact response of the trimorph plate independently. Such

validation can be carried out using finite element models developed in software packages like ABAQUS, ANSYS and COMSOL. Two finite element models can be tested and compared with the analytical results. The first finite element model would require homogenisation of the trimorph plate to obtain an equivalent monolithic plate with effective properties, and then, using the equivalent monolithic plate for elastoplastic analysis of a spherical impact. This approach was used by Majeed et al (2012) to investigate the elastoplastic impact response of a very thick carbon-epoxy laminate subjected to spherical impact. The second finite element model would require modelling the trimorph plate with its different layers, and using the composite trimorph plate for spherical impact analysis. Since an elastoplastic impact analysis is desired, post-yield stress-strain data for each material that make-up the trimorph plate would be needed for the finite element models. Such data are readily available from the literature.

The second area of the present work that require further validation is the modelling of the induced piezoelectric stiffness created by actively pre-stressing the host layer of the PZT/Al/PZT sandwich plate. Basic piezoelectric theory has been applied in the present research to derive the model for estimating this effect. A finite element model can be built to validate the estimation of this effect, and to demonstrate quantitatively the extent of elastoplastic impact damage mitigation that is possible.

An alternative validation approach to finite element modelling is experimentation. Although impact experiments are generally simple, an experiment to investigate the active mitigation of elastoplastic impact effects is not likely to be that simple. A relatively simpler experiment would be to investigate the elastoplastic impact response of the trimorph plate. This latter experimental investigation would involve two main stages namely: (a) preparation of the target specimen, which is a composite laminate plate, and (b) setting up the experimental rig. The impactor should not be controllable as obtained in many existing drop-weight impact testing machines e.g. a Zwick/Roell HIT230F drop weight tester. Rather, the impactor should be dropped freely from a height and allowed to rebound as a result of the impact resistance of the plate specimen, just like the experiments of Kharaz and Gorham (2000). Difficulties with the experiment may arise due to the need to achieve the correct boundary conditions and measure the permanent indentation

after impact. Nevertheless, a carefully planned experiment remains a preferable and more reliable means of validating the quantitative results.

Due to time constraint on the present research none of the validation exercises discussed above was conducted. However, any of the validation exercises discussed above could be carried out as the next logical step in continuing with the work presented in this thesis. The boundary and loading conditions used in this thesis are simply-supported on all edges (SSSS) and concentrated point load respectively. Further research can be carried out to improve the analytical models presented in this thesis to incorporate more realistic boundary and loading conditions. The impact load for a spherical impact can be more realistic represented by a load distributed over a circular patch (Nosier *et al*, 1994). Other boundary conditions such as clamped on all edges (CCCC), clamped-free (CFCF or CCFF) and elastically-restrained edges, to mention but a few, can be investigated using the analytical models presented in this thesis.

Appendix A.1: Algebra in the derivation of the cubic equation for δ_{tep}

For convenience, equation (3.43) is repeated here as equation (A1).

$$K_h\left(\delta_{tep}-\delta_y\right)^{3/2}-1.5K_h\left(\delta_{tep}-\delta_y\right)^{1/2}\left(\delta_{tep}-\delta_p\right)=F_{\delta=\delta_p}-K_h\delta_y^{3/2} \qquad (A1)$$

Substituting $X=\delta_{tep}-\delta_y$, $Y=\delta_{tep}-\delta_p$, and $Z=F_{\delta=\delta_p}-K_h\delta_y^{3/2}$, equation (A1) can be expressed as:

$$X^{3/2}-1.5X^{1/2}Y=Z/K_h \qquad (A2)$$

Taking the square of both sides of equation (A2), we get:

$$X^3-3X^2Y+2.25XY^2=(Z/K_h)^2 \qquad (A3)$$

From the terms in equation (A3), the following expansions apply.

$$X^3=\left(\delta_{tep}-\delta_y\right)^3=\delta_{tep}^3-3\delta_y\delta_{tep}^2+3\delta_y^2\delta_{tep}-\delta_y^3$$

$$X^2Y=\left(\delta_{tep}-\delta_y\right)^2\left(\delta_{tep}-\delta_p\right)=\delta_{tep}^3-\left(2\delta_y+\delta_p\right)\delta_{tep}^2+\left(\delta_y^2+2\delta_y\delta_p\right)\delta_{tep}-\delta_y^2\delta_p$$

$$XY^2=\left(\delta_{tep}-\delta_y\right)\left(\delta_{tep}-\delta_p\right)^2=\delta_{tep}^3-\left(\delta_y+2\delta_p\right)\delta_{tep}^2+\left(2\delta_y\delta_p+\delta_p^2\right)\delta_{tep}-\delta_y\delta_p^2$$

By substituting these expansions into equation (A3), collecting like terms, and simplifying, a cubic equation in terms of δ_{tep} is obtained as shown.

$$\delta_{tep}^3-\Lambda_1\delta_{tep}^2+\Lambda_2\delta_{tep}-\Lambda_3=0 \qquad (A4)$$

where

$\Lambda_1=6\delta_p-3\delta_y$; $\Lambda_2=9\delta_p^2-6\delta_y\delta_p$; $\Lambda_3=4\delta_y^3-12\delta_y^2\delta_p+9\delta_y\delta_p^2+(2Z/K_h)^2$.

Appendix A.2: Deformation work during contact loading

Using equations (3.26) – (3.30) the work done in each of the three loading regimes can be obtained as shown.

Work done during the elastic loading regime

$$W_e = \int_0^{\delta_y} F_e \, d\delta = \int_0^{\delta_y} K_h \delta^{3/2} \, d\delta = 0.4 K_h \delta_y^{5/2} \qquad (A5)$$

Work done during the nonlinear elastoplastic loading region

$$W_{ep}^{I} = \int_{\delta_y}^{\delta_{tep}} F_{ep}^{I} \, d\delta = \int_{\delta_y}^{\delta_{tep}} \left[K_h \left(\delta - \delta_y\right)^{3/2} + K_h \delta_y^{3/2} \right] d\delta$$

$$= 0.4 K_h \left(\delta_{tep} - \delta_y\right)^{5/2} + K_h \delta_y^{3/2} \left(\delta_{tep} - \delta_y\right) \qquad (A6)$$

Work done during the linear elastoplastic loading region

$$W_{ep}^{II} = \int_{\delta_{tep}}^{\delta_p} F_{ep}^{II} \, d\delta = \int_{\delta_{tep}}^{\delta_p} \left\{ K_l \left(\delta - \delta_{tep}\right) + K_h \left[\left(\delta_{tep} - \delta_y\right)^{3/2} + \delta_y^{3/2} \right] \right\} d\delta$$

$$= 0.5 K_l \left(\delta_p - \delta_{tep}\right)^2 + K_h \left[\left(\delta_{tep} - \delta_y\right)^{3/2} + \delta_y^{3/2} \right] \left(\delta_p - \delta_{tep}\right) \qquad (A7)$$

Work done during the fully plastic loading regime

$$W_{fp} = \int_{\delta_p}^{\delta_m} F_{fp} \, d\delta = \int_{\delta_p}^{\delta_m} \left[K_p \left(\delta - \delta_p\right) + F_p \right] d\delta$$

$$= 0.5 K_p \left(\delta_m - \delta_p\right)^2 + F_p \left(\delta_m - \delta_p\right) \qquad (A8)$$

Using equations (A5) – (A8), the following work done can be determined.

Work done up to the end of the elastic loading regime, W_y

$$W_y = W_e = 0.4 K_h \delta_y^{5/2} \qquad (A9)$$

Work done up to the end of region I, W_{tep}

$$W_{tep} = W_y + W_{ep}^{I} = 0.4 K_h \delta_y^{5/2} + 0.4 K_h \left(\delta_{tep} - \delta_y\right)^{5/2} + K_h \delta_y^{3/2} \left(\delta_{tep} - \delta_y\right) \qquad (A10)$$

Work done up to the end of region II, W_p

$$W_p = W_{tep} + W_{ep}^{II}$$

$$= 0.4 K_h \delta_y^{5/2} + 0.4 K_h \left(\delta_{tep} - \delta_y\right)^{5/2} + K_h \delta_y^{3/2} \left(\delta_{tep} - \delta_y\right)$$

$$+ 0.5 K_l \left(\delta_p - \delta_{tep}\right)^2 + \left[K_h \left(\delta_{tep} - \delta_y\right)^{3/2} + K_h \delta_y^{3/2} \right] \left(\delta_p - \delta_{tep}\right) \qquad (A11)$$

Work done up to a terminal point in the fully plastic regime, W_m

$$W_m = W_p + W_{fp}$$

$$= 0.4K_h\delta_y^{5/2} + 0.4K_h\left(\delta_{tep} - \delta_y\right)^{5/2} + K_h\delta_y^{3/2}\left(\delta_{tep} - \delta_y\right)$$

$$+ 0.5K_l\left(\delta_p - \delta_{tep}\right)^2 + \left[K_h\left(\delta_{tep} - \delta_y\right)^{3/2} + K_h\delta_y^{3/2}\right]\left(\delta_p - \delta_{tep}\right)$$

$$+ 0.5K_p\left(\delta_m - \delta_p\right)^2 + F_p\left(\delta_m - \delta_p\right) \qquad (A12)$$

Appendix B.1: Mathematica code to implement FILM algorithm for solution of half-space impact

```
(*FILM algorithm code for elastoplastic half-space impact
analysis based on the new contact model*)

(*Inputs for impactor properties*)
{Ei,ρi,υi,Ri}={600,14500,0.28,10}
(*Inputs for target properties*)
{Et,ρt,υt,Rt,Syt}={210,7825,0.30,Infinity,1}
{to,δo,Vo}={0,0,0.25}    (*Initial impact conditions*)
mi=ρi*(4*N[Pi]*(Ri/1000)^3)/3          (*For spherical ball*)
(*Calculation of effective properties*)
Reff=1/(1/Ri+1/Rt);Eeff=1/((1-υi^2)/Ei+(1-υt^2)/Et);
(*Calculation of model constants*)
Kh=(4/3)*Eeff*Reff^0.5
δy=(1.1*Pi*Reff*Syt/Kh)^2
Kp=4.6*Pi*Reff*Syt
δp=82.5*δy
ap=(2*Reff*δp-Reff*δy)^0.5
Fp=2.8*Pi*Syt*ap^2
δt=13.93*δy
Kl=1.5*Kh*(δt-δy)^0.5

Print[Style["Elastic Loading Phase", Blue]]
{n,m,tj,δj,velj}={5,5,to,δo,Vo};
Do[{Khu=n*δy^(1/2)*(((i+1)/n)^(3/2)-(i/n)^(3/2))*Kh;
Sol=DSolve[{mi*δ''[t]+Khu*δ[t]==Khu*δj-
Kh*δj^(3/2),δ[tj]==δj,δ'[tj]==velj},δ[t],t];
Sol1=Expand[Last[First[First[Sol]]]];Sol2=D[Sol1,t];
Const=(Khu*δj-Kh*δj^(3/2))/Khu;ω=Sqrt[Khu/mi];
A=Coefficient[Sol1,Sin[ω*t]];B=Coefficient[Sol1,Cos[ω*t]];
R=Sqrt[A^2+B^2];ψ=N[ArcTan[B/A]];βt=((i+1)*δy/n-Const)/R;
Exf=Re[ArcCos[βt]];tk=(0.5*Pi-Exf-ψ)/ω;
δk=N[First[Table[Sol1,{t,tk,tk}]]];
velk=N[First[Table[Sol2,{t,tk,tk}]]];
  Do[If [r<tk,disp=N[First[Table[Sol1,{t,r,r}]]];
  vel=N[First[Table[Sol2,{t,r,r}]]];
  F=Khu*(disp-δj)+Kh*δj^(3/2);
  Print[i,",",r,",",disp,",",vel,",",F,",",Khu],Break[]],{r,t
  j,tk,(tk-tj)/m}];
tj=tk;δj=δk;velj=velk;If[i==(n-1),iLast=i]},{i,0,n-1,1}]
If[iLast==(n-1),disp=N[First[Table[Sol1,{t,tk,tk}]]];
vel=N[First[Table[Sol2,{t,tk,tk}]]];
F=Khu*(disp-δj)+Kh*δj^(3/2);
Print[iLast,",",tk,",",disp,",",vel,",",F,",",Khu]];

Print[Style["Nonlinear Elastoplastic Loading Phase", Blue]]
{n,m}={5,5};tj=tk;δj=δk;velj=velk;
δm=First[δmax/.NSolve[0.5*mi*Vo^2==0.4*Kh*δy^2.5+0.4*Kh*(δmax
-δy)^2.5+Kh*δy^1.5(δmax-δy),δmax,Reals]]
```

```
Do[{Khu=n*Kh*(δm-δy)^(1/2)*(((i+1)/n)^(3/2)-(i/n)^(3/2));
Sol=DSolve[{mi*δ''[t]+Khu*δ[t]==Khu*δj-Kh*(δj-δy)^(3/2)-
Kh*δy^(3/2),δ[tj]==δj,δ'[tj]==velj},δ[t],t];
Sol1=Expand[Last[First[First[Sol]]]];Sol2=D[Sol1,t];
Const=(Khu*δj-Kh*(δj-δy)^(3/2)-Kh*δy^(3/2))/Khu;
ω=Sqrt[Khu/mi]; A=Re[Coefficient[Sol1,Sin[ω*t]]];
B=Re[Coefficient[Sol1,Cos[ω*t]]];R=Sqrt[A^2+B^2];
ψ=N[ArcTan[B/A]];βt=((δy+(i+1)*(δm-δy)/n)-Const)/R;
Exf=Re[ArcCos[βt]];tk=(0.5*Pi-Exf-ψ)/ω;
δk=Re[N[First[Table[Sol1,{t,tk,tk}]]]];
velk=Re[N[First[Table[Sol2,{t,tk,tk}]]]];
  Do[If [r<tk,disp=Re[N[First[Table[Sol1,{t,r,r}]]]];
  vel=Re[N[First[Table[Sol2,{t,r,r}]]]];
  F=Re[Khu*(disp-δj)+Kh*(δj-δy)^(3/2)+Kh*δy^(3/2)];
  Print[i,",",r,",",disp,",",vel,",",F,",",Khu],Break[]],{r,t
  j,tk,(tk-tj)/m}];
tj=tk;δj=δk;velj=velk;If[i==(n-1),iLast=i]},{i,0,n-1,1}]
If[iLast==(n-1),disp=N[First[Table[Sol1,{t,tk,tk}]]];
vel=N[First[Table[Sol2,{t,tk,tk}]]];
F=Re[Khu*(disp-δj)+Kh*(δj-δy)^(3/2)+Kh*δy^(3/2)];
tm=(0.5*Pi-ψ)/ω;Fm=F;
Print[iLast,",",tk,",",disp,",",vel,",",F,",",Khu]];

Print[Style["Restitution Phase", Blue]]
{n,m}={5,5};tj=tm;δj=δm;velj=0;
If[δm<=δy, Rd=Reff,If[δy<δm<=δt,Rd=Reff*(1+((δm-δy)/(δt-
δy))^1.5),If[δt<δm<=δp,Rd=Reff*(2.0+0.8*(δm-δt)/(δp-
δt)),Rd=2.8*Reff]]];
δf=δm-(3*Fm/(4*Eeff*Rd^0.5))^(2/3)
Ku=(4/3)*Eeff*Rd^0.5
Do[{Khu=n*Ku*(δm-δf)^(1/2)*(((i+1)/n)^(3/2)-(i/n)^(3/2));
Sol=DSolve[{mi*δ''[t]+Khu*δ[t]==Khu*δj-Ku*(δj-
δf)^(3/2),δ[tj]==δj,δ'[tj]==velj},δ[t],t];
Sol1=Expand[Last[First[First[Sol]]]];Sol2=D[Sol1,t];
Const=(Khu*δj-Ku*(δj-δf)^(3/2))/Khu;ω=Sqrt[Khu/mi];
A=Coefficient[Sol1,Sin[ω*t]];B=Coefficient[Sol1,Cos[ω*t]];
R=Sqrt[A^2+B^2];ψ=N[ArcTan[B/A]];
βt=((δf+i*(δm-δf)/n)-Const)/R;Exf=Re[ArcCos[βt]];
tk=(0.5*Pi+Exf-ψ)/ω;δk=N[First[Table[Sol1,{t,tk,tk}]]];
velk=N[First[Table[Sol2,{t,tk,tk}]]];invr=0;
  Do[If [r!=tk,disp=N[First[Table[Sol1,{t,r,r}]]];
  vel=N[First[Table[Sol2,{t,r,r}]]];
  F=Khu*(disp-δj)+Ku*(δj-δf)^(3/2);
  Print[i,",",r,",",disp,",",vel,",",F,",",Khu];If[(F<0||disp
  <δf),invr=1;Break[]],Break[]],{r,tj,tk,(tk-tj)/m}];
If[invr==1,Break[],tj=tk;δj=δk;velj=velk;
If[i==0,iLast=i]]},{i,n-1,0,-1}]


If[(iLast==0&&invr==0),disp=N[First[Table[Sol1,{t,tk,tk}]]];
vel=N[First[Table[Sol2,{t,tk,tk}]]];
F=Khu*(disp-δj)+Ku*(δj-δf)^(3/2);
Print[iLast,",",tk,",",disp,",",vel,",",F,",",Khu]];
```

Appendix B.2: Mathematica code to implement FILM algorithm for infinite plate impact

```
(*FILM algorithm code for infinite plate impact analysis*)
(*Definition of units: bending stiffness - kNmm=Nm, contact
stiffness - kN/mm^1.5, density - kg/mm^2, velocity -
m/s=mm/ms, mass – kg, distance- mm*)

(*Inputs for impactor properties*)
{Ei,ρi,υi,Ri}={210,7850,0.3,6.35}
(*Inputs for target - orthotropic laminate ply properties*)
{D11,D12,D22,D66}={154.9,4.760,91.4,8.970}
{ρt,Rt,l,w,h}={4.132*10^-6,Infinity, 200,200,2.69}
(*Other inputs*)
{mi,Vo}={8.3*10^-3,3} (*Calculation of effective properties*)
R=1/(1/Ri+1/Rt)
A=(D12+2*D66)/Sqrt[D11*D22]    (*A is non-dimensionsal*)
Dteff=((A+1)/2)*Sqrt[D11*D22];Dp=Dteff;
Eeff=9.72    (*Given but can be calculated as Eeff=1/((1-
υi)/Ei+1/Ez)*)

(*Calculation of model constants*)
Kh=(4/3)*Eeff*Sqrt[R]           (*units - *)

{m,n,q,tj,δj,velj}={10,50,70,0,0,3};maxcond=0;
(*maxcond has an initial value of 0, which is set to 1 when
maximum condition is reached*)

(*Initial value of maximum indentation used is that of a
half-space*)
δm=(5*mi*velj^2/(4*Kh))^(2/5)
Print[Style["Loading Phase", Blue]]
Do[{Krs=n*δm^(1/2)*(((i+1)/n)^(3/2)-(i/n)^(3/2))*Kh;
λrs=Krs/(8*Sqrt[Dp*ρt]);Prs=(Krs/mi)*δj-(Kh/mi)*δj^(3/2);
Sol=DSolve[{δ''[t]+λrs*δ'[t]+(Krs/mi)*δ[t]==Prs,δ[tj]==δj,δ'[
tj]==velj},δ[t],t];Sol1=Last[First[First[Sol]]];
Sol2=D[Sol1,t]; δk=(i+1)*δm/n;tk=t/.FindRoot[Sol1-
δk==0,{t,1.1*tj},MaxIterations→Infinity,AccuracyGoal→3,Preci
sionGoal→8]; velk=N[First[Table[Sol2,{t,tk,tk}]]];
  Do[If [r!=tk,disp=N[First[Table[Sol1,{t,r,r}]]];
  vel=N[First[Table[Sol2,{t,r,r}]]];
  F=Krs*(disp-δj)+Kh*δj^(3/2);velimp=vel+F/(8*Sqrt[Dp*ρt]);
  If[vel≤0.00001,tm=r;δm1=N[First[Table[Sol1,{t,tm,tm}]]];
  vm=N[First[Table[Sol2,{t,tm,tm}]]];
  Fm=Krs*(δm1-δj)+Kh*δj^(3/2);
  n=i;maxcond=1;Break[]],Break[]];
  Print[i,",",r*10^3,",",disp*10^3,",",vel*10^2,",",velimp*10
  ^2,",",F*10^3,",",Krs];,{r,tj,tk,(tk-tj)/m}];
If[maxcond==1,tj=tm;δj=δm1;velj=vm;Break[]];tj=tk;δj=δk;velj=
velk;},{i,0,n-1,1}]
```

```
Print[Style["Time at maximum indentation = ",
Red],Style[tm*10^3, Red]]
Print[Style["Maximum indentation = ", Red],Style[δm1*10^3,
Red]]
Print[Style["Relative velocity at maximum indentation = ",
Red],Style[vm*10^2, Red]]
Print[Style["Maximum Force = ", Red],Style[Fm*10^3, Red]]

n (*n is the discretisation where maximum condition occurs*)

(*n and δm are reset based on the segment at which maximum
condition is satisfied*)

Print[Style["Restitution Phase", Blue]]
endcond=0 ;(*endcond has an initial value of 0, which is set
to 1 when the end of the loading is reached*)
Do[{Krs=q*δm1^(1/2)*(((i+1)/q)^(3/2)-(i/q)^(3/2))*Kh;
λrs=Krs/(8*Sqrt[Dp*ρt]);Prs=(Krs/mi)*δj-(Kh/mi)*δj^(3/2);
Sol=DSolve[{δ''[t]+λrs*δ'[t]+(Krs/mi)*δ[t]==Prs,δ[tj]==δj,δ'[
tj]==velj},δ[t],t];Sol1=Last[First[First[Sol]]];
Sol2=D[Sol1,t];δk=(i)*δm1/q;tk=t/.FindRoot[Sol1-
δk==0,{t,1.1*tj},MaxIterations→Infinity,AccuracyGoal→3,Preci
sionGoal→8];velk=N[First[Table[Sol2,{t,tk,tk}]]];
  Do[If[r!=tk,disp=N[First[Table[Sol1,{t,r,r}]]];
  vel=N[First[Table[Sol2,{t,r,r}]]];
  F=Krs*(disp-δj)+Kh*δj^(3/2);velimp=vel+F/(8*Sqrt[Dp*ρt]);
  If[endcond==0,If[velimp≤0.00001,{te=r;de=N[First[Table[Sol1
  ,{t,te,te}]]];ve=N[First[Table[Sol2,{t,te,te}]]];Fe=Krs*(de
  -δj)+Kh*δj^(3/2);veimp=ve+Fe/(8*Sqrt[Dp*ρt]);endcond=1}]];
  If[(F≤1.0E-8||disp≤1.0E-8),Break[]];,Break[]];
  Print[i,",",r*10^3,",",disp*10^3,",",vel*10^2,",",velimp*10
  ^2,",",F*10^3,",",Krs];If[i==0&&r==tk-(tk-
  tj)/m,disp=N[First[Table[Sol1,{t,tk,tk}]]];
  vel=N[First[Table[Sol2,{t,tk,tk}]]];
  F=Krs*(disp-δj)+Kh*δj^(3/2);velimp=vel+F/(8*Sqrt[Dp*ρt]);
  Print[i,",",tk*10^3,",",disp*10^3,",",vel*10^2,",",velimp*1
  0^2,",",F*10^3,",",Krs];];,{r,tj,tk,(tk-tj)/m}];
 tj=tk;δj=δk;velj=velk;},{i,q-1,0,-1}]

Print[Style["Time at end of loading = ", Red],Style[te*10^3,
Red]]
Print[Style["Indentation at end of loading = ",
Red],Style[de*10^3, Red]]
Print[Style["Relative velocity at end of loading = ",
Red],Style[ve*10^2, Red]]
Print[Style["Impactor velocity at end of loading = ",
Red],Style[veimp*10^2, Red]]
Print[Style["Force at end of loading = ", Red],Style[Fe*10^3,
Red]]

ClearAll
```

Appendix B.3: Mathematica code to solve the impact model of the trimorph plate

```
(*Code for the solution of the trimorph plate impact model*)
{a,b,δ1,δ2,δ3,ν1,ν2,ν3,E1,E2,E3,den1,den2,den3}={0.1,0.1,0.00
1,0.001,0.008,0.3,0.44,0.33,64000000000,1100000000,7000000000
0,7600,1770,2700};{mp,V0,Ei,νi,Ri,Rp,Sy1,Sy2,Sy3,α}={1.0,0.30
,210000000000,0.3,0.01,Infinity,0.250,0.050,0.320,0};
h=δ1+δ2+δ3; (*Total thickness of the plate*)
den=(den1*δ1+den2*δ2+den3*δ3)/h   (*Density of the plate*)

(*Bending stiffnesses*)
D111=(E1/(1-ν1^2))*(δ1^3-1.5*h*δ1*(δ1-h/2));
D112=(E2/(1-ν2^2))*(δ2^3+3*δ2*(δ1-h/2)*(δ1+δ2-h/2));
D113=(E3/(1-ν3^2))*(δ3^3+3*δ3*(δ1+δ2-h/2)*(δ1+δ2+δ3-h/2));
D11=(D111+D112+D113)/3;
D121=(ν1*E1/(1-ν1^2))*(δ1^3-1.5*h*δ1*(δ1-h/2));
D122=(ν2*E2/(1-ν2^2))*(δ2^3+3*δ2*(δ1-h/2)*(δ1+δ2-h/2));
D123=(ν3*E3/(1-ν3^2))*(δ3^3+3*δ3*(δ1+δ2-h/2)*(δ1+δ2+δ3-h/2));
D12=(D121+D122+D123)/3;
D661=(E1/(1+ν1))*(δ1^3-1.5*h*δ1*(δ1-h/2));
D662=(E2/(1+ν2))*(δ2^3+3*δ2*(δ1-h/2)*(δ1+δ2-h/2));
D663=(E3/(1+ν3))*(δ3^3+3*δ3*(δ1+δ2-h/2)*(δ1+δ2+δ3-h/2));
D66=(D661+D662+D663)/6;

(*This section of the code calculates all the constants in
the ODE, solves the ODE, and plots the result to aid visual
assessment of the response*)
Ep=h/(δ1/E1+δ2/E2+δ3/E3);νp=(δ1*ν1+δ2*ν2+δ3*ν3)/h;
Syt=h/(δ1/Sy1+δ2/Sy2+δ3/Sy3)
Eeff=Ei*Ep/(Ep*(1-νi^2)+Ei*(1-νp^2));
Reff=1/(1/Ri+1/Rp);Kh=((4/3)*Eeff*Reff^0.5)/(1000^2.5)
δy=(1.1*Pi*Reff*1000*Syt/Kh)^2  (*Indentation at yield*)
velstress=Sqrt[Ep/den];tstress=h/velstress

(*Code for obtaining the set of ODEs and initial conditions
necessary for the solution of the ELASTIC impact response
based on the number of participating modes specified.*)
{m,n}={5,5}; (*Participating modes*)
z=0;ηa=0;Kb=0; (*Initialisation of number of participating
modes and approximate plate displacement*)
Do[
  Do[z=z+1;Dbar=((22/7)^4)*(i^4*D11/(a^4)+j^4*D11/(b^4)+2*i^2
  *j^2*(D12+2*D66)/(a^2*b^2))/(den*h);K=(1-α)*Dbar/1000000;
  ηa=ηa+StringReplacePart["ηz[t]",ToString[z],{2,2}]*Sin[i*Pi
  /2]*Sin[j*Pi/2];
  Fcoeff=(4*Kh/(den*a*b*h))*Sin[i*Pi/2]*Sin[j*Pi/2];
  eqn="η"<>ToString[z]<>"''[t]"+K*"η"<>ToString[z]<>"[t]=="<>
  ToString[Fcoeff*dis]<>"^1.5";If[z==1,modevars="η"<>ToString
  [z],modevars=modevars<>",η"<>ToString[z]];
```

```
  If[z==1,modeics="η"<>ToString[z]<>"[0]==0,η"<>ToString[z]<>
  "'[0]==0",modeics=modeics<>",η"<>ToString[z]<>"[0]==0,η"<>T
  oString[z]<>"'[0]==0"];
  If[z==1,modeeqns=ToString[eqn],modeeqns=modeeqns<>",
  "<>ToString[eqn]];,{j,1,n,2}]
,{i,1,m,2}];
reldis=ηb[t]-ηa  (*reldis is the Indentation. Since ηa is a
string at this stage reldis should be converted to expression
before using it in a computation.*);
modeeqns1=StringReplace[modeeqns,"dis"→"("<>ToString[reldis]
<>")"];pvars=StringSplit[StringReplace[modevars<>",ηb[t]","
→"[t],"],","]; (*Set of response variables solved for*)

(*Solution of the elastic impact response*)
td={};
ndSol1=NDSolve[{ToExpression[StringSplit["ηb''[t]+"<>ToString
[(Kh/mp)]<>"*("<>ToString[reldis]<>")^1.5==0,"<>modeeqns1,","
]],ToExpression[StringSplit[modeics<>",ηb[0]==0,ηb'[0]==V0","
,"]],WhenEvent[Re[ηb[t]-
#1]==0,AppendTo[td,t]]&[ηa/.str_String:→ToExpression[str]]},To
Expression[StringSplit[modevars<>",ηb","]],{t,0,10},MaxStep
s→Infinity];
tde=First[td]     (*time duration of elastic impact*)

dmaxlist={}           (*Initialization of list of all turning
points on the indentation curve during elastic impact*);
NDSolve[{ToExpression[StringSplit["ηb''[t]+"<>ToString[(Kh/mp
)]<>"*("<>ToString[reldis]<>")^1.5==0,"<>modeeqns1,","]],ToEx
pression[StringSplit[modeics<>",ηb[0]==0,ηb'[0]==V0","]],Wh
enEvent[Re[ηb'[t]-#1]==0,AppendTo[dmaxlist,{t,Re[ηb[t]-
#2]}]]&[D[ηa/.str_String:→ToExpression[str],t],ηa/.str_String
:→ToExpression[str]]},ToExpression[StringSplit[modevars<>",ηb
","]],{t,0,tde},MaxSteps→Infinity];

tme=First[SortBy[dmaxlist,Last][[-1]]]    (*Time at maximum
indentation of elastic loading response*)
dme=Last[SortBy[dmaxlist,Last][[-1]]]  (*Indentation maximum
of elastic loading response*)
If [dme≤δy,{(*Plot of impact force, dispacements and
indentation responses for elastic impact*)
Print[Plot[{(ToExpression[ToString[Kh]<>"*("<>"ηb[t]-
("<>ToString[ηa]<>"))^1.5"])/.ndSol1},{t,0,10},AxesLabel→{St
yle["Time [ms]",Medium,Bold],Style["Force
[kN]",Medium,Bold]},PlotRange→Automatic]];
Print[Plot[{ηb[t]/.ndSol1,ToExpression["("<>ToString[ηa]<>")"
]/.ndSol1,ToExpression["ηb[t]-
("<>ToString[ηa]<>")"]/.ndSol1},{t,0,tde},AxesLabel→{Style["
Time [ms]",Medium,Bold],Style["Disp.
[mm]",Medium,Bold]},PlotStyle→{Directive[Black,Dashing[Tiny]
],Directive[Black,Dashing[Small]],Directive[Black]}
,PlotLegends→{"Impactor disp.","Plate disp.
"<>ToString[(m+1)*(n+1)/4]<>" modes approx.","Indentation
```

```
"<>ToString[(m+1)*(n+1)/4]<>" modes
approx."},PlotRange→Automatic]];
Print[Plot[{ηb'[t]/.ndSol1,ToExpression["("<>StringReplace[To
String[ηa],"[t]"→"'[t]"]<>")"]/.ndSol1,(ηb'[t]-
ToExpression["("<>StringReplace[ToString[ηa],"[t]"→"'[t]"]<>
")"])/.ndSol1},{t,0,tde},AxesLabel→{Style["Time
[ms]",Medium,Bold],Style["Vel.
[m/s]",Medium,Bold]},PlotStyle→{Directive[Black],Directive[B
lack,Dashing[Small]],Directive[Black,Dashing[{0.06,0.02}]]},P
lotLegends→{"Impactor vel.","Plate vel.
"<>ToString[(m+1)*(n+1)/4]<>" modes approx.","Rel. vel.
"<>ToString[(m+1)*(n+1)/4]<>" modes
approx."},PlotRange→Automatic]];Abort[]},

{tyList={};NDSolve[{ToExpression[StringSplit["ηb''[t]+"<>ToSt
ring[(Kh/mp)]<>"*("<>ToString[reldis]<>")^1.5==0,"<>modeeqns1
,","]],ToExpression[StringSplit[modeics<>",ηb[0]==0,ηb'[0]==V
0","]],WhenEvent[Re[ηb[t]-#1]-
δy==0,AppendTo[tyList,t]]&[ηa/.str_String:→ToExpression[str]]}
,ToExpression[StringSplit[modevars<>",ηb","]],{t,0,10},MaxS
teps→Infinity];
ty=First[tyList](*Time at yield point*);
Print[Table[Re[Evaluate[ToExpression["ηb[t]-
("<>ToString[ηa]<>")"]/.ndSol1]],{t,ty,ty}]]   (*Indentation
obtained using ty*);

(*Code for obtaining the set of ODEs and initial conditions
necessary for the solution of the ELASTOPLASTIC impact
response based on the number of participating modes*)
s=0;
Do[
  Do[s=s+1;Dbar=((22/7)^4)*(i^4*D11/(a^4)+j^4*D11/(b^4)+2*i^2
  *j^2*(D12+2*D66)/(a^2*b^2))/(den*h);K=(1-α)*Dbar/1000000;
  Fcoeff=(4/(den*a*b*h))*Sin[i*Pi/2]*Sin[j*Pi/2];
  eqn="η"<>ToString[s]<>"''[t]"+K*"η"<>ToString[s]<>"[t]=="<>
  ToString[Fcoeff*Kh]<>"*("<>ToString[reldis-
  δy]<>")^1.5+"<>ToString[Fcoeff*Kh*δy^1.5];

  (*Determining the initial conditions of the elastoplastic
  stage. When the numerical value of the initial condition is
  small Mathematica automatically displays the number in
  Standard form. This makes it difficult for string
  operation. The Accounting form has been used to ensure that
  the numerical values are in general form. A conditional
  statement is used to account for negative sign with the
  Accounting form.*)
  If[s==1,modeeqns2=ToString[eqn],modeeqns2=modeeqns2<>",
  "<>ToString[eqn]];If[s==1,If[First[Re[Evaluate[ToExpression
  ["η"<>ToString[s]<>"[ty]"]/.ndSol1]]]<0,If[First[Re[Evaluat
  e[ToExpression["η"<>ToString[s]<>"'[ty]"]/.ndSol1]]]<0,
        modeics2="η"<>ToString[s]<>"[ty]==-
  "<>ToString[AccountingForm[First[Re[Evaluate[ToExpression["
```

```
  η"<>ToString[s]<>"[ty]"]/.ndSol1]]]]]<>",η"<>ToString[s]<>"
  '[ty]==-
  "<>ToString[AccountingForm[First[Re[Evaluate[ToExpression["
  η"<>ToString[s]<>"'[ty]"]/.ndSol1]]]]],modeics2="η"<>ToStri
  ng[s]<>"[ty]==-
  "<>ToString[AccountingForm[First[Re[Evaluate[ToExpression["
  η"<>ToString[s]<>"[ty]"]/.ndSol1]]]]]<>",η"<>ToString[s]<>"
  '[ty]=="<>ToString[AccountingForm[First[Re[Evaluate[ToExpre
  ssion["η"<>ToString[s]<>"'[ty]"]/.ndSol1]]]]]],If[First[Re[
  Evaluate[ToExpression["η"<>ToString[s]<>"'[ty]"]/.ndSol1]]]
  <0,modeics2="η"<>ToString[s]<>"[ty]=="<>ToString[Accounting
  Form[First[Re[Evaluate[ToExpression["η"<>ToString[s]<>"[ty]
  "]/.ndSol1]]]]]<>",η"<>ToString[s]<>"'[ty]==-
  "<>ToString[AccountingForm[First[Re[Evaluate[ToExpression["
  η"<>ToString[s]<>"'[ty]"]/.ndSol1]]]]],modeics2="η"<>ToStri
  ng[s]<>"[ty]=="<>ToString[AccountingForm[First[Re[Evaluate[
  ToExpression["η"<>ToString[s]<>"[ty]"]/.ndSol1]]]]]<>",η"<>
  ToString[s]<>"'[ty]=="<>ToString[AccountingForm[First[Re[Ev
  aluate[ToExpression["η"<>ToString[s]<>"'[ty]"]/.ndSol1]]]]]
  ]],

  If[First[Re[Evaluate[ToExpression["η"<>ToString[s]<>"[ty]"]
  /.ndSol1]]]<0,If[First[Re[Evaluate[ToExpression["η"<>ToStri
  ng[s]<>"'[ty]"]/.ndSol1]]]<0,
        modeics2=modeics2<>",η"<>ToString[s]<>"[ty]==-
  "<>ToString[AccountingForm[First[Re[Evaluate[ToExpression["
  η"<>ToString[s]<>"[ty]"]/.ndSol1]]]]]<>",η"<>ToString[s]<>"
  '[ty]==-
  "<>ToString[AccountingForm[First[Re[Evaluate[ToExpression["
  η"<>ToString[s]<>"'[ty]"]/.ndSol1]]]]],modeics2=modeics2<>"
  ,η"<>ToString[s]<>"[ty]==-
  "<>ToString[AccountingForm[First[Re[Evaluate[ToExpression["
  η"<>ToString[s]<>"[ty]"]/.ndSol1]]]]]<>",η"<>ToString[s]<>"
  '[ty]=="<>ToString[AccountingForm[First[Re[Evaluate[ToExpre
  ssion["η"<>ToString[s]<>"'[ty]"]/.ndSol1]]]]]],If[First[Re[
  Evaluate[ToExpression["η"<>ToString[s]<>"'[ty]"]/.ndSol1]]]
  <0,modeics2=modeics2<>",η"<>ToString[s]<>"[ty]=="<>ToString
  [AccountingForm[First[Re[Evaluate[ToExpression["η"<>ToStrin
  g[s]<>"[ty]"]/.ndSol1]]]]]<>",η"<>ToString[s]<>"'[ty]==-
  "<>ToString[AccountingForm[First[Re[Evaluate[ToExpression["
  η"<>ToString[s]<>"'[ty]"]/.ndSol1]]]]],modeics2=modeics2<>"
  ,η"<>ToString[s]<>"[ty]=="<>ToString[AccountingForm[First[R
  e[Evaluate[ToExpression["η"<>ToString[s]<>"[ty]"]/.ndSol1]]
  ]]]<>",η"<>ToString[s]<>"'[ty]=="<>ToString[AccountingForm[
  First[Re[Evaluate[ToExpression["η"<>ToString[s]<>"'[ty]"]/.
  ndSol1]]]]]]]];,{j,1,n,2}]
,{i,1,m,2}];

(*Display the initial conditions of elastoplastic loading
response for checking*)
```

```
ToExpression[StringSplit[modeics2<>",ηb[ty]=="<>ToString[Firs
t[Re[Evaluate[ηb[ty]/.ndSol1]]]]<>",ηb'[ty]=="<>ToString[Firs
t[Re[Evaluate[ηb'[ty]/.ndSol1]]]],","]];

(*Solution of the elastoplastic impact response*)
dmax1list={};
If[First[Re[Evaluate[ηb'[ty]/.ndSol1]]]<0,ndSol2=NDSolve[{ToE
xpression[StringSplit["ηb''[t]+"<>ToString[(Kh/mp)]<>"*("<>To
String[reldis-
δy]<>")^1.5+"<>ToString[(Kh/mp)*δy^1.5]<>"==0,"<>modeeqns2,",
"]],ToExpression[StringSplit[modeics2<>",ηb[ty]=="<>ToString[
First[Re[Evaluate[ηb[ty]/.ndSol1]]]]<>",ηb'[ty]==-
"<>ToString[AccountingForm[First[Re[Evaluate[ηb'[ty]/.ndSol1]
]]]],","]],WhenEvent[Re[ηb'[t]-
#1]==0,AppendTo[dmax1list,{t,Re[ηb[t]-
#2]}]]&[D[ηa/.str_String:→ToExpression[str],t],ηa/.str_String
:→ToExpression[str]]},ToExpression[StringSplit[modevars<>",ηb
",","]],{t,ty,1.2*tde},MaxSteps→Infinity],ndSol2=NDSolve[{To
Expression[StringSplit["ηb''[t]+"<>ToString[(Kh/mp)]<>"*("<>T
oString[reldis-
δy]<>")^1.5+"<>ToString[(Kh/mp)*δy^1.5]<>"==0,"<>modeeqns2,",
"]],ToExpression[StringSplit[modeics2<>",ηb[ty]=="<>ToString[
First[Re[Evaluate[ηb[ty]/.ndSol1]]]]<>",ηb'[ty]=="<>ToString[
AccountingForm[First[Re[Evaluate[ηb'[ty]/.ndSol1]]]]],","]],W
henEvent[Re[ηb'[t]-#1]==0,AppendTo[dmax1list,{t,Re[ηb[t]-
#2]}]]&[D[ηa/.str_String:→ToExpression[str],t],ηa/.str_String
:→ToExpression[str]]},ToExpression[StringSplit[modevars<>",ηb
",","]],{t,ty,1.2*tde},MaxSteps→Infinity]];

tm=First[SortBy[dmax1list,Last][[-1]]]      (*Time at maximum
indentation of the elastoplastic loading response*);
dm=Last[SortBy[dmax1list,Last][[-1]]]       (*Maximum
Indentation of elastoplastic loading response*);
Fm=First[First[Table[Re[Evaluate[(ToExpression[ToString[Kh]<>
"*("<>ToString[reldis-
δy]<>")^1.5+"<>ToString[Kh*δy^1.5]])/.ndSol2]],{t,tm,tm}]]]
(*Maximum force of elastoplastic loading response*);

teList={};
NDSolve[{ToExpression[StringSplit["ηb''[t]+"<>ToString[(Kh/mp
)]<>"*("<>ToString[reldis-
δy]<>")^1.5+"<>ToString[(Kh/mp)*δy^1.5]<>"==0,"<>modeeqns2,",
"]],ToExpression[StringSplit[modeics2<>",ηb[ty]=="<>ToString[
First[Re[Evaluate[ηb[ty]/.ndSol1]]]]<>",ηb'[ty]=="<>ToString[
AccountingForm[First[Re[Evaluate[ηb'[ty]/.ndSol1]]]]],","]],W
henEvent[Re[ηb'[t]]==0,AppendTo[teList,t]]},ToExpression[Stri
ngSplit[modevars<>",ηb","","]],{t,ty,tde},MaxSteps→Infinity];

te=First[teList]       (*Time at the end of the loading phase
i.e. when the velocity of the projectile is zero*);
Ve=Table[Re[Evaluate[ηb'[t]/.ndSol2]],{t,te,te}]
(*Velocity of impactor at the end of the loading phase.*);
```

```
de=First[First[Table[Re[Evaluate[(ηb[t]-
ToExpression["("<>ToString[ηa]<>")"])/.ndSol2]],{t,te,te}]]]
(*indentation at the end of the loading phase*);

(*Code for obtaining the set of ODEs and initial conditions
necessary for the solution of the ELASTIC UNLOADING impact
response based on the number of participating modes*)
x=0;
F1=First[First[Table[Re[Evaluate[(ToExpression[ToString[Kh]<>
"*("<>"ηb[t]-
("<>ToString[ηa]<>"))^1.5"])/.ndSol1]],{t,te,te}]]]
(*Elastic Impact force at te*);
Fe=First[First[Table[Re[Evaluate[(ToExpression[ToString[Kh]<>
"*("<>ToString[reldis-
δy]<>")^1.5+"<>ToString[Kh*δy^1.5]])/.ndSol2]],{t,te,te}]]]
(*Impact force at the end of elastoplastic loading*);
If[de<=δy,Rd=Reff,Rd=Reff*(1+((de-δy)/(12.93*δy))^1.5)]
(*Deformed effective radius*);
df=de-(3*Fe/(4*(Eeff*10^-9)*(1000*Rd)^0.5))^(2/3) (*Permanent
indentation at the end of the impact event*);
Ku=((4/3)*Eeff*Rd^0.5)/(1000^2.5);
Do[
  Do[x=x+1;Dbar=((22/7)^4)*(i^4*D11/(a^4)+j^4*D11/(b^4)+2*i^2
  *j^2*(D12+2*D66)/(a^2*b^2))/(den*h);K=(1-α)*Dbar/1000000;
  Fcoeff=(4/(den*a*b*h))*Sin[i*Pi/2]*Sin[j*Pi/2];
  eqn="η"<>ToString[x]<>"'[t]"+K*"η"<>ToString[x]<>"[t]=="<>
  ToString[Fcoeff*Ku]<>"*("<>ToString[reldis-
  df]<>")"<>"^1.5";
  If[x==1,modeeqns3=ToString[eqn],modeeqns3=modeeqns3<>",
  "<>ToString[eqn]];If[x==1,If[First[Re[Evaluate[ToExpression
  ["η"<>ToString[x]<>"[te]"]/.ndSol2]]]<0,If[First[Re[Evaluat
  e[ToExpression["η"<>ToString[x]<>"'[te]"]/.ndSol2]]]<0,mode
  ics3="η"<>ToString[x]<>"[te]==-
  "<>ToString[AccountingForm[First[Re[Evaluate[ToExpression["
  η"<>ToString[x]<>"[te]"]/.ndSol2]]]]<>",η"<>ToString[x]<>"
  '[te]==-
  "<>ToString[AccountingForm[First[Re[Evaluate[ToExpression["
  η"<>ToString[x]<>"'[te]"]/.ndSol2]]]],modeics3="η"<>ToStri
  ng[x]<>"[te]==-
  "<>ToString[AccountingForm[First[Re[Evaluate[ToExpression["
  η"<>ToString[x]<>"[te]"]/.ndSol2]]]]<>",η"<>ToString[x]<>"
  '[te]=="<>ToString[AccountingForm[First[Re[Evaluate[ToExpre
  ssion["η"<>ToString[x]<>"'[te]"]/.ndSol2]]]]],If[First[Re[
  Evaluate[ToExpression["η"<>ToString[x]<>"'[te]"]/.ndSol2]]]
  <0,modeics3="η"<>ToString[x]<>"[te]=="<>ToString[Accounting
  Form[First[Re[Evaluate[ToExpression["η"<>ToString[x]<>"[te]
  "]/.ndSol2]]]]]<>",η"<>ToString[x]<>"'[te]==-
  "<>ToString[AccountingForm[First[Re[Evaluate[ToExpression["
  η"<>ToString[x]<>"'[te]"]/.ndSol2]]]],modeics3="η"<>ToStri
  ng[x]<>"[te]=="<>ToString[AccountingForm[First[Re[Evaluate[
  ToExpression["η"<>ToString[x]<>"[te]"]/.ndSol2]]]]]<>",η"<>
  ToString[x]<>"'[te]=="<>ToString[AccountingForm[First[Re[Ev
```

```
  aluate[ToExpression["η"<>ToString[x]<>"'[te]"]/.ndSol2]]]]]
  ]],

  If[First[Re[Evaluate[ToExpression["η"<>ToString[x]<>"[te]"]
  /.ndSol2]]]<0,If[First[Re[Evaluate[ToExpression["η"<>ToStri
  ng[x]<>"'[te]"]/.ndSol2]]]<0,
        modeics3=modeics3<>",η"<>ToString[x]<>"[te]==-
  "<>ToString[AccountingForm[First[Re[Evaluate[ToExpression["
  η"<>ToString[x]<>"[te]"]/.ndSol2]]]]<>",η"<>ToString[x]<>"
  '[te]==-
  "<>ToString[AccountingForm[First[Re[Evaluate[ToExpression["
  η"<>ToString[x]<>"'[te]"]/.ndSol2]]]],modeics3=modeics3<>"
  ,η"<>ToString[x]<>"[te]==-
  "<>ToString[AccountingForm[First[Re[Evaluate[ToExpression["
  η"<>ToString[x]<>"[te]"]/.ndSol2]]]]<>",η"<>ToString[x]<>"
  '[te]=="<>ToString[AccountingForm[First[Re[Evaluate[ToExpre
  ssion["η"<>ToString[x]<>"'[te]"]/.ndSol2]]]]],If[First[Re[
  Evaluate[ToExpression["η"<>ToString[x]<>"'[te]"]/.ndSol2]]]
  <0,modeics3=modeics3<>",η"<>ToString[x]<>"[te]=="<>ToString
  [AccountingForm[First[Re[Evaluate[ToExpression["η"<>ToStrin
  g[x]<>"[te]"]/.ndSol2]]]]<>",η"<>ToString[x]<>"'[te]==-
  "<>ToString[AccountingForm[First[Re[Evaluate[ToExpression["
  η"<>ToString[x]<>"'[te]"]/.ndSol2]]]],modeics3=modeics3<>"
  ,η"<>ToString[x]<>"[te]=="<>ToString[AccountingForm[First[R
  e[Evaluate[ToExpression["η"<>ToString[x]<>"[te]"]/.ndSol2]]
  ]]]<>",η"<>ToString[x]<>"'[te]=="<>ToString[AccountingForm[
  First[Re[Evaluate[ToExpression["η"<>ToString[x]<>"'[te]"]/.
  ndSol2]]]]]]]];,{j,1,n,2}]
,{i,1,m,2}];

(*Display the initial conditions for the unloading impact
response*)
StringSplit[modeics3<>",ηb[te]=="<>ToString[AccountingForm[Fi
rst[Re[Evaluate[ηb[te]/.ndSol2]]]]]<>",ηb'[te]=="<>ToString[A
ccountingForm[First[Re[Evaluate[ηb'[te]/.ndSol2]]]]],","];

ToExpression[StringSplit[modeics3<>",ηb[te]=="<>ToString[Acco
untingForm[First[Re[Evaluate[ηb[te]/.ndSol2]]]]]<>",ηb'[te]==
-
"<>ToString[AccountingForm[First[Re[Evaluate[ηb'[te]/.ndSol2]
]]]],","]];

(*Solution of the unloading impact response*)
If[First[Re[Evaluate[ηb'[te]/.ndSol2]]]<0,ndSol3=NDSolve[{ToE
xpression[StringSplit["ηb''[t]+"<>ToString[(Ku/mp)]<>"*("<>To
String[reldis-
df]<>")^1.5"<>"==0,"<>modeeqns3,","]],ToExpression[StringSpli
t[modeics3<>",ηb[te]=="<>ToString[AccountingForm[First[Re[Eva
luate[ηb[te]/.ndSol2]]]]]<>",ηb'[te]==-
"<>ToString[AccountingForm[First[Re[Evaluate[ηb'[te]/.ndSol2]
]]]],","]]},ToExpression[StringSplit[modevars<>",ηb",","]],{t
,te,1.5*tde},MaxSteps→Infinity],ndSol3=NDSolve[{ToExpression
```

```
[StringSplit["ηb''[t]+"<>ToString[(Ku/mp)]<>"*("<>ToString[re
ldis-
df]<>")^1.5"<>"==0,"<>modeeqns3,","]],ToExpression[StringSpli
t[modeics3<>",ηb[te]=="<>ToString[AccountingForm[First[Re[Eva
luate[ηb[te]/.ndSol2]]]]]<>",ηb'[te]=="<>ToString[AccountingF
orm[First[Re[Evaluate[ηb'[te]/.ndSol2]]]]],","]]},ToExpressio
n[StringSplit[modevars<>",ηb","","]],{t,te,1.5*tde},MaxSteps→
Infinity]];

tueList={};
NDSolve[{ToExpression[StringSplit["ηb''[t]+"<>ToString[(Ku/mp
)]<>"*("<>ToString[reldis-
df]<>")^1.5"<>"==0,"<>modeeqns3,","]],ToExpression[StringSpli
t[modeics3<>",ηb[te]=="<>ToString[AccountingForm[First[Re[Eva
luate[ηb[te]/.ndSol2]]]]]<>",ηb'[te]=="<>ToString[AccountingF
orm[First[Re[Evaluate[ηb'[te]/.ndSol2]]]]],","]],WhenEvent[Re
[ηb[t]-#1]-
df==0,AppendTo[tueList,t]]&[ηa/.str_String:→ToExpression[str]]
},ToExpression[StringSplit[modevars<>",ηb","","]],{t,te,1.5*td
e},MaxSteps→Infinity];Print[tueList];tue1=First[tueList];
tue=t/.FindRoot[Re[Evaluate[(ToExpression[ToString[reldis-
df]])/.ndSol3]]==0,{t,1.*tde}];

(*Print[Plot[Piecewise[{{Re[(ToExpression[ToString[Kh]<>"*("<
>"ηb[t]-
("<>ToString[ηa]<>"))^1.5"])/.ndSol1],0≤t≤ty},{Re[(ToExpressi
on[ToString[Ky]<>"*("<>ToString[reldis-
δy]<>")+"<>ToString[Kh*δy^1.5]])/.ndSol2],ty≤t≤te},{Re[(ToExp
ression[ToString[Ku]<>"*("<>ToString[reldis-
df]<>")"<>"^1.5"])/.ndSol3],te≤t≤tue}}],{t,0,tue}]];*)

(*Displacement history plots for elastic impact*)
Print[Plot[{ηb[t]/.ndSol1,ToExpression["("<>ToString[ηa]<>")"
]/.ndSol1,ToExpression["ηb[t]-
("<>ToString[ηa]<>")"]/.ndSol1},{t,0,10},AxesLabel→{Style["T
ime [ms]",Medium,Bold],Style["Disp.
[mm]",Medium,Bold]},GridLines→Automatic,
PlotStyle→{Directive[Black,Dashing[Tiny]],Directive[Black,Da
shing[Small]],Directive[Black]} ,PlotLegends→{"Impactor
disp.","Plate disp. "<>ToString[(m+1)*(n+1)/4]<>" modes
approx.","Indentation "<>ToString[(m+1)*(n+1)/4]<>" modes
approx."},PlotRange→Automatic]];

(*Force history plot combining the different loading and
unloading stages of the impact*)
Print[Show[Plot[Re[(ToExpression[ToString[Kh]<>"*("<>"ηb[t]-
("<>ToString[ηa]<>"))^1.5"])/.ndSol1],{t,0,ty},PlotStyle→Blu
e],Plot[Re[(ToExpression[ToString[Kh]<>"*("<>ToString[reldis-
δy]<>")^1.5+"<>ToString[Kh*δy^1.5]])/.ndSol2],{t,ty,te},PlotS
tyle→Red],Plot[Re[(ToExpression[ToString[Ku]<>"*("<>ToString
[reldis-
df]<>")"<>"^1.5"])/.ndSol3],{t,te,tue},PlotStyle→Darker[Blac
```

```
k]],PlotRange→{{0,tue},Automatic},AxesLabel→{Style["Time
[ms]",Medium,Bold],Style["Force [kN]",Medium,Bold]}]];

(*Displacement history plots combining the different loading
and unloading stages of the impact*)
Print[Show[Plot[{ηb[t]/.ndSol1,ToExpression["("<>ToString[ηa]
<>")"]/.ndSol1,ToExpression["ηb[t]-
("<>ToString[ηa]<>")"]/.ndSol1},{t,0,ty},PlotStyle→{Directiv
e[Blue,Dashing[Tiny]],Directive[Blue,Dashing[Medium]],Directi
ve[Blue]}],Plot[{ηb[t]/.ndSol2,ToExpression["("<>ToString[ηa]
<>")"]/.ndSol2,ToExpression["ηb[t]-
("<>ToString[ηa]<>")"]/.ndSol2},{t,ty,te},PlotStyle→{Directi
ve[Red,Dashing[Tiny]],Directive[Red,Dashing[Medium]],Directiv
e[Red]}],Plot[{ηb[t]/.ndSol3,ToExpression["("<>ToString[ηa]<>
")"]/.ndSol3,ToExpression["ηb[t]-
("<>ToString[ηa]<>")"]/.ndSol3},{t,te,tue},PlotStyle→{Direct
ive[Darker[Black],Dashing[Tiny]],Directive[Darker[Black],Dash
ing[Medium]],Directive[Darker[Black]]}],PlotRange→{{0,tue},A
utomatic},AxesLabel→{Style["Time
[ms]",Medium,Bold],Style["Disp. [mm]",Medium,Bold]}]];

(*Velocity history plots combining the different loading and
unloading stages of the impact*)
Print[Show[Plot[{ηb'[t]/.ndSol1,ToExpression["("<>StringRepla
ce[ToString[ηa],"[t]"→"'[t]"]<>")"]/.ndSol1,(ηb'[t]-
ToExpression["("<>StringReplace[ToString[ηa],"[t]"→"'[t]"]<>
")"])/.ndSol1},{t,0,ty},PlotStyle→{Directive[Blue,Dashing[Ti
ny]],Directive[Blue,Dashing[Medium]],Directive[Blue]}],Plot[{
ηb'[t]/.ndSol2,ToExpression["("<>StringReplace[ToString[ηa],"
[t]"→"'[t]"]<>")"]/.ndSol2,(ηb'[t]-
ToExpression["("<>StringReplace[ToString[ηa],"[t]"→"'[t]"]<>
")"])/.ndSol2},{t,ty,te},PlotStyle→{Directive[Red,Dashing[Ti
ny]],Directive[Red,Dashing[Medium]],Directive[Red]}],Plot[{ηb
'[t]/.ndSol3,ToExpression["("<>StringReplace[ToString[ηa],"[t
]"→"'[t]"]<>")"]/.ndSol3,(ηb'[t]-
ToExpression["("<>StringReplace[ToString[ηa],"[t]"→"'[t]"]<>
")"])/.ndSol3},{t,te,tue},PlotStyle→{Directive[Darker[Black]
,Dashing[Tiny]],Directive[Darker[Black],Dashing[Medium]],Dire
ctive[Darker[Black]]}],PlotRange→{{0,tue},Automatic},AxesLab
el→{Style["Time [ms]",Medium,Bold],Style["Vel.
[m/s]",Medium,Bold]}]];

Print["ty = ",ty,", te = ",te,", tm = ",tm,", tue = ",tue,",
td = ",tde, ", df = ",df, ", Fe = ",Fe, ", de = ",de, ", dm =
",dm, ", Fm = ",Fm];}]

(*Obtaining data points from the solutions*)
If[dme>δy,{Print["Elastic Impact response"];Do[Print[t," ,
",First[Re[(ToExpression[ToString[Kh]<>"*("<>"ηb[t]-
("<>ToString[ηa]<>"))^1.5"])/.ndSol1]]," ,
",First[Re[ToExpression["ηb[t]-
("<>ToString[ηa]<>")"]/.ndSol1]]," ,
```

```
",First[Re[ToExpression["("<>ToString[ηa]<>")"]/.ndSol1]]," ,
",First[Re[ηb[t]/.ndSol1]]],{t,0,tde,tde/40}];
Print["Elastic loading"]
Do[Print[t," ,
",First[Re[(ToExpression[ToString[Kh]<>"*("<>"ηb[t]-
("<>ToString[ηa]<>"))^1.5"])/.ndSol1]]," ,
",First[Re[ToExpression["ηb[t]-
("<>ToString[ηa]<>")"]/.ndSol1]]," ,
",First[Re[ToExpression["("<>ToString[ηa]<>")"]/.ndSol1]]," ,
",First[Re[ηb[t]/.ndSol1]]],{t,0,ty,ty/20}]
Print["Elastoplastic loading"]
Do[Print[t," ,
",First[Re[(ToExpression[ToString[Kh]<>"*("<>ToString[reldis-
δy]<>")^1.5+"<>ToString[Kh*δy^1.5]])/.ndSol2]]," ,
",First[Re[ToExpression["ηb[t]-
("<>ToString[ηa]<>")"]/.ndSol2]]," ,
",First[Re[ToExpression["("<>ToString[ηa]<>")"]/.ndSol2]]," ,
",First[Re[ηb[t]/.ndSol2]]],{t,ty,te,(te-ty)/20}]
Print["Elastic unloading"]
Do[Print[t," ,
",First[Re[(ToExpression[ToString[Ku]<>"*("<>ToString[reldis-
df]<>")"<>"^1.5"])/.ndSol3]]," ,
",First[Re[ToExpression["ηb[t]-
("<>ToString[ηa]<>")"]/.ndSol3]]," ,
",First[Re[ToExpression["("<>ToString[ηa]<>")"]/.ndSol3]]," ,
",First[Re[ηb[t]/.ndSol3]]],{t,te,tue,(tue-
te)/20}]},{Print["Elastic Impact response"];
Do[Print[t,"                                                    ,
",First[Re[(ToExpression[ToString[Kh]<>"*("<>"ηb[t]-
("<>ToString[ηa]<>"))^1.5"])/.ndSol1]],"                        ,
",First[Re[ToExpression["ηb[t]-
("<>ToString[ηa]<>")"]/.ndSol1]],"                              ,
",First[Re[ToExpression["("<>ToString[ηa]<>")"]/.ndSol1]]," ,
",First[Re[ηb[t]/.ndSol1]]],{t,0,tde,tde/40}]}]
```

REFERENCES

Abramovich, H. (1998): Deflection Control of Laminated Composite Beams with Piezoceramic Layers - Closed Form Solutions, *Composites Structures*, 43, 217 – 231.

Abrate, S. (1998): Impact on Composite Structures, *Cambridge University Press*, Cambridge.

Abrate, S. (2001): Modeling of Impacts on Composite Structures, *Computers and Structures*, 51, pp 129 – 138.

Abrate, S. (2011): Impact Dynamics, In: Abrate, S. (ed) Impact Engineering of Composite Structures, *SpingerWien*, New York.

Alcalá, J., Giannakopoulos, A.E., Suresh, S. (1998): Continuous Measurements of Load Penetration Curves with Spherical Microindenters and the Estimation of Mechanical Properties, *Journal of Materials Research*, 13, pp 1390–1400.

Anderson, T.A. (2005): An Investigation of SDOF Models for Large Mass Impact on Sandwich Composites, *Composites: Part B*, 36, pp 135 – 142.

Angioni, S.L., Meo, M., Foreman, A. (2011): Impact Damage Resistance and Damage Suppression Properties of Shape Memory Alloys in Hybrid Composites – A Review, *Smart Materials and Structures*, 20, 013001.

Auricchio, F. and Sacco, E. (2003): Refined First-Order Shear Deformation Theory Models for Composite Laminates, *Journal of Applied Mechanics*, 70, pp 381 – 390.

Bartier, O., Hernot, X., Mauvoisin, G., (2010): Theoretical and experimental analysis of contact radius for spherical indentation, *Mechanics of Materials*, 42, pp 640–656.

Bert, C.W. and Chen, T.L.C. (1978): Effect of Shear Deformation on Vibration of Antisymmetric Angle-Ply Laminated Rectangular Plate, *International Journal of Solids and Structures*, 14, pp 465 – 473.

Bicho, E., Mallet, P., Schoner, G. (2000): Target Representation on an Autonomous Vehicle with Low-level Sensors, *International Journal of Robotics Research*, 19 (5), pp 424 – 447.

Big-Alabo, A. and Cartmell, M.P. (2011): Vibration Analysis of a Trimorph Plate for Optimised Damage Mitigation, *Journal of Theoretical and Applied Mechanics*, 49 (3), pp 641 – 664.

Big-Alabo, A. and Cartmell, M.P. (2012): Vibration Analysis of a Trimorph Plate as a Precursor Model for Smart Automotive Bodywork, *Journal of Physics: Conference Series*, 382 (012012).

Big-Alabo, A., Harrison P., Cartmell, M.P. (2014a): Elastoplastic Half-space Impact Analysis Using a Novel Contact Model that Accounts for Post-yield Effects, *Proceedings of the 9th International Conference on Structural Dynamics, EURODYN*, Porto, 30 June – 2 July.

Big-Alabo, A., Harrison P., Cartmell, M.P. (2014b): Algorithm for the solution of elastoplastic half-space impact: Force-Indentation Linearisation Method, *Proc. IMechE, Part C: Journal of Mechanical Engineering Sciences*, Early Online Publication, DOI: 10.1177/0954406214541431.

Big-Alabo, A., Harrison, P., Cartmell, M.P. (2015a): Contact Model for Elastoplastic Analysis of Half-space Indentation by a Spherical Impactor, *Computers and Structures,* 151, pp 20 – 29.

Big-Alabo, A., Harrison, P., Cartmell, M.P. (2015b): Preliminary Investigations of the Low-Velocity Impact Response of a Smart Trimorph Plate for Active Damage Mitigation, *5th Thematic Conference on Computational Methods in Structural Dynamics and Earthquake Engineering, COMPDYN*, Crete Island, Greece, 25 – 27 May, 2015.

Brake, M.R. (2012): An Analytical Elastic-Perfectly Plastic Contact Model, *International Journal of Solids and Structures*, 49, pp 3129 – 3141.

Cairns, D.S. (1991): A Simple, Elasto-Plastic Contact Law for Composites, *Journal of Reinforced Plastics and Composites*, 10, pp 423 – 433.

Carrera, E. (2004): On the Use of the Murakami's Zig-Zag Function in the Modelling of Layered Plates and Shells, *Computers and Structures*, 82, pp 541 – 554.

Carvalho, A. and Guedes Soares, C. (1996): Dynamic Response of Rectangular Plates of Composite Materials Subjected to Impact Loads, *Composite Structures*, 34, pp 55 – 63.

Chai, G.B. and Zhu, S. (2011): A Review of Low-Velocity Impact on Sandwich Structures, *Proc. IMechE, Part L: Journal of Materials Design and Applications*, 225, pp 207 – 230.

Chopra, I. (2002): Review of State of Art of Smart Structures and Integrated Systems, *AIAA Journal*, 40 (11), pp 2145 – 2187.

Christoforou, A.P. and Swanson, S.R. (1991): Analysis of Impact Response in Composite Plates, *International Journal of Solids and Structures*, 27 (2), pp 161 – 170.

Christoforou, A.P. and Yigit, A.S. (1995): Transient Response of a Composite Beam Subject to Elastic-Plastic Impact, *Composite Engineering*, 5 (5), pp 459 – 470.

Christoforou, A.P. and Yigit, A.S. (1998a): Characterisation of Impact in Composite Plates, *Composite Structures*, 43, pp 15 – 24.

Christoforou, A.P. and Yigit, A.S. (1998b): Effect of Flexibility on Low Velocity Impact Response, *Journal of Sound and Vibration*, 217 (3), pp 563 – 578.

Corbett, G.G., Reid, S.R., Johnson, W. (1996): Impact Loading of Plates and Shells by Free-flying Projectiles: A Review, *International Journal of Impact Engineering*, 18 (2), pp 141 – 230.

Dharmarajan, S. and McCutchen, H. (Jr) (1973): Shear Coefficient for Orthotropic Beams, *Journal of Composite Materials*, 7, pp 530 – 535.

Donadon *et al*, (2002): Stiffening Effects on the Natural Frequencies of Laminated Plates with Piezoelectric Actuators, *Composites: Part B*, 33, pp 335 – 342.

Edery-Azulay, L. and Abramovich, H. (2006): Active Damping of Piezo-composite Beams, *Composites Structures*, 74, 458 – 466.

Emile, G. and Matthew, H. (2003): The Assessment of Novel Materials and Processes for the Impact Tolerant Design of Stiffened Composite Aerospace Structures, *Composites: Part A*, 34, pp 151 – 161.

Foo, C.C., Seah, L.K., Chai, G.B. (2011): A Modified Energy-Balance to Predict Low-Velocity Impact Response for Sandwich Composites, *Computers and Structures*, Vol. 93, pp 1385 – 1393.

Ganilova, O.A. and Cartmell, M.P. (2010): An Analytical Model for the Vibration of a Composite Plate Containing an Embedded Periodic Shape Memory Alloy Structure, *Composites Structures*, Vol. 92, pp 39 – 47.

Ghugal, Y.M. and Shimpi, R.P. (2002): A Review of Refined Shear Deformation Theories of Isotropic and Anisotropic Laminated Plates, *Journal of Reinforced Plastics and Composites*, 21 (9), pp 775 – 813.

Goldsmith, W. (2001): Impact: The Theory and Physical Behaviour of Colliding Solids, *Dover Publications*, New York.

Grunenfelder, L.K., Suksangpanya, N., Salinas, C., Milliron, G., Yaraghi, N., Herrera, S., Evans-Lutterodt, K., Nutt, S.R., Zavattieri, P., Kisailus, D. (2014): Bio-inspired Impact-resistant Composites, *Acta Biomaterialia*, 10 (9), pp 3997 – 4008.

Hardy, C., Baronet, C.N., Tordion, G.V. (1971): The Elasto-Plastic Indentation of a Half-Space by a Rigid Sphere, *International Journal for Numerical Methods in Engineering*, 3, pp 451-462.

Hernandes, J.A., Almeida, S.F.M., Nabarrete, A. (2000): Stiffening Effects on the Free Vibration Behavior of Composite Plates with PZT Actuators, *Composite Structures*, 49, pp 55 – 63.

Hill, R., Storakers, B., Zdunek, A.B. (1989): A Theoretical Study of Brinell Hardness Test, *Proceedings of Royal Society London A*, 423, pp 301 – 330.

Hunter, S.C. (1957): Energy Absorbed by Elastic Waves During Impact, *Journal of Mechanics and Physics of Solids*, 5, pp 162 – 171.

Hutchings, I.M. (1979): Energy Absorbed by Elastic Wave During Plastic Impact, *Journal of Physics D: Applied Physics*, 12, pp 1819 – 1824.

Israr, A. (2008): Vibration Analysis of Cracked Aluminium Plates, PhD Thesis, *Department of Mechanical Engineering*, University of Glasgow, UK.

Jackson, R.L. and Green, I. (2005): A Finite Element Study of Elasto-Plastic Hemispherical Contact Against a Rigid Flat, *Journal of Tribology*, 127, pp 343 – 354.

Jackson, R.L., Green, I., Marghitu, D.B. (2009): Predicting the Coefficient of Restitution of Impacting Elastic-Perfectly Plastic Spheres, *Nonlinear Dynamics*, 60 (3), pp 217 – 229.

Johnson, K.L. (1985): Contact Mechanics, *Cambridge University Press*, Cambridge.

Jones, R.M. (1999): Mechanics of Composite Materials, 2nd Edition, *Taylor and Francis*, Philadelphia.

Kamiya R., Cheeseman, B.A., Popper, P., Chou, T.W. (2000): Some Recent Advances in the Fabrication and Design Three-dimensional Textile Preforms: A Review, *Composites Science and Technology*, 60, pp 33 – 47.

Karas, K. (1939): Platten unter seitchem stoss, *Ingenieur Archiv*, 10, pp 237-250.

Kazanci, Z. and Mecitoğlu, Z. (2008): Nonlinear dynamic behavior of simply supported laminated composite plates subjected to blast load, *Journal of Sound and Vibration*, 317, pp 883 – 897.

Khalili, M.R., Malekzadeh, K., Mittal, R.K. (2007c): Effect of Physical and Geometrical Parameters on the Transverse Low-Velocity Impact Response of Sandwich Panels with a Transversely Flexible Core, *Composite Structures*, 77, pp 430 – 443.

Khalili, S.M.R., Shokuhfar, A., Ghasemi, F.A. (2007d): Effect of Smart Stiffening Procedure on Low-velocity Impact Response of Smart Structures, *Journal of Materials Processing Technology*, 190, pp 142 – 152.

Khalili, S.M.R., Shokuhfar, A., Ghasemi, F.A., Malekzadeh, K. (2007a): Dynamic Response of Smart Hybrid Composite Plate Subjected to Low-Velocity Impact, *Journal of Composite Materials*, 41 (19), pp 2347 – 2370.

Khalili, S.M.R., Shokuhfar, A., Malekzadeh, K., Ghasemi, F.A. (2007b): Low-Velocity Impact Response of Active Thin-walled Hybrid Composite Structures Embedded with SMA Wires, *Thin-walled Structures*, 45, pp 799 – 808.

Kharaz, A.H. and Gorham, D.A. (2000): A Study of Coefficient of Restitution in Elastic-Plastic Impact, *Philosophical Magazine Letters*, 80 (8), pp 549 – 559.

Larson, R.A. and Palazotto, A.N. (2009): Property Estimation in FGM Plates Subject to Low-Velocity Impact Loading, *Journal of Mechanics of Materials and Structures*, 4 (7-8), pp 1429 – 1451.

Lau, K., Ling, H., Zhou, L. (2004): Low-velocity Impact on Shape Memory Alloy Stitched Composite Plates, *Smart Materials and Structures*, 13, pp 364 – 370.

Lazarus, K.B. (1989): Induced Strain Actuation of Composite Plates, SM Thesis, *Aero. and Astro. Dept.,* MIT Cambridge USA.

Lee, C.K. (1999): Theory of Laminated Piezoelectric Plates for the Design of Distributed Sensors/Actuators. Part I: Governing Equations and Reciprocal Relationships, *Journal of Acoustical Society of America*, 87 (3), pp 1144 – 1158.

Leissa, A.W. (1969): Vibration of Plates, *NASA SP-160*, U.S. Government Printing Office.

Li, L.Y., Thornton, C., Wu, C.Y. (2000): Impact Behaviour of Elastoplastic Spheres with a Rigid Wall, *Proc. IMechE, Part C: Journal of Mechanical Engineering Science*, 214, pp 1107 – 1114.

Li, L.Y., Wu, C.Y., Thornton, C. (2002): A theoretical model for the contact of elastoplastic bodies, *Proc. IMechE, Part C: Journal of Mechanical Engineering Science*, 216, pp 421 – 431.

Li, N. and Mirza, S. (1995): Vibration of Antisymmetric Angle-Ply Laminated Plates Including Transverse Shear Deformation, *Mechanics of Composite Materials and Structures*, 2 (2), pp 163 – 175.

Liew, K. M., Kitipornchai, S., Wang, C. M., Xiang, Y (1998): Vibration of Mindlin Plates: Programming the P-Version Ritz Method, 1st Edition, *Elsevier*, Amsterdam.

Liew, K.M., He, X.Q., Tan, M.J., Lim, H.K. (2004): Dynamic Analysis of Laminated Composite Plates with Piezoelectric Sensor/Actuator Patches using

the FSDT Mesh-free Method, *International Journal of Mechanical Sciences*, 46, pp 411 – 431.

Lifshitz, J.M. and Kolsky, H. (1964): Some Experiments on Anelastic Rebound, *Journal of Mechanics and Physics of Solids*, pp 12, 35 – 43.

Lin, J. and Nien, M.H. (2007): Adaptive Modeling and Shape Control of Laminated Plates using Piezoelectric Actuators, *Journal of Material Processing Technology*, 189, pp 231 – 236.

Madabhusi-Raman, P. and Daralos, J.F. (1996): Static Shear Correction Factor for Laminated Composite Rectangular Beams, *Composites: Part B*, 27, pp 285 – 293.

Majeed, M.A., Yigit, A.S., Christoforou, A.P. (2012): Elastoplastic Contact/Impact of Rigidly Supported Composites, *Composites: Part B*, 43, pp 1244 – 1251.

Manoach, E. and Trendifilova, I. (2008): Large amplitude vibrations and damage detection of rectangular plates, *Journal of Sound and Vibration*, 315, pp 591 – 606.

Mitchell, J.A. and Reddy, J.N. (1995): A Refined Hybrid Plate Theory for Composite Laminates with Piezoelectric Laminae, *International Journal of Solids and Structures*, 32 (6), pp 2345 – 2367.

Moita, J. M. S., Correia, I. F.P., Soares, C. M. M., Soares, C. A. M. (2004): Active Control of Adaptive Laminated Structures with Bonded Piezoelectric Sensors and Actuators, *Computers and Structures*, 82, pp 1349 – 1358.

Mok, C.H. and Duffy, J. (1965): The Dynamic Stress-Strain Relation of Metals as Determined from Impact Test with a Hard Ball, *International Journal of Mechanical Sciences*, 7, pp 355 – 371.

Mouritz, A.P. and Cox, M.K. (2010): A Mechanistic Interpretation of the Comparative In-plane Mechanical Properties of 3D Woven, Stitched and Pinned Composites, *Composites: Part A*, 41, pp 709 – 728.

Mouritz, A.P., Bannister, M.K., Falzon, P.J., Leong, K.H. (1999): Review of Applications for Advanced Three-dimensional Fibre Textile Composites, *Composites: Part A*, 30, pp 1445 – 1461.

Mujica, F. (2014): Scalable Electronics Driving Autonomous Vehicle Technologies, *Texas Instruments Inc.*, http://www.ti.com/lit/wp/sszy010a/sszy010a.pdf, Accessed: 5 December 2014.

Nguyen, Q. and Tong, L. (2004): Shape Control of Smart Composite Plate with Non-rectangular Piezoelectric Actuators, *Composites Structures*, 66, pp 207 – 214.

Nosier, A., Kapania, R.K., Reddy, J.N. (1994): Low-Velocity Impact of Laminated Composite Plates Using a Layerwise Theory, *Computational Mechanics*, 13, pp 360 – 379.

Oguamanam, D.C.D., Almeida, S.F.M., Hansen, J.S. (1998): Stress Stiffening Effects in Laminated Beams with Piezoelectric Actuators, *Journal of Intellingent Materials Systems and Structures*, 9, pp 137 – 145.

Olsson, R. (1992): Impact Response of Orthotropic Composite Laminates Predicted by a One-Parameter Differential Equation, *AIAA Journal*, 30 (6), pp 1587 – 1596.

Olsson, R. (2000): Mass Criterion for Wave Controlled Impact Response of Composite Plates, *Composites: Part A*, 31, pp 879 – 887.

Olsson, R. (2001): Analytical Prediction of Large Mass Impact Damage in Composite Laminates, *Composites: Part A*, 32, pp 1207 – 1215.

Olsson, R. (2002): Engineering Method for Prediction of Impact Response and Damage in Sandwich Panels, *Journal of Sandwich Structures and Materials*, 4, pp 3 – 29.

Olsson, R. (2003): Closed Form Prediction of Peak Load and Delamination Onset Under Small Mass Impact, *Composite Structures*, 59, pp 341 – 349.

Olsson, R., Donadon, M.V., Falzon, B.G. (2006): Delamination Threshold Load for Dynamic Impact on Plates, *International Journal of Solids and Structures*, 43, pp 3124 – 3141.

Omidvar, B. (1998): Shear Coefficient in Orthotropic Thin-Walled Composite Beams, *Journal of Composites for Construction*, 2 (1), pp 46 – 56.

Preumont, A. (2011): Vibration Control of Active Structures, 3rd Edition, *Springer-Verlag*, Berlin.

Reddy, J.N. (1984): A Refined Non-Linear Theory of Plates with Transverse Shear Deformation, *International Journal of Solids and Structures*, 20 (9-10), pp 881 – 896.

Reddy, J.N. (1999): On Laminated Composite Plates with Integrated Sensors and Actuators, *Engineering Structures*, 21, pp 568 – 593.

Reddy, J.N. (2004): Mechanics of Laminated Composite Plates and Shells: Theory and Analysis, 2nd Edition, *CRC Press*, Boca Raton.

Saravanos, D.A. and Christoforou, A.P. (2002): Impact Response of Adaptive Piezoelectric Laminated Plates, *AIAA Journal*, 40 (10), pp 2087 – 2095.

Sears, J.E. (1908): On the Longitudinal Impact of Metal Rods with Rounded Ends, *Proceedings of the Cambridge Philosophical Society*, 14, pp 257 – 286.

Shariyat, M. and Farzan, F. (2013): Nonlinear Eccentric Low-Velocity Impact Analysis of Highly Prestressed FGM Rectangular Plate, Using a Refined Contact Law, *Archive of Applied Mechanics*, 83, pp 623–641.

Shariyat, M. and Jafari, R. (2013): A Micromechanical Approach for Semi-Analytical Low-Velocity Impact Analysis of Bidirectional Functionally Graded Circular Plate Resting on an Elastic Foundation, *Meccanica*, 48, pp 2127 – 2148.

Shimpi, R.P., Patel, H.G., Arya, H. (2007): New Fisrt-Order Shear Deformation Plate Theories, *Journal of Applied Mechanics*, 74, pp 523 – 533.

Staab, G.H. (1999): Laminar Composites, *Butterworth Heinemann*, Boston.

Stronge, W.J. (2000a): Impact Mechanics, *Cambridge University Press*, Cambridge.

Stronge, W.J. (2000b): Contact Problems for Elasto-Plastic Impact in Multi-Body Systems, In: Bernard Brogliato (Ed.) Impacts in Mechanical Systems: Analysis and Modelling, *Springer*, Berlin.

Sun, C. T. and Yang, S. H. (1980): Contact Law and Impact Responses of Laminated Composites, *NASA Report – CR 159884*.

Sutherland, L.S. and Guedes Soares, C. (2005): Contact indentation of marine composites, *Composites Structures*, 70, pp 287– 294.

Szilard, R. (2004): Theory and Applications of Plate Analysis: Classical, Numerical and Engineering Methods, *John Wiley & Sons Inc.*, New Jersey.

Tabor, D. (1951): Hardness of Metals, *Oxford University Press*, London.

Teh, K.K and Haung, C.C (1979): Shear Deformation Coefficient for Generally Orthotropic Beam, *Fibre Science and Technology*, 12, pp 73 – 80.

Thai, H.T. and Choi, D.H. (2013): A Simple First-Order Shear Deformation Theory for Laminated Composite Plates, *Composite Structures*, 106, pp 754 – 763.

Thompson, S.P. and Loughlan, J. (1995): The Active Buckling Control of some Composite Column Strips using Piezoceramic Actuators, *Composite Structures*, 32, pp 59 – 67.

Thornton, C. and Ning, Z. (1998): A Theoretical Model for Stick/Bounce Behaviour of Adhesive Elastic-Plastic Spheres, *Powder Technology*, 99, pp 154 – 162.

Tillett, J.P.A. (1954): A Study of the Impact of Spheres on Plate, *Proceedings of the Physical Society: Section B*, 67 (9), pp 677 – 688.

Timoshenko, S. and Woinowsky-krieger, S. (1959): Theory of Plates and Shells, 2nd Edition, *McGraw-Hill*, New York.

Timoshenko, S.P. (1913): Zur farge nach der wirkung eines Stosses auf einen Balken, *Z.A.M.P.*, 62, pp 198 – 209.

Turner, J.R. (1980): Contact on a Transversely Isotropic Half-space, or between Two Transversely Isotropic Bodies, *International Journal of Solids and Structures*, 16(5), pp 409 – 419.

Vinson, J.R. and Sierakowski, R.L. (2004) The Behaviour of Structures Composed of Composite Materials, 2nd Edition, *Kluwer Academic Publishers*, New York.

Waisman, H. and Abramovich, H. (2002): Active Stiffening of Laminated Composite Beams using Piezoelectric Actuators, *Composites Structures*, 58, pp 109 – 120.

Wittrick, W.H. (1987): Analytical, Three-Dimensional Elasticity Solutions to Some Plate Problems, and Some Observations on Mindlin's Plate Theory, *International Journal of Solids and Structures*, 23 (4), pp 441 – 464.

Wolfram Research Inc. (2012): Mathematica Version 9.0, *Wolfram Research Inc.*, Champaign, Illinois.

Wu, C., Li, L., Thornton, C. (2003): Rebound behaviour of spheres for plastic impacts, *International Journal of Impact Engineering*, 28, pp 929 – 946.

Wu, C.Y., Li, L.Y., Thornton, C., (2005): Energy Dissipation During Normal Impact of Elastic and Elastic-Plastic Spheres, *International Journal of Impact Engineering*, 32, pp 593 – 604.

Wu, E. and Shyu, K. (1993): Response of Composite Laminates to Contact Loads and Relationship to Low-Velocity Impact, *Journal of Composite Materials*, 27, pp 1443 – 1464.

Yigit, A.S. and Christoforou, A.P. (1994): On the Impact of a Spherical Indenter and an Elastic-Plastic Isotropic Half-Space, *Composite Engineering*, 4 (11), pp 1143 – 1152.

Yigit, A.S. and Christoforou, A.P. (1995): Impact Dynamics of Composite Beams, *Composite Structures*, 32, pp 187 – 195.

Yigit, A.S. and Christoforou, A.P. (2000): Control of Low-velocity Impact Response on Composite Plates, *Journal of Vibration and Control*, 6, pp 429 – 447.

Zak, A.J. and Cartmell, M.P. (2000): Analytical Modelling of Shape Memory Alloys and Flat Multilayered Composite Beams and Plates with Shape Memory Alloy Wires, Technical Report (Grant number: GR/N06267/01), *Department of Mechanical Engineering*, University of Glasgow, UK.

Zak, A.J., Cartmell, M.P. and Ostachowicz, W. (2003): Dynamics of Multilayered Composite Plates with Shape Memory Alloy Wire, *Journal of Applied Mechanics*, 70, pp 313 – 327.

Zener, C. (1941): The Intrinsic Inelasticity of Large Plates, *Physical Review*, 59, pp 669 – 673.

Zheng, D. and Binienda, W.K. (2007): Effect of Permanent Indentation on the Delamination Threshold for Small Mass Impact on Plates, *International Journal of Solids and Structures*, 44, pp 8143 – 8158.

Zhu, F.,Wang, Z., Lu, G., Nurick, G. (2010): Some Theoretical Considerations on the Dynamic Response of Sandwich Structures Under Impulsive Loading, *International Journal of Impact Engineering*, 37, pp 625 – 637.